

ACOUSTIC TRANSDUCTION – MATERIALS AND DEVICES

Period 1 January 2000 to 31 December 2000

Annual Report

VOLUME VI

**OFFICE OF NAVAL RESEARCH
Contract No: N00014-96-1-1173**

**APPROVED FOR PUBLIC RELEASE –
DISTRIBUTION UNLIMITED**

**Reproduction in whole or in part is permitted for any
purpose of the United States Government**

Kenji Uchino

PENNSTATE



**THE MATERIALS RESEARCH LABORATORY
UNIVERSITY PARK, PA**

20010817 101

ABSTRACT

This report describes research performed over the period 1st January 2000 to 31st December 2000 on a MURI under Office of Naval Research contract N00014-96-1-1173 on the topic "Acoustic Transduction Materials and Devices". This program brings together researchers from the Materials Research Laboratory (MRL), the Applied Research Laboratory (ARL) and the Center for Acoustics and Vibrations (CAV) at the Pennsylvania State University. As has become customary over many years, research on the program is detailed in the technical appendices of published work, and only a brief narrative description connecting these studies is given in the text.

The program combines a far reaching exploration of the basic phenomena contributing to piezoelectric and electrostrictive response with the highly applied thrusts necessary to produce the "pay-off" in new applications relevant to Navy needs. Polarization vector tilting in the ferroelectric phase of perovskite structure crystals at compositions close to a morphotropic phase boundary (MPB) was first underscored on this program some four years ago, and is now widely accepted as one mode for exploiting the large intrinsic spontaneous strain in the ferroelectric to produce exceedingly strong anhysteretic piezoelectric response and very large electric field controlled elastic strain. New evidence for the importance of both spontaneous (monoclinic) and electric field induced tilting on the properties of both single and polycrystal MPB systems is presented in this report.

The puzzling phenomena associated with relaxor ferroelectric response have long been a topic of study in MRL, where the micro-polar region model and the application of Vogel/Fulcher to the dielectric slowing down were first applied. The current "pay-off" is in the greatly enhanced relaxor ferroelectric electrostrictive response from high electron energy irradiated polyvinylidene difluoride: trifluoroethylene (PVDF: TrFE) co-polymer discussed in this report. This development opens a new field of high strain, high energy density actuators with tremendous practical applicability. Now the possibility of engineering this response by chemical manipulation in the terpolymer systems without irradiation further enhances the exciting possibilities.

In composite structures, the early promise of the flextensional cymbal type actuators is now being fully realized and programs exploring large area cymbal transducer arrays are progressing very well, both at MRL/ARL and at NRL. The connection with CAV at Penn State is particularly important in keeping the MURI faculty aware of problems endemic to water as our host medium and the effects of turbulence in flow and the need for many types of acoustic noise control.

New designs of piezoelectric transformers and motors are demanding materials with lower loss levels under continuous high driving, and important progress is reported in separating and understanding the components of this loss and in designing new doping schemes for ceramics which enhance power capability almost tenfold. New piezoelectric micro-motor designs look particularly attractive and appear to offer significant advantages over electromagnetics for very small-scale applications. Thick and thin film studies for MEMS are progressing well and offering new insights into fatigue and switching behavior in the ferroelectrics.

**ACOUSTIC TRANSDUCTION –
MATERIALS AND DEVICES**

Period 1 January 2000 to 31 December 2000

Annual Report

VOLUME VI

**OFFICE OF NAVAL RESEARCH
Contract No: N00014-96-1-1173**

**APPROVED FOR PUBLIC RELEASE –
DISTRIBUTION UNLIMITED**

**Reproduction in whole or in part is permitted for any
purpose of the United States Government**

Kenji Uchino

APPENDICES

VOLUME I

GENERAL SUMMARY PAPERS

1. Uchino, K., Encyclopedia of Vibration, Partial Charge "Electrostrictive Materials", Academic Press, London (2000). [in press]
2. Uchino, K., and Y. Ito, Encyclopedia Smart Materials, J. Harvey, Edit., Partial Charge "Smart Ceramics: Transducers, Sensors and Actuators", John Wiley & Sons, New York (2000). [in press]
3. Wennu Ma, L.E. Cross, "Observation of the flexoelectric effect in relaxor PB ($\text{Mg}_{1/3}\text{Nb}_{2/3}$) O_3 ceramics", Applied Physics Letters. Volume #8 number 19 pp. 2920
4. R. Hatt and W. Cao, "Landau-Ginzburg Model for Antiferroelectric Phase Transition Based on Microscopic Symmetry", Phys. Rev. B, vol. 62, pp. 818-823 (2000).

2.0 MATERIALS STUDIES

2.1 Polycrystal Perovskite Ceramics

5. A.S. Bhalla, R. Guo, R. Roy, "The Perovskite Structure - A Review of Its Role in Ceramic Science and Technology, "Mat. Res. Innovat., 4(1), 3-26, (2000)
6. E.F. Alberta, R. Guo, L.E. Cross, A.S. Bhalla, "Structure-Property Diagrams of Ferroic Solid Solutions. Part I: Perovskite Ferroelectrics with Morphotropic Phase Boundaries," *Ferroelectrics Review*, 3, 1, (2001)
7. B. Noheda, J.A. Gonzalo, L.E. Cross, R. Guo, S-E. Park, D.E. Cox, G. Shirane, "Tetragonal-to-Monoclinic Phase Transition in a Ferroelectric Perovskite: the Structure of $\text{PbZr}_{0.52}\text{Ti}_{0.48}\text{O}_3$, "Phys. Rev. B, 61(13), 8687-8689, (2000)
8. B. Noheda, D.E. Cox, G. Shirane, R. Guo, B. Jones, L.E. Cross, "Stability of the monoclinic phase in the ferroelectric perovskite $\text{PbZr}_{(1-x)}\text{Ti}_x\text{O}_3$, "Los Alamos Natl. Lab., Prepr. Arch., Condens. Matter, 1-8, arXiv:cond-mat/0006152, (2000)
9. R. Guo, L.E. Cross, S-E. Park, B. Noheda, D.E. Cox, G. Shirane, "Origin of the high piezoelectric response in $\text{PbZr}_{1-x}\text{Ti}_x\text{O}_3$," Phys. Rev. Letters, 84(23), 5423-5426, (2000)
10. W. Jiang and W. Cao, "Nonlinear Elastic Properties of Lead Zirconate Titanate Ceramics", J. Appl. Phys. vol. 88: 6684-6689 (2000).
11. Chen, Y. H., D. Viehland and K. Uchino, "Substituent Effects in $0.65\text{Pb}(\text{Mg}_{1/3}\text{Nb}_{2/3})\text{O}_3$ - 0.35PbTiO_3 Piezoelectric Ceramics" J. Electroceramics, 6, 13-20 (2001). (First Author Supervised by Candidate).
12. W.H. Jiang and W. Cao, "Intrinsic and Coupling-induced Elastic Nonlinearity of Lanthanum-doped Lead Magnesium Niobate-Lead Titanate Electrostrictive Ceramic", Appl. Phys. Lett., vol. 77, pp. 1387-1389 (2000).

VOLUME II

2.0 MATERIALS STUDIES

2.2 *Single Crystal Systems*

13. L.E. Cross, J. Fousek, "Engineering Multidomain Ferroic Samples", *Ferroelectrics*, 2001, Vol. 252, pp. 171-180.
14. Wada, Satoshi, Takaaki Tsurumi, Miour Osada, Masato Kakihana, Seung Eek Park, L.Eric Cross and Thomas R. Shrout. "Change of Macroscopic and Microscopic Symmetries in Relaxor PZN Single Crystal Under Bias Field." Transactions of the Material Research Society of Japan, **25** (1). 281-284 (2000).
15. Wada, Satoshi, Takaaki Tsurumi, Miour Osada, Masato Kakihana, Seung Eek Park, L.Eric Cross and Thomas R. Shrout. "Dipolar Behavior in PZN Relaxor Single crystals under Bias Fields." Transactions of the Materials Research Society of Japan **25** (1), 281-284 (2000).
16. Belegundu, U., X. Du and K. Uchino, "Switching Current in $\text{Pb}(\text{Zn}_{1/3}\text{Nb}_{2/3})\text{O}_3\text{-PbTiO}_3$ Single Crystals," Symp. LL Proc., Mater. Res. Soc. Fall Mtg. '99, (LL.1.9, Boston, Nov. 29-Dec.3. 1999), Vol.**604**, 39-44 (2000).
17. Yu Lu, D.-Y. Jeong, Z. Y. Cheng, Q. M. Zhang, H. Luo, Z. Yin, and D. Viehland. Phase Transitional Behavior and Piezoelectric Properties of the orthorhombic Phase of PMN-PT Single Crystals. *Appl. Phys. Lett.* **78**, 3109 (2001).
18. Yu Lu, Z.-Y. Cheng, E. Park, S. F. Liu and Q. M. Zhang. Linear Electro-optic Effect of $0.88\text{Pb}(\text{Zn}_{1/3}\text{Nb}_{2/3})\text{-}0.12\text{PbTiO}_3$ Single Crystal. *Jpn. J. Appl. Phys.* **39**, 141-145 (2000).
19. Y. Barad, Yu Lu, Z. Y. Cheng, S. E. Park, and Q. M. Zhang. Composition, Temperature, and Crystal Orientation Dependence of Linear Electro-optic Properties of PZN-PT Single Crystals. *Appl. Phys. Lett.* **77**, 1247-1249 (2000).
20. Y. Lu, Z.-Y. Cheng, Y. Barad, and Q. M. Zhang. Photoelastic Effects in the Tetragonal PZN-PT Single Crystals near the Morphotropic Phase Boundary. *J. Appl. Phys.* **89**, 5075 (2001).

2.3 *High Strain Polymers*

21. Vivek Bharti, H. S. Xu, G. Shanthi, Q. M. Zhang, and Kuming Liang. Polarization and Structural Properties of High Energy Electron Irradiated P(VDF-TrFE) Copolymer Films. *J. Appl. Phys.* **87**, 452-461 (2000).
22. Haisheng Xu, G. Shanthi, V. Bharti, Q. M. Zhang, and T. Ramatowski. Structural, Conformational, and Polarization Changes of P(VDF-TrFE) Copolymer Induced by High Energy Electron Irradiation. *Macromolecules*, **33**, 4125-4131(2000).
23. Q. M. Zhang, Z. Y. Cheng, and Vivek Bharti. Relaxor Ferroelectric Behavior in High Energy Electron Irradiated P(VDF-TrFE) copolymers. *Appl. Phys.* **A70**, 307-312 (2000).
24. Vivek Bharti and Q. M. Zhang. Dielectric Study of Relaxor Ferroelectric P(VDF-TrFE) Copolymer System. *Phys. Rev. B*. **63**, 184103 (2001).
25. Z.Y. Cheng, Vivek Bharti, T.B. Xu, Hansheng Xu, T. Mai, and Q. M. Zhang. Electrostrictive P(VDF-TrFE) Copolymers. *Sensors and Actuators A-Phys.* **90**, 138-147 (2001)

26. Z. Y. Cheng, V. Bharti, T. Mai, T. B. Xu, Q. M. Zhang, K. Hamilton, T. Ramotowski, K. A. Wright, and R. Ting. Effect of High Energy Electron Irradiation on the Electromechanical Properties of Poly(vinylidene fluoride-trifluoroethylene) 50/50 and 65/35 Copolymers. *IEEE Trans. UFFC* 47, 1296 (2000).
27. Vivek Bharti, Z.-Y. Cheng, T. Mai, Q. M. Zhang, T. Ramotowski, K. A. Wright. High Electromechanical Coupling Factor and Electrostrictive Strain over a Broad Frequency Range in Electrostrictive Poly(vinylidene fluoride-trifluoroethylene) Copolymer. *Jpn. J. Appl. Phys.* 40, 672 (2001).
28. Vivek Bharti, G. Shanthi, H. Xu, Q. M. Zhang, and K. Liang. Evolution of Transitional Behavior and Structure of Electron Irradiated P(VDF-TrFE) Copolymer Films. *Mater. Lett.* 47, 107-111 (2001).
29. F. Xia, H. Xu, F. Fang, B. Razivi, Z. Y. Cheng, Yu Lu, Baoming Xu, and Q. M. Zhang. Thickness Dependence Behavior of Ferroelectric Switching in P(VDF-TrFE) Spin Cast Films. *Appl. Phys. Lett.* 78, 1122 (2001).
30. Q. M. Zhang, H. S. Xu, Fei Fang, Z.-Y. Cheng, Xia Feng, and H. You. Observation of Critical Thickness of Crystallization in Spin Cast Ferroelectric Thin Films. *J. Appl. Phys.* 89, 2613 (2001).
31. Shizhuo Yin, Q. M. Zhang, K.-W. Chung, R. Yang, Z. Y. Cheng, and Yu Lu. Investigation of the Electro-optic Properties of Electron-irradiated P(VDF-TrFE) Copolymer. *Opt. Eng.* 39, 670-672 (2000).
32. Hai-Sheng Xu, Z.-Y. Cheng, Vivek Bharti, Shexi Wang, and Q. M. Zhang. All-Polymer Electromechanical Systems Consisting of Electrostrictive Poly(vinylidene fluoride-trifluoroethylene) and Conductive Polyaniline. *J. Appl. Poly. Sci.* 75, 945-951 (2000).
33. H. Xu, Z.Y. Cheng, D. Olson, T. Mai, Q. M. Zhang, and G. Kavarnos. Ferroelectric and Electromechanical Properties of P(VDF-TrFE-CTFE) Terpolymer. *Appl. Phys. Lett.* 78, 2360 (2001).

3.0 TRANSDUCER STUDIES

3.1 *Composite Structures*

34. Uchino, K., "Piezoelectro Composites," Chap.5.24, *Comprehensive Composite Materials*, Elsevier Science, Oxford, UK (2000).
35. Tressler, J. and K. Uchino, "Piezoelectric Composite Sensors," Chap.5.22, *Comprehensive Composite Materials*, Elsevier Science, Oxford, UK (2000).

VOLUME III

36. Meyer, R.J. Jr., A. Dogan, C. Yoon, S. Pilgrim and R.E. Newnham, "Displacement Amplification of Electroactive Materials Using the Cymbal Flexensional Transducer," *Sensors & Actuators A*, vol.87, pp. 157-162 (2001).
37. Dogan, A., K. Uchino and R. E. Newnham, "Flexensional Composite Transducers: Designing, Fabrication and Application," *Proc. NATO- Advanced Research Workshop: Piezoelectric Materials: Advance in Science, Technology and Applications*, (Predeal, Romania, May 24-27, 1999, Kluwer Academic Publ., p.357-374 (2000).

38. Zhang, J., A.C. Hladky-Hennion, W.J. Hughes, and R.E. Newnham, "Modeling and Underwater Characterization of Cymbal Transducers and Arrays," IEEE Transactions on Ultrasonics, Ferroelectrics, and Frequency Control, vol. 48 (2), pp. 560-568 (2001).
39. Zhang, J., W. J. Hughes, R. J. Meyer Jr., K. Uchino and R. E. Newnham, "Cymbal Array: A Broad Band Sound Projector," Ultrasonics 37, 523-529 (2000).
40. Zhang, J., A.C. Hladky-Hennion, W.J. Hughes, and R.E. Newnham, "A Miniature Class V flexensional cymbal transducer with directional beam pattern: The Double-Driver," Ultrasonics, vol. 39, pp. 91-95 (2001).
41. Meyer, R.J. Jr. and R.E. Newnham, "Flexensional transducers with Shape Memory Caps for Tunable Devices," Journal of Intelligent Materials Systems and Structures, vol. 11, pp. 199-205 (2001).
42. Meyer, R.J. Jr., S. Alkoy, J. Cochran, T. Ritter, and R.E. Newnham, "Pre-focused Lead Titanate > 25 MHz Single Element Transducers from Hollow Spheres," IEEE Transactions on Ultrasonics, Ferroelectrics, and Frequency Control, vol. 48 (2), pp. 488-493 (2001).
43. Y. Bai, Z.Y. Cheng, V. Bharti, H. S. Xu, and Q. M. Zhang. High Dielectric Constant Ceramic Powder Polymer Composites. Appl. Phys. Lett. 76, 3804-3806 (2000).
44. M.R. Shen and W. Cao, "Acoustic Bandgap Formation in a Periodic Structure with Multilayer Unit Cells", J. Phys. D: Applied Physics, vol. **33**, pp. 1150-1154 (2000).
45. T.B. Xu, Z-Y. Cheng, Q. M. Zhang, R. Baughman, C. Cui, A. Zakhidov, and J. Su. Fabrication and Characterization of 3-Dimensional Periodic Ferroelectric Polymer-Silica Opal Composites and Inverse Opal. J. Appl. Phys. 88(1), 405-409 (2000).

3.2 *Piezoelectric Transformers*

46. Uchino, K., B. Koc, P. Laoratanakul and A. Vazquez Carazo, "Piezoelectric Transformers –New Perspective--," Proc. 3rd Asian Mtg. Ferroelectrics, D1d.1, Hong Kong, Dec. 12-15 (2000).
47. Koc, B., and K. Uchino, "Disk Type Piezoelectric Transformer with Crescent Shape Input Electrodes," Proc. NATO- Advanced Research Workshop: Piezoelectric Materials: Advance in Science, Technology and Applications, (Predeal, Romania, May 24-27, 1999, Kluwer Academic Publ., p.375-382 (2000).

3.3 *High Power Level Materials*

48. Uchino, K. and S. Hirose, "Loss Mechanisms in Piezoelectrics: How to Measure Different Losses Separately," IEEE UFFC Transactions, **48**, 307-321 (2001).
49. Uchino, K., and J. Zheng, Y. H. Chen, X. Du and S. Hirose, "Loss Mechanisms in Piezoelectrics and Resonance/ Antiresonance," Proc. 101st Annual Mtg. of Amer. Ceram. Soc., Symp. Electronic Ceramic Materials and Devices, (Indianapolis, April 25 – 28, 1999), p.79-100 (2000).
50. Uchino, K., J. Zheng, Y. H. Chen, X. Du, S. Hirose and S. Takahashi, "Loss Mechanisms in Piezoelectrics –Extrinsic and Intrinsic Losses--," Mater. Res. Soc. Fall Mtg. '99, (LL.1.6, Boston, Nov. 29-Dec.3, 1999), Vol. **604**, 25-31 (2000).

51. Chen, Y. H., S. Hirose, D. Viehland and K. Uchino, "Doping Effects in $\text{Pb}(\text{Mg}_{1/3}\text{Nb}_{2/3})\text{O}_3\text{-PbTiO}_3$ Ceramics for High Power Transduction Applications," Mater. Res. Soc. Fall Mtg. '99, (LL.5.8, Boston, Nov. 29-Dec.3, 1999), Vol. **604**, 215-220 (2000).
52. Chen, Y. H., S. Hirose, D. Viehland, S. Takahashi and K. Uchino, " Mn-Modified $\text{Pb}(\text{Mg}_{1/3}\text{Nb}_{2/3})\text{O}_3\text{-PbTiO}_3$ Ceramics: Improved Mechanical Quality Factors for High-Power Transducer Applications," Jpn. J. Appl. Phys. **39**, 4843-4852 (2000).
53. Gao, Y. Y. H. Chen, J. Ryu, K. Uchino and D. Viehland, " Eu and Yb Substituent Effects on the Properties of $\text{Pb}(\text{Zr}_{0.52}\text{Ti}_{0.48})\text{O}_3\text{-Pb}(\text{Mn}_{1/3}\text{Sb}_{2/3})\text{O}_3$ Ceramics: Development of a New High-Power Piezoelectric with Enhanced Vibrational Velocity," Jpn. J. Appl. Phys., **40**, 79-85 (2001).

VOLUME IV

3.4 *Fluid Structure Interactions*

54. Lauchle, G. C., W. A. Kargus IV. Scaling of Turbulent Wall Pressure Fluctuations Downstream of a Rearward Facing Step. *J. Acoust. Soc. Am.* **107**: L1-L6 (2000).
55. Capone, D. E., G. C. Lauchle. Modeling the Unsteady Lift and Drag on a Finite-Length Cylinder in Cross Flow. *J. Fluids and Struct.* **14**: 799-817 (2000).
56. Gavin, J. R., G. C. Lauchle. Modeling the Space-Time Correlations in the Wake Region of a Turbulent Boundary Layer. *Proc. of the ASME Noise Control and Acoustics Division 2000*, NCA-Vol. 27, pp 227-241 (2000).
57. Gavin, J. R., G. C. Lauchle, M. L. Jonson. Prediction of Turbulence Ingestion Forces for Rotors with Arbitrary Rake and Skew. *Proc. of the ASME Noise Control and Acoustics Division 2000*. NCA-Vol. 27, pp 217-226 (2000).
58. Lauchle, G. C, D. K. McLaughlin. Review of: *Acoustics of Fluid Structure Interactions* by M. S. Howe in *Noise Control Eng. J.* **48**: 70-71 (2000).

4.0 ACTUATOR STUDIES

4.1 *Materials and Designs*

59. Koc, B. and K. Uchino, "Piezoelectric Ultrasonic Motors," Chap.6.34, *Comprehensive Composite Materials*, Elsevier Science, Oxford, UK (2000).
60. Uchino, K., "Recent Trend of Piezoelectric Actuator Developments –Material, Design and Drive Technique Related Issues--," *Proc. Actuator 2000 (7th Int'l Conf. New Actuators, June 19-21, 2000)*, p.34-39 (2000).
61. Yao, K., K. Uchino, Y. Xu, S. Dong, and L. C. Lim, "Compact Piezoelectric Stacked Actuators for High Power Applications," *IEEE Trans. UFFC*, **47**, 819-825 (2000).
62. Liu, Rubin, L.e. Cross, Gareth Knowles, Bruce Bower, and Brookd Childers. " A Stackable Bonding-Free Flexensional Piezoelectirc Actuator" *Journal of Electroceramics* **4** (1), 201-206 92000)
63. A. E. Glazounov, Q. M. Zhang, C. Kim. Torsional Actuator Based on Mechanically Amplified Shear Piezoelectric Response. *Sensors and Actuators A* **79**, 22-30 (2000).

4.2 Photostriction

64. Poosanaas, P., K. Tonooka and K. Uchino, "Photostrictive Actuators," J. Mechatronics **10**, 467-487 (2000).
65. Uchino, K., P. Poosanaas and K. Tonooka, "Photostrictive Actuators–New Perspective-," Proc. 3rd Asian Mtg. Ferroelectrics, C3p.105, Hong Kong, Dec. 12-15 (2000).
66. Uchino, K., P. Poosanaas and K. Tonooka, "Photostrictive Actuators–New Perspective-," Proc. 5th Euroconf. Appl. Polar Dielectrics, O-43, Jurmala, Latvia, Aug. 27-30 (2000).
67. Poosanaas, P., K. Tonooka, I. R. Abothu, S. Komarneni, and K. Uchino, "Influence of Composition and Dopant on Photostriction in Lanthanum-Modified Lead Zirconate Titanate Ceramics," J. Intelligent Mater. Systems and Structures **10**, 439-445 (2000). (
68. Poosanaas, P., Dogan, A., Prasadarao, A. V., Komarneni, S. and Uchino, K., "Effect of Ceramic Processing Methods on Photostrictive Ceramics", J. Advanced Performance Mater. **6**, 57-69 (1999).

VOLUME V

4.3 High Force Actuators

69. A. E. Glazounov, Q. M. Zhang, and C. Kim. Torsional Actuator and Stepper Motor Based on Piezoelectric d_{15} Shear Response. J. Intel. Mater. Syst. & Struct. **11**(6), 456-468 (2000).
70. Galante, T., J. Frank, J. Bernard, W. Chen, G.A. Lesieutre, and G.H. Koopmann, "A High-Force, High-Displacement Piezoelectric Inchworm Actuator," Journal of Intelligent Materials Systems and Structures, Vol. 10, No. 12, December, 2000, pp. 962-972.

4.4 Piezoelectric Motors

71. Koc, B. and K. Uchino, "Piezoelectric Ultrasonic Motors," Chap.6.34, Comprehensive Composite Materials, Elsevier Science, Oxford, UK (2000).
72. Uchino, K., and B. Koc, "Compact Piezoelectric Ultrasonic Motors," Proc. NATO-Advanced Research Workshop: Piezoelectric Materials: Advance in Science, Technology and Applications, (Predeal, Romania, May 24-27, 1999, Kluwer Academic Publ., p.309-320 (2000).
73. Koc, B., J. F. Tressler and K. Uchino, "A Miniature Piezoelectric Rotary Motor Using Two Orthogonal Bending Modes of a Hollow Cylinder," Proc. Actuator 2000 (7th Int'l Conf. New Actuators, June 19-21, 2000), p.242-245 (2000).
74. Koc, B., J. F. Tressler and K. Uchino, "A Miniature Piezoelectric Rotary Motor Using Two Orthogonal Bending Modes of a Hollow Cylinder," Proc. Actuator 2000 (7th Int'l Conf. New Actuators, June 19-21, 2000), p.242-245 (2000).
75. Bouchilloux, P., B. Koc and K. Uchino, "New Concept for Resonant Longitudinal-Shear Ultrasonic Motor," Symp. LL Proc., Mater. Res. Soc. Fall Mtg. '99, (LL.2.10, Boston, Nov. 29-Dec.3, 1999), Vol. **604**, 71-78 (2000).

76. Koc. B., P. Bouchilloux, and K. Uchino, "Piezoelectric Micromotor Using A Metal-Ceramic Composite Structure," IEEE Trans. Ultrasonic, Ferroelectrics, and Frequency Control **47** (4), 836-843 (2000).
- 4.5 *Acoustic Absorbers*
77. Davis, C.L. and G.A. Lesieutre, "An Actively Tuned Solid State Vibration Absorber Using Capacitive Shunting of Piezoelectric Stiffness," Journal of Sound and Vibration, Vol. 232(3), 4 May 2000, pp. 601-617.
 78. Patricia L. Driesch, Hisao Iwata, Gary H. Koopmann, and Jeff Dosch. Nov. 2000. Development and evaluation of a surface acoustic intensity probe. Review of Scientific Instruments, 71 (11), pp. 1-6.
 79. W. Huang. G. H. Koopmann, S. J. Sharp, and W. Chen. April 2000. Enhanced Low Frequency Transmission Loss of Lightweight Trim Panels. Journal of Intelligent Material Systems and Structures, Volume 11, No 4.
 80. E.W. Constans, A.D. Belegundu, and G.H. Koopmann. 2000. Optimally Designed Shell Enclosures with Tuned Absorbers for Minimizing Sound Power. Optimization and Engineering, 1, 67-86, (an International Journal, Kluwer Publishers)

VOLUME VI

5.0 MODELING AND CHARACTERIZATION

5.1 *Design and Simulation*

81. K. Uchino, "Designing With Piezoelectric Devices" International Center for Actuators and Transducers, Materials Research Institute, The Pennsylvania State University, University Park, PA (2000)
82. W.K. Qi, and W. Cao, "Finite Element Study on 1-D Array Transducer Design", IEEE Transaction, Ultra. Ferro. and Frequency Control, vol. **47**, pp. 949-955 (2000).
83. T.A. Ritter, K. K. Shung, W. Cao and T. R. Shrout, "Electromechanical Properties of Thin Strip Piezoelectric Vibrators at High Frequency", J. Applied Phys, vol. **88**, pp. 394-397 (2000).
84. T.A. Ritter, K. K. Shung, W. Cao and T. R. Shrout, "Electromechanical Properties of Thin Strip Piezoelectric Vibrators at High Frequency", J. Applied Phys, vol. **88**, pp. 394-397 (2000).

5.2 *Thick and Thin Films*

85. Kalpat, S., X. Du, I. R. Abothu, A. Akiba, H. Goto and K. Uchino, "Effect of Crystal Orientation on Dielectric Properties of Lead Zirconate Titanate Thin Films Prepared by Reactive RF-Sputtering," Jpn. J. Appl. Phys., **40**, 158-162 (2001).
86. Kalpat, S., X. Du, I. R. Abothu, A. Akiba, H. Goto, S. Trolier-McKinstry and K. Uchino, "Dielectric Properties of Highly Oriented Lead Zirconate Titanate Thin Films Prepared by Reactive RF-Sputtering," Symp. LL Proc., Mater. Res. Soc. Fall Mtg. '99, (LL.1.3, Boston, Nov. 29-Dec.3, 1999), Vol. **604**, 3-8 (2000).
87. S. Trolier-McKinstry, "Piezoelectric Films for MEMS Applications," J. Ceram. Soc. Jpn. **109** (5) S76-S79 (2001).

88. Jeong Hwan Park, Fei Xu, and Susan Trolier-McKinstry, "Dielectric and Piezoelectric Properties of Sol-Gel Derived Lead Magnesium Niobium Titanate Films with Different Textures," *J. Appl. Phys.* 89(1) 568 - 574 (2001).
89. Q. F. Zhou, E. Hong, R. Wolf, and S. Trolier-McKinstry, "Dielectric and Piezoelectric Properties of PZT 52/48 Thick Films with (100) and Random Crystallographic Orientation," *Ferroelectric Thin Films*, Vol 655 (2000).
90. L.-P. Wang, R. Wolf, Q. F. Zhou, S. Trolier-McKinstry and R. J. Davis, "Wet-etch patterning of lead zirconate titanate (PZT) thick films for microelectromechanical systems (MEMS) application," *Mat. Res. Soc. Symp.* Vol.657 (MEMS)

5.3 Domain Studies

91. Uchino, K., and H. Aburatani, "Field Induced Acoustic Emission in Ferroelectric Ceramics," *Proc. 101st Annual Mtg. of Amer. Ceram. Soc., Symp. Electronic Ceramic Materials and Devices*, SE-56, (Indianapolis, April 25 – 28, 1999), (2000).
92. J. Fousek^{ab}, L.E. Cross^b, "Engineering Multidomain Ferroic Samples, Dept of Physics and International Center for Piezoelectric Research, University of Technology, Liberec, 46117 Czech Republic and ^b Materials Research Laboratory, The Pennsylvania State University, University Park, PA 16802, USA. (June 2000)
93. J.H. Yin, and W. Cao, "Domain Configurations in Domain-Engineered 0.955Pb(Zn_{1/3}Nb_{2/3})O₃-0.045PbTiO₃ Single Crystals", *J. Appl. Phys.*, vol. 87, pp. 7438-7441 (2000).
94. Rajeev Ahluwalia, "Computer Simulations of Domain Pattern Formation in Ferroelectrics", *AIP Conference Proceedings Series*, © 2001 American Institute of Physics, *Proceedings of the 2001 Workshop on Fundamental Physics of Ferroelectrics* Williamsburg, Va, 2001
95. R. Ahluwalia and W. Cao, "Influence of Dipolar Defects on Switching Behavior in Ferroelectrics", *Phys. Rev. B*, vol. 63, pp. 012103 (2000)
96. Uchino, K., and H. Aburatani, "Field Induced Acoustic Emission in Ferroelectric Ceramics," *Proc. 101st Annual Mtg. of Amer. Ceram. Soc., Symp. Electronic Ceramic Materials and Devices*, SE-56, (Indianapolis, April 25 – 28, 1999), (2000).

MODELING and CHARACTERIZATION

Design and Simulation

APPENDIX 81

DESIGNING WITH PIEZOELECTRIC DEVICES

Kenji Uchino

International Center for Actuators and Transducers, Materials Research Institute
The Pennsylvania State University, University Park, PA 16802

ABSTRACT

The performance of piezoelectric ceramic devices is dependent on complex factors, which are divided into three major categories: the properties of the ceramic itself, and coupled issues with the device design and drive technique. This paper reviews their designing issues from these viewpoints. Optimization of the piezo-ceramic composition, doping, and the cut angle of a single crystal sample is necessary to enhance the induced strains under a high stroke level drive, and to stabilize temperature and external stress dependence. The device design affects considerably its durability and lifetime, as well as its improved performance. Failure detection or "health" monitoring methods of ceramic actuators will increase the reliability remarkably. Regarding drive techniques, pulse drive and ac drive require special attention; the vibration overshoot after applying a sharp-rise step/pulse voltage to the actuator causes a large tensile force and a long-term application of AC voltage generates considerable heat.

INTRODUCTION

The application area of piezoelectric ceramics has become remarkably broad particularly in actuators and transformers [1,2]. Accordingly, their designing algorithm is now being established. The device designing has two major roles: improvement in the device characteristics and in the reliability/lifetime. The performance of ceramic actuators is dependent on complex factors, which are divided into three major categories: the properties of the ceramic itself, and the coupled issues of the device design and drive technique. This paper considers the piezoelectric device designing issues from these viewpoints for improving both performance and reliability.

MATERIALS IMPROVEMENTS

Performance

Higher strain or stress is the primary key factor to the actuator/transducer materials. Because the lead zirconate titanate (PZT) used to be obtained only in a polycrystalline phase, the previous researchers used the sample geometry with the applied electric field only parallel to the spontaneous polarization (i.e., poling direction). Figure 1 shows the typical strain curves for a piezoelectric lanthanum-doped PZT (PLZT) and an electrostrictive $\text{Pb}(\text{Mg}_{1/3}\text{Nb}_{2/3})\text{O}_3\text{-PbTiO}_3$ (PMN) [1]. Note the maximum strain level of 0.1%.

However, after the discovery of superior characteristics in single crystals $\text{Pb}(\text{Zn}_{1/3}\text{Nb}_{2/3})\text{O}_3\text{-PbTiO}_3$ [3], the crystal orientation dependence of piezoelectricity has been focused, and the strain up to 1.3% has been reported [4,5]. Figure 2 demonstrates the crystal orientation dependence of the piezoelectric d_{33} constant calculated for PZT 60/40, using the Devonshire phenomenological theory for a solid solution system [6]. As is shown, a maximum of the apparent piezoelectric constant can be obtained by canting the electric field direction from the spontaneous polarization (perovskite $\langle 111 \rangle$ axis) by 57 degree. This suggests that the [100] epitaxially grown PZT film with a rhombohedral composition should exhibit 3 times larger strain under the same electric

field level, as compared with the case of the [111] film (this is the conventional configuration!). Furthermore, due to the simpler domain reversal process, the ideal square-like hysteresis loops can be expected in the polarization or strain versus electric field for the same [100] films (Fig. 3), which is very essential for designing MEMS devices.

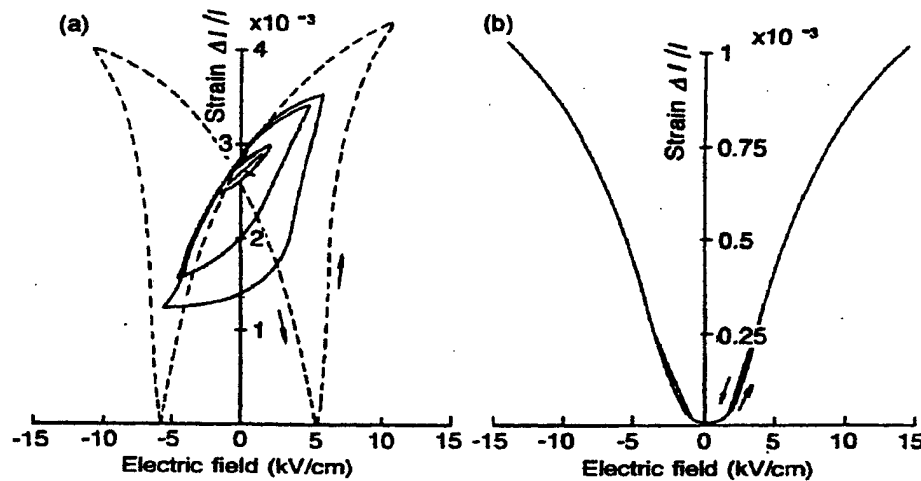


Fig.1 Field induced strain curves observed in a piezoelectric PLZT (a) and an electrostrictive PMN-PT ceramics.

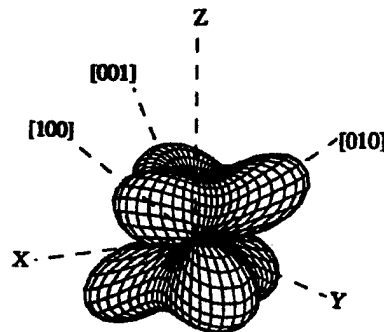


Fig.2 Crystal orientation dependence of the effective piezoelectric constant d_{33}^{eff} for a rhombohedral PZT 60/40, calculated from the Devonshire phenomenological theory.

Reliability

The reproducibility of the strain characteristics depends on grain size, porosity and impurity content, in general. Increasing the grain size enhances the magnitude of the field-induced strain, but degrades the fracture toughness and increases the hysteresis [7]. Thus, the grain size should be optimized for each application. On the other hand, porosity does not affect the strain behavior significantly. The tip deflection of unimorphs made from a $\text{Pb}(\text{Mg}_{1/3}\text{Nb}_{2/3})\text{O}_3$ -based material with various sample porosities did not show variation below 8% of the porosity [8]. Hence, fine powders made from wet chemical processes such as coprecipitation and sol-gel will be required, and suitable ceramic preparation process should be designed to optimize grain size and porosity.

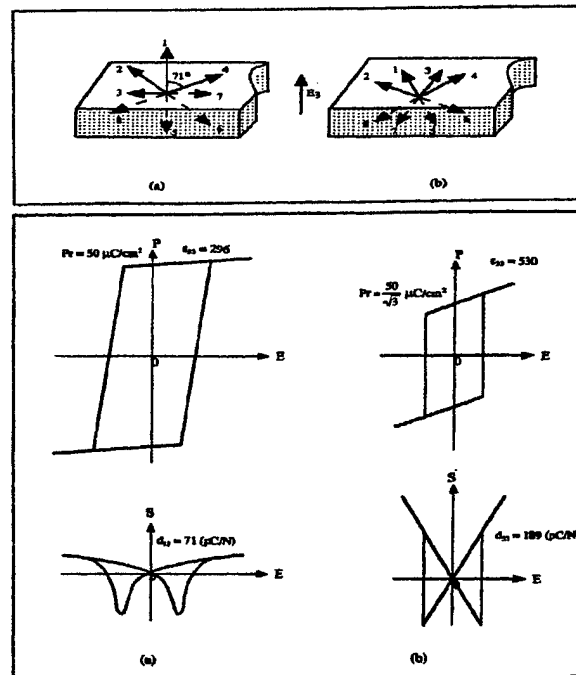


Fig.3 Possible domain states (top) and the expected polarization and strain hysteresis curves (bottom) for the [111] (left) and [100] (right) plates of a rhombohedral PZT.

The impurity (donor- or acceptor-type) level is another key material-design parameter which provides remarkable changes in strain and hysteresis/loss. Figure 4 shows dopant effects on the quasi-static field-induced strain in $(\text{Pb}_{0.73}\text{Ba}_{0.27})(\text{Zr}_{0.75}\text{Ti}_{0.25})\text{O}_3$ [9]. Since donor (valence $> +4$) doping provides "soft" characteristics, the sample exhibits larger strains and less hysteresis when driven under a high pseudo-DC electric field (1 kV/mm).

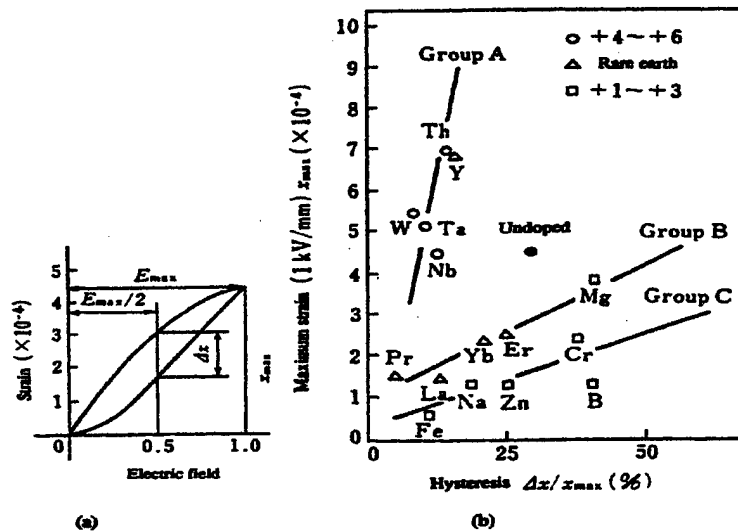


Fig.4 Dopant effects on the quasi-static field-induced strain in the base ceramic $(\text{Pb}_{0.73}\text{Ba}_{0.27})(\text{Zr}_{0.75}\text{Ti}_{0.25})\text{O}_3$. Donor (valence $> +4$) doping provides larger strains and less hysteresis.

To the contrary, the acceptor doping provides "hard" characteristics, leading to a small hysteretic loss and a large mechanical quality factor when driven under a small AC electric field, suitable to ultrasonic motor and piezo-transformer applications. Figure 5 shows the temperature rise versus vibration velocity for undoped, Nb-doped and Fe-doped $\text{Pb}(\text{Zr,Ti})\text{O}_3$ samples driven at a resonance mode. The suppression of heat generation is remarkable in the Fe-doped (acceptor-doped) ceramic [10].

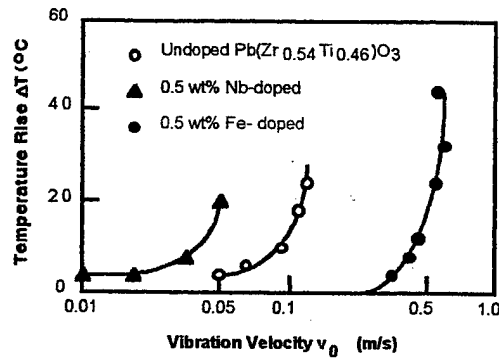


Fig.5 Temperature rise versus vibration velocity for undoped, Nb-doped and Fe-doped $\text{Pb}(\text{Zr,Ti})\text{O}_3$ samples. Heat generation is remarkably suppressed in the Fe-doped ceramic.

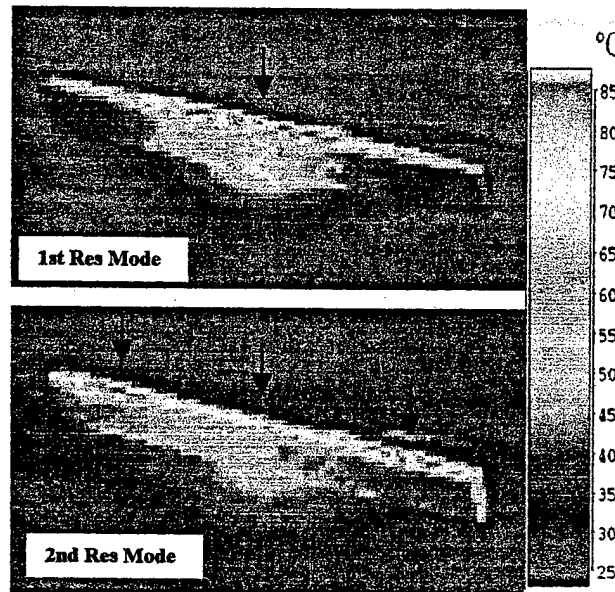


Fig.6 Temperature distribution on a rectangular PZT plate driven at the first and second extensional k_{31} resonance modes.

Figure 6 shows the temperature distribution on a rectangular PZT plates driven at the first and second extensional k_{31} resonance modes. It is important to note that the maximum temperature is observed at the nodal points where the maximum stress and strain are induced

when the sample is driven at the resonance mode. The major loss factor contributing to this temperature rise is considered as the (intensive) mechanical loss of the PZT.

Figure 7 shows the mechanical Q_m versus basic composition x at two effective vibration velocities $v_0=0.05$ m/s and 0.5 m/s for $\text{Pb}(\text{Zr}_x\text{Ti}_{1-x})\text{O}_3$ doped with 2.1 at.% of Fe [11]. The decrease in mechanical Q_m with an increase of vibration level is minimum around the rhombohedral-tetragonal morphotropic phase boundary (52/48). Thus, the morphotropic boundary composition should be adopted for designing the high power piezoelectric devices.

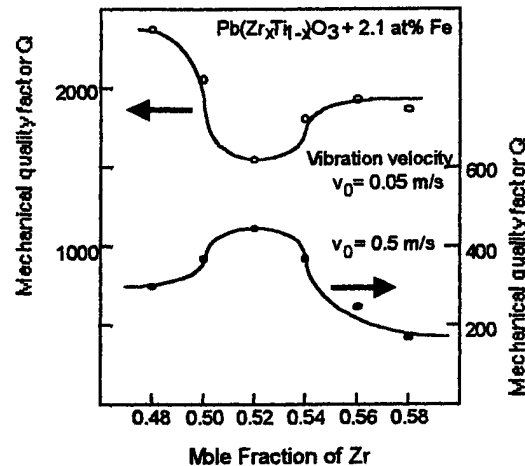


Fig.7 Mechanical Q_m versus basic composition x at two effective vibration velocities $v_0=0.05$ m/s and 0.5 m/s for $\text{Pb}(\text{Zr}_x\text{Ti}_{1-x})\text{O}_3$ doped with 2.1 at.% of Fe.

As shown above, the conventional piezo-ceramics have the limitation in the maximum vibration velocity (v_{\max}), more than which all the additionally input electrical energy converts into heat, rather than into mechanical energy. The typical rms value of v_{\max} for the commercialized materials, defined by the temperature rise of 20°C from the room temperature, is around 0.3 m/sec for the rectangular k_{31} samples [11]. $\text{Pb}(\text{Mn},\text{Sb})\text{O}_3$ (PMS) - lead zirconate tatanate (PZT) ceramics with the v_{\max} of 0.62 m/sec have been reported [12]. By doping rare-earth ions such as Yb, Eu and Ce additionally into the PMS-PZT, we recently developed the high power piezoelectrics, which can exhibit the v_{\max} up to 0.9 m/sec. Compared with commercially available piezoelectrics, one order of magnitude higher input electrical energy and out mechanical energy can be expected from this new material without generating significant temperature rise. This demonstrates the importance of ion doping from the material designing viewpoint.

The temperature dependence of the strain characteristics must be stabilized using either composite or solid solution techniques [13]. The recent new trends are found in developing high temperature actuators for engine surroundings and cryogenic actuators for laboratory equipment and space structures. Ceramic actuators are recommended to use under bias compressive stress, because the ceramic is, in general, relatively weak under externally applied tensile stress. The compressive uniaxial stress dependence of the weak-field piezoelectric constants d in various PZT ceramics indicated the significant enhancement in the d values for hard piezoelectric ceramics [14]. Systematic studies on the stress dependence of induced strains are eagerly awaited, including the composition dependence of mechanical strength, which will help in designing the stress bias mechanism for the actuator application.

DEVICE IMPROVEMENTS

Performance

One of the significant drawbacks in piezoelectrics is their small strains (only about 0.1%). Thus, lots of effort have been put to amplify the displacement. There are two categories: amplification with respect to space and to time. The first is demonstrated by bimorphs and moonies/cymbals, and the latter is exemplified by inchworms and ultrasonic motors.

Moonies/cymbals: Two of the most popular actuator designs are the multilayers and bimorphs [15] (see Fig. 8). The multilayer, in which roughly 100 thin piezoelectric/electrostrictive ceramic sheets are stacked together, has the advantages of low driving voltage (100 V), quick response (10 μ s), high generative force (1000 N), and high electromechanical coupling. But the displacement, on the order of 10 μ m, is not sufficient for some applications. This contrasts with the characteristics of the bimorph which consists of multiple piezoelectric and elastic plates bonded together to generate a large bending displacement of several hundred μ m, but has relatively low response time (1 ms) and generative force (1 N).

A composite actuator structure called the "moonie" (or "cymbal") has been designed to provide characteristics intermediate between the multilayer and bimorph actuators; this transducer exhibits an order of magnitude larger displacement than the multilayer, and much larger generative force with quicker response than the bimorph [16]. The device consists of a thin multilayer piezoelectric element (or a single disk) and two metal plates with narrow moon-shaped cavities bonded together as shown in Fig. 8. The moonie with a size of $5 \times 5 \times 2.5 \text{ mm}^3$ can generate a 20 μ m displacement under 60 V, eight times as large as the generative displacement produced by a multilayer of the same size [17]. This new compact actuator has been utilized in a miniaturized laser beam scanner.

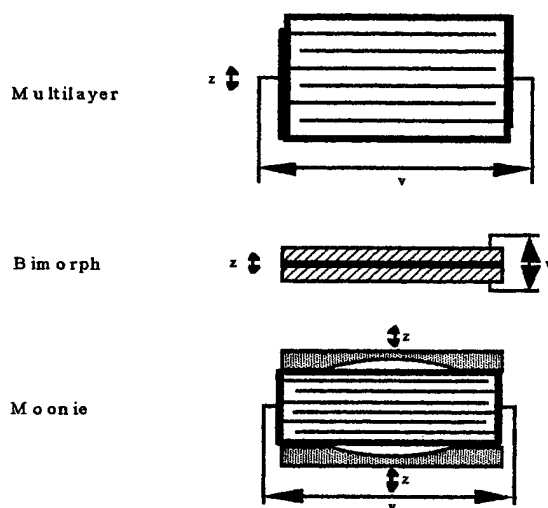


Fig. 8 Typical designs for ceramic actuators: multilayer, bimorph and moonie.

Compact Ultrasonic Motors: Figure 9 shows the famous Sashida motor [18]. By means of the traveling elastic wave induced by a thin piezoelectric ring, a ring-type slider in contact with the "rippled" surface of the elastic body bonded onto the piezoelectric is driven in both directions by exchanging the sine and cosine voltage inputs. Even the ripple displacement is not large, the

repetition of displacement at a very high frequency (15-200 kHz) provides relatively high speed to the slider. The PZT piezoelectric ring is divided into 16 positively and negatively poled regions and two asymmetric electrode gap regions so as to generate a 9th bending mode propagating wave at 44 kHz. A prototype was composed of a brass ring of 60 mm in outer diameter, 45 mm in inner diameter and 2.5 mm in thickness, bonded onto a PZT ceramic ring of 0.5 mm in thickness with divided electrodes on the back-side. The rotor was made of polymer coated with hard rubber or polyurethane.

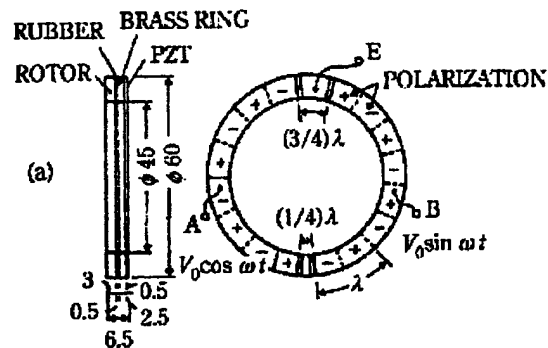


Fig. 9 Stator structure of Sashida's motor.

Canon utilized the "surfing" motor for a camera automatic focusing mechanism, installing this ring-type motor compactly in the lens frame. Using basically the same principle, Seiko Instruments miniaturized the ultrasonic motor to a diameter as small as 10 mm [19]. A driving voltage of 3 V provides torque of 0.1 mN·m. Seiko installed this tiny motor into a wrist watch as a silent alarm. AlliedSignal developed ultrasonic motors similar to Shinsei's, which would be utilized as mechanical switches for launching missiles [20].

A significant problem in miniaturizing this sort of traveling wave motor can be found in the ceramic manufacturing process; without providing a sufficient buffer gap between the adjacent electrodes, the electrical poling process (upward and downward) easily initiates the crack on the electrode gap due to the residual stress concentration. This may restrict the further miniaturization of the traveling wave type motors. To the contrary, standing wave type motors, the structure of which is less complicated, are more suitable for miniaturization as we will discuss in the following. They require only one uniformly poled piezo-element, less electric lead wires and one power supply. Another problem encountered in these traveling wave type motors is the support of the stator. In the case of a standing wave motor, the nodal points or lines are generally supported; this causes minimum effects on the resonance vibration. To the contrary, a traveling wave does not have such steady nodal points or lines. Thus, special considerations are necessary. In Fig. 8, the stator is basically fixed very gently along the axial direction through felt so as not to suppress the bending vibration.

We adopted the following concepts for designing new compact ultrasonic motors: (a) to simplify the structure and reduce the number of component, (b) to use simple (i.e., uniform) poling configuration, and (c) to use the standing-wave type for reducing the number of the drive circuit components.

A *Windmill* motor design with basically a flat and wide configuration, using a metal-ceramic composite structure is a good example to explain [21,22]. The motor is composed of four components: stator, rotor, ball-bearing and housing unit [Fig. 10(a)]. The piezoelectric part has a simple structure of a ring electroded on its top and bottom surfaces (ϕ 3.0mm) poled

uniformly in the thickness direction. The metal ring machined by Electric Discharge Machining has four inward arms placed 90° apart on its inner circumference. The metal and piezoelectric rings are bonded together, but the arms remain free; they thus behave like cantilever beams [Fig. 10(b)]. The length and cross-sectional area of each arm were selected such that the resonance frequency of the second bending mode of the arms is close to the resonance frequency of the radial mode of the stator. The rotor is placed at the center of the stator and rotates when an electric field is applied at a frequency between the radial and bending resonance modes. The truncated cone shape at the rotor end guarantees a permanent contact with the tips of the arms.

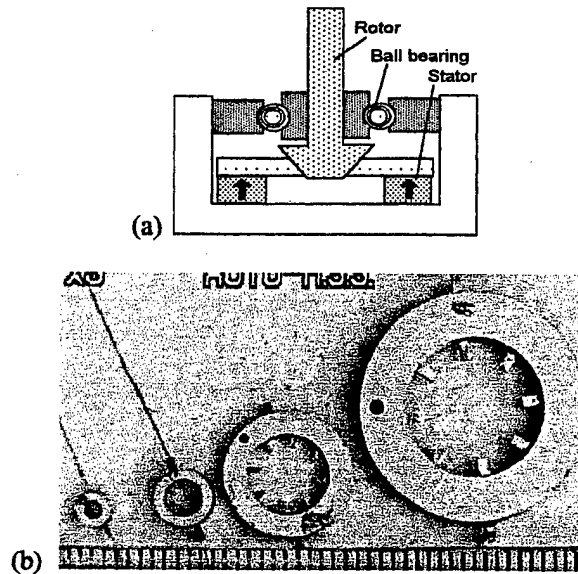


Fig. 10 "Windmill" motor using a metal coupler with multiple inward arms. (a) Cross sectional view, and (b) photos of various size stators (3-20 mm ϕ).

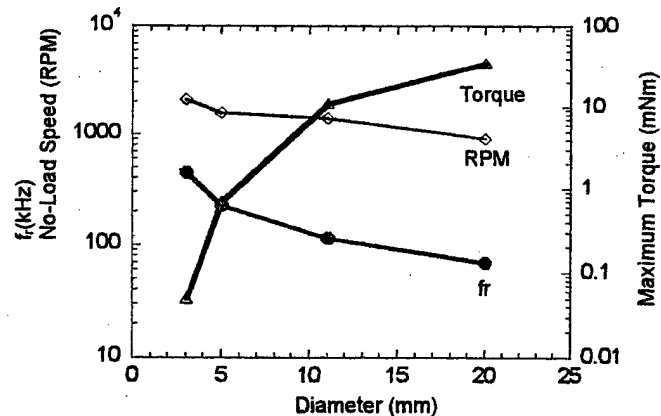


Fig. 11 Radial mode resonance frequency, no-load speed and starting torque vs. diameter of the stator, measured at 15.7 V.

The operating principle of this motor is as follows: in the contraction cycle of the stator, the four arms at the center of the metal ring clamp the rotor and push it in the tangential direction. Since the radial mode frequency of the stator is close to the second bending mode frequency of the arms, the respective deformations are added and the tips of the arms bend down. In the expansion cycle, the arms release the rotor from a different path such that their tips describe an elliptical trajectory on the surface of the rotor. This motion seems to be a human finger's grasping-and-rotating action.

Figure 11 shows the size dependence of the motor characteristics. This sort of scaling principle is useful for designing the ultrasonic motors. When driven at 160 kHz, the maximum revolution 2000 rpm and the maximum torque 0.8 mNm were obtained for a 5 mm ϕ motor [22].

Another example is a *metal tube* type with a thin and long configuration, as shown in Fig. 12(a) [23]. We utilized a metal hollow cylinder, bonded with two PZT rectangular plates uniformly poled. Both can be easily found/prepared and cheap in price. When we drive one of the PZT plates, Plate X, a bending vibration is excited basically along x axis. However, because of an asymmetrical mass (Plate Y), another hybridized bending mode is excited with some phase lag along y axis, leading to an elliptical locus in a clockwise direction. On the other hand, when Plate Y is driven, counterclockwise wobble motion is excited. Also note that only a single-phase power supply is required. The motion is analogous to a "dish-spinning" performance, then two rotors were made to contact the wobbling tube ends for achieving rotation [Fig. 12(b)].

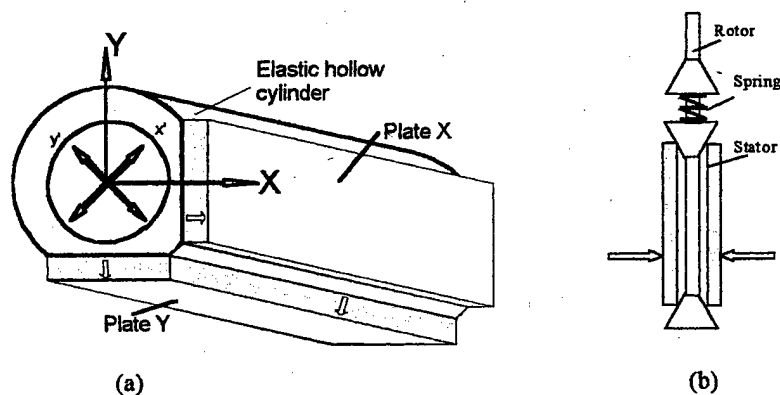


Fig. 12 (a) Structure of a metal tube stator, and (b) assembly of the motor.

The Finite Element Analysis is a very useful tool to obtain realistic vibration modes in a stator. We used an ATILA software code (Magsoft Corporation) for the metal tube stator calculation. The result is shown in Fig. 13, where (b) shows the deformation of the tube slightly after the time for (a), when only Y plate is excited (X plate is electrically short-circuited in the calculation). These figures clearly show a counterclockwise rotation of the metal tube.

The rotor of this motor was a brass cylindrical rod with a pair of stainless ferrule pressed with a spring. The assembly is shown in Fig. 12(b). The no-load speed in the clockwise and counterclockwise directions as a function of input rms voltage was measured for a motor with 2.4 mm ϕ in diameter and 12 mm in length. The motor was driven at 62.1 kHz for both directions, just by exchanging the drive PZT plate. The no-load speed of 1800 rpm and the output torque of more than 1.0 mNm were obtained at 80 V for both directions. This significantly high torque was obtained due the dual stator configuration and the high pressing force between the stator and rotors made of metal.

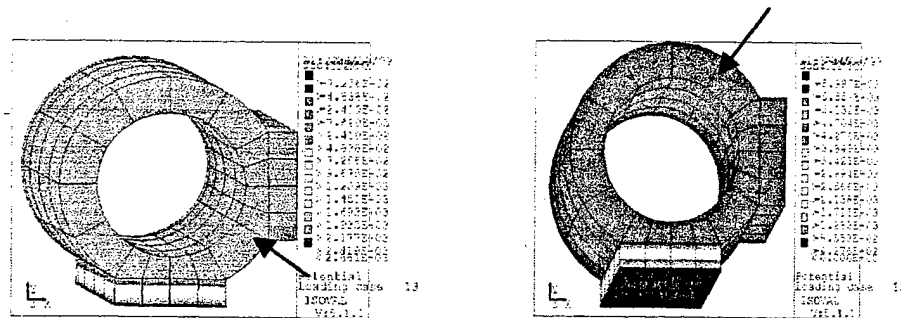


Fig. 13 FEA calculation results for a metal tube stator, when only Y plate (the bottom plate) is excited (Y plate is short-circuited). Notice the counterclockwise rotation.

MEMS devices: PZT thin films are deposited on a silicon membrane, which can be micro-machined as total for fabricating micro actuators and sensors, i.e., micro electromechanical systems. Figure 14 illustrates a blood tester developed in collaboration with OMRON Corporation in Japan. Applying voltage to two surface interdigital electrodes, the surface PZT film generates surface membrane waves, which soak up blood and test chemical from the two inlets, then mix them in the center part, and send the mixture to the monitor part through the outlet. The FEM calculation was conducted to evaluate the flow rate of the liquid by changing the thickness of PZT or the Si membrane, inlet and outlet nozzle size, cavity thickness etc.

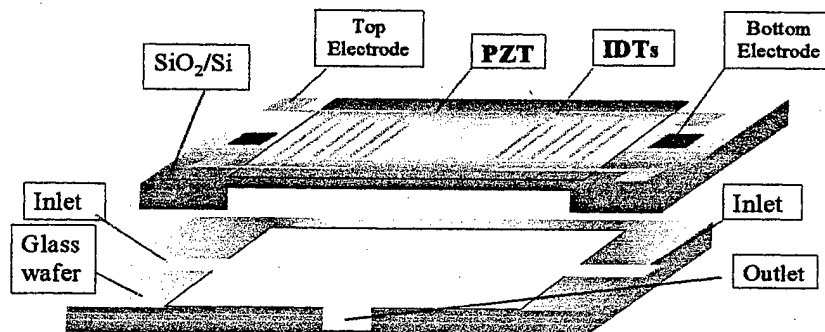


Fig. 14 Structure of a PZT/silicon MEMS device, blood tester.

Reliability

Popular silver electrodes have a serious problem of migration under a high electric field and high humidity. This problem can be overcome with usage of a silver-palladium alloy (or more expensive Pt). To achieve inexpensive ceramic actuators, we need to introduce Cu or Ni electrodes, which require a sintering temperature as low as 900°C. Low temperature sinterable actuator ceramics will be the next target of research.

Delamination of the electrode layer is another problem in multilayer types as well as bimorphs. To enhance adhesion, composite electrode materials with metal and ceramic powder colloid, ceramic electrodes, and electrode configurations with via holes are recommended [24]. Internal stress concentration during the electric field application sometimes initiates the crack in

the actuator device. We calculate the stress concentration for a multilayer (8 layers) type piezo-actuator (Fig. 15) with an ATILA software code. Large tensile stress (x-x) concentration (which may cause a crack) can be clearly observed just outside of the internal electrode edge. In principle, we need to design the electrode pattern so as not to generate a maximum tensile stress more than the critical ceramic mechanical strength. From this sense, several electrode configurations have been proposed, as shown in Fig. 16: plate-through type, slit-insert type, and float-electrode-insert type [25]. These new three types can enhance the actuator lifetime. However, the plate-through type requires a special expensive task to make an external insulative coating, and the maintenance of very thin slits is a major drawback for the slit-insert type. The reason why the lifetime is extended with decreasing layer thickness has not yet been clarified.

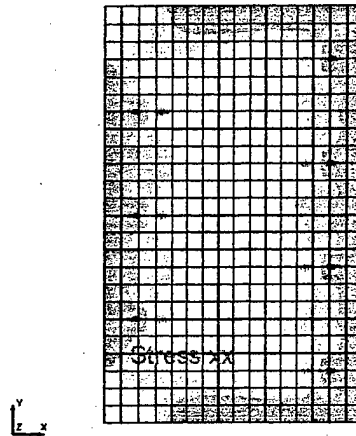


Fig.15 Stress concentration for a multilayer (8 layers) type piezo-actuator calculated with an ATILA software code.

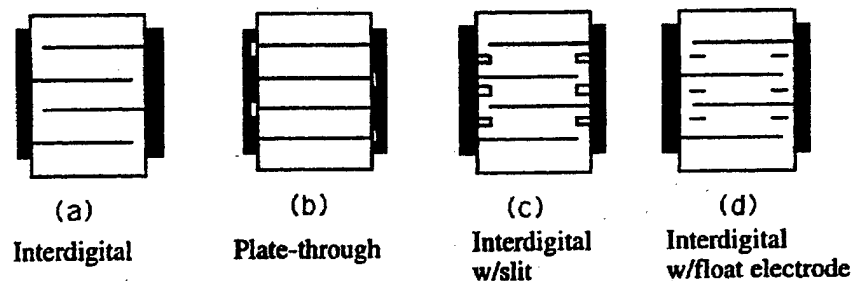


Fig.16 New electrode patterns to suppress the internal stress concentration: plate-through type (b), slit-insert type (c), and float-electrode-insert (d) types.

A similar internal stress consideration is required when we design piezoelectric transformers. The initial Rosen type had a reliability problem; that is, easy mechanical breakdown at the center portion due to the coincidence of the residual stress concentration (through the poling process) and the vibration nodal point (highest induced stress). In addition to improved mechanically tough ceramic materials, by using a multilayer type without generating any poling direction mismatch (Philips Components, NEC [26]), or by redesigning the electrode configuration and exciting a 3rd longitudinal vibration mode of the rectangular plate (NEC) [27],

the piezo-transformers shown in Fig. 17 have been commercialized as a back-light inverter for the liquid crystal displays.

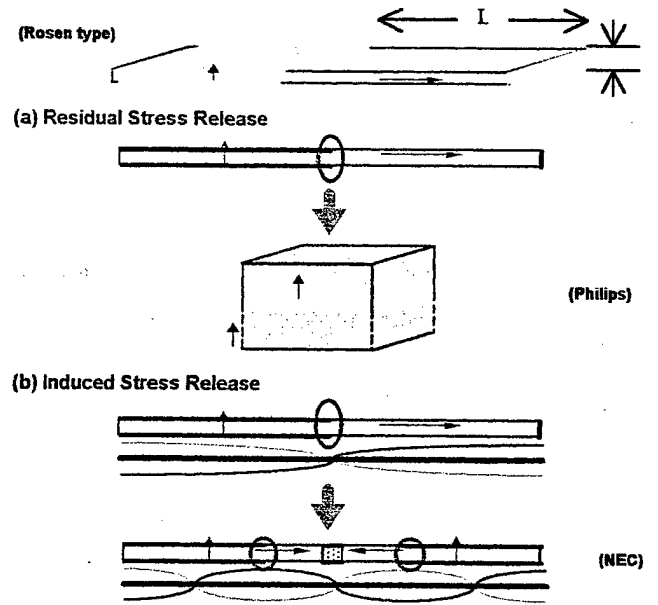


Fig. 17 New types of piezoelectric transformer with a consideration of residual stress due to the polarization (a), or of induced stress (b).

Heat generation also provides additional key requirement in designing the multilayer actuator. Zheng et al. reported the heat generation from various sizes of multilayer type piezoelectric ceramic actuators [28]. Figure 18 shows the temperature change in the actuators when driven at 3 kV/mm and 300 Hz, and Fig. 19 plots the saturated temperature as a function of V_e/A , where V_e is the effective volume (electrode overlapped part) and A is the surface area. This linear relation is reasonable because the volume V_e generates the heat and this heat is dissipated through the area A . Thus, if we need to suppress the temperature rise, a small V_e/A design is preferred. For example, a hollow cylinder actuator is preferred to a solid rod actuator, when we consider the heat suppression. It is notable that in this off-resonance case, the loss contributing to the heat generation is not the intensive mechanical loss like in the resonance, but the intensive dielectric loss (i.e., P-E hysteresis loss) [28].

Although the aging effect is very important, not many investigations have been done so far. The aging effect arises from two factors: depoling and destruction. Creep and zero-point drift of the displacement are caused by the depoling of the ceramic. Another serious degradation of the strain is produced by a very high electric field under an elevated temperature, humidity and mechanical stress. Change in lifetime of a multilayer piezoelectric actuator with temperature and DC bias voltage has been reported by Nagata [29]. The lifetime t_{DC} under DC bias field E obeys an empirical rule:

$$t_{DC} = A E^{-n} \exp(W_{DC}/kT), \quad (1)$$

where n is about 3 and W_{DC} is an activation energy ranging from 0.99 - 1.04 eV. This is another important issue in designing the device.

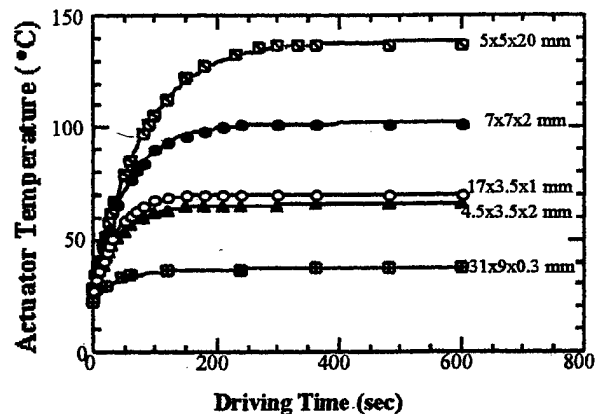


Fig.18 Temperature rise for various actuators while driven at 300 Hz and 3 kV/mm.

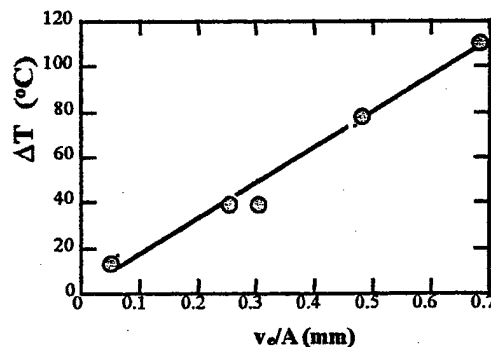


Fig.19 Temperature rise versus V_e/A (3 kV/mm, 300 Hz), where V_e is the effective volume generating the heat and A is the surface area dissipating the heat.

Lifetime prediction or "health" monitoring systems have been proposed using failure detection techniques [30]. Figure 20 shows such an "intelligent" actuator system with acoustic emission (AE) monitoring. The actuator is controlled by two feedback mechanisms: position feedback, which can compensate the position drift and the hysteresis, and breakdown detection feedback which can stop the actuator system safely without causing any serious damages to the work, e.g. in a lathe machine. Acoustic emission measurements of a piezo-actuator under a cyclic electric field provides a good predictor for lifetime. AE is detected largely when a crack propagates in the ceramic actuator at the maximum speed. During normal drive of a 100-layer piezoelectric actuator, the number of AE was counted and a drastic increase by three orders of magnitude was detected just before complete destruction. Note that part of the piezo-device can be utilized as an AE sensor.

A recent new electrode configuration with a strain gauge type (Fig. 21) is another intriguing alternative for health monitoring [31]. By measuring the resistance of the strain-gauge shaped electrode embedded in the ceramic actuator, we can monitor both electric-field induced strain and the symptom of cracks in the ceramic.

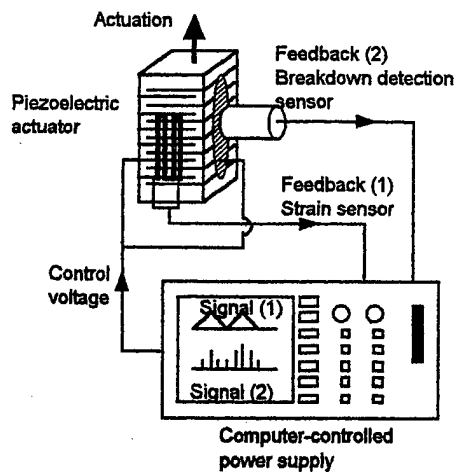


Fig.20 Intelligent actuator system with both position feedback and breakdown detection feedback mechanisms.

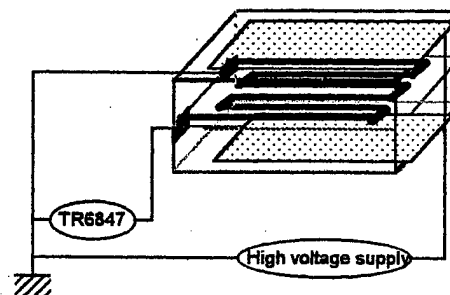


Fig.21 Strain gauge configuration of the internal electrode for an intelligent actuator.

DRIVE/CONTROL TECHNIQUES

Performance

Piezoelectric/electrostrictive actuators are classified into two categories, based on the type of driving voltage applied to the device and the nature of the strain induced by the voltage (Fig. 22): (1) rigid displacement devices for which the strain is induced unidirectionally along the direction of the applied DC field, and (2) resonating displacement devices for which the alternating strain is excited by an AC field at the mechanical resonance frequency (ultrasonic motors). The first can be further divided into two types: servo displacement transducers (positioners) controlled by a feedback system through a position-detection signal, and pulse drive motors operated in a simple on/off switching mode, exemplified by dot-matrix printers.

The material requirements for these classes of devices are somewhat different, and certain compounds will be better suited to particular applications. The ultrasonic motor, for instance, requires a very hard piezoelectric with a high mechanical quality factor Q_m , to suppress heat generation. The servo displacement transducer suffers most from strain hysteresis and, therefore, a PMN electrostrictor is used for this purpose. The pulse drive motor requires a low permittivity material aimed at quick response with a certain power supply rather than a small hysteresis, so soft PZT piezoelectrics are preferred rather than the high-permittivity PMN for this application.

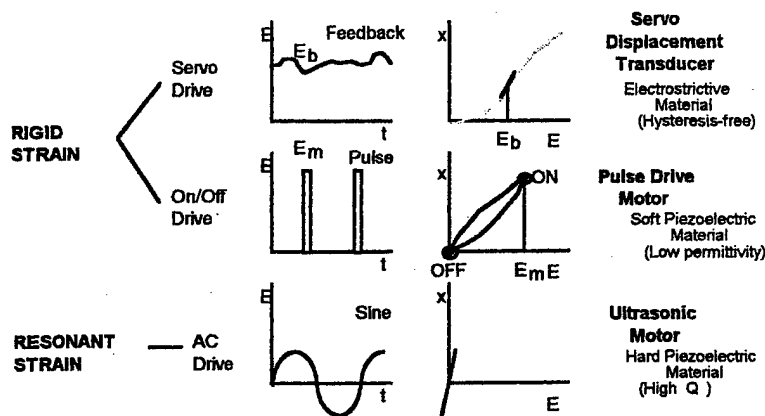


Fig.22 Classification of piezoelectric/electrostrictive actuators.

Recently, we proposed a new application of a piezoelectric transformer, that is, driving piezoelectric actuators. Because of advantages of the piezo-transformer to the conventional electromagnetic types in (a) small size/weight, (b) high efficiency, (c) no magnetic noise generation, and (d) non-flammable structure, the piezoelectric types will expand the application area rapidly, including the piezoelectric actuators. Notice that because most of the piezo-actuators are driven under 100-1000V, a transformer is inevitably required when we use a battery driven circuitry. The basic concept is illustrated in Fig. 23. When we tune the transformer operating frequency exactly to the same frequency of an ultrasonic motor's resonance (for example, designing a ring transformer, using the same size piezo-ring as the ultrasonic motor), we may use it as a drive system, or fabricate a transformer-integrated motor. When we couple a rectifier with the transformer, we can drive a multilayer or bimorph piezoelectric actuator.

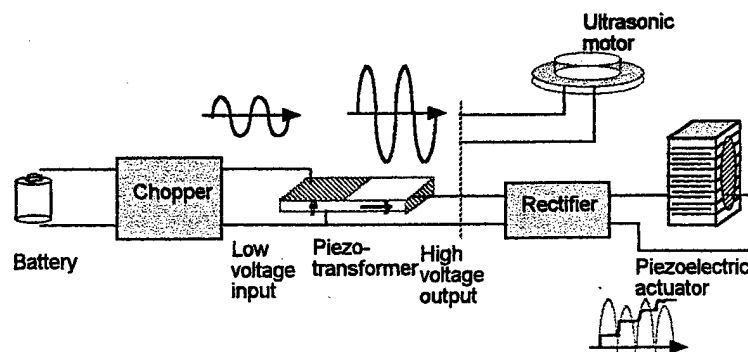


Fig.23 Basic concept of piezo-actuator drive systems (AC or pseudo DC) using a piezoelectric transformer.

In the following, we introduce a compact drive system designing with piezoelectric transformers for a multilayer piezoelectric actuator, aiming at active vibration control on a helicopter. In this sort of military application, we need to realize a compact, light-weight and electromagnetic-noise free system with keeping quick response (minimum 200Hz). For this sake, we have chosen a multilayer piezoelectric device as an actuator, and piezo-transformers (rather than

electromagnetic transformers) as drive system components. Figure 24 summarizes our compact drive system for piezoelectric actuator control, using piezoelectric transformers [32].

We have targeted to develop two kinds of power supplies with piezo-transformers driven by a helicopter battery $24V_{DC}$: one is a high voltage DC power supply ($100\text{--}1000V$, $90W$) for driving the piezoelectric actuator, and the other is an AC adapter ($\pm 15V_{DC}$, $0.1\text{--}0.5W$) for driving the supporting circuitry. We utilized large and small multi-stacked piezo-transformer elements both with an insulative glass layer between the input and output parts for ensuring the complete floating condition, for the high power supply and the adapter, respectively. The used actuator was supplied from Tokin Corp., which has the size of $10 \times 10 \times 20 \text{ mm}^3$, and is capable to generate a $16\mu\text{m}$ displacement under the maximum voltage of $100V$.

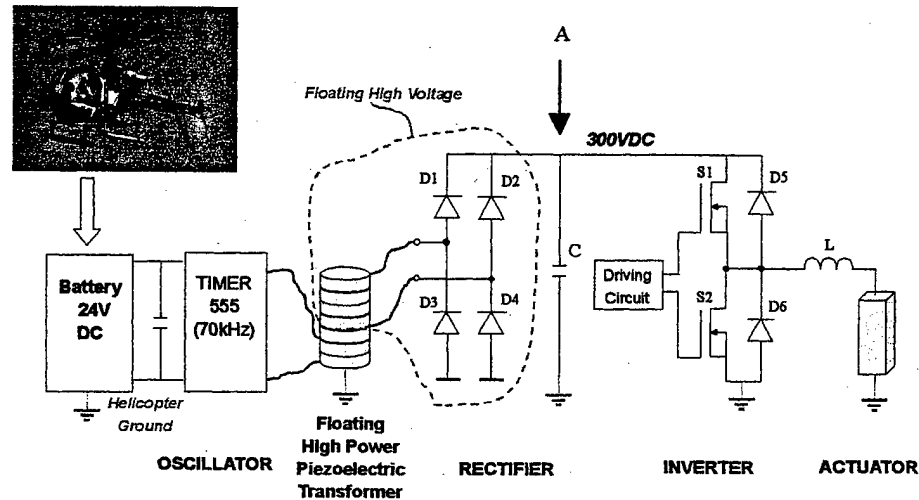


Fig. 24 Compact drive system for piezoelectric actuator control.

We initially tried to drive the actuator by applying the rectified high voltage directly after the power transformer (i.e., voltage at the point A in Fig. 24). However, because of a very slow response during a rising or falling voltage process (~ 1 sec), we decided to use this rectified voltage as a constant high DC voltage, and additionally use a power amplifier to control the voltage applied to the actuator. Among various power amplifier families [33], we have chosen a Class-D switching amplifier (see the inverter in Fig. 8), because it has some advantages over the other switching and linear amplifiers, such as permitting amplitude and frequency control and realizing fast actuation response of the actuator by chopping a DC voltage. The voltage level generated in the transformer was $300V$ for the input voltage of $75V$ applied through a timer 555. The signal from a PWM (pulse width modulation) driving circuit was applied to two power MOSFET's of the half bridge. Thus, the constant $300V_{DC}$ voltage from the piezo-transformer was chopped, and control of frequency and magnitude was achieved. This output voltage was applied to the piezo-actuator through a filtering inductance of 100mH [34]. The PWM carrier frequency was chosen as 40kHz , which is below the mechanical resonance frequency of the used piezo-actuator ($\sim 60\text{kHz}$).

Figure 25 shows the displacement curves of the actuator driven by the newly developed power amplifier. The displacement was directly measured with an eddy current sensor. As seen in this figure, the displacement $\pm 1.5\mu\text{m}$ was controlled by $\pm 20V$ applied voltage. This drive system could be used at least up to 500Hz , which is sufficient for the active vibration control on a helicopter. Note that the new drive system is compact, light-weight, and magnetic-noiseless.

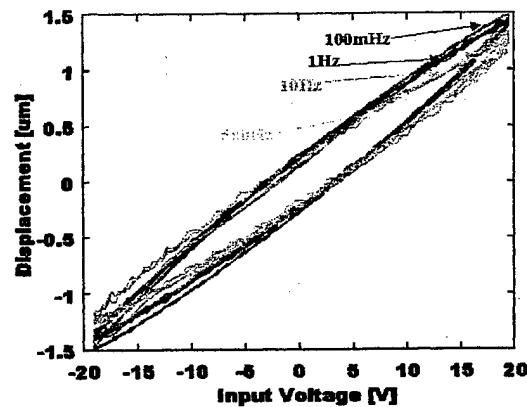


Fig.25 Displacement curves of the piezoelectric actuator driven by the newly developed power amplifier with piezoelectric transformers.

Reliability

Pulse Drive: Pulse drive of the piezoelectric / electrostrictive actuator generates very large tensile stress in the device, sometimes large enough to initiate cracks. In such cases, compressive bias stress should be employed on the device through clamping mechanisms such as a helical spring and a plate spring. Figure 26 shows another solution to suppress this problem; that is, suppression of the transient vibrations of a bimorph by choosing a suitable pseudo-step voltage applied. In Fig. 26, the rise time is varied around the resonance period (n is the time scale with a unit of $T_0/2$, where T_0 stands for the resonance period). It is concluded that the overshoot and ringing of the tip displacement is completely suppressed when the rise time is precisely adjusted to the resonance period of the piezo-device (i.e., for $n = 2$) [35].

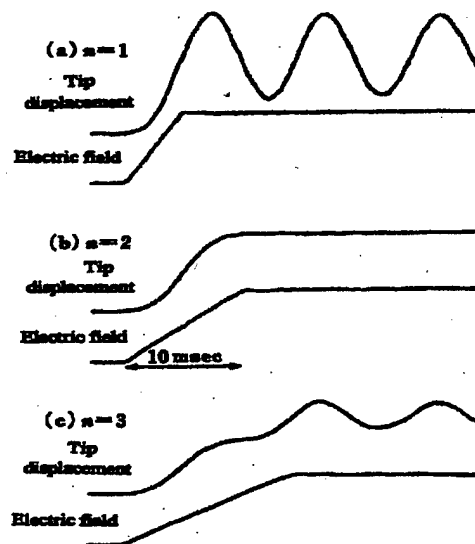


Fig. 26 Transient vibration of a bimorph excited after a pseudo-step voltage applied. n is a time scale with a unit of half of the resonance period, i.e., $2n = \text{resonance period}$.

Temperature rise is occasionally observed, particularly when the actuator is driven cyclically in the pulse drive. The rise time adjustment is also very important from the heat generation viewpoint. In consideration of the pulse drive using a trapezoidal wave, like an application to diesel engine injection systems, we examined the temperature rise. The trapezoidal wave with a maximum voltage 100 V, 60 Hz, and a duty ratio 50 % was applied to the Ceramtech multilayer actuator. The results are summarized in Table I and Fig. 27. The temperature rise is surprisingly dependent on the step rise time, which is basically due to the actuator's vibration overshoot and ringing. As shown in Fig. 28, for the shorter rise time, the actuator shows significant vibration ringing, which provides the additional heat generation through a sort of mechanical resonance. Depending on the degree of the overshoot, the temperature rise was increased by more than 50 % than in the case without any vibration ringing (this corresponds to roughly the off-resonance condition). Thus, when the piezoelectric actuator is used under a pulse drive condition, in addition to the off-resonance heat generation due to the intensive dielectric (P-E hysteresis) loss, the resonance type loss due to the intensive mechanical loss is superposed. Care must be taken for reducing the mechanical vibration overshoot and ringing by changing the step rise time, in order to suppress the heat generation minimum. The rise time should be chosen as a resonance period of the actuator.

Table I. Heat generation of the Ceramtech actuator under various rise time driving (trapezoidal waveform, 50% duty cycle, 60 Hz, 100V unipolar voltage).

Rise time (usec)	72	85	97	102	146	240	800
Temperature rise (C)	23.7	21.6	20.5	20.2	20.3	18.6	16.6
V_{rms} (V)	72.9	72.8	72.7	72.7	72.6	72.1	71.3

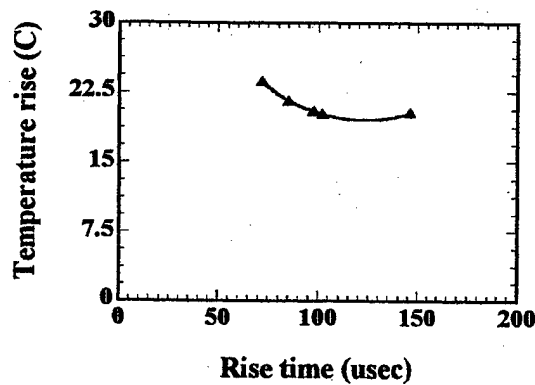


Fig. 27 Rise time dependence of heat generation for the actuator driven under 100 V (unipolar) trapezoid waveform at frequency of 60 Hz.

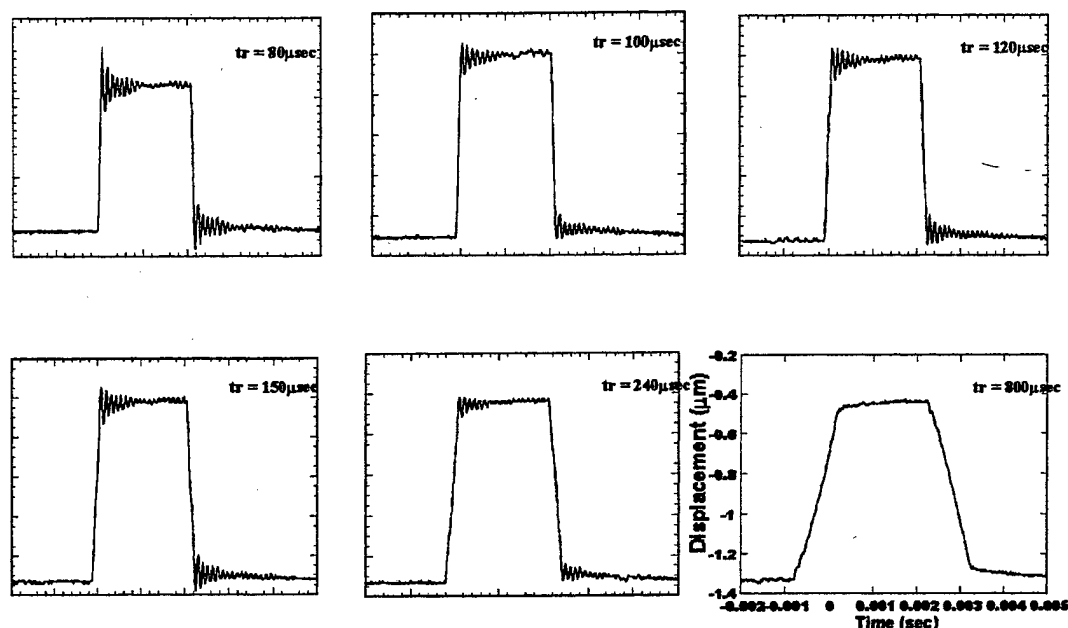


Fig. 28 Rise time dependence of the vibration ringing for the Ceramtech multilayer actuator driven under 100 V (unipolar) trapezoid waveform at frequency of 60 Hz.

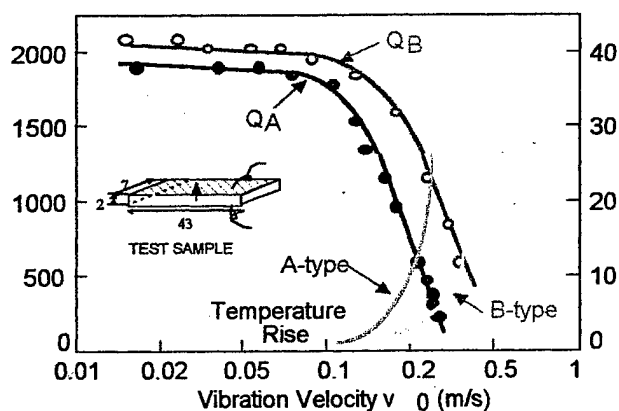


Fig. 29 Vibration velocity dependence of the quality factor Q and temperature rise for both A (resonance) and B (antiresonance) type resonances of a longitudinally vibrating PZT ceramic transducer through transverse piezoelectric effect d_{31} .

Antiresonance Drive: Regarding ultrasonic motors, the usage of the antiresonance mode has been proposed [36]. Quality factor Q and temperature rise have been investigated on a PZT ceramic rectangular bar, and the results for the fundamental resonance (A-type) and antiresonance (B-type) modes are illustrated in Fig. 29 as a function of vibration velocity. It is recognized that Q_B is higher than Q_A over the whole vibration velocity range. In other words, the antiresonance mode can provide the same mechanical vibration level without generating heat. In

a typical piezoelectric material with k_{31} around 30 %, the plate edge is not a vibration nodal point and can generate a large vibration velocity.

All the previous ultrasonic motors have utilized the mechanical resonance mode at the so-called "resonance" frequency. However, the mechanical resonant mode at the "antiresonance" frequency reveals higher Q and efficiency than the "resonance" state. Moreover, the usage of "antiresonance," whose admittance is very low, requires low current and high voltage for driving, in contrast to high current and low voltage for the "resonance." This means that a conventional inexpensive power supply may be utilized for driving the ultrasonic motor.

SUMMARY AND FUTURE

We discussed the design issues of piezoelectric devices, particularly of piezoelectric actuators. The design is considered from two aspects: improvement of performance and reliability. Also because the actuator is really an interdisciplinary device, we need to consider materials, device designs and drive/control techniques totally.

As an example, we will present a typical flow of an ultrasonic motor designing.

Materials: (1) Using a phenomenological theory for a solid solution system, the maximum electromechanical coupling factor k and d composition is derived in the PZT system (e.g., around 52-48 morphotropic phase boundary).

(2) When the sample is a single crystal, the optimum crystal cut angle should be selected (e.g., [001] plates for a rhombohedral composition).

(3) Doping an acceptor-type ion, a larger Q material is sought.

(4) In order to increase the fracture toughness, smaller grain samples are prepared, designing the ceramic fabrication process.

Devices: (5) In order to increase the lifetime, a simple motor design with uniformly poled PZT specimen is considered.

(6) The vibration modal analysis will be conducted using an FEM program (e.g., ATILA software code).

(7) In order to suppress the heat generation, the surface area of the device should be increased, or a air circulation should be considered.

(8) Cost-efficient fabrication process is considered. Particular focus is put on supporting techniques such as resin and frictional coating materials.

Drive/Control Systems:

(9) Since the ultrasonic motor is pure capacitive, we need to design an energy efficient drive circuit (e.g., the application of piezoelectric transformers is one of a promising approach).

(10) The antiresonance mode application (rather than the conventional resonance mode) may provide a breakthrough in developing drive/control systems for high power ultrasonic motors.

High power piezoelectric actuators and transformers are very promising 21st Century technologies. In order to expand the application fields, we need to establish the designing principle of these devices as soon as possible, as well as the standardization of the evaluation methods.

ACKNOWLEDGEMENTS

This work was partly supported by US Army Research Office and Office of Naval Research through Contracts No. DAAL 03-92-G-0244, No. N00014-91-J-4145 and N00014-96-1-1173.

Many parts of this article were cited from my textbooks, "Piezoelectric Actuators and Ultrasonic Motors," Kluwer Academic Publishers (1996), and "Ferroelectric Devices," Marcel Dekker (2000).

REFERENCES

- ¹K. Uchino, *Ceramic Actuators and Ultrasonic Motors*, Kluwer Academic Pub., Boston, 1996.
- ²K. Uchino, *Ferroelectric Devices*, Marcel Dekker, New York, 2000.
- ³J. Kuwata, K. Uchino and S. Nomura, "Phase Transitions on the $\text{Pb}(\text{Zn}_{1/3}\text{Nb}_{2/3})\text{O}_3$ - PbTiO_3 System," *Ferroelectrics*, **37**, 579 (1981).
- ⁴K. Yanagiwawa, H. Kanai and Y. Yamashita, *Jpn. J. Appl. Phys.*, **34**, 536 (1995).
- ⁵S.E. Park and T.R. Shrout, "Relaxor Based Ferroelectric Single Crystals for Electromechanical Actuators," *Mat. Res. Innovt.*, **1**, 20 (1997).
- ⁶X.H. Du, J. Zheng, U. Belegundu and K. Uchino, "Crystal Orientation Dependence of Piezoelectric Properties of Lead Zirconate Titanate: Theoretical Expectation for Thin Films," *Jpn. J. Appl. Phys.*, **36**, 5580 (1997).
- ⁷K. Uchino and T. Takasu, "Evaluation Method of Piezoelectric Ceramics from a Viewpoint of Grain Size," *Inspec.*, **10**, p.29, (1986).
- ⁸K. Abe, K. Uchino and S. Nomura, "The Electrostrictive Unimorph for Displacement Control," *Jpn. J. Appl. Phys.*, **21**, p.L408, (1982).
- ⁹A. Hagimura and K. Uchino, "Impurity Doping Effect on Electrostrictive Properties of $(\text{Pb,Ba})(\text{Zr,Ti})\text{O}_3$," *Ferroelectrics*, **93**, p.373, (1989).
- ¹⁰S. Takahashi and S. Hirose, *Jpn. J. Appl. Phys.*, **32**, Pt.1, p.2422, (1993).
- ¹¹K. Uchino, J. Zheng, A. Joshi, Y.H. Chen, S. Yoshikawa, S. Hirose, S. Takahashi and J.W.D. de Vries, "High Power Characterization of Piezoelectric Materials," *J. Electroceramics*, **2**, 33 (1998).
- ¹²S. Takahashi, Y. Sakaki, S. Hirose and K. Uchino, "Electro-Mechanical Properties of PbZrO_3 - PbTiO_3 - $\text{Pb}(\text{Mn}_{1/3}\text{Sb}_{2/3})\text{O}_3$ Ceramics under Vibration-Level Change," *Mater. Res. Soc. Symp. Proc.* **360**, 305, Mater. Res. Soc., Pittsburgh, 1995.
- ¹³K. Uchino, J. Kuwata, S. Nomura, L.E. Cross and R.E. Newnham, "Interrelation of Electrostriction with Phase Transition Diffuseness," *Jpn. J. Appl. Phys.*, **20**, Suppl.20-4, 171, (1981).
- ¹⁴Q.M. Zhang, J. Zhao, K. Uchino and J. Zheng, "Change of the Weak Field Properties of $\text{Pb}(\text{Zr,Ti})\text{O}_3$ Piezoceramics with Compressive Uniaxial Stresses," *J. Mater. Res.*, **12**, 226, (1997).
- ¹⁵Y. Sugawara, K. Onitsuka, S. Yoshikawa, Q.C. Xu, R.E. Newnham and K. Uchino, "Metal-Ceramic Composite Actuators," *J. Amer. Ceram. Soc.*, **75**(4), 996 (1992).
- ¹⁶A. Dogan, K. Uchino and R.E. Newnham, "Composite Piezoelectric Transducer with Truncated Conical Endcaps "Cymbal"," *IEEE Trans. UFFC*, **44**, 597 (1997).
- ¹⁷H. Goto, K. Imanaka and K. Uchino, "Piezoelectric Actuators for Light Beam Scanners," *Ultrasonic Techno.* **5**, 48 (1992).
- ¹⁸T. Sashida, *Mech. Automation of Jpn.*, **15** (2), 31 (1983).
- ¹⁹M. Kasuga, T. Satoh, N. Tsukada, T. Yamazaki, F. Ogawa, M. Suzuki, I. Horikoshi and T. Itoh, *J. Soc. Precision Eng.*, **57**, 63 (1991).
- ²⁰J. Cummings and D. Stutts, *Amer. Ceram. Soc. Trans.* "Design for Manufacturability of Ceramic Components", p.147 (1994).
- ²¹B. Koc, A. Dogan, Y. Xu, R. E. Newnham and K. Uchino, "An Ultrasonic Motor Using a Metal-Ceramic Composite Actuator Generating Torsional Displacement," *Jpn. J. Appl. Phys.* **37**, 5659 (1998).
- ²²B. Koc, P. Bouchilloux, and K. Uchino, "Piezoelectric Micromotor Using a Metal-Ceramic Composite Structure," *IEEE Trans.-UFFC*, **47**, 836 (2000).
- ²³B. Koc, J. F. Tressler and K. Uchino, "A Miniature Piezoelectric Rotary Motor Using Two Orthogonal Bending Modes of a Hollow Cylinder," *Proc. 7th Actuator 2000*, p.242-245, Axon, Bremen (2000).

- ²⁴K. Uchino, "Materials Issues in Design and Performance of Piezoelectric Actuators: An Overview," *Acta Mater.* 46[11], 3745 (1998).
- ²⁵H. Aburatani, K. Uchino, A. Furuta and Y. Fuda, "Destruction Mechanism and Destruction Detection Technique for Multilayer Ceramic Actuators," *Proc. 9th Int'l Symp. Appl. Ferroelectrics*, p.750 (1995).
- ²⁶NEC, "Thickness Mode Piezoelectric Transformer," US Patent No. 5,118,982 (1992).
- ²⁷S. Kawashima, O. Ohnishi, H. Hakamata, S. Tagami, A. Fukuoka, T. Inoue and S. Hirose, "Third order longitudinal mode piezoelectric ceramic transformer and its application to high-voltage power inverter," *IEEE Int'l Ultrasonic Symp. Proc.*, Nov. (1994).
- ²⁸J. Zheng, S. Takahashi, S. Yoshikawa, K. Uchino and J.W.C. de Vries, "Heat Generation in Multilayer Piezoelectric Actuators," *J. Amer. Ceram. Soc.* 79, 3193 (1996).
- ²⁹K. Nagata, "Lifetime of Multilayer Actuators," *Proc. 49th Solid State Actuator Study Committee, JTTAS, Tokyo, Jan.* (1995).
- ³⁰K. Uchino and H. Aburatani, "Destruction Detection Techniques for Safety Piezoelectric Actuator Systems," *Proc. 2nd Int'l Conf. Intelligent Mater.*, p.1248, (1994).
- ³¹K. Uchino, "Reliability of Ceramic Actuators," *Proc. Int'l Symp. Appl. Ferroelectrics*, Vol. 2, 763 (1997).
- ³²K. Uchino, B. Koc, P. Laoratanakul and A. Vazquez Carazo, "Piezoelectric Transformers – New Perspective–," *Proc. 3rd Asian Mtg. Ferroelectrics*, Dec. 12-15, Hong Kong (2000) [in press].
- ³³N. O. Sokal, "RF Power Amplifier, Classes A through S," *Proc. Electron. Ind. Forum of New England*, p. 179-252 (1997).
- ³⁴Motorola, "Actuator Drive and Energy Recovery System," US Patent No. 5,691,592 (1997).
- ³⁵S. Sugiyama and K. Uchino, "Pulse Driving Method of Piezoelectric Actuators," *Proc. 6th IEEE Int'l Symp. Appl. Ferroelectrics*, p.637 (1986).
- ³⁶K. Uchino and S. Hirose, "Loss Mechanisms in Piezoelectrics," *IEEE UFFC Trans.* (2001) [in press].

APPENDIX 82

Finite Element Study on 1-D Array Transducer Design

Wenkang Qi and Wenwu Cao

Abstract—A comprehensive study using finite element analysis (FEA) was performed on 1-D transducer arrays. Crosstalk reduction, subdicing effects, directivity pattern, and baffle effects were quantified numerically. It was found that the directivity pattern strongly depends on the transducer size and kerf filling materials. The FEA is particularly powerful to reveal the inhomogeneous nature of the vibrational characteristic of transducer surface, which allows more accurate beam pattern computation in 3-D. The simulated directivity pattern also was satisfactorily verified by experimental measurements.

I. INTRODUCTION

ULTRASONIC transducer arrays are widely used in clinical ultrasound diagnosis [1]. Designing better array transducers is the critical issue for further improving the quality of ultrasonic imaging. For this purpose, it is necessary to gain better fundamental understanding on the transducer operations in order to design new and better arrays. Many issues in array design—such as crosstalk, baffle effect, directivity pattern—cannot be accurately studied using analytic method due to the complexity of the partial differential equations involved. Finite element analysis (FEA) is the only appropriate way to gain more detailed information [2].

Reducing the element crosstalk level is very important in array designs, especially for phased arrays, because the crosstalk between elements affects the directivity pattern and the sensitivity. Another important issue in transducer design is to avoid lateral modes, which may couple to the thickness mode to affect the transducer operation, similar to the case of single-element composite transducers [3]–[9]. Subdicing of the elements has been used in practice to solve this lateral mode problem. It also was shown experimentally that using lossy kerf filler material could substantially reduce those lateral modes. Here we will use simulation to help understand the mechanism of these practical methods employed by many transducer engineers.

Under 1-D approximation, the baffle effects on an array element can be described by a $\cos \theta$ function as described in most of the existing literature, which implies that the baffle was treated as a pressure-release baffle and the array

was assumed to be infinite in size. Using FEA, we can show that the baffle effect is much more complicated than a $\cos \theta$ function because the actual array is always finite in size, and the baffle is not purely the pressure-release type. This paper will provide more technical details for the 1-D array design through FEA simulations.

Most of the results were obtained using the ANSYS finite element package, and the general meshing scheme is to maintain at least 8 elements per wavelength. Optimized meshing size was obtained by continuously reducing the element size until the relative error for a calculated target quantity between consecutive runs is less than 1%. Because very large simulation models become numerically unstable, we used the boundary element method (BEM) for transducer beam pattern calculation and obtained satisfactory results.

II. EFFECTS OF SUBDICING, BAFFLE INFLUENCE AND DIRECTIVITY PATTERN

A. Effect of Subdicing

As a requirement, the width, d , of each element in a 1-D array should be large enough so the acoustic impedance loaded on the element will not be purely imaginary (in which case the element cannot radiate acoustic energy into the medium). However, the aspect ratio h/d of each element must be greater than 2 in order to separate the lateral modes from the thickness mode, where h is the height of the element.

In many current 1-D array transducers, each element is subdiced, which can effectively decrease the aspect ratio of each element. Our simulation results demonstrated the importance of element subdicing. Fig. 1 shows the impedance spectrum for a 1-D array with the kerf width, element size, and element height to be 50 μm , 200 μm , and 300 μm , respectively. This design does not obey the rule of aspect ratio > 2 ; therefore, one can clearly see a lateral mode on the impedance curve near 7 MHz (see the solid line). When all the elements in the array are subdiced to make the aspect ratio greater than 2, the lateral mode disappeared as shown in the dashed line in Fig. 1. The lateral mode was not suppressed by the subdicing; it was simply being pushed to frequencies much higher than the thickness mode.

Introducing high mechanical damping into the filler material also can reduce the amplitude of the lateral modes in 1-D arrays, particularly in high frequencies. Fig. 2 shows

Manuscript received July 28, 1999; accepted February 3, 2000. This research is supported by the national resource grant from the NIH Grant # p41-RR11795-01A1.

W. Qi currently is with GE Disonics, San Jose, CA 95112.

W. Cao is with the Materials Research Laboratory, The Pennsylvania State University, University Park, PA 16802 (e-mail: cao@math.psu.edu).

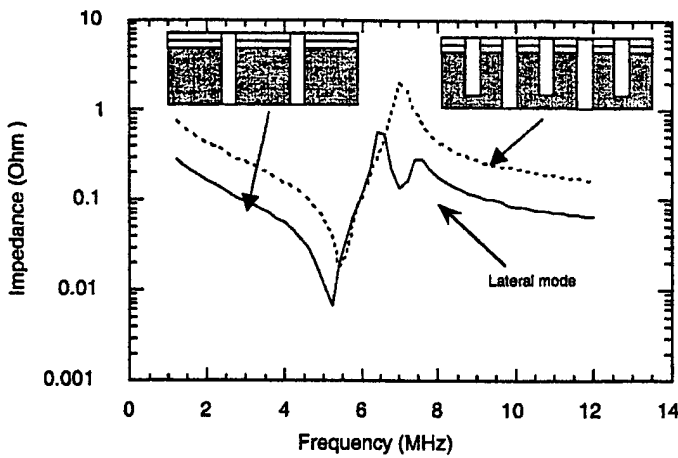


Fig. 1. Calculated impedance spectrum for a 1-D array with 50 μm kerf, 0.2 mm element size, and element height of 0.3 mm. The solid curve is for the case without element subdicing; the dashed curve is for the model with element subdicing.

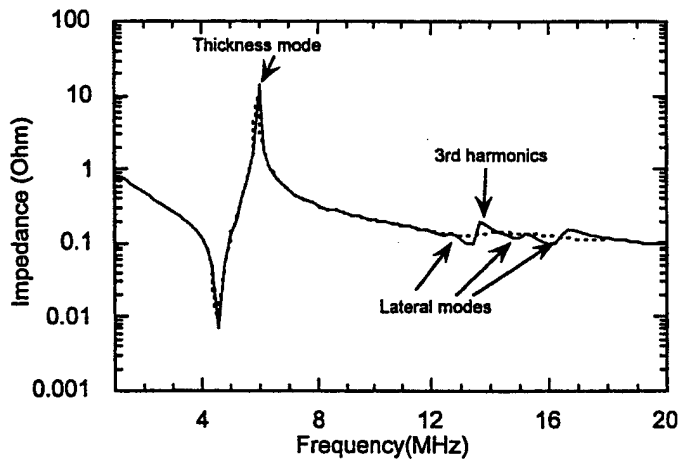


Fig. 2. The calculated impedance curve for a 5 MHz 1-D array transducer with 35 μm kerf width, 300 μm pitch, and 420 μm element height. For the solid curve, the Rayleigh damping ratios for the ceramic and the filler were set at $\beta_c = 3 \cdot 10^{-10}$ s and $\beta_p = 5 \cdot 10^{-10}$ s, respectively. For the dashed curve, the Rayleigh damping ratios for the ceramic and the filler were $\beta_c = 3 \cdot 10^{-10}$ s, and $\beta_p = 5 \cdot 10^{-9}$ s, respectively.

the comparison between the impedance spectra of two transducers with the same design but different kerf filler materials. The solid line is for a design using low loss filler material. Three lateral modes are visible in the impedance curve for this case. When the filler damping is increased by an order of magnitude in our simulation model, while keeping all other parameters unchanged, the lateral modes as well as the third harmonic disappeared (dashed line in Fig. 2).

The baffle effect for each element in an array was not given enough attention before. It is usually described by a cosine function assuming the baffle to be a pressure-release baffle and the array to be infinite in the elevation dimension. However, this assumption is not accurate for real transducers. Using numerical methods, we were able

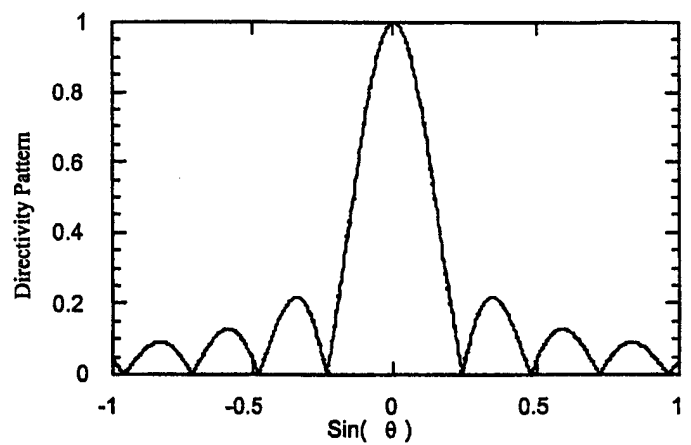


Fig. 3. The normalized directivity pattern of a uniformly vibrating square transducer in a rigid baffle. The transducer is a 5 mm \times 5 mm square, and the center frequency is 1.25 MHz. The numerical results are identical with the analytic results.

to successfully calculate the baffle effect in realistic conditions. A direct computation of transducer beam pattern using the finite element method (FEM) was not successful because the water medium was too large and error accumulation rendered the solution unstable, particularly for the far field pressure distribution. To resolve this problem, we used a smaller FEM model to calculate the pressure and velocity distributions at the transducer surface, then used the BEM to solve the Helmholtz integral.

B. Verification of the Beam Pattern Obtained from Numerical Methods

We used two simple models to verify the numerical results. The first verification was a uniformly vibrating 5 mm by 5 mm square transducer with an infinite rigid baffle. The Helmholtz integral for the pressure distribution $p(x)$ is given by:

$$p(x) = \int_S \left\{ p(\sigma) \frac{\partial G(x, \sigma)}{\partial n_\sigma} + i\omega \rho v(\sigma) G(x, \sigma) \right\} ds(\sigma) \quad (1)$$

where $G(x, \sigma) = \frac{1}{4\pi} \frac{e^{-ik|x-\sigma|}}{|x-\sigma|}$ is the Green's function, σ is the space variable on the transducer surface, $p(\sigma)$ and $v(\sigma)$ are the pressure and velocity, respectively, at the transducer surface, and n_σ is the surface normal.

The first term in (1) is zero for a rigid baffle so that the integral can be simplified as:

$$p(x) = \int_S \{ i\omega \rho v(\sigma) G(x, \sigma) \} ds(\sigma) \quad (2)$$

One can solve (2) analytically, and the solution provides us a control check for the numerical results. The analytic and numerical results are identical as shown in Fig. 3, which confirmed the validity of our numerical procedure.

The second test is for a uniformly vibrating square piston transducer in a pressure-release baffle. For this model,

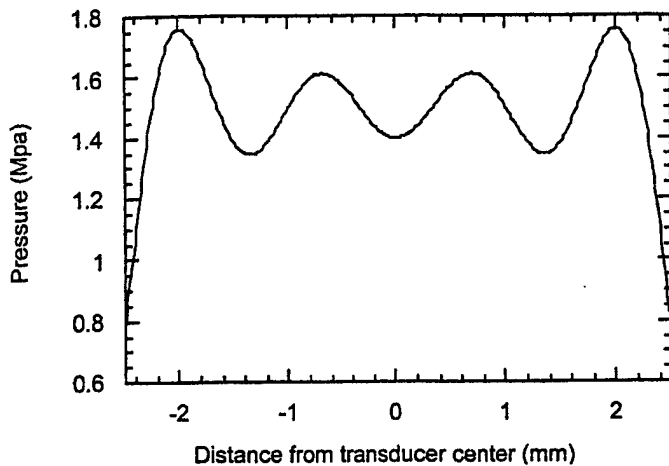


Fig. 4. The pressure amplitude distribution on the surface of a uniformly vibrating transducer immersed in water, the size of the square transducer is 5 mm × 5 mm with a center frequency of 1.25 MHz.

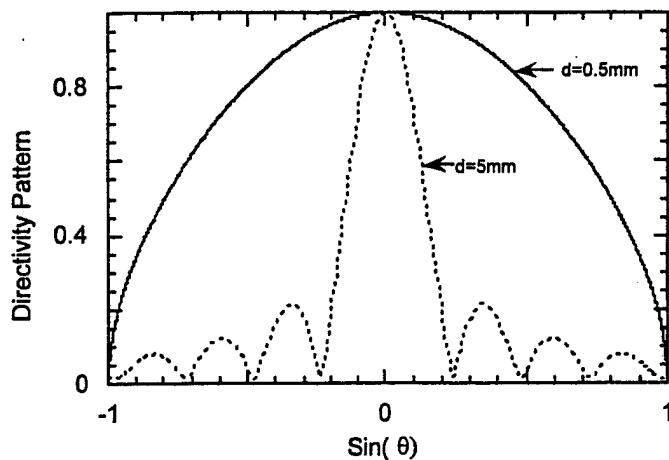


Fig. 5. Comparison between the normalized directivity patterns of two transducers with a diameter of 0.5 mm and 5 mm, respectively. The center frequency for both transducers is 1.25 MHz.

the second term $G(x, \sigma)$ is zero; therefore, (1) can be rewritten as:

$$p(x) = \int_S \left\{ p(\sigma) \frac{\partial G(x, \sigma)}{\partial n_\sigma} \right\} ds(\sigma) \quad (3)$$

In this model, the normal vibrating velocity is a constant, and the pressure distribution at the transducer surface may be calculated by using (3). The pressure distribution was nonuniform at the transducer surface, although the normal vibrating velocity is a constant (Fig. 4). The analytical solution of the directivity pattern is equal to the product of a *sinc* function and $\cos \theta$, in which the $\cos \theta$ term represents the effect of a pressure-release baffle [4]. The calculated directivity using (3) is exactly the same as the analytical solution as shown in Fig. 5 (the two curves overlap). The directivity pattern calculated in Fig. 5 is almost a half circle for a transducer of 0.5 mm square (solid curve), which is much smaller than the wavelength of 1.2 mm. The dashed line is for a 5 mm square, single-

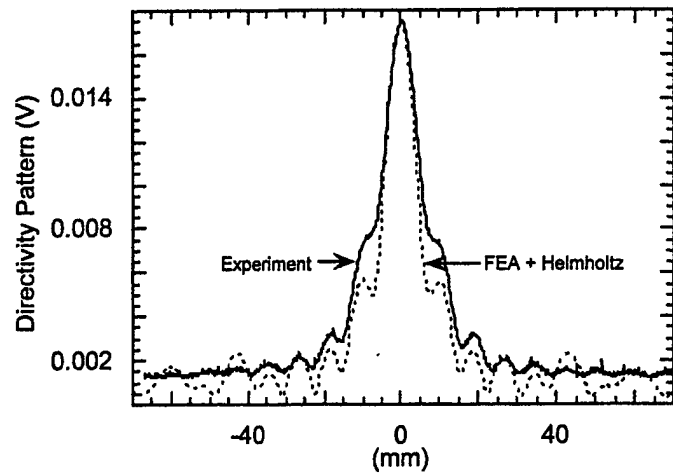


Fig. 6. The directivity pattern of a 32 element array transducer. The measurement was performed at a distance 30 cm from the face of the array; the peak value of the calculated pressure is normalized to the peak value of the measured voltage.

element transducer; and its dimension is much larger than the wavelength of 1.2 mm. Sidelobes appeared in the directivity pattern for the latter case.

After the two confidence checks, our numerical code was applied to calculate the beam pattern of a 1-D array and compared to experimental measurements. Fig. 6 is the comparison of the calculated and measured directivity patterns for a 1-D array with all elements excited in phase (note: the calculated beam pattern was normalized to voltage based on the peak value of the experimental observations). The calculated results match reasonably well with the experimental results. Both the computations the experiments were performed using water as the medium.

C. Directivity Pattern of an Element Embedded in a 1-D Array

After the verification procedure described in the last section, the combined FEM and BEM method was applied to simulate the transducer beam pattern of one element embedded in a finite 1-D array. In this model, the baffle is neither a pressure-release type nor a rigid type; therefore, one cannot solve the problem analytically. Fig. 7 shows a 32-element 1-D array FEA model with partially diced backing, 2 matching layers, a fluid-structure interface layer, and a portion of the water medium. The kerf size is 0.1 mm, the element size is 0.15 mm, and the element height is 1.12 mm. Absorbing boundary conditions were applied at the boundaries of water medium to eliminate reflections.

As an example, we excited the 16th element in the array using a broadband pulse. The pressure and normal velocity distributions were obtained using harmonic analysis in the ANSYS® FEA code. Fig. 8 shows the real and imaginary parts of the pressure distributions, respectively, at the transducer surface. In the same computation, we also obtained the real and imaginary parts of the velocity distributions, respectively, at the surface of the array as shown

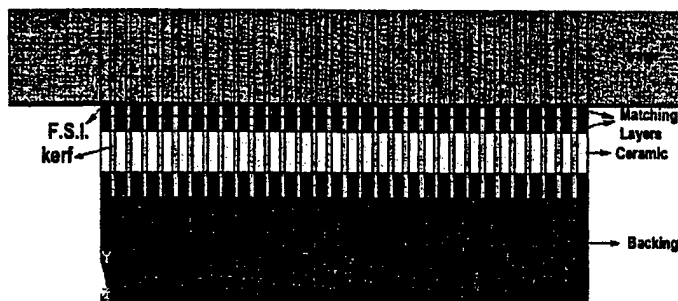


Fig. 7. The FEA model for a 32 element 1-D array. Both matching layer and part of backing were diced to reduce crosstalk.

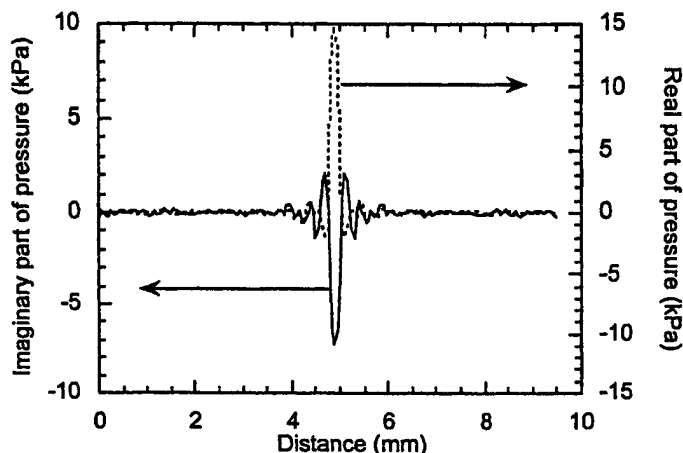


Fig. 8. The real (dashed line) and imaginary (solid line) parts of pressure distribution at the surface of a 32 element 1-D array when the 16th element was being excited.

in Fig. 9. Using these pressure and velocity distribution data, the directivity pattern of the 16th element can be calculated using the Helmholtz integral (1). The results are given in Fig. 10 as the solid line. For comparison, the analytic result of $\text{sinc}(2\pi\kappa d * \sin\theta) * \cos\theta$ is also shown in Fig. 10 by the dashed line. One can see that the directivity pattern obtained from FEA is much more complicated than the simple product of $\text{sinc}(2\pi\kappa d * \sin\theta) * \cos\theta$. There are many oscillations in the directivity pattern calculated by the FEA + BEM method. These variations are caused by the crosstalk among elements and reflect the effect of finite dimension with a nonuniform baffle.

The directivity pattern also depends on other factors, such as the properties of the kerf filler and the geometry of the array structure. Fig. 11 shows the comparison of the directivity patterns produced by arrays with a hard and a soft filler material, respectively. The intensity of the sound field is higher when the kerf is filled with harder material. For a soft kerf filler, the phase lagging between the kerf and the ceramic becomes larger, which causes the vibrating intensity of the whole array to decrease.

D. Beam Pattern of a 1-D Linear Array

Using the combined FEA+BEM method, we also calculated the beam pattern of the whole 1-D array transducer.

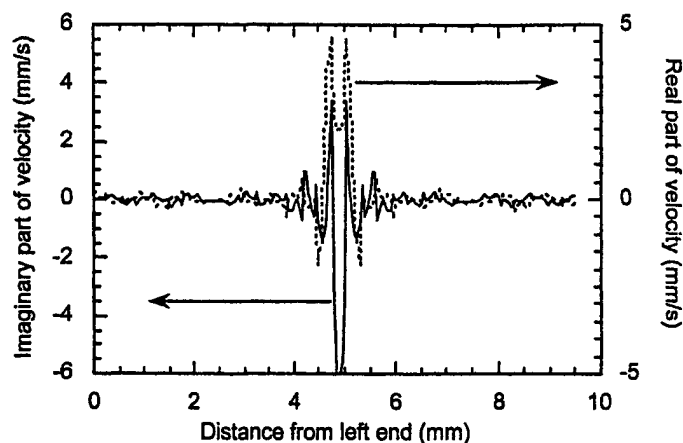


Fig. 9. The real (dashed line) and imaginary (solid line) parts of the velocity distribution on the surface of a 32 element 1-D array with the 16th element being excited.

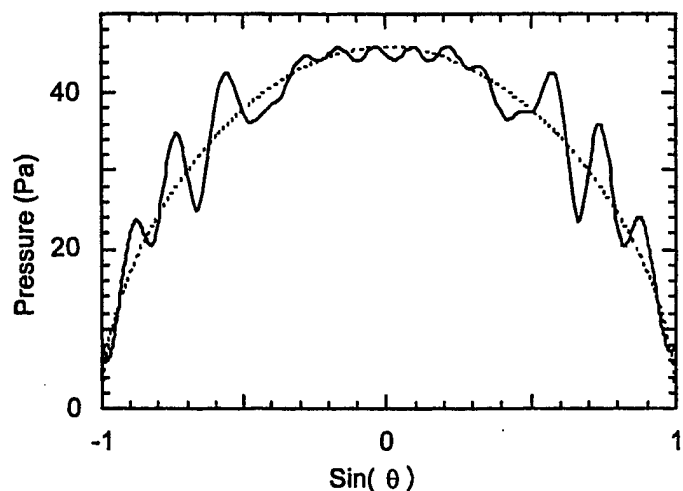


Fig. 10. The directivity pattern of one center element in a 1-D array.

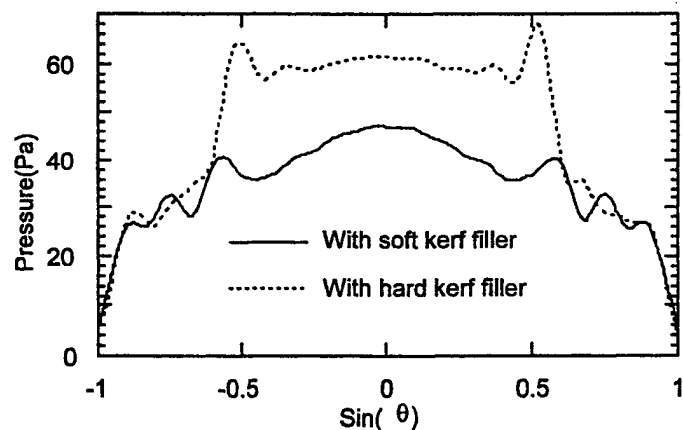


Fig. 11. Comparison between the directivity patterns (acceptance angle) of an array element with soft (solid line) and hard (dashed line) kerf filler.

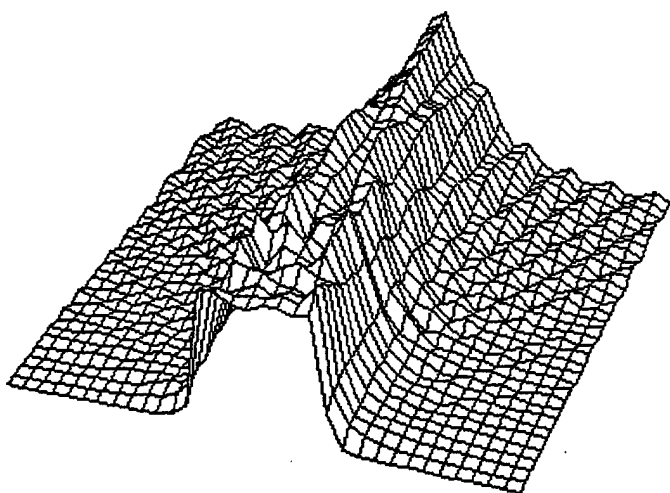


Fig. 12. The surface plot of the beam pattern of a 32 element 1-D linear array.

This FEA model array has a 0.6 mm pitch and 0.2 mm kerf, and the height of the element is 1 mm. The backing material is a composite of tungsten powder and polymer. The two quarter-wavelength matching layers were made of polymer and aluminum oxide powder; the aluminum oxide volume percentage was 17.5% for the inner matching layer and 7% for the outer matching layer. The kerf filler is a very light and soft polymer material. Except for the attenuation, all the input material parameters in the simulation model were measured experimentally.

Fig. 12 is a surface plot of the calculated beam pattern of this 1-D array. All detailed characteristics of the beam pattern, particularly the near-field variation, the focal point, beam size, and sidelobes are shown clearly in Fig. 12. The most significant result from the calculation is the detailed near-field beam pattern, which is very difficult to obtain experimentally because the measurement probe often interferes with the transducer beam to be measured. The calculations provided some critical information for transducer designs, such as beam width, focal distance, and sidelobe level (or grating lobe level). The directivity of partially excited array is plotted in Fig. 13. There are 128 elements in the FEA model array, but only 32 elements in the center region were excited for the directivity calculation. This partial excitation can help us to understand the baffle effect.

The establishment of the modeling procedure is very important for improving transducer designs and exploring new designs. Using the FEA simulation, we can optimize the element geometry, pitch size, and all the active and passive materials used in the transducer. In other words, it can help us find the best combination to produce a desired transducer.

The simulation procedure also can be used to study 1-D phased array by applying phase delayed electrical signals to consecutive elements. One can study the angular dependence of the beam pattern by steering the beam using simulation with phase-delayed excitation. Fig. 14 is a

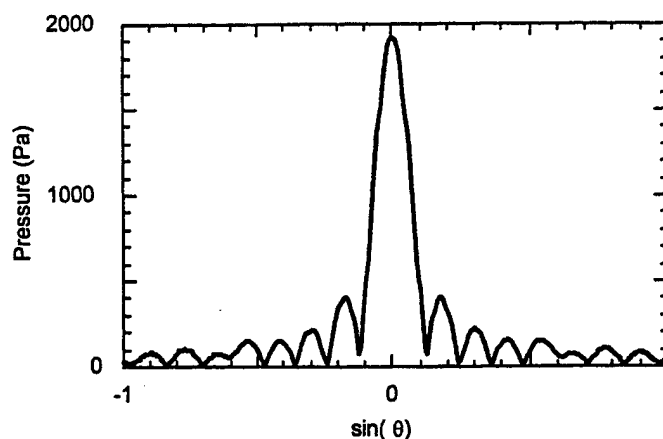


Fig. 13. The calculated directivity pattern of 32 elements in the center region of a 128 element linear array.

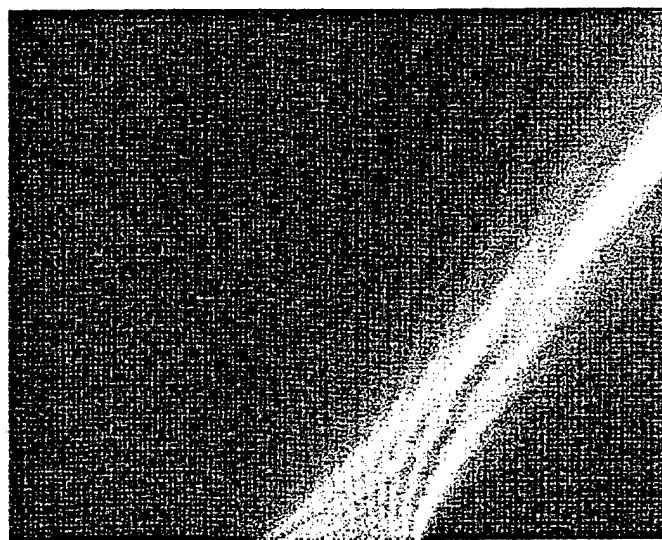


Fig. 14. Beam pattern of a phased array with 54° steering angle.

typical steered beam pattern with a steering angle of 54°. The width of the main beam, the sidelobe, and the focal distance all changed slightly as a function of the steering angle because the array has a finite size. The model phased array has a kerf size of 0.1 mm and a pitch size of 0.3 mm, which is equal to one-half of the wavelength, so there are no grating lobes [10]. The beam pattern in Fig. 14 was calculated by using harmonic analysis in ANSYS at 2.5 MHz, then use BEM to carry out the Helmholtz integral.

III. CROSSTALK

The crosstalk in arrays degrades the contrast resolution and causes artifacts in ultrasonic imaging. It is of great importance to reduce the crosstalk level in designing better medical imaging transducers. Crosstalk has two sources: mechanical and electrical. Here we only analyze the mechanical crosstalk as the electrical crosstalk is less than -43 dB as analyzed in [4]. For convenience in the FEA, a

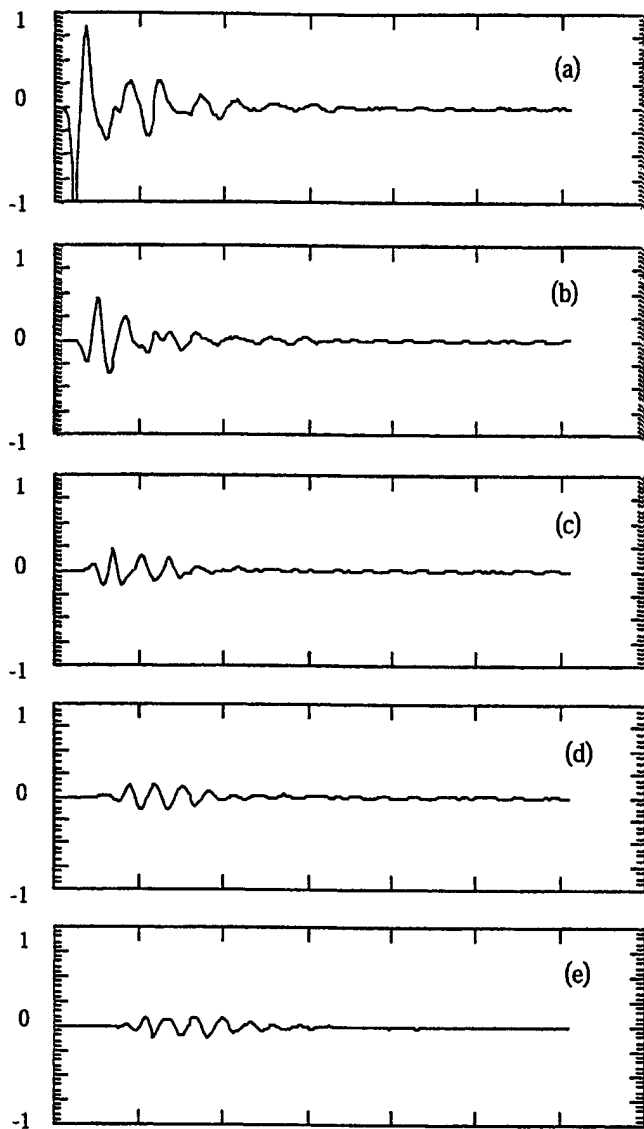


Fig. 15. Impulse responses of the excited element (a), first neighbor (b), second neighbor (c), third neighbor (d), and fourth neighbor (e), respectively.

new measure is defined for the mechanical crosstalk [5], [6] as the following:

$$\text{relative response} = -20 \log \left(\frac{\text{RMS of the displacement of the excited element}}{\text{RMS of the displacement of the neighboring element}} \right).$$

Because we are using the RMS to define the mechanical crosstalk level, it has a unique value even for nonuniform displacement of each element. The new measure only reflects the strength of mechanical coupling; the electrical coupling was not included.

We have explored different kerf cutting schemes to reduce the mechanical crosstalk. The dimensions of the array under investigation are the same as that of the linear array shown in Fig. 7. The outer matching layer for this model design was a single sheet and the inner matching layer was diced together with the element. From Fig. 15(a) to (e), one can see that the amplitude of the impulse response of

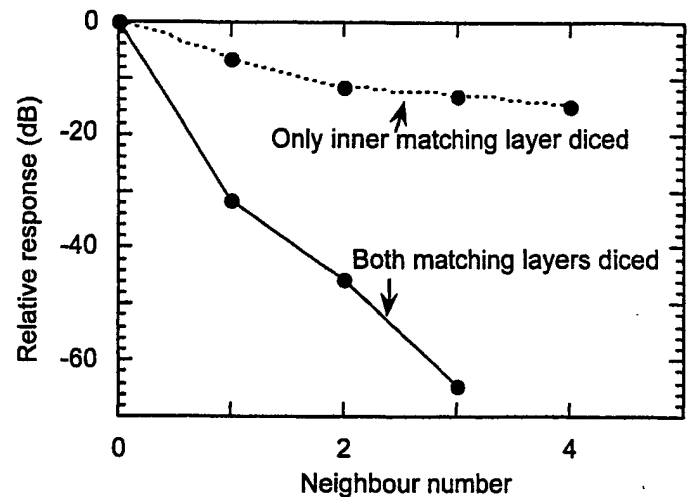


Fig. 16. Comparison of the crosstalk levels of array designs with one of the matching layers being diced and both matching layers being diced.

the neighboring elements gradually decreases with distance from the excited element. Our calculation showed that dicing both matching layers is very important for reducing the mechanical coupling between different elements (acoustic isolation). Fig. 16 plots the comparison of the mechanical crosstalk levels for two cases: 1) one inner matching layer was diced together with the element, and 2) both matching layers were diced together with the elements. As shown in Fig. 16 the crosstalk level is much reduced for the latter model. As a rule of thumb in transducer design, the crosstalk level for the nearest neighbor should be less than -30 dB in order to avoid artifacts in ultrasonic imaging; based on our calculations, the one layer dicing scheme is not sufficient to satisfy this requirement.

A lens is often used on top of the array transducer to change its focus. This lens may cause extra mechanical cross coupling if it is made of solid material. It was found that the main coupling mechanism is through shear wave; therefore, one way to reduce the lens coupling is to use materials that have very small shear modules. If the array is not air backed, the backing will also provide additional mechanical coupling. In practical designs, this problem is resolved by partially dicing the lossy transducer backing.

IV. SUMMARY AND CONCLUSIONS

We have reported a combined FEA and BEM study to simulate 1-D array transducers, which allowed us to study the subdicing effect, directivity pattern, baffle effect, and crosstalk in 1-D array transducers. It was shown that lateral modes might be decoupled from the thickness mode by either subdicing each element, which effectively moves the spurious modes to higher frequencies, or heavy damping. The baffle effects for an element embedded in a 1-D array have been accurately calculated using this combined simulation scheme. Three different types of baffles were studied, and the results were confirmed by both an-

alytical solutions and experiments. From the simulation results, the baffle effect cannot be simply represented by a $\cos \theta$ function as assumed in practice. Although harder filler materials in the kerfs can increase the sensitivity of the transducer, softer filler for the kerfs can reduce the mechanical coupling among elements and the strength of the lateral modes. The simulation results also indicated that the mechanical crosstalk level could be greatly reduced when both matching layers were diced. Lossy backing and lossy kerf filler also can help to broaden the acceptance angle response of each element in the array.

REFERENCES

- [1] K. Kirk Shung, M. B. Smith, and B. W. M. Tsui, in *Principles of Medical Imaging*. San Diego: Academic Press, 1992.
- [2] G. S. Kino, in *Acoustic Waves*. New York: Prentice Hall, 1987.
- [3] R. Lerch, H. Landes, and H. T. Kaarmann, "Finite element modeling of the pulse-echo behavior of ultrasound transducers," *Proc. IEEE Ultrason. Symp.*, 1994, pp. 1021-1026.
- [4] R. Lerch, "Simulation of piezoelectric devices by two- and three-dimensional finite element methods," *IEEE Trans. Ultrason., Ferroelect., Freq. Contr.*, vol. 37, pp. 233-246, 1990.
- [5] W. Qi and W. Cao, "Finite element analysis and experimental studies on the thickness resonance of piezocomposite transducers," *Ultrason. Imag.*, vol. 18, pp. 1-9, 1996.
- [6] W. Qi and Wenwu Cao, "Finite element analysis of periodic and random 2-2 piezocomposite transducers with finite dimensions," *IEEE Trans. Ultrason., Ferroelect., Freq. Contr.*, vol. 44, pp. 1168-1171, 1997.
- [7] W. Cao and W. Qi, "Plane wave propagation in finite 2-2 composite," *J. Appl. Phys.*, vol. 78, pp. 4627-4632, 1995.
- [8] W. Cao and W. Qi, "Multisource excitations in a stratified bi-plane structure," *J. Appl. Phys.*, vol. 78, pp. 4640-4646, 1995.
- [9] C. G. Oakley, "Analysis and development of piezoelectric composites for medical ultrasonic transducer applications," Ph.D. Dissertation, The Pennsylvania State University, University Park, PA, 1991.
- [10] W. Friedrich, H. Kaarmann, and R. Lerch, "Finite element modeling of acoustic radiation from piezoelectric phased array antennas," *Proc. IEEE Ultrason. Symp.*, pp. 763-767, 1990.



Wenkang Qi received his B.S. and M.S. degrees in Biomedical Engineering in 1988 and 1991, respectively, from Tsinghua University, China. In 1997, he earned his Ph.D. degree in Bioengineering from The Pennsylvania State University. He joined GE Diasonics as an ultrasonic transducer researcher and designer in 1997.

Dr. Qi is a senior member of the IEEE and a member of the SPIE. His research interest is in the design of medical ultrasonic transducer arrays, ultrasound imaging systems, and other

biomedical instruments.



Wenwu Cao received his B.S. degree in physics from Jilin University, Changchun, China, in 1982 and the Ph.D. degree in condensed matter physics from The Pennsylvania State University in 1987.

He is currently holding a joint appointment between the Department of Mathematics and the Materials Research Laboratory of The Pennsylvania State University as Associate Professor of Mathematics and Materials Science. He has conducted both theoretical and experimental research in the area of condensed matter physics and materials, including theories on proper- and improper-ferroelastic phase transitions and static and dynamic properties of domains and domain walls in ferroelectric and ferroelastic materials. He has also performed measurements on second- and third-order elastic constants, linear and nonlinear dielectric constants, and piezoelectric constants in single crystals and ceramics. His current interests also include the static and dynamic behavior of piezoelectric ceramic-polymer composites, simulation design of piezoelectric sensors, transducers and actuators for underwater acoustics, and medical ultrasonic imaging as well as ultrasonic NDE and signal processing.

Dr. Cao is a member of the Society for Industrial and Applied Mathematics and the American Physical Society.

APPENDIX 83

Electromechanical properties of thin strip piezoelectric vibrators at high frequency

Timothy Ritter,^{a)} K. Kirk Shung, Wenwu Cao, and Thomas R. Shrout
NIH Resource Center for Medical Ultrasonic Transducer Technology, Penn State University, 205 Hallowell Building, University Park, Pennsylvania 16802

(Received 8 March 2000; accepted for publication 3 April 2000)

A method was developed and used to determine the electromechanical properties of high frequency (>20 MHz) piezoelectric strip vibrators. A nonlinear regression technique was employed to fit the impedance magnitude and phase as predicted by Mason's model to measured values. Results from experimental measurements on 30 MHz array elements supported by an attenuative backing indicated degraded performance when compared to values predicted from the electromechanical properties measured at low frequency. This degradation may be attributed to damage incurred during fabrication and grain size effects, with a fine grain sized material providing superior relative performance. This technique may be used in the evaluation and comparison of different fabrication processes and materials for high frequency medical imaging arrays. © 2000 American Institute of Physics. [S0021-8979(00)05913-2]

I. INTRODUCTION

Ultrasonic imaging at frequencies from 20 to 100 MHz can provide high spatial resolution for dermatological, ophthalmological, articular, and intravascular applications.¹ Current imaging systems in this frequency range rely on mechanically scanned single element transducers to interrogate the tissue of interest. For enhanced performance a solid-state array is desired, where multiple thin strip resonators are placed adjacently and are mechanically and electrically isolated. The small scale required of devices operating above 20 MHz, where individual elements are less than 100 μm tall and 50 μm wide, has severely limited the development of high frequency arrays. Fabrication techniques capable of achieving devices of this scale often alter the electromechanical properties due to physical damage and departures from the desired geometry. In addition, piezoelectric materials display frequency dispersion in most electromechanical properties.² It is therefore desirable to determine the properties of high frequency array elements after fabrication.

The resonance technique is often used for measuring the electromechanical properties at low frequencies, where it is practical to fabricate and test air-loaded resonators.³ Above 20 MHz, the electrical interconnect and measurement of air loaded array elements is problematic due to the small device size. It is therefore desirable to support the element with a conductive substrate. Supported piezoelectric films have been characterized using a comparison of experimental electrical impedance data and an analytical solution of the one-dimensional wave equation.⁴ This technique is not directly suited to high frequency array elements, however, due to coupling between the width and height resonances. A method for approximating the coupling between these resonances has also been described, but the procedure is cumbersome and does not lend itself to determining the full electromechanical properties.⁵ A simplified method of analyzing the

elastic, piezoelectric, and dielectric properties of high frequency array elements supported by a substrate is proposed herein. This technique has been used to determine the properties of two commonly used polycrystalline piezoelectric materials when applied to a high frequency linear array design.

II. CHARACTERIZATION METHOD

A popular method of predicting the performance of piezoelectric devices is to approximate them as one-dimensional vibrators and develop an equivalent circuit by application of network theory. The Mason equivalent circuit, shown in Fig. 1 for a one-dimensional thickness extensional vibrator, has been used extensively for modeling piezoelectric and transducer performance.⁶ Other circuits such as the KLM model are also used extensively,⁷ but since they are based on the same differential equations they differ only in form and reduce to the same solution.⁸ For this work the Mason model was used to determine the electromechanical properties of a piezoelectric array element, as opposed to the traditional use of predicting electrical or acoustic performance based on previously measured properties.

Figure 2 shows the geometry of a representative 30 MHz linear array element. The z axis represents the direction of poling. The y axis is assumed to be effectively infinite and presents a boundary condition of zero strain (S) near the height resonance. The boundary condition in the x direction is neither zero stress nor zero strain, but approaches a condition of zero stress (T) as the ratio of height to width approaches infinity. The electromechanical properties applicable to this geometry, labeled with a prime ($'$) according to the convention of DeSilets,⁹ are c_{33}' , k_{33}' and ϵ_{33}' . It is helpful to write each of these properties as complex quantities (denoted with an $*$) according to the following convention:¹⁰

$$c_{33}'^* = c_{33}' (1 + i \tan \delta_m), \quad (1)$$

$$\epsilon_{33}'^* = \epsilon_{33}' (1 - i \tan \delta_e), \quad (2)$$

$$k_{33}'^* = k_{33}' (1 + i \tan \delta_k). \quad (3)$$

^{a)}Electronic mail: tar145@psu.edu

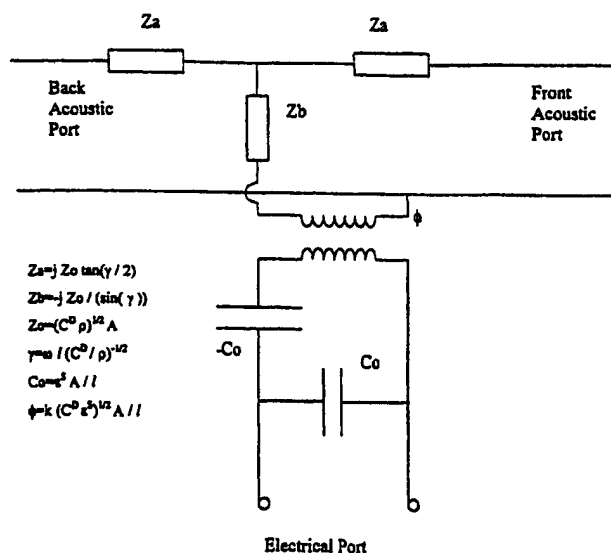


FIG. 1. Mason's model for a thickness-resonant device. k is the coupling coefficient, C^D is the elastic constant, ϵ^s is the clamped permittivity, ρ is the density of the piezoelectric, A is the electroded area, l is the thickness, and ω is the angular frequency. Additional loads on either acoustic port can be represented either by a T network for finite dimensions or by an impedance for infinite dimensions (see Ref. 6).

Given the geometry in Fig. 2 it is possible to determine the properties of an array element using the Mason model. The advantage of doing this is that the elements can be supported by a substrate (often referred to as a backing material) during measurement. The properties can then be extracted from the measured data using nonlinear regression to fit measured and modeled electrical impedance. It has previously been shown that one-dimensional models can provide an excellent approximation to the performance of backed array elements resonating in air as long as the ratio of width to height (aspect ratio) does not exceed 0.7.^{9,11} In order to effectively approximate this multidimensional problem using a one-dimensional model it is important to point out the following limitations:

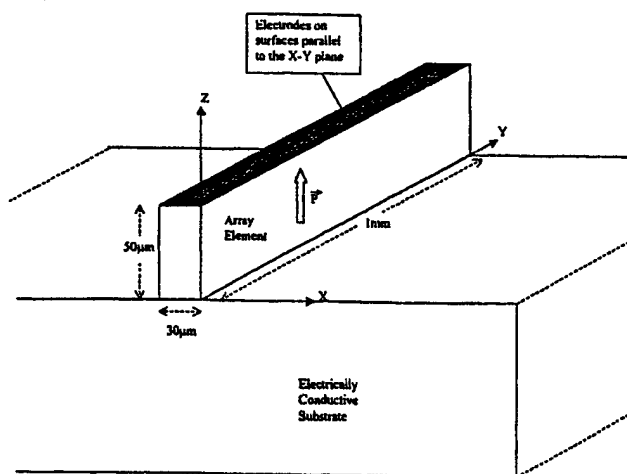


FIG. 2. The geometry of a representative element used in a 30 MHz linear array. The z axis represents the direction of poling, and electrodes are applied to the top and bottom faces.

(1) The backing must present a real and well-defined acoustic load. DeSilets⁹ has shown that as long as the product of the wave number for a longitudinal plane wave and the width exceeds one, the effective load impedance is equal to the longitudinal plane wave impedance of the backing.

(2) The measured properties (especially the elastic constant) depend on the aspect ratio and cannot be generalized to other configurations. This limitation is true with air loaded resonators as well.

(3) Care must be taken to avoid acoustic interactions between elements if a multi-element array is tested. The use of a high attenuation backing is recommended, as is the use of a wide separation between the elements.

(4) The elements are often damaged during fabrication. For example, laser dicing can result in tapered element cross sections, thermal damage, and redeposited material, thereby changing the resonant behavior. One of the uses of the model, therefore, would be to assess the effects of the fabrication process.

Two different piezoelectric materials were fabricated using fine scale mechanical dicing: a fine grain size ($<2 \mu\text{m}$) PZT-5H equivalent material (TRS600FG, TRS Ceramics, Inc., State College, PA) and an ultrahigh permittivity material with a $6.5 \mu\text{m}$ grain size (TRSHK1, TRS Ceramics, Inc., State College, PA). The material in the form of a thin plate was lapped to the desired thickness and backed with a highly attenuative silver-epoxy thermoset composite. The acoustic impedance of this backing was measured to be 5.92 MRayls at 30 MHz and the longitudinal attenuation was over 100 dB/mm. The elements were connected using a flexible circuit bonded across the face of a rigid frame. The backed piezoceramic was then bonded into a slot machined into the center of the assembly such that the interconnect traces extended beyond the frame on both sides. Sputtered Cr/Au was used to electrically connect the flexible circuit and the piezomaterial. The ends of the circuit were then folded out of the way and the elements were diced using a K&S model 982-6 dicing saw. After fabrication the piezoelectric elements were re-poled under an electric field of 30 kV/cm for 5 min at room temperature and aged for 24 h. Electrical measurements were obtained using an HP 4194 impedance analyzer using the Z-probe attachment.

The curve-fitting routine was implemented in Matlab using a Gauss-Newton algorithm to fit six variables: $c_{33}^{D'}$, k_{33}' , $\epsilon_{33}^{S'}$, $\tan \delta_m$, $\tan \delta_e$, and $\tan \delta_k$. The thickness of the sputtered gold was accounted for in the Mason model using a T network,⁶ since the electrode mass loads the ceramic and shifts the resonant spectrum at high frequencies. The routine was implemented in two parts: (1) a fit to $|Z|$ was used to obtain the variables $c_{33}^{D'}$, k_{33}' , $\epsilon_{33}^{S'}$, $\tan \delta_m$, and $\tan \delta_k$ and (2) a fit to the electrical phase angle was used to obtain $\tan \delta_e$, since the dielectric loss tangent is heavily dependent on the phase angle.¹⁰ 120 data points were used in the range from 25 to 40 MHz, and three iterations of the program resulted in convergence for all cases. Figure 3 shows a block diagram describing the program.

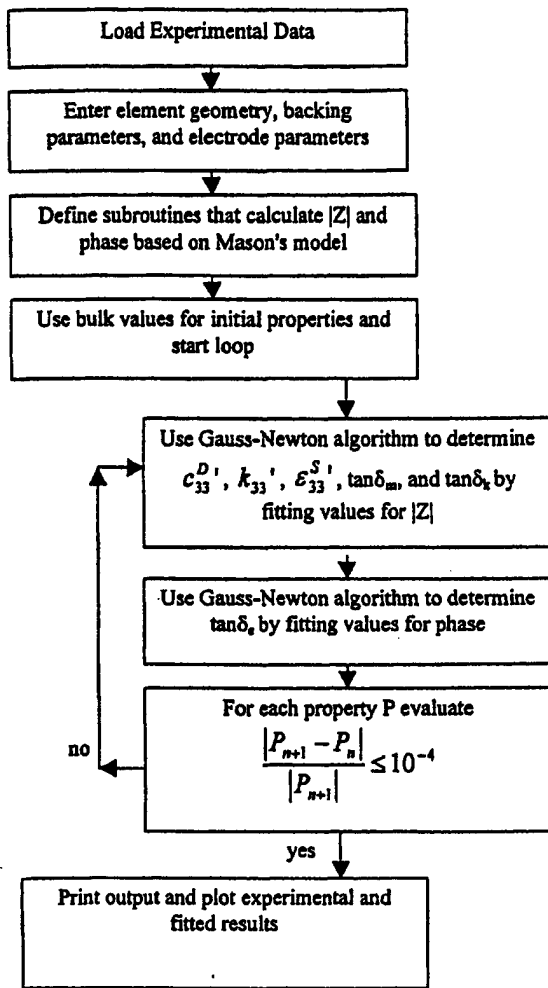


FIG. 3. A flow chart showing the algorithm used to determine the properties of array elements.

III. RESULTS AND DISCUSSION

Array elements with nominal parallel resonance frequencies near 35 MHz were prepared, tested, and characterized as described earlier. Groups of three elements were tested simultaneously for each of the two materials, with physical separations of 100 μm between the elements. A summary of the results is shown in Table I and an example of the fitted data is shown in Fig. 4.

Physical inspection of the elements after fabrication revealed visible chipping and grain pullout on the elements fabricated from TRSHK1, while damage to the TRS600FG material was minimal. This physical damage would be expected to correspond to a reduction in the effective dielectric permittivity and piezoelectric coupling. A comparison of the

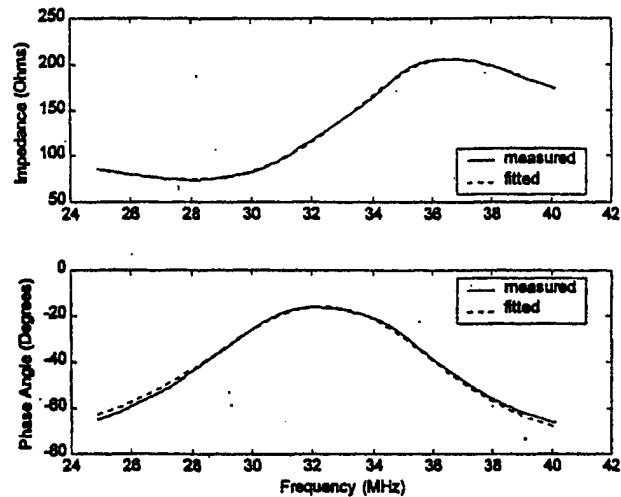


FIG. 4. The measured and curve-fitted impedance and phase angle spectra for the TRSHK1 material.

measured k'_{33} and ϵ'_{33} to the values predicted from the bulk electromechanical properties reveals this effect. It is important to point out that the bulk properties were measured using air-loaded resonators at frequencies well below 10 MHz. The diced TRS600FG elements demonstrated k'_{33} and ϵ'_{33} values that were 90% and 85% of the expected values, respectively. The TRSHK1 elements displayed a greater reduction in performance, with k'_{33} and ϵ'_{33} values that were only 80% and 70% of the predicted values. Thickness coupling in thin plates has been shown to degrade at a rate of 0.6%–2% per decade of frequency above 20 MHz.¹² A similar effect occurring for array elements would account for only a small fraction of the degradation observed. The degree of physical damage may therefore be determined from the measured properties. In addition, the difficulty in fabrication and the increased $\tan \delta_m$ evident for the TRSHK1 may be a result of the large grain size.¹² This indicates that the TR600FG is preferred for high frequency applications.

IV. CONCLUSIONS

A method of measuring the properties of high frequency piezoelectric strip vibrators based on the Mason model has been presented. Both the substrate supporting the elements and the width of the elements must be properly selected when implementing this method. Measurements on two piezoelectric materials, fabricated using mechanical dicing, indicated degraded performance when compared to values predicted from the bulk electromechanical properties. These reductions may be attributed to damage that occurred during

TABLE I. Properties of supported array elements measured by curve-fitting experimental impedance data to the Mason model. Values for k'_{33} and $\epsilon'_{33}/\epsilon_0$ determined from bulk electromechanical properties are also listed for comparison.

Material	Height (mm)	Width (mm)	c'_{33} (N/m ²)	k'_{33}	k'_{33} (bulk)	$\epsilon'_{33}/\epsilon_0$	$\epsilon'_{33}/\epsilon_0$ (bulk)	$\tan \delta_e$	$\tan \delta_m$	$\tan \delta_e$
TRS600	0.050	0.029	10.9×10^{10}	0.62	0.69	1290	1500	-0.03	0.01	0.03
TRSHK1	0.052	0.028	11.4×10^{10}	0.56	0.68	1950	2900	-0.05	0.09	0.04

fabrication and to grain size effects, with the fine grain material providing superior relative performance. The technique presented here may be used in the evaluation and comparison of different fabrication processes and materials for high frequency array applications.

ACKNOWLEDGMENT

Financial support for this work was provided through NIH Grant No. P41-RR11795.

¹G. R. Lockwood, D. H. Turnbull, D. A. Christopher, and F. S. Foster, *IEEE Eng. Med. Biol. Mag.* **15**, 60 (1996).

²H. Wang, W. Jiang, and W. Cao, *J. Appl. Phys.* **85**, 8083 (1999).

³IEEE Std. 176-1987 (IEEE, New York, 1987).

⁴M. Lukacs, T. Olding, M. Sayer, R. Tasker, and S. Sherit, *J. Appl. Phys.* **85**, 2835 (1999).

⁵M. Onoe and H. F. Tiersten, *IEEE Trans. Ultrasonics Eng.* **10**, 32 (1963).

⁶P. D. Edmonds, *Ultrasonics, Methods of Experimental Physics* Vol. 19 (Academic, New York, 1981).

⁷R. Krimholtz, D. A. Leedom, and G. L. Matthaei, *Electron. Lett.* **6**, 398 (1970).

⁸S. Sherit, S. Leary, B. Dolgin, and Y. Bar-Cohen, *Proc. IEEE Ultr. Symp., Lake Tahoe, NV, October, 1999* (in press).

⁹C. S. DeSilets, Ph.D. thesis, Stanford (Edward L. Ginzton Laboratory, Stanford, 1978).

¹⁰K. W. Kwok, H. L. W. Chan, and C. L. Choy, *IEEE Trans. Ultrason. Ferroelectr. Freq. Control* **44**, 733 (1997).

¹¹A. R. Selfridge, Ph.D. thesis, Stanford (Edward L. Ginzton Laboratory, Stanford, 1982).

¹²M. J. Zipparo, K. K. Shung, and T. R. Shrout, *IEEE Trans. Ultrason. Ferroelectr. Freq. Control* **44**, 1038 (1997).

APPENDIX 84

Low Frequency Multi-Mode Ultrasonic Lamb Wave Method for Characterization of the Ultra-Thin Elastic Layer

ZHANG Rui¹, WAN Ming-xi¹, GONG Xin-zhou¹, CAO Wen-wu²

(1. Department of Biomedical Engineering, Xi'an Jiaotong University, Xi'an 710049, China; 2. Intercollege Materials Research Laboratory, Pennsylvania State University, University Park, PA, 16802, USA)

Abstract: A low-frequency multi-mode ultrasonic Lamb wave method suitable for characterizing shear and longitudinal wave velocities, thickness and density of ultra-thin elastic layers is presented. By "ultra-thin", we mean that the plate is only a fraction of the ultrasound wavelength. In conjunction with the geometric calculations and leaky Lamb wave frequency-domain analysis, the lowest order symmetrical mode Lamb wave method, the approximate method and the lowest order anti-symmetrical mode Lamb wave method are used to characterize the parameters of the plate coupled by water. The reasons for evaluation error of the parameters and the sensitivity of all methods for different parameters are analyzed. Using a pair of broadband water immersion longitudinal wave with 2MHz center frequency transducers, we have accurately characterized the parameters of aluminum foil with the thickness down to 26 μm .

Key words: Ultra-thin elastic layer; Ultrasonic characterization; Lamb wave; Quantity NDE

低频多模式超声兰姆波超薄弹性层定征方法

张 锐¹, 万明习¹, 巩欣洲¹, Cao Wenwu²

(1. 西安交通大学生物医学工程与仪器系, 西安 710049; 2. Intercollege Materials Research Laboratory, Pennsylvania State University, University Park, PA, 16802, USA)

摘要: 提出了用低频多模式超声兰姆波定征方法来估计超薄弹性层的纵波声速、横波声速、厚度和密度等参数。这里“超薄”是指材料厚度 h 远小于材料中的声波波长 λ , 由此导致在时域上材料前后界面的各次回波信号相互混迭。文中采用水浸耦合方式, 结合空间波场设计和泄漏兰姆波频域分析方法获取了材料零阶对称与反对称模式兰姆波色散曲线, 并以色散特性为基础的零阶对称模式兰姆波定征方法、简化方法、零阶反对称模式兰姆波定征方法和最小二乘意义下以材料色散曲线为基础的反向算法对材料进行了参数估计。文中分析了影响估计准确性的各种因素, 研究了低频多模式超声兰姆波定征方法对各材料参数的灵敏度及其在误差传递中的意义。实验结果表明, 该方法能够准确估计厚度小到 $26\mu\text{m}$ 铝箔的材料参数。

关键词: 超薄弹性层; 超声定征; 兰姆波; 定量无损估计

中图分类号: TB551 **文献标识码:** A

1 引言

在对诸如材料表面保护涂层、粘贴型复合材料粘贴层、稀有金属箔状材料、心脏瓣膜等多种超薄层状材料或结构进行超声波测试时, 以往的单载频脉冲重合法、共振法以及脉冲-回波等方法受原理的限制, 只适用于测试 $h > \lambda$ (h 为材料厚度, λ 为测量声波在材料中的波长) 的样本^[1-4]。这里“超薄”是指材料厚度 h 远小于材料中的声波波长 λ 。虽然可以使用频带更宽和频率更高的单脉冲超声波来测量厚度越来越小的样品, 但是当使用上百兆赫高频超声波检测超薄层材料或结构时, 材料对声波的衰减很大, 探测深度受到限制; 并且材料中的各种微结构对超声波的散射将干扰回波信号, 使声学参数的测量变得困难。国内外学者提出用低频频域定征方法和低频直接测量方法来对厚度小到 0.01λ 的超薄层材料进行参数定征, 但由于只激发了单一模式的体积波, 因此只能估计材料纵波声速^[5-10]。我们希望寻找一种方便准确的低频超声波参数定征方法, 使之能对超薄层状材料参数进行更为全面的估计。

与传统体积波方法对应, 具有多种传播模式和色散特性、沿薄板传播的兰姆波是一种超声波导波, 其传播特性与材料的纵波声速、横波声速、厚度和密度等多种参数有着直接的关系, 信

收稿日期: 1998-12-26; 修订日期: 1999-03-10

基金项目: 中国国家自然科学基金资助项目(69631020); 美国 Office of Naval Research 基金资助项目(Grant: # N00014-93-1-0340)

号中蕴涵的信息远多于传统体积波方法,可以用来对超薄弹性层进行多参数的定征^[11-15]。本文提出用低频多模式兰姆波色散特性为基础的零阶对称模式兰姆波定征方法、简化方法、零阶反对称模式兰姆波定征方法和在最小二乘意义下以低频多模式兰姆波色散曲线为基础的反向算法对超薄弹性层的纵波声速、横波声速、厚度、密度等参数进行了估计分析,分析了影响估计准确度的各种因素,并研究了低频多模式超声兰姆波定征方法对材料各参数的灵敏度及其在误差传递中的意义。实验结果与理论符合得非常好。

2 方法

2.1 低频零阶对称模式兰姆波定征方法及简化方法

水浸耦合方式下,在层状弹性薄板中传播的对称模式兰姆波的色散特性由下列方程决定^[16]:

$$f_s(v_l, v_s, h, \rho, \bar{\omega}, v_b) = (k^2 + s^2)^2 \operatorname{cth}\left(\frac{qh}{2}\right) - 4k^2 q s \operatorname{cth}\left(\frac{sh}{2}\right) - i \frac{\rho_w}{\rho} \frac{q k_t^4}{\sqrt{k_w^2 - k^2}} \quad (1)$$

式中: v_l 、 v_s 、 h 和 ρ 分别是薄板的纵波声速、横波声速、厚度和密度; v_w 和 ρ_w 分别是水中声速和水密度; v_b 是层状弹性薄板中兰姆波声速; $\bar{\omega}$ 是入射超声波的角频率; $k = \omega/v_b$; $k_l = \omega/v_l$; $k_t = \omega/v_s$, $k_w = \omega/v_w$; $s = \sqrt{k^2 - k_t^2}$; $q = \sqrt{k^2 - k_l^2}$ 。

使用低频零阶对称模式兰姆波定征方法对超薄弹性层的参数估计,即是通过在最小二乘误差意义下材料的低频零阶对称模式兰姆波色散曲线与理论色散特性方程的比较,估算出材料的声学参数值,材料参数的实验估计值应使下式取得最小值:

$$E(p) = \frac{1}{N} \sum_{j=1}^N \|f_s(v_l, v_s, h, \rho, \bar{\omega}^j, v_b^j)\|^2 \quad (2)$$

式中: N 是待测材料厚度与发射及接收时传感器的频宽乘积带内对应的速度扫描点数, p 为 v 、 h 、 ρ 中之一。

同时,我们注意到在超声波入射频率 f 与材料厚度 h 乘积较小的范围内,低频零阶对称模式兰姆波几乎是非色散的,也就是说在此范围内兰姆波的声速几乎是不变的,近似于 $f \cdot h$ 等于零处的兰姆波波速,由如下的公式给出:

$$v_b = 2v_s \sqrt{1 - (v_s/v_l)^2} \quad (3)$$

由于在实验中采用一对中心频率为 2MHz 的低频纵波宽带压电换能器对超薄弹性层状材料进行估计,我们尝试分别使用下面的式(4)和式(5)来估计超薄弹性层的横波声速和纵波声速(以下简称此为简化方法):

$$v_s = \sqrt{\frac{v_l^2 - v_l \sqrt{v_l^2 - v_b^2}}{2}} \quad (4)$$

$$v_l = \frac{2v_s^2}{\sqrt{4v_s^2 - v_b^2}} \quad (5)$$

2.2 低频零阶反对称模式兰姆波定征方法

在使用低频零阶对称模式兰姆波定征方法对超薄层材料进行参数估计时,发现该方法对材料厚度和密度参数的定征准确度较差。为此,我们引入低频零阶反对称模式兰姆波定征方

法。水浸耦合方式下,在薄层材料中传播的反对称模式兰姆波的色散特性方程为

$$f_a(v_1, v_s, h, \rho, \bar{\omega}, v_b) = (k^2 + s^2)^2 \operatorname{th}\left(\frac{qh}{2}\right) - 4k^2 q s \operatorname{th}\left(\frac{sh}{2}\right) - i \frac{\rho_w}{\rho} \frac{q k_i^4}{\sqrt{k_w^2 - k^2}} = 0 \quad (6)$$

低频零阶反对称模式兰姆波定征方法所使用的反向算法同低频零阶对称模式兰姆波定征方法相似,只是将公式(2)中的 $f_s(v_1, v_s, h, \rho, \bar{\omega}, v_b)$ 改为 $f_a(v_1, v_s, h, \rho, \bar{\omega}, v_b)$, 这里从略。

由于本文采用水浸耦合和倾斜入射及接收测试方式,因此,当超薄弹性层材料的厚度小于一定值的时候,低频零阶反对称模式兰姆波定征方法无法对材料参数进行定征。在本文的实验结果与讨论部分,将对该方法的定征阈值进行更详细的讨论。

2.3 反向计算方法

由于水浸耦合方式的影响,兰姆波在材料中传播时会不断向水中泄漏,造成兰姆波的衰减,所以式(1)和(6)中的波数参数 k 是复数值,即 $k = k_1 + ik_2$, k_1, k_2 分别代表水浸方式下超薄弹性层中兰姆波的波数和传播衰减。我们采用二维割线法解出使式(2)中 $E(P)$ 为最小的材料参数值,迭代初值为材料参数的预估值,在材料参数真值的约 $\pm 30\%$ 范围内。

3 实验

3.1 测量系统

实验测量系统如图1所示。将一对精密匹配、中心频率为2MHz的纵波宽带压电传感器放在材料的同侧倾斜地浸于水中,发射传感器T的入射角度、接收传感器R的接收角度和两个传感器与材料表面之间的距离由一套精密机械控制装置控制,从而保证接收传感器接收的是漏兰姆波信号。在计算机的控制下,触发脉冲发生器CTS-5产生尖脉冲激励发射传感器,CTS-5将接收传感器收到的信号经内部放大器预放后送至TDS-724C型数字示波器进行采样,示波器的采样频率 $f_s = 100\text{MHz}$ 是预先设定的。为了减小随机噪声对实验结果的影响,数字示波器进行持续5分钟的多次采样,并且一边采样,一边将采样信号进行平均。最后,平均后的采样信号通过 GPIB(IEEE-488)总线送入计算机做进一步分析。

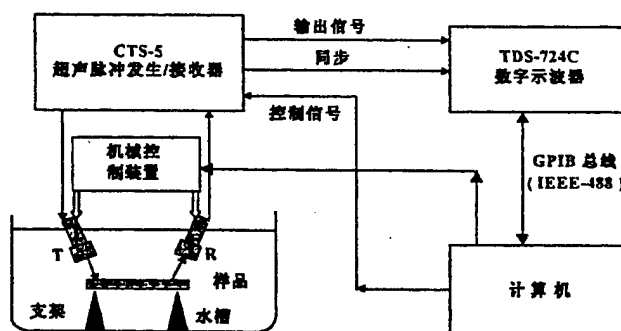


图1 实验测量系统原理框图

实验用的测试材料是各种不同厚度的铝箔、铁箔、铜箔和玻璃薄层,其纵波、横波声速及厚度数据是在美国宾夕法尼亚州购买时由商家提供的,我们使用电子测厚仪对厚度参数进行了校准,仪器的测量误差是 $\pm 2.54\mu\text{m}$ 。密度参数是利用阿基米德原理测量的。整个实验在恒温环境中进行,吸水水槽内的水温控制在 $23 \pm 0.1^\circ\text{C}$ 。

3.2 漏兰姆波空间波场设计

由于兰姆波在路径上的衰减,为了保证一定的信噪比,要尽可能减小两传感器的距离。但是当距离太近时,材料表面对入射信号的反射会很大程度上影响对漏兰姆波信号的接收,而反射信号对漏兰姆波信号的干扰程度又取决于传感器在水中的波场形状、两传感器之间及它们与材料之间的距离、超声波入射角度和接收角度等因素,所以必须妥善安排两传感器之间以及它们与待测材料之间的位置,以保证接收到正确的漏兰姆波信号^[15],漏兰姆波实验方法空间波场设计如图 2 所示。

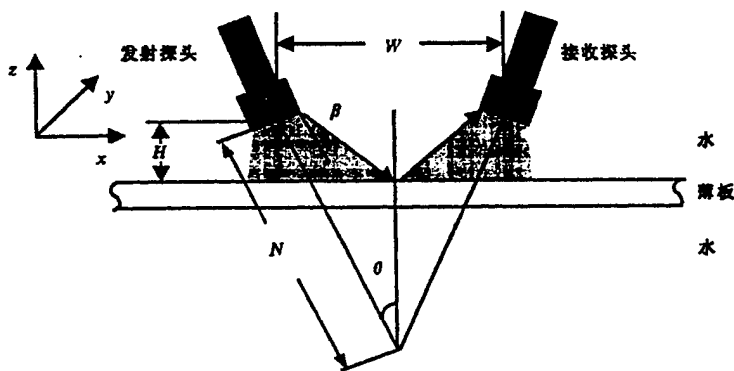


图 2 漏兰姆波实验方法空间波场设计示意图

图 2 中, N 为传感器近场距离, β 为传感器主波束半开角, 分别由以下两式决定:

$$N = (D^2 - \lambda^2)/4\lambda \quad (7)$$

$$\beta = \arcsin(1.2\lambda/D) \quad (8)$$

式中: D 为传感器半径, λ 为发射声波在水中的波长。 θ 为超声波入射角, W 为发射传感器与接收传感器之间的距离, H 为传感器与材料表面之间的距离, 这 3 个参数由机械控制装置调节。为使接收传感器接收的信号不受材料表面的反射信号干扰而只接收漏兰姆波, W 和 H 必须满足以下两式:

$$W \geq 2N\sin\theta \quad (9)$$

$$H \leq \frac{N\sin\theta}{\tan(\theta + \beta)} \quad (10)$$

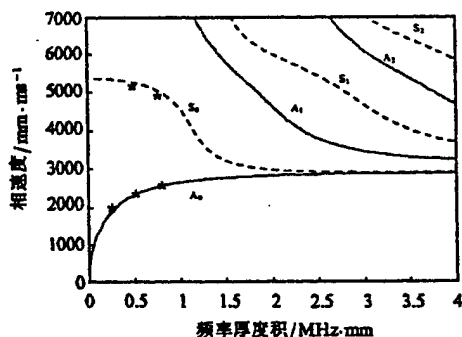


图 3 兰姆波色散曲线(A:反对称模式;S:对称模式;下标为阶数)

(材料:铝, $v_l = 6.206 \text{ nm}/\mu\text{s}$, $v_s = 3.045 \text{ nm}/\mu\text{s}$, $h = 256 \mu\text{m}$)

3.3 漏兰姆波频域分析方法

准确调整系统传感器与材料空间位置并获取漏兰姆波信号之后,通过分析信号的频谱可

以发现,由于传感器波束宽度与发射信号带宽的影响,接收到的漏兰姆波信号也是宽带信号,并且在频域上存在一些峰值点,这些谱峰即意味着此频率处的漏兰姆波信号的声速是发射信号主轴方向与材料表面的临界角对应的兰姆波声速。所以,漏兰姆波频谱方法的核心是控制入射及接收角度,以选择和决定何种模式的兰姆波以多大的速度沿弹性薄层传播,并确定此速度的兰姆波对应的频率成分。精确控制入射波入射角度,在一段角度范围内以一定角度间隔改变入射角,并记录不同入射角所对应频率峰值点,就可以得到材料的色散曲线。以铝为例,其色散曲线如图3所示,其中“*”点是兰姆波色散曲线测量值。

4 实验结果与讨论

我们分别使用低频对称模式和反对称模式兰姆波对铝、铁等材料进行了测量与参数估计,测量结果如表1、2所示,表中有“*”号上标的参数为各材料参数的标称值,缺省项是指对材料参数的估计误差大于10%。

表1 对称模式兰姆波定征方法及简化方法对材料纵波声速、横波声速参数的估计结果

样品	材料	h^*	ρ^*	v_l^*	v_s^*	低频零阶对称模式 兰姆波定征方法				低频零阶对称模式 兰姆波简化定征方法			
						v_l		v_s		v_l		v_s	
						mm/ μ s	Err(%)	mm/ μ s	Err(%)	mm/ μ s	Err(%)	mm/ μ s	Err(%)
1	铝	26	2.69	6.206	3.045	6.060	-2.4	3.011	-1.1	6.049	-2.7	3.007	-1.2
2	铝	112	2.69	6.206	3.045	6.068	-2.2	3.015	-1.0	5.996	-3.4	2.995	-1.6
3	铝	256	2.69	6.206	3.045	6.079	-2.0	3.024	-0.7	5.762	-7.2	2.933	-3.7
4	铝	521	2.69	6.206	3.045	6.077	-2.0	3.019	-0.9	/	/	/	/
5	铁	76	7.86	5.949	3.241	5.880	-1.0	3.219	-0.7	5.868	-1.2	3.214	-0.9
6	黄铜	101	8.47	4.714	2.093	4.797	1.8	2.103	0.5	4.644	-1.5	2.086	-0.5
7	玻璃	115	2.32	5.579	3.319	5.574	-0.1	3.313	-0.2	5.558	-0.4	3.304	-0.4

表2 零阶反对称模式兰姆波定征方法对材料参数的估计结果

样品	材料	h^*	ρ^*	v_l^*	v_s^*	h		ρ		v_l		v_s	
		μ m	g/mm ³	mm/ μ s	mm/ μ s	μ m	Err(%)	g/mm ³	Err(%)	mm/ μ s	Err(%)	mm/ μ s	Err(%)
1	铝	152	2.69	6.206	3.045	156	2.6	/	/	6.310	1.7	3.065	0.7
2	铝	256	2.69	6.206	3.045	252	-1.6	2.89	7.5	6.100	1.2	3.023	-0.7
3	铁	106	7.86	5.949	3.241	105	-0.1	7.96	0.9	5.850	-1.5	3.220	-0.7
4	黄铜	381	8.47	4.714	2.039	382	0.3	8.35	-1.4	4.726	0.3	2.094	0.1
5	玻璃	216	2.32	5.579	3.319	217	0.5	2.27	-2.0	5.591	0.2	3.323	0.1

综合表1和表2可以看出,低频零阶对称模式兰姆波定征方法与其简化方法对超薄层材料的纵波、横波速度参数的定征具有同样的准确度,误差小于2%。但低频零阶对称模式兰姆波定征方法的定征准确度不会因为材料厚度的变化而发生变化,而其简化方法对材料纵波、横波速度参数的定征准确度在材料厚度增大的情况下越来越差。图4为在假定不存在测量误差前提下,在一定频率厚度积范围内,简化定征方法估计铝质薄层横波速度的预计误差的比较曲线。由图4可知,为保证对铝质薄层横波速度的估计误差不大于2%,低频零阶对称模式兰姆波简化定征方法只适用于入射频率材料厚度积小于0.6MHz·mm的范围。

经过分析我们发现,低频零阶对称模式与反对称模式兰姆波定征方法测量材料参数的估计误差主要是由传感器角度分辨率决定的兰姆波速度测量误差引起的,图 5 所示为超声波在不同入射角度时可能带来的兰姆波速度测量误差。由于实验中的待测材料在低频率厚度积条件下的兰姆波速度对应的角度范围为 16° 左右,由图可以看出在此范围中,存在约 2% 的兰姆波速度误差。

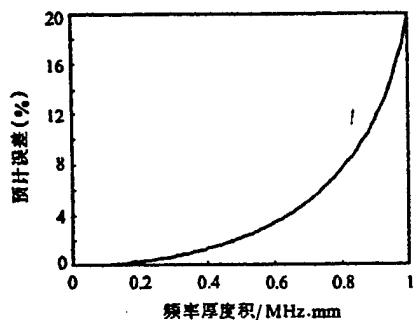


图 4 低频对称模式兰姆波简化定征方法估计横波速度的预计误差曲线
(材料: 铝, $v_1 = 6.206 \text{ mm}/\mu\text{s}$, $v_s = 3.045 \text{ mm}/\mu\text{s}$)

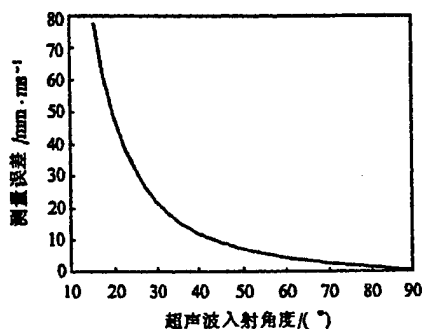


图 5 不同入射角对应的兰姆波速度测量误差
(传感器角度分辨率为 0.5°)

图 6 为零阶对称模式兰姆波定征方法对材料各声学参数的估计误差曲线,由图可以看出,当使用零阶对称模式兰姆波定征方法并存在兰姆波声速测量误差时,零阶对称模式兰姆波定征方法对横波速度的灵敏度从总体上来讲大于对纵波速度的灵敏度,在同样的兰姆波声速测量误差条件下,对纵波的反演误差较大。大致上看,兰姆波测量误差与横波测量误差之间存在着线性关系。由于零阶对称模式兰姆波定征方法主要用于超薄弹性层,零阶对称模式兰姆波简化定征方法的估计误差曲线与图 6 所示十分相似,这里从略。

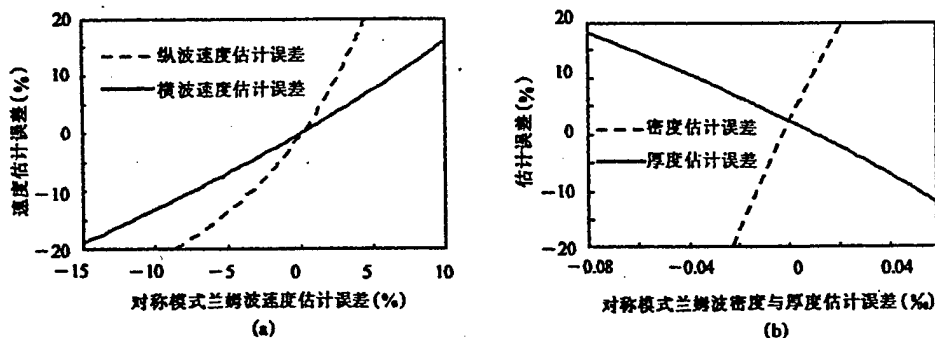


图 6 零阶对称模式兰姆波定征方法声学参数估计误差
(a) 纵波及横波速度估计误差; (b) 厚度及密度估计误差
(材料: 铝, $v_1 = 6.206 \text{ mm}/\mu\text{s}$, $v_s = 3.045 \text{ mm}/\mu\text{s}$, $h = 26 \mu\text{m}$)

零阶反对称模式兰姆波定征方法对横波和纵波速度的估计的灵敏度略小于零阶对称模式兰姆波定征方法,但对厚度和密度的估计灵敏度远大于零阶对称模式兰姆波定征方法,如图 7 所示。结合图 5 所示,可知零阶反对称模式兰姆波测量误差远小于零阶对称模式兰姆波测量误差,两者之间可以相差 4 倍之多。综合这两种因素,可知零阶反对称模式兰姆波定征方法的定征准确度从总体上大于零阶对称模式兰姆波定征方法,尤其适用于对材料的厚度和密度参

数进行估计。

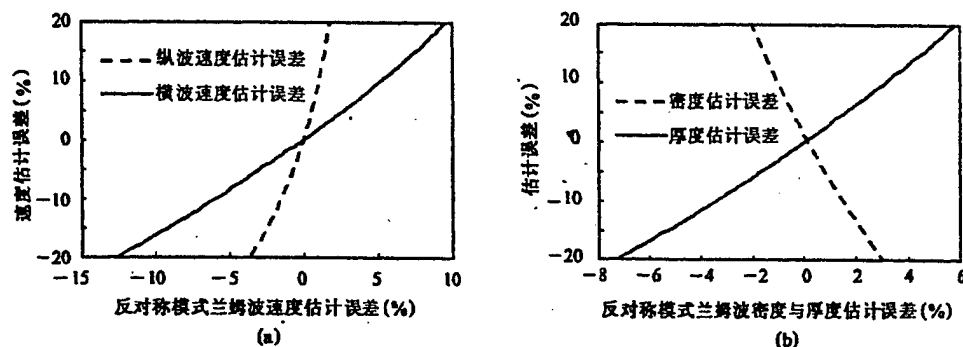


图 7 零阶反对称模式兰姆波定征方法声学参数估计误差

(a) 纵波及横波速度估计误差; (b) 厚度及密度估计误差

(材料: 铝, $v_l = 6.206 \text{ mm}/\mu\text{s}$, $v_s = 3.045 \text{ mm}/\mu\text{s}$, $h = 152 \mu\text{m}$)

同时,我们还注意到低频零阶反对称模式兰姆波定征方法的定征阈值可以通过采用空气耦合传感器来提高,在表 3 中列出了使用空气耦合传感器时,该方法对厚度参数的定征阈值。表中 h 为材料厚度, λ_l 为与薄层材料纵波声速对应的纵波波长。从表 3 中可以看出,在使用空气耦合传感器条件下,该方法可以对小于百分之一纵波波长的超薄层材料进行定征。

表 3 零阶反对称模式兰姆波定征方法厚度阈值

样 品	材 料	水耦合方式		空气耦合方式	
		$h(\text{mm})$	h/λ_l	$h(\text{mm})$	h/λ_l
1	铝	0.069	0.022	0.015	0.005
2	铁	0.068	0.023	0.015	0.005
3	钢化玻璃	0.069	0.024	0.015	0.005
4	黄铜	0.134	0.057	0.030	0.009

注:入射超声波频率为 2MHz。

4 结论

本文通过理论分析和实验验证,证实了一种新的低频超声波无损估计超薄弹性层参数(声速、厚度、密度和衰减等)方法的有效性。

1. 低频零阶对称模式兰姆波定征方法及其简化方法可以用来定征超薄弹性层的纵波速度和横波速度参数,定征误差小于 2%。

2. 低频零阶对称模式兰姆波简化定征方法的定征准确度随材料厚度的增大而降低,对铝质薄层而言,为保证定征误差不大于 2%,只能适用于入射频率材料厚度积小于 $0.6 \text{ MHz} \cdot \text{mm}$ 的范围。

3. 对铝质薄层而言,低频零阶反对称模式兰姆波定征方法可以对厚度小至十分之一波长薄板的纵波速度、横波速度、厚度、密度等参数进行定征。

4. 低频零阶反对称模式兰姆波定征方法对材料厚度参数的定征存在阈值,为了对超薄层材料的定征,可以使用空气耦合传感器提高兰姆波方法的检测阈值。

5. 结合低频零阶对称模式和反对称模式兰姆波的多模式兰姆波定征方法可以对超薄弹性层的纵波速度、横波速度、厚度、密度等参数进行定征。该定征方法的定征精度与发射、接收

传感器频带特性、波束特性、角度分辨率和材料的色散特性等因素有密切的关系。

参 考 文 献

- [1] Papadakis E P. Ultrasonic velocity and attenuation: Measurement methods with scientific and industrial applications [A]. In: Physical Acoustics Principles and Methods (Vol. 12) . Mason W P, Thurston R N, (eds). New York: Academic Press, 1976, 277~374.
- [2] Krautkramer J, Krautkramer M. Ultrasonic testing of materials (4th fully revised edition) [M]. Springer Verlag, 1990.
- [3] Chang F H, Couchman J C, Yee B G W. Ultrasonic resonance measurements of sound velocity in thin composite laminates [J]. *J Composite Material*, 1974, 8(10): 356~363.
- [4] Challis R E, Alper T, Freemantle R J, *et al.* Acoustic wave velocities in ceramics and other material measured by a broadband goniometric method [J]. *Ultrasonics*, 1995, 33(4): 311~319.
- [5] Kinra V K, Iyer V R. Ultrasonic measurement of the thickness, phase velocity, density of attenuation of a thin viscoelastic plate. Part I: The forward problem [J]. *Ultrasonics*, 1995, 33(2): 95~110.
- [6] Kinra V K, Iyer V R. Ultrasonic measurement of the thickness, phase velocity, density or attenuation of a thin viscoelastic plate. Part II: the inverse problem [J]. *Ultrasonics*, 1995, 33(2): 111~122.
- [7] Kinra V K, Zhu C. Time-domain ultrasonic NDE of the wave velocity of sub-half-wavelength elastic layer [J]. *J Testing and Evaluation*, 1993, 21(1): 29~35.
- [8] Wan Mingxi, Jiang B, Cao Wenwu. Direct measurement of ultrasonic velocity of thin elastic layers [J]. *J Acoust Soc Am*, 1997, 101(1): 626~628.
- [9] Qing Ming, Wan Mingxi, Cao Wenwu. Ultrasonic characterization of ultra-thin elastic layer using retrieve function [J]. *Chinese Journal of Acoustics*, 1998, 17(4): 329~340.
- [10] Wan Mingxi, Zhang Rui, Cao Wenwu. The ultrasonic Lamb wave methods for shear wave velocity measurement of thin elastic layers [J]. *J Acoust Soc Am* (to be published).
- [11] 张锐, 万明习. 超薄弹性层低频超声频域定征方法 [J]. *计量学报*, 1998, 19(4): 291~298.
- [12] Karim M R, Mal A K, Bar-Cohen Y. Inversion of leaky Lamb wave data by simplex algorithm [J]. *J Acoust Soc Am*, 1991, 89: 482-491.
- [13] Lowe J S, Cawley P. Comparison of reflection coefficient minimum with dispersion curves for ultrasonic waves in the embedded layers [J]. *Review in Progress of QNDE*, 1995, 14: 1505.
- [14] Biagi E, Fort A, Vignoli V. Guided acoustic wave propagation for procelain coating characterization [J]. *IEEE Trans Ultrason Ferroelect Contr*, 1997, 44(4): 906~916.
- [15] Karpur P, Benson D M, Matikas T E, *et al.* An approach to determine the experimental transmitter-receiver geometry for the reception of leaky Lamb waves [J]. *Material Evaluation*, 1995, 53(12): 1348.
- [16] Viktorov I A. Rayleigh and Lamb wave: physical theory and application [M]. New York: Plenum Press, 1967: 117~121.

MODELING and CHARACTERIZATION

Thick and Thin Films

APPENDIX 85

Effect of Crystal Orientation on Dielectric Properties of Lead Zirconium Titanate Thin Films Prepared by Reactive RF-Sputtering

Sriram KALPAT, X. DU, Issac R. ABOTHU¹, Akira AKIBA², Hiroshi GOTO² and Kenji UCHINO

*International Center for Actuators and Transducers, Materials Research Laboratory,
The Pennsylvania State University, University Park, Pa 16802, U.S.A*

¹*Institute of Materials Research and Engineering, Kent Ridge, Singapore 119260*

²*OMRON Corporation, Tsukuba, Ibaraki 300-4247, Japan*

(Received July 28, 2000; accepted for publication October 16, 2000)

Theoretical calculations based on phenomenology of ferroelectrics have been previously reported for lead zirconium titanate (PZT) system, this paper offers an experimental comparison of the crystal orientation dependence of dielectric properties for PZT thin films grown using reactive RF-sputtering. Highly oriented PZT thin films with a rhombohedral composition have been grown in different orientations using selective rapid thermal annealing cycles. The PZT(100) oriented films showed larger dielectric constant and loss compared to PZT(111) films. The PZT(100) films possessed sharp square-like hysteresis loops indicating a instantaneous switching of domains at the coercive field whereas the PZT(111) films showed smooth hysteresis loops as expected from our phenomenological calculations.

KEYWORDS: PZT, highly oriented films, magnetron sputtering, composition, atomic force microscopy, dielectric constant, polarization, coercive field, domains

1. Introduction

During the past decade there has been an explosion of interest in the field of micro-electro-mechanical systems (MEMS). Recently MEMS^{1,2)} technology has become critical in the growth of various fields like medical, automotive, chemical, and space technology. Lead zirconium titanate (PZT) thin films hold great potential as actuator materials in MEMS devices.³⁾ Explicit knowledge of the dielectric and piezoelectric properties of PZT thin films at different crystal orientations needs to be investigated to enhance its performance and hence meet the challenging requirements of the MEMS industry.

Our group has previously reported theoretical calculations based on the phenomenological consideration of the crystal orientation dependence of the dielectric and piezoelectric properties in PZT thin films.⁴⁾ We have reported that for PZT 60/40 in the rhombohedral region of the phase diagram, the electric field induced polarization hysteresis loops are expected to be sharper and square-like for PZT(100) when compared to the smoother and slanted loops for PZT(111). The piezoelectric property dependence on crystal orientation has also been reported, changing the crystal orientation significantly enhances the effective piezoelectric constant d_{33} , as shown in Fig. 1. A schematic explanation for this expectation is shown in Fig. 2. The d_{33}^{eff} value is three times larger for the [001] direction compared to that of the [111] direction. High d_{33}^{eff} values for PZT(100) compared to PZT(111) in the rhombohedral phase could mean significant improvement in the piezo-response of a micro-actuator in MEMS.

In the rhombohedral phase there are 8 possible polarization directions. For the (111) orientation, the possible polarization directions 2, 3, and 4 are equivalent and are about 70.5° away from the spontaneous polarization direction 1. The other possible directions are 6, 7, 8 and 5. When electric field is applied to a completely poled sample along axis 5, the polarization gets reversed. The polarization reversal has various possibilities 5-1; 5-(2, 3, 4); 5-(6, 7, 8); 5-(6, 7, 8)-1; 5-(6, 7, 8)-(2, 3, 4); 5-(2, 3, 4)-1 etc., hence the reverse segments in the polarization curves are inclined. In the (100) film, there are two sets of equivalent directions, namely

(1, 2, 3, 4) and (5, 6, 7, 8) at 54.7° away from the domains; along (1, 2, 3, 4) are reversed at the same time leading to abrupt polarization reversal.

Theoretically the remnant polarization of the (100) films is expected to be $1/\sqrt{3}$ times that of (111) oriented films, a similar magnitude of the remnant polarization is expected due to the square-like hysteresis behavior of the (100) oriented films. Accordingly, we can expect an ideal strain curve like a "butterfly hysteresis". Based on the above background we are investigating highly oriented PZT thin films in various crystal orientations. In this paper, the fabrication process and the dielectric property dependence of highly oriented PZT thin films will be discussed.

2. Experimental Procedure

PZT thin films were deposited by reactive RF-sputtering using multi-elemental metallic targets of lead, zirconium and titanium. A 3" circular target was designed using individual wedges of Pb, Zr and Ti. The target composition (Pb : Zr : Ti = 4 : 8 : 9) was adjusted so as to fabricate a rhombohedral composition of PZT(70/30). The composition of the deposited films were characterized using electron probe micro analysis (EMPA). Composition analysis of both as-deposited and annealed films were made in order to optimize the lead content in the films. The target composition and sputtering parameters were optimized after making several composition analysis of the films at different sputtering conditions. The target composition was selected at Pb : Zr : Ti = 4 : 8 : 9 so as to deposit films with $\text{Pb}/(\text{Zr} + \text{Ti}) = 1$ and $\text{Zr}/(\text{Zr} + \text{Ti}) = 0.7$. Substrates used were highly (111) oriented platinum (150 nm coated (400 μm) Si/(10 μm) SiO₂ wafer. All the substrates were thoroughly cleaned with isopropyl alcohol and rinsed in de-ionized water prior to film deposition. The substrates were clamped to a stainless steel holder and heated by quartz lamps to 450°C. The RF-sputtering system (Anelva SPC-350) was evacuated to a base pressure of 1×10^{-4} Pa, the films were grown at 20 mTorr pressure with Ar/O₂ ratio at 50/50. The films were grown at RF-power of 150 W at a deposi-

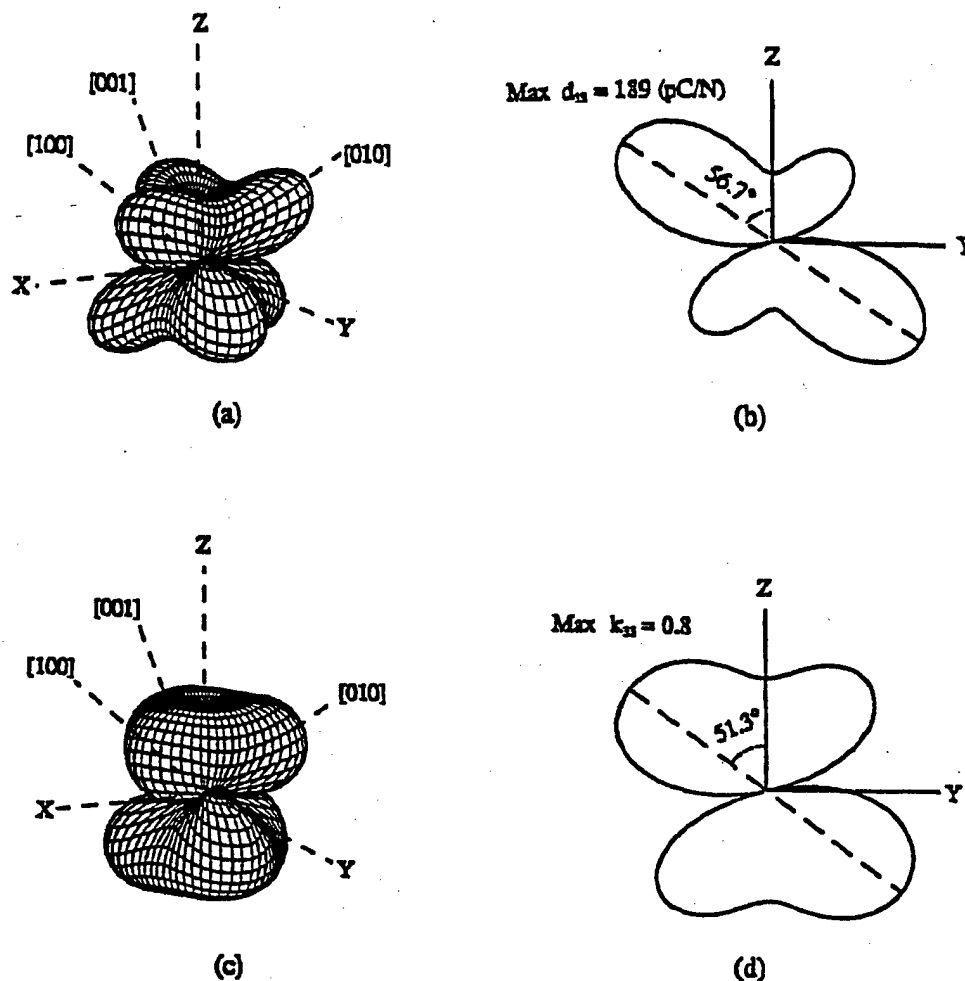


Fig. 1. Crystal orientation dependence of piezoelectric d_{33} constant:⁴⁾ (a) Piezoelectric d_{33} of rhombohedral PZT. (b) Cross-section curve of (a) cut along Y - Z plane. Maximum value of d_{33} is on Y - Z plane and 56.7° away from Z -axis. (c) Electromechanical coupling factor k_{33} of rhombohedral PZT. (d) Cross-section of fig (c) cut along Y - Z plane. The maximum d_{33} is along Y - Z plane and 51.3° from the axis.

tion rate of $0.1 \mu\text{m/h}$. The as-deposited films were amorphous with some microcrystallization of the perovskite phase. The films were selectively annealed using rapid thermal annealing (RTA). The structural characterization of the films was carried out by X-ray diffraction (XRD) using the $\text{Cu-K}\alpha$ radiation. The microstructural characterization of the films were performed using atomic force microscopy (AFM). For the electrical characterization, the crystallized films were coated with 150 nm thick platinum top electrodes deposited by dc sputtering using a shadow mask; the electrode areas used were 2.38×10^{-3} – $1.77 \times 10^{-2} \text{ cm}^2$. The polarization versus electric field hysteresis loop, the quasi-static capacitance-voltage measurements, and the resistivity measurements were made using RT66A standardized hysteresis tester (Radiant Technologies). The dielectric constant and loss factor were measured as a function of frequency using a multi-frequency LCR meter (HP4275) in the frequency range between 100 Hz and 1 MHz .

3. Results and Discussion

The as-grown films were amorphous with some micro-crystallization of the perovskite phase. The

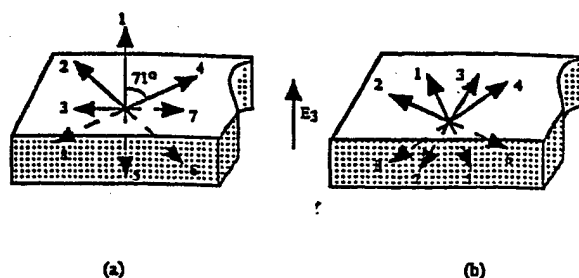


Fig. 2. Possible spontaneous polarization directions:⁴⁾ (a) PZT(111) oriented films (b) PZT(001) oriented films.

as-deposited films were subsequently annealed using RTA at different rates so as to crystallize the films to (100)/(111) perovskite structure. EMPA composition analysis of the films showed $\text{Pb}/(\text{Zr} + \text{Ti}) \sim 1$ and a rhombohedral composition of $\text{Zr}/(\text{Zr} + \text{Ti}) = 0.7$ for the annealed films. The lead content in the as-deposited films was $\text{Pb}/(\text{Zr} + \text{Ti}) \sim 1.1$ but after RTA, the composition of the films maintained at $\text{Pb}/(\text{Zr} + \text{Ti}) \sim 1$. The zirconium and titanium content in the

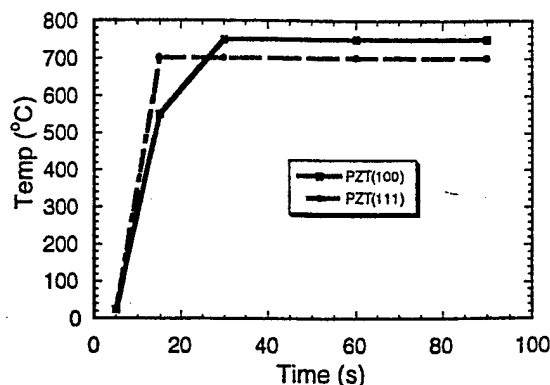


Fig. 3. Crystallization of highly oriented films using selective rapid thermal annealing cycles for PZT(111) and PZT(100) films.

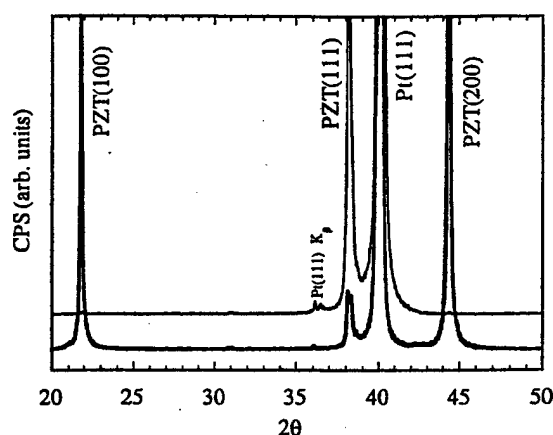


Fig. 4. XRD pattern of highly oriented PZT(111) and PZT(100) on Pt(111)/Si/SiO₂ in the rhombohedral composition 70/30 annealed using rapid thermal annealing.

films remained the same for as-deposited and annealed films. The crystal orientation of the substrate is critical in obtaining the desired orientation of the PZT films.^{5,6} Highly oriented PZT(111) films can be easily grown on Pt(111)/Si/SiO₂, but obtaining PZT(100) oriented film on Pt(111)/Si/SiO₂ substrate has not been widely reported.^{7,8} The surface energy for the PZT(111) orientation is lower on Pt(111)/Si/SiO₂ as compared to that for PZT(100), hence the growth of PZT(111) is kinetically favored. However PZT(100) growth plane has the lowest activation energy for nucleation, and in the absence of any microcrystallization of pyrochlore phase, the nucleation of (100) orientation is easier and subsequent growth of the (100) plane is favored. Selective rapid thermal annealing (RTA) cycles were used as shown in Fig. 3. to obtain the desired PZT(100) and PZT(111) on the same Pt(111)/Si/SiO₂ substrate. The XRD patterns of the annealed films are shown in Fig. 4. The XRD patterns indicate highly preferred orientation for both PZT(100) and PZT(111) films. The degree of crystal orientation was calculated from the integrated intensity of the PZT(111) and PZT(100) peaks and can be expressed as $\alpha_{(111)} = I(111)/[I(111) + I(100)]$. The degree of crystal orientation for $\alpha_{(111)} > 98\%$ and for $\alpha_{(100)} > 95\%$ was obtained. Figure 5. shows AFM micrographs for both PZT(111) and PZT(100) oriented

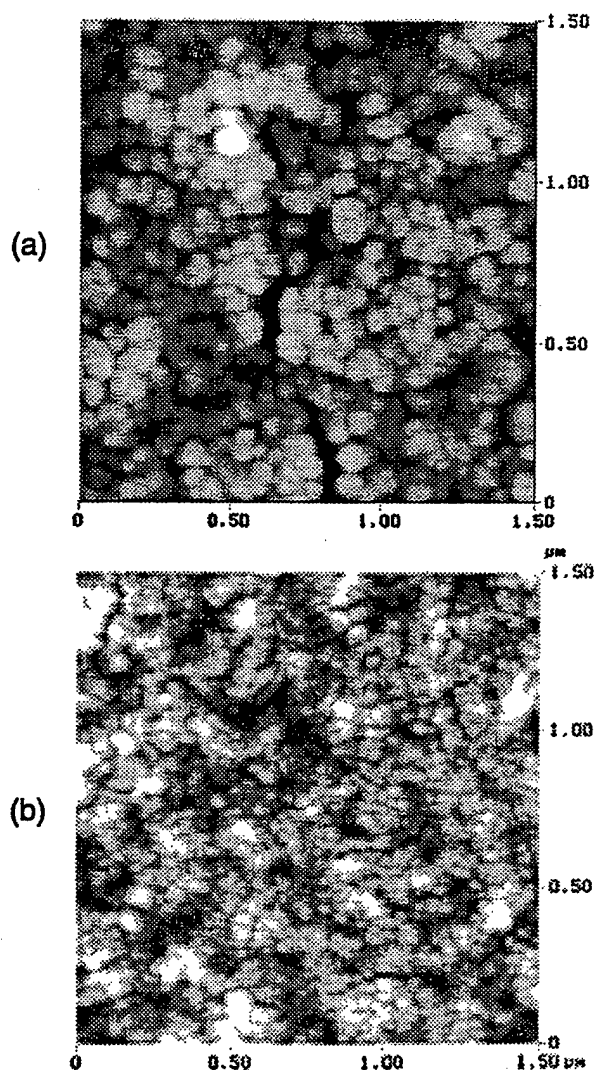


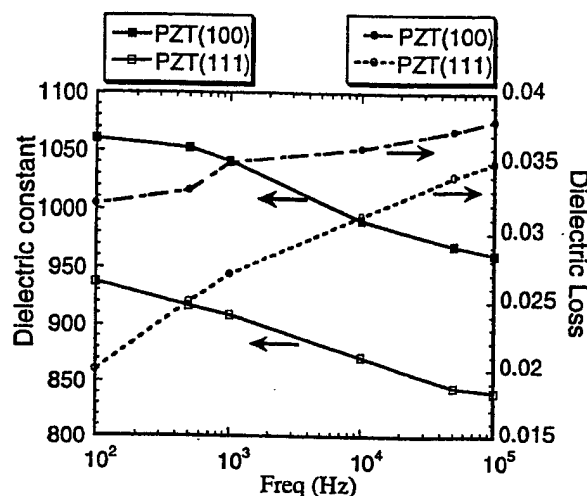
Fig. 5. AFM micrographs of (a) PZT(100) and (b) PZT(111) oriented films 1 μ m thick.

films. The PZT(100) oriented films had a larger grain size (70–90 nm) and larger roughness (10–18 nm) when compared to PZT(111) films of grain size 50–60 nm and roughness 8–13 nm. The cross-section SEM analysis of the films shows a continuous film growth as opposed to a columnar growth that is expected for sputtered films grown at high growth temperatures.

The electrical characterization of the films were performed after depositing top electrodes of platinum (1500 Å) by dc sputtering using shadow masks. The dielectric constant and the loss factors are shown in Fig. 6 as a function of frequency for both (111) and (100) films. The films were poled at an electric field of 150 kV/cm for 30 min and then aged for an hour prior to measuring the dielectric constant at an oscillating ac frequency of 0.01 V. The dielectric constant and the loss factors are shown in Table I, PZT(100) oriented films possess a larger dielectric constant and loss values compared to PZT(111) oriented films. The loss values for PZT(100) were larger compared to PZT(111) films at a frequency of

Table I. Dielectric properties of PZT(111) and PZT(100) oriented films 1 μm thick at rhombohedral 70/30 composition.

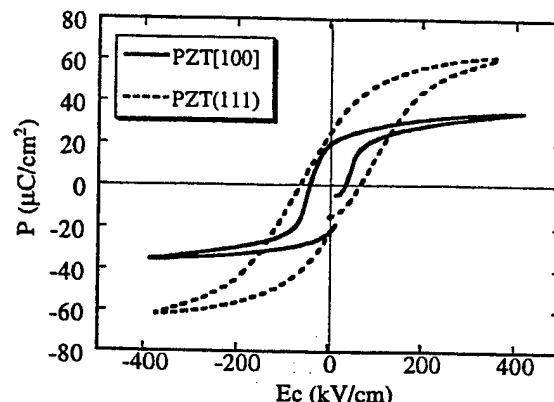
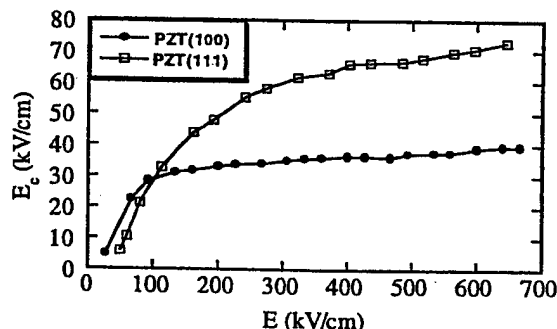
Property	Dielectric constant @ 1 kHz	Dielectric loss factor @ 1 kHz	Saturation polarization ($\mu\text{C}/\text{cm}^2$)	Remnant polarization ($\mu\text{C}/\text{cm}^2$)	Coercive field (kV/cm)
PZT(111)	900	0.025	55	25	65
PZT(100)	1050	0.035	28	20	35

Fig. 6. Dielectric constant and loss factors versus frequency at 0.01 V oscillating voltage for 1 μm thick PZT(111) and PZT(100) oriented films in the rhombohedral 70/30 composition.

1 kHz. Figure 7 shows the P - E hysteresis loops for both PZT(111) and (100) films with a rhombohedral 70/30 composition. The polarization curve in the case of PZT(100) is abrupt and square-like whereas it is relatively smooth in the case of PZT(111) as expected from our theoretical calculation. The saturation polarization values for PZT(111) oriented films are larger compared to PZT(100) oriented films by a factor of $\sqrt{3}$ as proposed by the theoretical calculation. The coercive field is smaller for the PZT(100) films when compared to (111) films, from Fig. 8 it can be seen that there is an abrupt saturation of the coercive field value in PZT(100) films at an applied field of 150 kV/cm whereas the saturation is gradual in (111) films until breakdown. Table I. summarizes the dielectric constant, loss, coercive field, spontaneous polarization and remnant polarization for the PZT(100) and (111) films.

4. Conclusions

Highly oriented PZT(100) and PZT(111) thin films with a rhombohedral composition have been grown by reactive RF-magnetron sputtering using multi-elemental metallic targets. The crystal orientation dependence of the dielectric properties of PZT(111) and PZT(100) on $\text{Pt}/\text{Si}/\text{SiO}_2$ substrates have been investigated to compare it with the reported theoretical calculation for PZT thin films. The dielectric constant and loss for PZT(100) were found to be larger compared to PZT(111). The P - E hysteresis loops were found to be sharper for PZT(100) films compared to PZT(111) indicating that the domain wall movement in (100) films occurs simultaneously at a particular field compared to that of the (111)

Fig. 7. Difference in the hysteresis behavior between PZT(111) and PZT(100) measured using RT66A Ferroelectric tester for 1 μm thick films in the rhombohedral 70/30 composition.Fig. 8. Coercive Field versus applied electric field for PZT(111) and PZT(100) oriented films for 1 μm thick films in the rhombohedral 70/30 composition.

oriented films. The saturation polarization for PZT(111) is about $\sqrt{3}$ times larger than that for PZT(100). The experimental observation seems to have good agreement with the reported theoretical calculations made for PZT thin films based on phenomenology. In conclusion, rhombohedral PZT(100) oriented films are more suitable for MEMS applications as well as ferroelectric memory applications when compared to the PZT(111) oriented films. The piezoelectric property measurements of these films are currently underway.

Acknowledgements

The authors would like to thank the Office of Naval Research for the supporting this work through the project contract N00014-91-J-4145.

- Nara, 1991, p. 33.
- 2) M. Mehgany: *Circuits & Devices* 1 (1993) 14.
 - 3) D. L. Polla and P. J. Schiller: *Integrat. Ferroelectr.* 7 (1995) 359.
 - 4) X. Du, U. Belegundu and K. Uchino: *Jpn. J. Appl. Phys.* 36 (1997) 5580.
 - 5) K. Ijima, I. Ueda and K. Kugimiya: *Jpn. J. Appl. Phys.* 30 (1991) 2149.
 - 6) T. Ogawa, A. Senda and T. Kasanami: *Jpn. J. Appl. Phys.* 30 (1991) 2145.
 - 7) J. Senzaki, O. Mitsunaga, T. Uchida, T. Uena and K. Kuroiwa: *Jpn. J. Appl. Phys.* 35 (1996) 4195.
 - 8) A. Masuda, Y. Yamanaka, M. Tazoe, Y. Yonezawa, A. Morimoto and T. Shimizu: *Jpn. J. Appl. Phys.* 34 (1997) 5154.

APPENDIX 86

DIELECTRIC PROPERTIES OF HIGHLY ORIENTED LEAD ZIRCONIUM TITANATE THIN FILMS PREPARED BY REACTIVE RF-SPUTTERING

S. Kalpat^{*}, X.Du^{*}, I.R.Abothu^{**}, A.Akiba^{***}, and H.Goto^{***}, S.Trolier McKnistry^{*} and K.Uchino^{*}

^{*} International Center for Actuators and Transducers, Materials Research Laboratory, The Pennsylvania State University, University Park, Pa 16802, ^{**} Institute of Materials Research and Engineering, Kent Ridge, Singapore 119260, ^{***} OMRON Corporation, Tsukuba city, Ibaraki-Pref, Japan 300-4247

ABSTRACT

Highly (100) and (111) oriented lead zirconium titanate (PZT) thin films have been grown by using reactive rf-sputtering. PZT thin films with rhombohedral composition have been grown in different orientations using selective rapid thermal annealing cycles. The polarization versus electric field curves and the resistivity of the films were measured using a standardized RT66A ferroelectric test system. The dielectric constant and the loss were determined using an impedance analyzer. The PZT(100) oriented films showed larger dielectric constant and loss than the PZT(111) films. The PZT(100) films possessed sharper square-like hysteresis loops compared to the PZT(111) films, as expected from our phenomenological calculations.

INTRODUCTION

Rooted in early research on materials and processes for the emerging field of integrated circuits in the late 1960's, there has been significant progress in the area of microelectromechanical systems (MEMS) in the past two decades [1,2]. During the past few years there has been an explosion of interest in MEMS, which has become a critical technology in the growth of various fields like medical, automotive, chemical, and space technology. PZT thin films hold great potential as actuator materials in MEMS devices [3]. Explicit knowledge of the dielectric and piezoelectric properties of PZT thin films at different crystal orientations needs to be investigated to enhance its performance and hence meet the challenging requirements of the MEMS industry.

Our group has previously reported theoretical calculations based on the phenomenological consideration of the crystal orientation dependence of the dielectric and piezoelectric properties in PZT thin films [4]. We have reported that for PZT 60/40 in the rhombohedral region of the phase diagram, the electric field induced polarization hysteresis loops are expected to be sharper and square-like for PZT(100) when compared to the smoother and slanted loops for PZT(111). The piezoelectric property dependence on crystal orientation has also been reported. Changing the crystal orientation dramatically enhances the effective piezoelectric constant d_{33} . Figure 1 shows the change in d_{33}^{eff} with crystal orientation. Figure 2 gives the schematic explanation for this expectation. The d_{33}^{eff} value is three times larger for the [001] direction compared to that of the [111] direction. In the rhombohedral phase there are 8 possible polarization directions. Considering the (111) oriented films, the possible polarization directions 2, 3, and 4 are equivalent and are about 70.5° away from the spontaneous polarization direction 1. The other possible directions are 6, 7, 8 and 5. When the electric field of a completely poled sample along axis 5, the polarization gets reversed, the polarization reversal has various possibilities 5-1; 5-(2,3,4); 5-(6,7,8); 5-(6,7,8)-1; 5-(6,7,8)-(2,3,4); 5-(2,3,4)-1 etc., hence the reverse segments in the polarization curves are inclined. In the (100) film, there are two sets of equivalent directions, (1,2,3,4) and (5,6,7,8). The polarization directions are 54.7° away from the normal of the film,

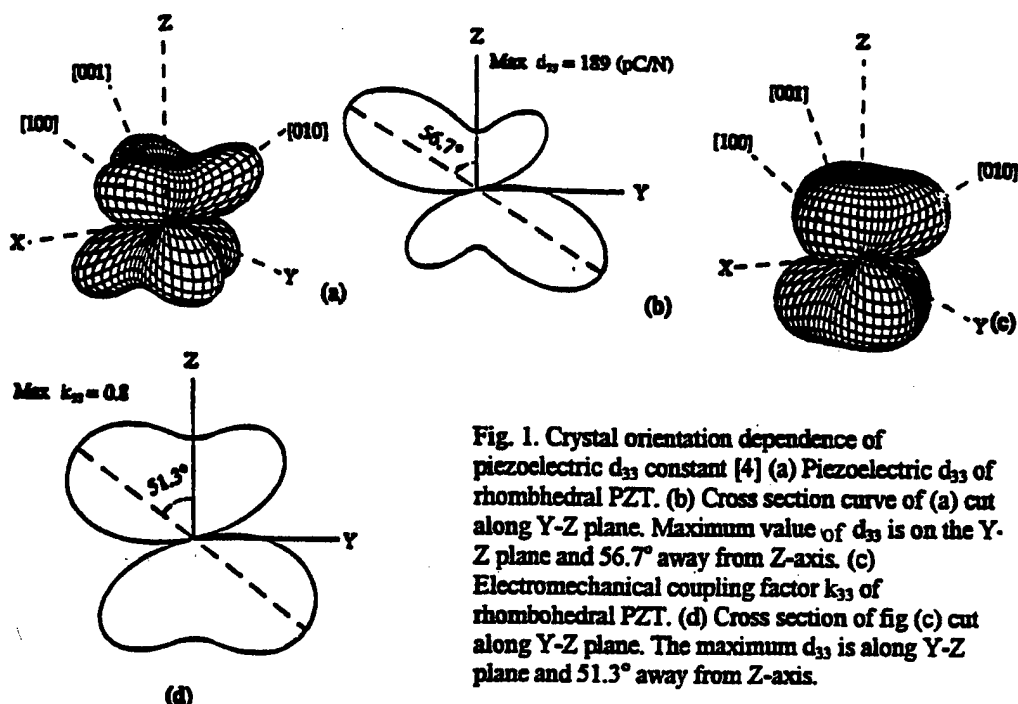


Fig. 1. Crystal orientation dependence of piezoelectric d_{33} constant [4] (a) Piezoelectric d_{33} of rhombohedral PZT. (b) Cross section curve of (a) cut along Y-Z plane. Maximum value of d_{33} is on the Y-Z plane and 56.7° away from Z-axis. (c) Electromechanical coupling factor k_{33} of rhombohedral PZT. (d) Cross section of fig (c) cut along Y-Z plane. The maximum d_{33} is along Y-Z plane and 51.3° away from Z-axis.

when the electric field E_3 is switched from positive to negative, the domains along 1,2,3,4 are reversed at the same time leading to abrupt polarization reversal. Theoretically the remnant polarization of the (100) films is expected to be $1/\sqrt{3}$ times that of (111) oriented films, a similar magnitude of the remnant polarization is expected due to the square-like hysteresis behavior of the (100) oriented films. Accordingly, we can expect an ideal strain curve like a butterfly hysteresis. Based on the above background we are investigating highly oriented PZT thin films in various crystal orientations. In this paper, the fabrication process and the dielectric property dependence of highly oriented PZT thin films will be discussed.

EXPERIMENTATION

PZT thin films were deposited by reactive rf-sputtering using multielement metallic targets of lead, zirconium and titanium. A 3" circular target was made using individual wedges of the Pb, Zr and Ti. The target composition (Pb:Zr:Ti::4:8:9) was adjusted so as to fabricate a rhombohedral composition of PZT(70/30). Substrates used were highly (111) oriented platinum coated SiO_2/Si wafers. All the substrates were thoroughly cleaned with isopropyl alcohol and rinsed in deionized water prior to film deposition. The substrates were clamped to a stainless steel holder and heated by quartz lamps to 450°C . The rf-sputtering system (Anelva SPC-350) was evacuated to a base pressure of 1×10^{-4} Pa, the films were grown at 20 mTorr pressure with Ar/O_2 ratio at 50/50. The films were grown at rf-power of 150 watts at a deposition rate of $0.1 \mu\text{m/hr}$. The as-deposited films were amorphous with some microcrystallization of the perovskite phase, annealed using rapid thermal annealing (RTA). The structural characterization of the films was made by X-ray diffraction using the $\text{Cu K}\alpha$ radiation. For electrical characterization, the crystallized films were coated with 150 nm thick platinum top electrodes by dc sputtering using a shadow mask; the electrode area used was $2.38 \times 10^{-3} - 1.77 \times 10^{-2} \text{ cm}^2$. The polarization versus

electric field hysteresis loop, the quasi-static capacitance-voltage measurements, and the resistivity measurements were made using RT66A standardized hysteresis tester(Radiant Technologies). The quasi-static C-V measurements were made using the RT66A hysteresis tester at a frequency of 60 Hz. The dielectric constant and loss factor were measured as a function of frequency using an impedance analyzer(HP4192) in the frequency range between 10 Hz and 1 MHz.

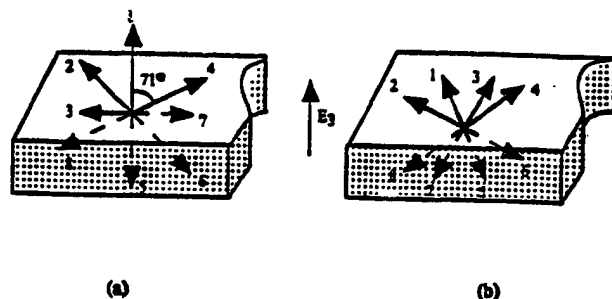


Fig 2. Possible spontaneous polarization directions[4] (a) (111) oriented films (b) (001) oriented films.

RESULTS AND DISCUSSION

The XRD patterns of the annealed films are shown in Fig.3. The XRD patterns indicate that highly oriented PZT(100) and PZT(111) films have been fabricated. The degree of crystal orientation was calculated from the integrated intensity of the PZT(111) and PZT(100) peaks and can be expressed as $\text{Int}_{(111)} = I(111)/[I(111) + I(100)]$. The degree of crystal orientation obtained for $\text{Int}_{(111)}$ was $> 98\%$ and that for $\text{Int}_{(100)}$ was $> 95\%$. The deposited films were annealed using a rapid thermal annealing(RTA) at different rates so as to crystallize the films to (100)/(111) perovskite structure. The crystal orientation of the substrate is critical in obtaining the desired orientation of the PZT films[5,6]. Highly oriented PZT(111) films can be easily grown on Pt(111)/SiO₂/Si, but obtaining PZT(100) oriented film on Pt(111)/SiO₂/Si substrate has not been widely reported[7,8]. The surface energy for the PZT(111) orientation is lower on Pt(111)/SiO₂/Si as compared to that for PZT(100), hence the growth of PZT(111) is kinetically

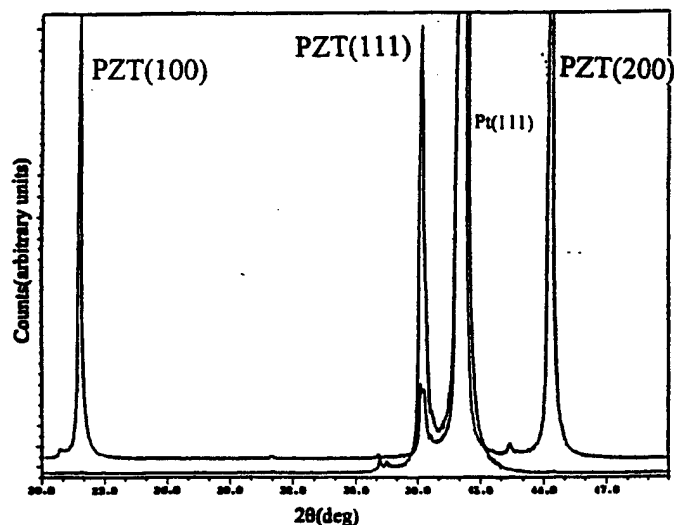


Fig. 3. XRD pattern of highly oriented PZT(111) and PZT(100) on Pt(111)/SiO₂/Si in the rhombohedral composition 70/30 annealed using rapid thermal annealing(RTA).

However PZT(100) growth plane has the lowest activation energy for nucleation, and in the absence of any microcrystallization of pyrochlore phase, the nucleation of (100) orientation is easier and subsequent growth of the (100) plane is favored. Figure.4 shows the selective rapid thermal annealing(RTA) cycles for obtaining PZT(100) and PZT(111) on the same Pt(111)/SiO₂/Si substrate.

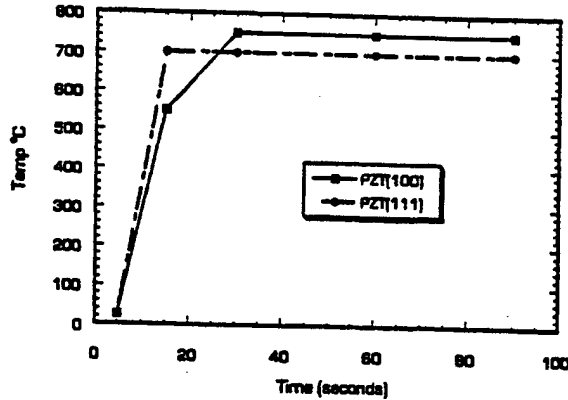


Fig. 4. Crystallization of highly oriented films using selective rapid thermal annealing cycles for PZT(111)/Pt/SiO₂/Si and PZT(100)/Pt/SiO₂/Si.

The electrical characterization of the films was made after making the top electrodes of platinum by dc sputtering using shadow masks. The dielectric constant and the loss factors are shown in fig.5 as a function of frequency for both the (111) and the (100) films. The films were poled with an electric field of 150 kV/cm for 30 minutes and then aged for an hour prior to measuring the dielectric constant at an oscillating ac frequency of 0.01 V. The dielectric constant and the loss factors are shown in Table 1, PZT(100) possess a larger dielectric constant and loss values compared to PZT(111). The loss values for the PZT(100) were in the range 0.03-0.035 and were larger than those for PZT(111) films which ranged from 0.02-0.03 at a frequency of 1 kHz. Figure 6 (a) and (b) show the P-E hysteresis loops and the quasi-static C-V curves(which is equivalent to the derivative of the P-E curves) for both PZT(111) and PZT(100) films.

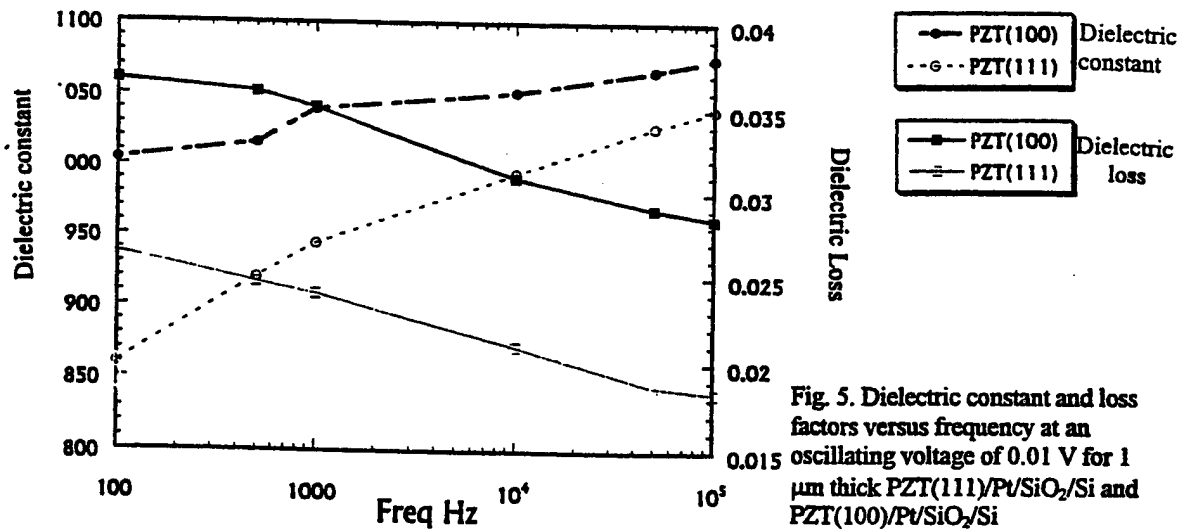


Fig. 5. Dielectric constant and loss factors versus frequency at an oscillating voltage of 0.01 V for 1 μ m thick PZT(111)/Pt/SiO₂/Si and PZT(100)/Pt/SiO₂/Si

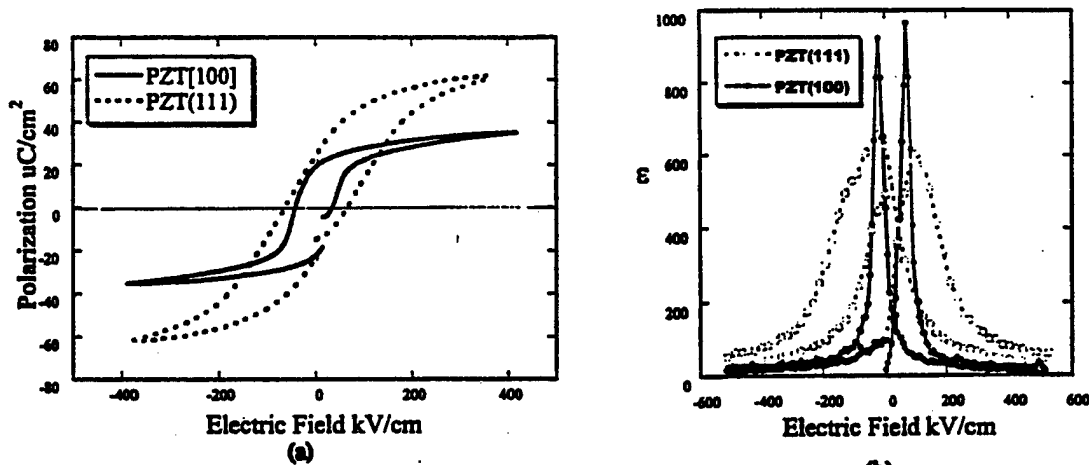


Fig. 6(a) Difference in the dielectric hysteresis between PZT(111) and PZT(100) measured using RT66A Ferroelectric tester. (b) Dielectric constant versus voltage characteristics of PZT(111) and PZT(100) 1 μ m thick films.

The saturation polarization values for PZT(111) oriented films are larger than those for the PZT(100) oriented films by a factor of $\sqrt{3}$ as proposed by theoretical calculation[4]. The coercive field is smaller for the (100) films when compared to (111) films. From fig.7 it can be seen that there is an abrupt saturation of the coercive field value in PZT(100) films at an applied field of 150 kV/cm whereas the saturation is gradual in (111) films until breakdown. The polarization curve in the case of PZT(100) is abrupt and square-like and is relatively smooth in the case of PZT(111). This result is expected from our theoretical calculation. Figure 6(b) shows the C-V loops for PZT(100) and PZT(111). The (100) films have a higher maximum than the (111) films, which indicates that domain switching occurs readily near the coercive field for the (100) films. The (100) films have sharper peaks compared to the broader peaks for the (111) films.

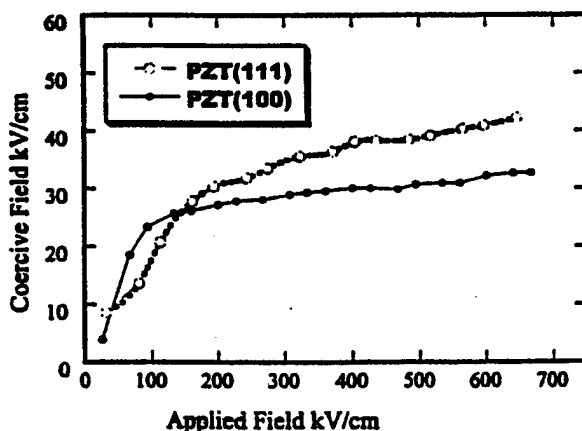


Fig. 7. Difference in the coercive field versus applied maximum field for PZT(100) and PZT(111) films.

Table 1 summarizes the dielectric constant, loss, coercive field, spontaneous polarization and remnant polarization for the PZT(100) and PZT(111) films. The piezoelectric characterization of the films is currently underway.

Table 1. Dielectric properties of PZT(111) and PZT(100) oriented films on Pt/SiO₂/Si.

Property	Dielectric Constant	Dielectric loss factor @ 1 kHz	Spontaneous Polarization ($\mu\text{C}/\text{cm}^2$)	Remnant polarization ($\mu\text{C}/\text{cm}^2$)	Coercive Field (kV/cm)
PZT(111)	900	.025	55	25	65
PZT(100)	1050	.035	28	20	35

CONCLUSIONS

Highly oriented PZT(100) and PZT(111) thin films have been grown by reactive rf magnetron sputtering using multielemental metallic targets. The crystal orientation dependence of the dielectric properties of PZT(111) and PZT(100) on Pt/SiO₂/Si substrates has been investigated to compare the results with the reported theoretical calculation for PZT thin films. The dielectric constant and loss for PZT(100) were found to be larger than those for PZT(111). The P-E hysteresis loops and the C-V loops were found to be sharper for the (100) than for (111) indicating that the domain wall movement in (100) films occurs simultaneously at a particular field compared to the gradual switching of the (111) oriented films. The saturation polarization for PZT(111) is about $1/\sqrt{3}$ times larger than that for PZT(100). The experimental observation seems to have good agreement with the reported theoretical calculations made for PZT thin films based on the phenomenology.

REFERENCES

1. K.D.Wise, Proc. IEEE Micro Electro Mechanical Systems Workshop, Nara, p33-38, 1991
2. M.Mehgany, Circuits and Devices, pp14-22, 1993
3. D.L.Polla and P.J.Schiller, Integrated Ferroelectrics, Vol 7, pp 359-370, 1995
4. X.Du, U.Belegundu and K.Uchino, Jpn. J. Appl. Phy., Vol 36 Pt 1, No:9 A, pp 5580- 5587, 1997
5. K.Ijima, I.Ueda and K.Kugimiya, Jpn. J. Appl. Phy., Vol 30, No:9 B, pp2149-2151,1991
6. T.Ogawa, A.Senda, T.Kasanami, Jpn. J. Appl. Phy., Vol 30, No:9 B, pp 2145-2148, 1991
7. J.Senzaki, O.Mitsunaga, T.Uchida, T.Uena, K.Kuroiwa, Jpn. J. Appl. Phy., Vol 35, Pt 1, No:8, pp 4195-4198, 1996
8. A.Masuda, Y.Yamanaka, M.Tazoe, Y.Yonezawa, A.Morimoto, T.Shimiza, Jpn. J. Appl. Phy., Vol 34, pp 5154-5157, 1997

ACKNOWLEDGEMENTS

The authors would like to thank the Office of Naval Research for supporting this work through the contract, N00014-91-J-4145.

APPENDIX 87



Special Review "Launching into The Great New Millennium"

Piezoelectric Films for MEMS Applications

圧電体薄膜の MEMS 応用

Susan TROLIER-MCKINSTRY

Materials Research Laboratory, The Pennsylvania State University, University Park, PA 16802, USA

Piezoelectric Films for MEMS Applications

圧電体薄膜の MEMS 応用

Susan TROLIER-MCKINSTRY

Materials Research Laboratory, The Pennsylvania State University, University Park, PA 16802, USA

Piezoelectric thin films are attractive for applications in MicroElectroMechanical Systems (MEMS) due to the combination of high energy density and low power requirements relative to other on-chip actuation mechanisms. As such, they can be utilized for applications as diverse as the pumping systems in miniature analytical instrumentation, high sensitivity accelerometers and hydrophones, miniature motors, and high frequency biomedical ultrasound, for example. Critical in all of these applications is the magnitude of the electromechanical response that can be generated. This paper will focus on the factors which affect the measured piezoelectric response of ferroelectric thin films. Particular emphasis will be placed on the effects of substrate clamping, clamping of the extrinsic contributions to the properties, and the role of preferred polarization directions in increasing the long-term reliability of ferroelectric films for piezoelectric applications.

[Received October 2, 2000]

Key-words: Thin films, Lead zirconate titanate, Piezoelectricity

1. Introduction

AS the field of microelectromechanical systems (MEMS) continues to grow, improved methods of sensing and actuation are desirable. Piezoelectricity is attractive for such applications since it enables electrically driven actuation or stress/strain sensing with an electrical output. Both of these phenomena can be readily integrated with circuitry, which can simplify implementation of devices.

Piezoelectricity can be displayed by oriented films of materials such as ZnO or AlN (in which the polarization direction is fixed by the crystallography, and so cannot be reoriented permanently by an applied electric field), or by poled ferroelectric films. Of these, ZnO and AlN may be somewhat easier to implement in MEMS devices since they involve only a single cation, and can often be prepared at low deposition temperatures. In contrast, ferroelectric films such as lead zirconate titanate (PZT) and lead magnesium niobate-lead titanate (PMN-PT) involve multiple cations, and so stoichiometry control is made more complicated. They also typically require processing temperatures in excess of 500°C in oxidizing ambients, which in turn, necessitates changes in the electrode materials as well. They are, however, interesting for MEMS applications because their piezoelectric coefficients are more than one order of magnitude higher than that of piezoelectric films such as ZnO or AlN.^{1),6)}

A wide array of MEMS devices employing piezoelectric films have been reported, including accelerometers, force sensors, pressure and acoustic sensors, miniature motors, pumps, etc.²⁾⁻⁵⁾ Excellent review articles in this area are available.^{2),6)}

This article will concentrate on ferroelectric thin films as candidates for piezoelectrics in MEMS. As such, it will cover several of the factors which affect the measured piezoelectric coefficients in thin films. Due to the high piezoelectric coefficients that are available, emphasis will be placed on the lead-based perovskites, including lead zirconate titanate (PZT) and lead magnesium niobate-lead titanate (PMN-PT)

2. Piezoelectric MEMS

Many MEMS designs employ a bending structure in which the active piezoelectric layer is supported by a passive material such as silicon or silicon nitride²⁾ (see Fig. 1). In most cases, when an electric field is applied, the piezoelectric

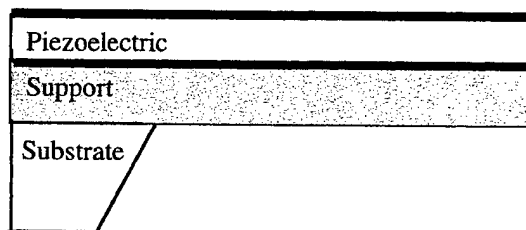


Fig. 1. A typical bending-mode actuator or sensor configuration. Not to scale vertically.

lectric film undergoes strains in both the thickness and in-plane dimensions, according to:

$$x_{jk} = d_{ijk} E_i,$$

where x_{jk} is the induced strain, d_{ijk} is the piezoelectric coefficient, and E_i is the applied electric field. In many perovskite-structured ferroelectrics, $d_{333} \sim -2d_{311}$ (In matrix notation: $d_{33} \sim -2d_{31}$). For actuator applications the field-induced transverse strain in the piezoelectric film is amplified and transferred to a vertical bending displacement because of the clamping of the passive layer to the piezoelectric film. For sensor applications a vertically applied force or pressure is converted to a substantial in-plane stress by mechanical bending of the thin element. This produces either a surface charge or an electric field on the electrodes.

Mechanical bending elements of this type can be realized using silicon micromachining technology.^{7),3)} Thus, many bending-type cantilever or diaphragm MEMS devices are under development for a variety of sensors and actuators.^{2),3),6),8)}

Alternatively, it is possible to utilize interdigitated "comb" electrodes on the top surface of the film piezoelectric film to either apply electric fields or sense in-plane stresses.^{9),10)} This has the advantage of decoupling the device capacitance from the thickness of the film, which can result in much larger voltage sensitivities.

3. Factors affecting the piezoelectric coefficient of ferroelectric films

Much of the incentive to incorporate ferroelectric films such as PZT or PMN-PT into MEMS structures stems

from the large piezoelectric coefficients that are available in bulk ceramics of these compositions. This offers the possibility of generating larger strains at the same applied field, or of utilizing thinner films for the same displacement than is possible with non-ferroelectric compositions such as ZnO or AlN. Many groups have shown that it is possible to develop a significant fraction of the bulk d_{ij} coefficients in thin films. Indeed, if effective piezoelectric e_{ij} coefficients are defined, i.e.,

$$\sigma_i = -e_{ij}E_j$$

(where σ_i are the stresses) there are data suggesting that thin films can show the same e_{ij} values as bulk ceramics.⁶⁾

There are, however, several reasons why the piezoelectric coefficients d_{ij} of ferroelectric thin films are smaller than those of bulk ceramics of the same composition. First, it has been found that the piezoelectric effect in PZT thin films is inferior to bulk ceramics due to the limited extrinsic contributions in thin films, particularly when the films are less than a micron in thickness.¹¹⁾ It is well known that in bulk PZT ceramics, extrinsic contributions associated with non-180° domain wall mobility account for up to half of the room temperature d_{33} and d_{31} coefficients.¹²⁾ Extrinsic contributions are particularly important in donor-doped "soft" PZTs due to the high domain wall mobility in these materials. However, extrinsic contributions to the piezoelectric properties are very strongly clamped in thin PZT films up to several microns in thickness.¹³⁾ As a result, this mechanism for generating piezoelectric strains or charges is less important in thin films than in bulk materials. It is not clear whether in-plane ferroelastic reorientation of domains will be as limited as in the case of films measured through the thickness.

Secondly, PZT films deposited on substrates with smaller thermal expansion coefficients such as silicon are under tensile stress after cooling from the crystallization temperature into the ferroelectric phase, and this leads to a tendency to pull the ferroelectric polarization into the plane of the film.¹⁴⁾ Due to the limited ferroelastic reorientation which is possible in thin films (in contrast to bulk ceramics of the same composition),¹⁵⁾ it is not possible to reorient many of these domains perpendicular to the film plane. The consequence in a film poled through-the-thickness is a lower remanent polarization and reduced piezoelectric

coefficients. This effect appears to be most critical in thin films with small lateral grain sizes.

Thirdly, clamping of the piezoelectric effect by the substrate can also markedly reduce the measured piezoelectric response. Most perovskite ferroelectrics expand longitudinally and contract laterally when an electric field is applied parallel to the polarization direction. Since for many measurement geometries, the film is rigidly attached to a much thicker substrate, the field-induced distortion in the plane of the substrate can be heavily clamped. Thus, effective piezoelectric coefficients, rather than the free coefficients of the film are measured.^{6),16),17)} The in-plane constraints also lead to small differences between the piezoelectric coefficients measured by direct and converse methods.¹⁸⁾ Kholkin et al. have experimentally demonstrated the importance of this clamping in measurements of PZT and Ca-doped PbTiO₃ films. The latter have very low d_{31} values, and as a result the in-plane clamping was greatly reduced, and the resulting films had d_{33} coefficients very close to those of the bulk material.¹⁹⁾ In contrast, in PZT, PMN-PT, and many other perovskites,²⁰⁾⁻²²⁾ $d_{33} \sim -2d_{31}$, so clamping effects are significant.

4. Role of preferred polarization directions

It is desirable, once the polarization direction has been set, that it not be perturbed during operation of the device. While this is a straightforward condition to fulfill in irreversible piezoelectrics such as ZnO and AlN, in ferroelectric films, temperature and field excursions, as well as aging, affect the remanent polarization, and hence the piezoelectric coefficients. This is shown in Fig. 2, where the magnitude of the piezoelectric coefficient is shown as a function of the number of times a poled film was exposed to an alternating electric field with a magnitude less than the coercive field. It is clear that the higher the reverse field the film is exposed to, the more rapidly the film depoles. Aging rates for the piezoelectric coefficients can also be quite rapid in many ferroelectric films ($\sim 3\text{--}15\%$ /decade).^{23),24)}

Since there are a number of applications where it may be helpful to apply an electric field which opposes the remanent polarization (i.e. to close or open a cantilever-based MEMS switch), it is important to stabilize the desired polarization direction. Similarly, this will be required in developing sen-

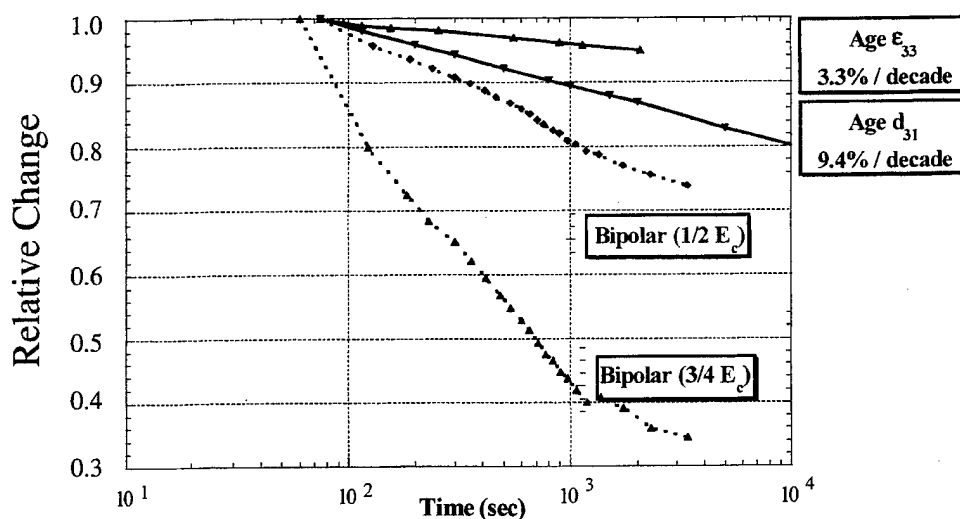


Fig. 2. Comparison of aging rates for permittivity (ϵ_{33}), piezoelectric coefficient (d_{31}), and the degradation in d_{31} caused by bipolar cycling of the electric field at 1/2 and 3/4 of the coercive field.

sors with stable outputs. It has been found that if a preferred polarization direction is developed in the film, the aging rates, as well as depoling on exposure to reverse electric fields can be greatly lessened.²⁵⁾

Several approaches can be used to develop such a preferred polarization direction, including:

- **Aligning defect dipoles.** As is described elsewhere,²⁶⁾ if it is possible to align polar defects in a ferroelectric matrix, then these defects can impart a net alignment field. This is widely used in bulk hard PZT ceramics to stabilize the polarization directions, so that higher electric field drive levels can be utilized. In the case of PZT (and probably the other lead-based perovskites), the defect dipole can be a result of paired V_{Pb}'' and V_O^\bullet . Since the V_O^\bullet has relatively high mobilities, it can be realigned under the poling fields, but then tends to stay aligned at lower fields.²⁷⁾ It is very likely that many thin films possess comparatively high levels of these defects, so stabilization of the polarization with such defect dipoles is probable in lead-based perovskite films.

- **Utilizing space charge.** Charges can be trapped at the ends of domains to compensate any polarization discontinuity.²⁸⁾ These charges also act to stabilize the existing domain structure.

- **Employing asymmetric electrodes.** If the two electrodes on the ferroelectric film are different in character, then it is possible to develop an internal electric field in the film due to the asymmetry in the Schottky barriers at the film/electrode interfaces.^{29),30)}

- **Bombarding a growing film.** In examining the ferroelectric film literature, it is evident that many films, particularly those grown by vapor phase techniques involving bombardment, can show appreciable net piezoelectric or pyroelectric effects as grown, i.e. they are poled as grown.^{31),32)} While this has sometimes been attributed to strain gradients imposed by lattice-mismatched substrates,³¹⁾ the fact that not all epitaxial films on the same substrates show the same effect suggests that another factor is responsible. Study of the effect of bombardment on the film properties is complicated by the fact that the processing window is not always sufficiently wide to separate the role of bombardment from simultaneous changes in stoichiometry and microstructure. In growth of PMN-PT films, it has been noted that the degree of imprint in a film (that is, the shift of the polarization-electric field hysteresis loop along the field axis) was correlated with the lattice constant extension characteristic of growth under higher bombardment conditions.³³⁾ The mechanism by which this leads to a preferred polarization direction is not clear, though it is effective. Bombardment after deposition can also lead to imprint, although in this case, the mechanism may be associated with development of defect dipoles at the bombarded surface.³⁴⁾

- **Incorporating different molecular groups.** This has been used to great effect in bulk triglycine sulfate single crystals. In that case, replacing glycine molecules with l-alanine, it is found that the material can essentially be made polar, but not ferroelectric. This, in turn, was used in pyroelectric detectors to stabilize the pyroelectric response to temperature excursions.

- **Imposing a strain gradient.** Since a gradient in strain is a vector quantity, it can in principle be used to develop a net polarization direction in a ferroelectric (see Fig. 3). The resulting asymmetry in the unit cell could encourage displacement of largest volume sublattice in the direction of larger lattice parameter. There is, as yet, no clear indication of the magnitude of the strain gradient that would be required, though there is some suggestive work in bulk specimens.³⁵⁾ It is probable that this effect will be more ap-

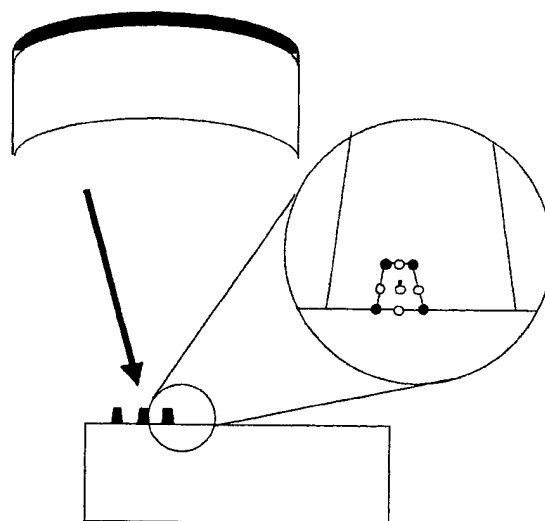


Fig. 3. Strain gradient in a patterned ferroelectric film. The original curvature of the film/substrate system is relieved by laterally subdividing the ferroelectric film.

parent in thin films than in bulk ceramics of the same composition, since ferroelastic reorientation of domains by the applied stresses would be less important.

- **Employing a composition gradient.** If a material with a low transition temperature was deposited on a higher transition temperature material, it should be possible to pole the ensemble. If then the system was exposed to a temperature excursion, the top of film could thermally depole when driven above T_c . As the temperature dropped again, repoling of the top of film could be forced by the underlying material, which is still poled. This would enable the full paraelectric-ferroelectric strain to be utilized in a MEMS device. To the knowledge of the author, this has not yet been employed in a MEMS device.

5. Conclusions

Piezoelectric thin films are being widely explored as candidate materials for on-chip sensing and actuation functions. Utilizing bending elements facilitates generation of sufficient stress amplification to make high sensitivity sensors, and likewise magnifies the small displacements that are available in thin film specimens. Stabilization of the piezoelectric response is essential in MEMS devices with reasonable long-term reliability. This can be achieved by development of preferred polarization directions in the ferroelectric films.

Acknowledgments The author is grateful for the financial support provided by the National Science Foundation (DMR-9502431) and the Office of Naval Research for financial support for this work.

References

- 1) Cross, L. E. and Trolier-McKinstry, S., *Encl. Appl. Phys.*, **21**, 429-51 (1997).
- 2) Polla, D. L. and Francis, L. F., *Mater. Res. Soc. Bull.*, **21**, (7), 59-65 (1996).
- 3) Bernstein, J. J., Finderg, S. L., Houston, K., Niles, L. C., Chen, H. D., Cross, L. E., Li, K. K. and Udayakumar, K. R., *IEEE Trans. UFFC*, **44**, 960-69 (1997).
- 4) Flynn, A. M., Tavrow, L. S., Bart, S. F., Brooks, R. A., Ehrlich, D. J., Udayakumar, K. R. and Cross, L. E., *J. Microelectromech. Syst.*, **1**, 44-51 (1992).
- 5) Dubois, M.-A. and Muralt, P., *IEEE Trans. UFFC*, **45**,

- 1169-77 (1998).
- 6) Muralt, P., *IEEE Trans. UFFC*, **47**(4), 903-15 (2000).
- 7) Kim, J. H., Wang, L., Zurn, S. M., Li, L., Yoon, Y. S. and Pol-
la, D. L., *Integr. Ferroelec.*, **15**, 325-32 (1997).
- 8) Lee, C., Itoh, T. and Suga, T., *IEEE Trans. UFFC*, **43**,
553-59 (1996).
- 9) Xu, B., Ye, Y., Cross, L. E., Bernstein, J. J. and Miller, R.,
Appl. Phys. Lett., **74**(23), 3549-51 (1999).
- 10) Xu, B., Polcawich, R. G., Trolrier-McKinstry, S., Ye, Y.,
Cross, L. E., Bernstein, J. J. and Miller, R., *Appl. Phys. Lett.*
75(26), 4180-82 (1999).
- 11) Trolrier-McKinstry, S., Shepard, J. F., Jr., Lacey, J. L., Su,
T., Zavala, G. and Fendler, J., *Ferroelectrics*, **206**-207,
381-92 (1998).
- 12) Zhang, X. L., Chen, Z. X., Cross, L. E. and Schulze, W. A., *J.*
Mater. Sci., **18**, 968 (1983); Damjanovich, D. and Demartin,
M., *J. Phys. D: Appl. Phys.*, **29**, 2057-60 (1996).
- 13) Xu, F., Trolrier-McKinstry, S., Ren, W., Xie, Z. L. and Hem-
ker, K. J., accepted by *J. Appl. Phys.*
- 14) Tuttle, B. A., Garino, T. J., Voigt, J. A., Headley, T. J., Di-
mos, D. and Eatough, M. O., "Science and Technology of
Electroceramic Thin Films," Ed. by Auciello, O. and Waser
R., Kluwer Academic Publishers, The Netherlands (1995) p.
117.
- 15) Shepard, J. F., Jr., Chu, F., Xu, B. and Trolrier-McKinstry, S.,
MRS Proc. **493**: Ferroelectric Thin Films VI, 69-74 (1998).
- 16) Lefki, K. and Dormans, G. J. M., *J. Appl. Phys.*, **76**, 1764-67
(1994).
- 17) Steinhausen, R., Hauke, T., Seifert, W., Mueller, V., Beige,
H., Seifert, S., and Lobmann, P., *Proc. 11th ISAF*, 93-96
IEEE (1998).
- 18) Xu, F., Chu, F. and Trolrier-McKinstry, S., *J. Appl. Phys.*, **86**,
588-94 (1999).
- 19) Kholkin, A. L., Calzada, M. L., Ramos, P., Mendiola, J. and
Setter, N., *Appl. Phys. Lett.*, **69**, 3602-04 (1996).
- 20) Edo Electroceramics Piezoelectric Products Catalog. Data for
EC-98 (<http://www.edoceramic.com>)
- 21) Liu, S.-F., Park, S.-E., Shrout, T. R. and Cross, L. E., *J. Appl.*
Phys., **85**, 2810-14 (1999).
- 22) Jaffe, B., Cook, W. R., Jr. and Jaffe, H., "Piezoelectric Crys-
tals," Academic Press (1971).
- 23) Kholkin, A. L., Tagantsev, A. K., Colla, E. L., Taylor, D. V.
and Setter, N., *Integrated Ferroelectrics*, **15**, 317-24 (1997).
- 24) Shepard, J. F., Chu, F., Kanno, I. and Trolrier-McKinstry, S.,
J. Appl. Phys., **85**, 6711-16 (1999).
- 25) Polcawich, R. G. and Trolrier-McKinstry, S., accepted by *J.*
Mater. Res. (2000).
- 26) Lines, M. E. and Glass, A. M., "Principles and Applications of
Ferroelectrics and Related Materials," Clarendon Press, Ox-
ford (1977).
- 27) Jaffe, B., Cook, W. R. and Jaffe, H., "Piezoelectric Ceram-
ics," Academic Press (reprinted by R. A. N. Publishers,
Marietta, OH) (1971).
- 28) Dimos, D., Warren, W. L., Sinclair, M. B., Tuttle, B. A. and
Schwartz, R. W., *J. Appl. Phys.*, **76**, 4305-15 (1994).
- 29) Wurfel, P. and Batra, I. P., *Phys. Rev.*, **B8**(11), 5126-33
(1973).
- 30) Lee, J. J. and Desu, S. B., *Ferro. Lett.*, **20**, 27-34 (1995).
- 31) Cattani, E., Manceau, J.-F., Haccart, T., Biwersi, S., Velu, G.,
Remiens, D. and Bastien, F., *Ferroelectrics*, **224**, 307-14
(1999).
- 32) Abe, K. et al., *Jpn. J. Appl. Phys.*, **36**, 5575-79 (1997).
- 33) Maria, J. P., Ph. D. Thesis, The Pennsylvania State Universi-
ty (1998).
- 34) Maiwa, H., Ichinose, N. and Okazaki, K., *Jpn. J. Appl. Phys.*,
34, part 1(9B) 5136-40 (1995).
- 35) Bursian, E. V., Zaikovskiy, O. I. and Makarov, K. V., *J. Phys.*
Soc. Jpn., **28**, 416 (1970).



Susan Trolrier-McKinstry is Associate Director of the Materials Research Laboratory and an Associate Professor of Ceramic Science and Engineering at the Pennsylvania State University. Her main research interests include ferroelectricity, thin films for actuator and dielectric applications, textured piezoelectric ceramics, and spectroscopic ellipsometry. She is a member of the American Ceramic Society, Keramos, the Materials Research Society, IEEE, ASM, and ASEE. She is co-chair of the committee revising the IEEE Standard on Ferroelectricity. She is an elected member of the IEEE Ultrasonics, Ferroelec-
trics, and Frequency Control Society advisory committee. She has served on the organiz-
ing committees for the International Symposium on Ferroic Domains and Mesoscopic
Structures-5, the International Symposium on Applications of Ferroelectrics, the
US-Japan meeting on Dielectric and Piezoelectric Ceramics, and MRS symposia on
Materials for Smart Systems.

APPENDIX 88

Dielectric and piezoelectric properties of sol-gel derived lead magnesium niobium titanate films with different textures

Jeong Hwan Park, Fei Xu, and Susan Trolier-McKinstry^{a)}

Materials Research Laboratory, The Pennsylvania State University, University Park, Pennsylvania 16802

(Received 23 December 1999; accepted for publication 18 September 2000)

The piezoelectric and dielectric constants for $\text{Pb}(\text{Mg}_{1/3}\text{Nb}_{2/3})\text{O}_3$ - PbTiO_3 (PMN-PT, 70/30) films with different orientations were measured. PMN-PT films were deposited on Pt(111)-passivated silicon substrates using a modified sol-gel process. The room temperature dielectric constants K for the {100}-oriented films were 2500–2600, while K for {111}-oriented films were 1900–2000. In both cases $\tan \delta$ was less than 0.03. The dependence of the piezoelectric coefficient d_{31} of the PMN-PT films on the poling fields was investigated. The d_{31} coefficients of {100}-oriented PMN-PT films were found to range from -28 to -69 pC/N with poling field. The {100}-oriented PMN-PT films showed larger piezoelectric coefficient than {111}-oriented films. The d_{33} coefficients of the $1.5 \mu\text{m}$ thick {100} oriented PMN-PT films were ~ 170 – 183 pC/N. The aging rate of $-d_{31}$ was $\sim 4\%$ – 10% /decade. © 2001 American Institute of Physics.
[DOI: 10.1063/1.1324685]

INTRODUCTION

There has been significant interest in Pb-based ferroelectric thin films such as $\text{Pb}(\text{Mg}_{1/3}\text{Nb}_{2/3})\text{O}_3$ (PMN), PbTiO_3 (PT), PbZrO_3 , and $\text{Pb}(\text{Zr}_{0.5}\text{Ti}_{0.5})\text{O}_3$ (PZT) because of their potential advantages for electro-optic and microelectronic applications, including capacitors, pyroelectric detectors, surface acoustic wave devices, nonvolatile semiconductor memories, and piezoelectric devices.^{1,2} Of these, piezoelectric thin films have attracted considerable attention since they can add functionality to microfabricated devices such as microsensors and actuators. Microfabricated devices incorporating ferroelectric actuation or sensing typically include compositions from the $\text{Pb}(\text{Zr}, \text{Ti})\text{O}_3$ system.^{3–5} In that case, it was demonstrated that properties such as the dielectric constant, pyroelectric coefficients, piezoelectric constants, and P - E hysteresis could be improved by preferentially controlled orientation.^{6–9}

Recently, ultralarge piezoelectric responses have been observed in single crystal solid solutions of relaxor ferroelectrics and PT. For example, for single crystals of the rhombohedral $\text{Pb}(\text{Zn}_{1/3}\text{Nb}_{2/3})\text{O}_3$ - PbTiO_3 system, Park *et al.* have reported that a d_{33} piezoelectric coefficient as high as 2600 pC/N can be obtained when oriented and measured along the [001] direction.^{10,11} They suggested that no driving force exists for non-180° domain wall motion in the case of a well-poled (001)-oriented rhombohedral crystal measured normal to the face. This is interesting from the standpoint of piezoelectric films since ferroelastic wall motion is difficult to achieve in many ferroelectric thin films.¹² Maria *et al.* have also demonstrated that d_{31} piezoelectric coefficients as high as -180 pC/N can be realized in (001) epitaxial rhombohedral PMN-PT thin films on SrRuO_3 /(001) LaAlO_3 substrates.¹³ Taking these results into account, similar advances

in piezoelectric characteristics can be expected for highly {100}-oriented relaxor-PT film relative to polycrystalline ones.

Thus an investigation of the dielectric and electromechanical properties of oriented PMN-PT films by sol-gel has been initiated. The specific composition investigated was 70%PMN–30%PT, which lies on the rhombohedral side of the room temperature morphotropic phase boundary between PMN and PT. In this study, the effects of crystallographic texture ({100} and/or {111} fiber texture) on the dielectric and piezoelectric properties of the PMN-PT thin films have been characterized. In addition, aging of the piezoelectric coefficients in {100} and {111} oriented films has been investigated.

EXPERIMENTAL PROCEDURE

Lead acetate trihydrate, $\text{Pb}(\text{C}_2\text{H}_3\text{O}_2)_2 \cdot 3\text{H}_2\text{O}$, magnesium ethoxide, $\text{Mg}(\text{OC}_2\text{H}_5)_2$, niobium ethoxide, $\text{Nb}(\text{OC}_2\text{H}_5)_5$, and i.e. $\text{Pb}(\text{C}_2\text{H}_3\text{O}_2)_2 \cdot 3\text{H}_2\text{O}$ titanium(IV) isopropoxide, $\text{Ti}(\text{OCH}(\text{CH}_3)_2)_4$ (Aldrich Chemical, Milwaukee, WI) were used as starting materials. 2-methoxyethanol was used as a solvent (Aldrich Chemical, Milwaukee, WI) and formamide as a drying control chemical additive. PMN-PT solutions were synthesized with a 70:30 ratio (on the rhombohedral side of the morphotropic phase boundary) using a modification of the route described elsewhere.^{8,14}

Stable polymeric methoxyethoxide complex precursors were synthesized through distillation and refluxing of the starting materials in 2-methoxyethanol under a dry N_2 atmosphere. A flow chart for the chemical solution processing of PMN-PT precursors is presented in Fig. 1. To compensate for lead loss during rapid thermal annealing, 15 mol% excess lead was added to the precursor solution. 0.5 M solutions were synthesized and then spin coated at 2500 rpm for 30 s on Pt(111)-coated {100} silicon substrates 1500 \AA Pt/200 \AA Ti/1 μm SiO_2/Si . Following pyrolysis at 360 °C

^{a)}Author to whom correspondence should be addressed; electronic mail: stmckinstry@psu.edu

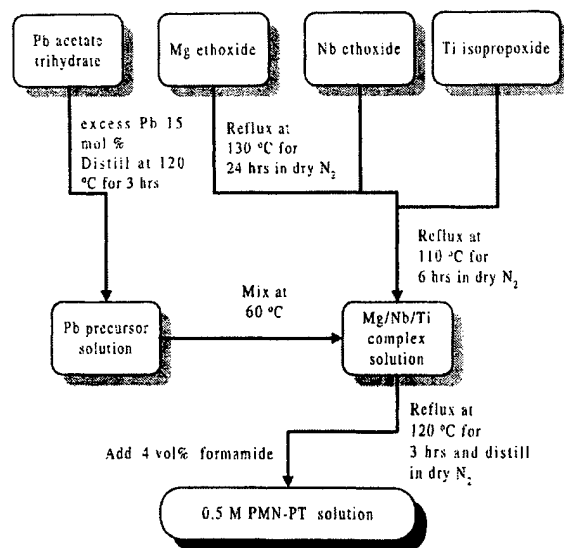


FIG. 1. Schematic diagram of PMN-PT (70/30) precursor solution by sol-gel processing.

for 3 min, additional layers were spin coated to build up the desired thickness. Films were crystallized by rapid thermal annealing (Heatpulse 610, A.G. Associates, San Jose, CA) at 650–800 °C for 60 s. Individual crystallization steps were conducted for thicker films after every fourth coating to minimize cracking of the resulting film. The final film thicknesses were about 1.2–1.5 μm thick. In some cases, a very thin PT layer (~ 30 nm) was deposited and heat treated at 550 °C for 30 s, prior to deposition of PMN-PT films.

The structure and crystallinity of the films were characterized by x-ray diffraction (XRD) (Rigaku Co., Tokyo, Japan, $\text{Cu K}\alpha$ radiation, 40 kV, 50 mA). A second diffractometer (Philips, Eindhoven, Netherlands) was employed for θ - 2θ scans and pole figures. The film morphology was observed by scanning electron microscopy (SEM) (Hitachi, S4200, Japan). Electrical measurements were made through the film thickness using Pt top electrodes 1.6 mm in a diameter prepared by sputtering through a shadow mask. Electrical contact was made to the bottom electrode with a probe wire, whereas the top contact was made with a microprobe tip. Low field dielectric properties were determined by an impedance analyzer (Model 4184A, Hewlett-Packard, Palo Alto, CA) with an oscillation of 30 mV and frequencies of 0.1–10 kHz as a function of temperature (-50 – 180 °C). High and low temperature measurements were made using a laboratory oven with both refrigerating and heating capabilities. High field hysteresis properties were characterized using a RT66A (Radiant Technology, Albuquerque, NM) ferroelectric test system. The coercive field of the film was measured and used to calculate the poling field to be applied for the subsequent piezoelectric characterization. The d_{31} coefficients of the thin films were characterized using a modification of wafer flexure method described previously.¹⁵ For this investigation, all samples were poled with the top electrode negative at room temperature with various electric fields. The poling time used for the experiments was taken to

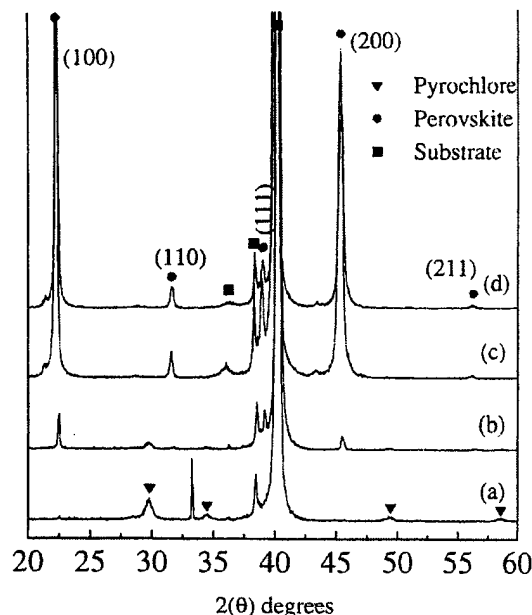


FIG. 2. XRD patterns of sol-gel derived PMN-PT films without a perovskite seed layer as a function of temperature: (a) 650 °C, (b) 700 °C, (c) 750 °C, and (d) 800 °C.

be 5 min. In this method, a piece of a PMN-PT coated wafer was glued to a 3 in. Si(100) substrate. This substrate was suspended over the cavity, and the pressure inside the cavity was changed periodically, yielding a biaxial stress in the film. The microstrain generated at the film surface was calibrated using a strain gauge attached to bare Si single crystal substrate combined with a lock-in amplifier (model 7260 EG&G Instrument) and a strain indicator (model 3800, Vishay measurements, Raleigh, NC). The aging of the d_{31} coefficients was measured 0.5–3000 min after the poling field was removed.

d_{33} coefficients were also measured using the pneumatic pressure method. For this experiment the back of the wafer was polished using diamond paste (0.5–1 μm), and the sample (3 cm \times 3 cm) was then inserted between two cavities, using lubricated O-rings as pressure seals. High-pressure gas was introduced into the cavities, and the net amount of charge fluctuation was measured after releasing the pressure. The detailed experimental procedure for measurement of d_{33} was described elsewhere.¹⁶

RESULTS AND DISCUSSION

Figure 2 shows the XRD patterns for PMN-PT films with various annealing temperatures. All peak indexing for the perovskite films is done on the basis of the pseudocubic unit cell. The pyrochlore phase was dominant when the annealing temperature was lower than 700 °C, as shown by the strong pyrochlore (222) peak in Fig. 2(a). Above 700 °C, highly {100}-oriented PMN-PT films ($f_{100} \sim 92\%$) on Pt(111)-coated Si substrate were obtained with increasing crystallization temperature. These {100}-oriented films were nearly phase-pure perovskite within XRD detection limits.

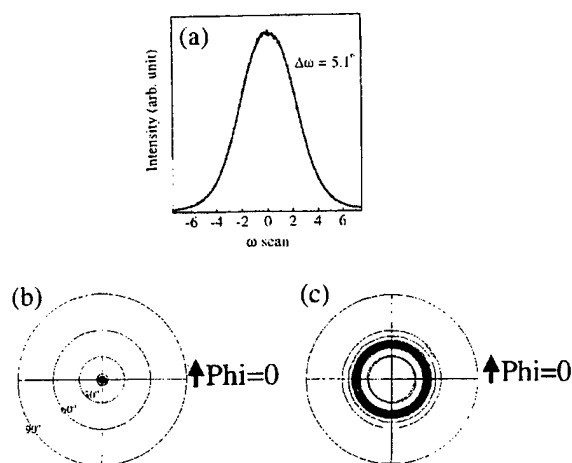


FIG. 3. (a) (200) plane rocking curve of the {100} oriented PMN-PT film, (b) (100) pole figure of the {100}-oriented PMN-PT film, and (c) (110) pole figure of the {100}-oriented PMN-PT film.

XRD ω scans of the (200) plane were collected for a {100}-oriented PMN-PT film crystallized at 750 °C on a Pt(111) substrate to examine the crystallinity and degree of film orientation. Next, to investigate the in-plane alignment of the oriented films prepared on Pt(111) substrates, (100) and (110) pole figure analyses were performed as shown in Fig. 3. Figure 3(a) shows the rocking curve for the {100} oriented film measured at $2\theta = 45.35^\circ$. The rocking curve width (FWHM) of the film heat treated at 750 °C is about 5.1° and shows relatively good alignment (grain orientation) perpendicular to the substrate surface. Figures 3(b) and 3(c) show the pole figures obtained at $2\theta = 22.15^\circ$ and 31.48° (100 and 110 peaks) for the PMN-PT film. From the (100) and (110) pole figures, it can be shown that the 100 peak is within 5° of the surface normal, and the 110 peak was found 45° away, corresponding to the calculated values. The circular pole contours indicated that the PMN-PT film grew with {100} perpendicular to the substrate surface but with random orientation in the plane. From the above observations, it can be seen that the PMN-PT films are fiber textured on Pt(111)-passivated substrates.

For perovskite PMN-PT deposition by sol-gel, a high nucleation energy barrier must be overcome by relatively higher annealing temperatures than are used for PT or PZT deposition.¹⁷ This high nucleation energy barrier can be reduced by the use of a template layer with a good match in lattice and structure. Ishikawa *et al.*¹⁸ have reported that the use of a PT seeding layer reduces the nucleation temperature of perovskite PZT films and changes their texture development. Furthermore, Cattani *et al.*¹⁹ have shown that for PZT films grown on PT films with a thickness above 200 Å, the PT buffer layer promoted (111) PZT orientation. Therefore, the ready formation of perovskite PT and the tendency toward development of {111} texture on Pt(111) coated substrate should both decrease the nucleation barrier for PMN-PT perovskite formation and allow development of alternative film orientations.

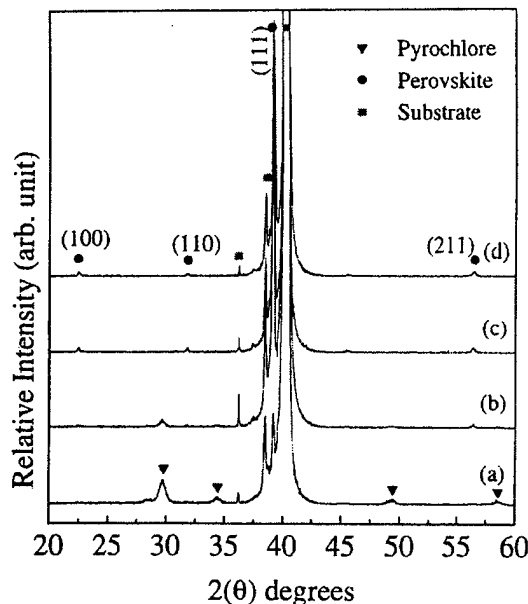


FIG. 4. XRD patterns of sol-gel derived PMN-PT films with a perovskite seed layer as a function of temperature: (a) 650 °C, (b) 700 °C, (c) 750 °C, and (d) 800 °C.

Figure 4 shows XRD patterns of PMN-PT films on Pt(111)-coated substrates with a PT buffer layer. The very thin PT buffer layer (~ 30 nm) was heat treated at 550 °C for 30 s by rapid thermal annealing before deposition of the PMN-PT film.

As shown in Fig. 4(a), the perovskite 111 peak was detected even at a crystallization temperature of 650 °C for PMN-PT films with a perovskite buffer layer. This is lower than the temperature required for PMN-PT films without a perovskite buffer layer [Fig. 2(a)]. Other research groups have also reported the benefit of a perovskite PT interlayer in promoting the perovskite phase.^{8,18,20}

The perovskite peak intensity corresponding to {111} perovskite was found to increase with increasing annealing temperature. Above 750 °C, highly {111}-oriented PMN-PT films ($f_{111} \sim 95\%$) were phase-pure perovskite within XRD detection limits. The resulting {111} PMN-PT texture may be due to a strongly textured PT thin film. The {111} texture of the PT thin film on (111) Pt substrates may be attributed to the small lattice mismatch between PT ($a = 3.961$ Å) and Pt ($a = 3.923$ Å).

Figure 5 shows SEM photographs of {100}-oriented and {111}-oriented PMN-PT films. The cross sectional view of the film in Fig. 5 shows that the thickness was about 1.2 μm . The {100} film consisted of small and large grains, with a grain size distribution of 150–500 nm. On the other hand, the {111}-oriented films, with an average grain size of ~ 50 nm, showed much smaller and more uniform grains than {100}-oriented films. There may be a difference in the nucleation density for the two processing routes. The grain size distributions of the {100}- and {111}-oriented films did not change significantly with film thickness. A similar observation between the orientation and grain size distribution has

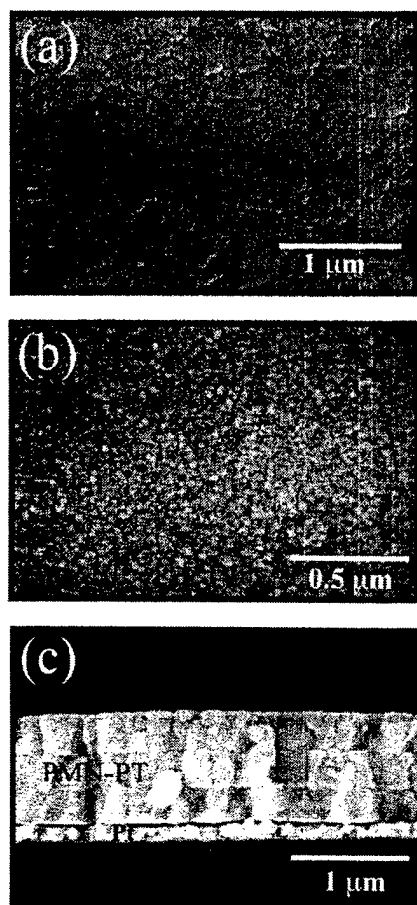


FIG. 5. SEM photographs of {100}- and {111}-oriented PMN-PT films: (a) {100} oriented PMN-PT film, (b) {111}-oriented PMN-PT film, and (c) cross-sectional view of the films.

also been reported in sol-gel derived PZT and PMN-PT (50/50) films.^{7,8}

Figure 6 shows the temperature dependence of the dielectric constant for the 1.2 μm thick {100}- and {111}-oriented PMN-PT films as a function of frequency. The dielectric constants of {100}-oriented and {111}-oriented films were ~ 2500 and ~ 2000 at 1 kHz and room temperature, respectively. The dielectric constants for {100}-oriented films were, in general, higher than those of {111}-oriented films. This was consistent for many independent measurements of the temperature dependent dielectric behaviors of the films. In terms of the loss values of differently oriented PMN-PT films, the temperature dependence was quite similar for both film orientations. No noticeable trends in $\tan \delta$ values with different orientation of the films were found in this present study.

As shown in Fig. 6, the curves at different frequency show broad maxima, with a T_{max} of $\sim 115^\circ\text{C}$. These films show the dispersive dielectric data characteristic of relaxor ferroelectrics below T_{max} . This is more dispersion that is seen in bulk crystals of the same composition, but is consistent with other data on PMN-PT (70/30) films. The transi-

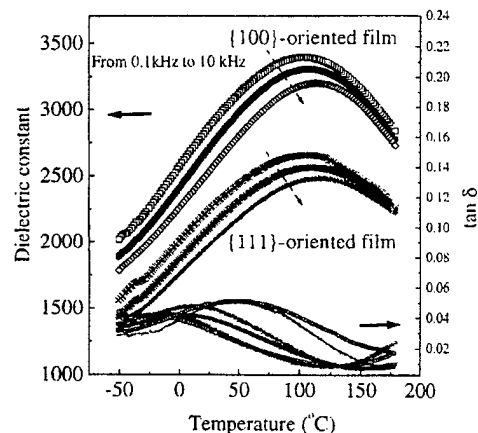


FIG. 6. The temperature dependences of the dielectric constants and $\tan \delta$ for {100}- and {111}-oriented PMN-PT films.

tion temperature is somewhat lower than that of bulk ceramics of equivalent composition (140°C).²¹

Figure 7 shows the polarization reversal for PMN-PT films with different orientations. As shown in Fig. 7, {100}-oriented films showed lower remanent polarizations than {111}-oriented films. The values of maximum polarization P_{max} and remanent polarization P_r of the {111}-oriented film were ~ 41 and $\sim 11.7 \mu\text{C}/\text{cm}^2$ at 200 kV/cm, respectively. The values of P_{max} and P_r of the {100}-oriented film were ~ 36 and $\sim 10 \mu\text{C}/\text{cm}^2$ at the same applied field, respectively. Regardless of the preferred orientation of these films on Si, the remanent polarization values of these films on the same composition were lower compared to those of epitaxial PMN-PT films of the same composition on LaAlO_3 substrates prepared by pulsed laser deposition.²² This might be due, in part, to the tensile stress developed in the film due to the thermal expansion mismatch with the Si substrate during cooling.^{23,24}

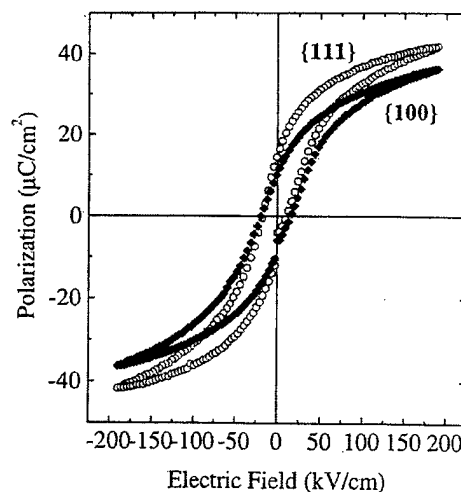


FIG. 7. Comparison of high-field hysteresis properties for the {100}- and {111}-oriented PMN-PT films.

Several methods to characterize the piezoelectric properties of thin films have been reported including double beam laser interferometry²⁵ and charge-based techniques.²⁶ Among them, Xu *et al.*¹⁶ and Shepard *et al.*¹⁵ have described measurement of thin film piezoelectric properties by the pneumatic pressure method and the wafer flexure technique as previously reported. Both methods measure the effective piezoelectric response of thin films on their substrates. The effective piezoelectric coefficient d_{33} of a piezoelectric film measured by the pneumatic pressure method¹⁶ is determined by introducing high pressure gas to cavities on either side of a film-coated wafer in order to generate a uniaxial stress, and the resulting charge is collected.

d_{33} is then calculated from

$$d_{33} = \frac{Q}{\Delta P A}, \quad (1.1)$$

where Q is the pressure-induced charge collected by the charge integrator, ΔP is the pressure change inside the cavity, and A is the area of the top electrode.

In contrast, the wafer flexure method entails suspending a film-coated wafer over a cavity and oscillating the cavity pressure to flex the wafer. The effective piezoelectric coefficient d_{31} of the films can be determined by the stress-strain relationship using plate theory.²⁷ The in-plane stress (σ_l) of the film at the center point generated by the oscillating pressure (5 Hz) in the cavity is

$$\sigma_l = \frac{E\varepsilon}{1-\nu}. \quad (2.1)$$

Assuming that the biaxial stress σ_{tot} is the same in two perpendicular directions on the sample surface

$$\sigma_{\text{tot}} = \sigma_1 + \sigma_2, \quad (2.2)$$

where E is the Young's modulus of the film, ν is Poisson's ratio of the sample ($\nu \sim 1/3$), and ε is the in-plane strain in the sample mounted on the stress rig measured with a strain gauge. The strain gauge was attached to the center of the sample surface using superglue.

d_{31} is thus given by

$$d_{31} = \frac{Q}{2\sigma_1 A}. \quad (2.3)$$

As shown in Eqs. (2.1)–(2.3), this measurement technique requires information about the film elastic modulus. If this information is known, d_{31} values of the films can be measured quickly, even using a small piece of the sample.

The d_{33} coefficients of 1.5 μm thick {100}- and {111}-oriented films were characterized by the pneumatic pressure method.¹⁶ Both films were poled at 85 kV/cm for 30 min and the generated charges were measured using a 10^{-8} F integrating capacitor. For the {100}- and {111}-oriented PMN-PT films, the values of d_{33} measured were 170–183 and 90–100 pC/N, respectively. This measurement technique does not require knowledge of the film or substrate elastic modulus as shown in Eq. (1.1). For the same films poled under the same conditions, the values of d_{31} of the {100}- and {111}-oriented PMN-PT films were –95––100 and –55––60 pC/N, respectively. These values were calculated

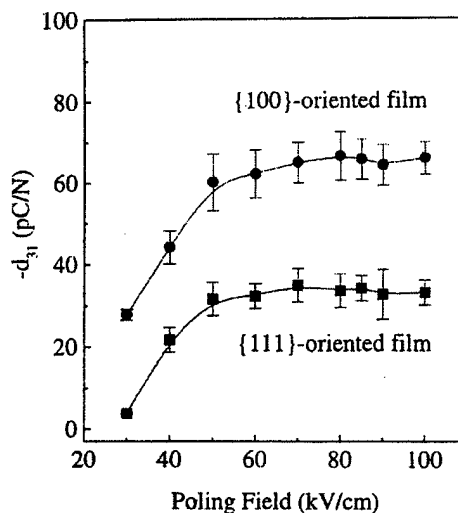


FIG. 8. Poling curves for the {100}- and {111}-oriented PMN-PT films with various poling fields for 5 min.

assuming a Young's modulus for the films of 35 GPa, the number reported by Park and Shrout²⁸ for the same composition of single crystalline PMN-PT (70/30) oriented along (001).

In general, in many perovskite ferroelectrics, including piezoelectric PMN-PT ceramics and 0.955Pb(Zn_{1/3}Nb_{2/3})O₃–0.045PbTiO₃ single crystals, $d_{31} \sim -0.43d_{33}$.^{29–31} There are some literature sources which give different d_{33}/d_{31} ratios for PMN-PT, particularly when samples prepared by different groups or poled under different conditions are compared.³² However, for a given sample, this ratio is a good approximation. This is supported by the observation of low hydrostatic d coefficients $d_h = d_{33} + 2d_{31}$ for PMN-PT ceramics near the morphotropic phase boundary²⁹ (similar low values are observed in (001) piezoelectric single crystals of lead zinc niobate–lead titanate).³³ That is, for a single sample, d_{33} is close to $-2d_{31}$. Thus, the available data for a (001) oriented single crystal relaxor ferroelectric-PbTiO₃ solid solution was taken as a first approximation (i.e., $d_{31} \sim -0.43d_{33}$). Assuming that this value is appropriate for thin films, the actual d_{31} values of the {100} and {111}-oriented PMN-PT films should be –73 to –78 and –39 to –43 pC/N, respectively. This suggests that the appropriate Young's moduli to use in the d_{31} calculations are ~44 and ~49 GPa for {100} and {111} films. That is, for polycrystalline PMN-PT films, it may be appropriate to use a Young's modulus of 45 GPa to calculate d_{31} values by the wafer flexure technique.

The d_{31} coefficients of 1.2 μm thick {100}- and {111}-oriented films by the wafer flexure technique were characterized as a function of poling field. Figure 8 show the poling curves for the PMN-PT films. These values were calculated assuming a Young's modulus for the {100}- and {111}-oriented films of 44 and 49 GPa, respectively, which were the values experimentally determined by analyzing the d_{33} and d_{31} values obtained using the pneumatic pressure and wafer flexure technique, as mentioned above.

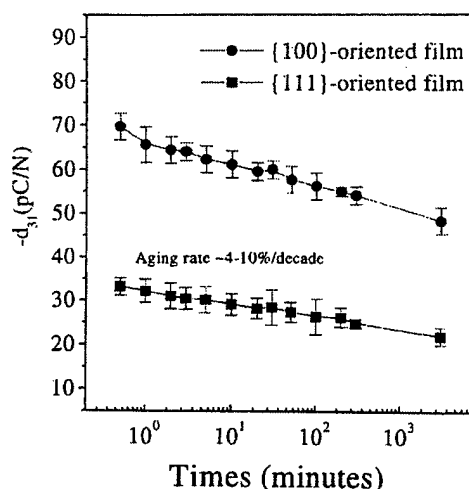


FIG. 9. Aging curves for {100}- and {111}-oriented PMN-PT films.

The measured phase angle θ corresponds to the phase of the piezoelectric response (charge or current) with respect to the pressure oscillation. The poling direction is therefore differentiated by the measurement phase angle. In the case of {100}-oriented samples, the direction of the preferred orientation is from the film/substrate interface to the surface. Therefore, d_{31} was characterized after poling with the top electrode negative. As shown in Fig. 8, the piezoelectric coefficient of the films increases in a logarithmic fashion with poling field. For all films tested here the piezoelectric coefficients were largely saturated after poling at 60–80 kV/cm. For a {100}-oriented film 1.2 μm thick, a larger piezoelectric coefficient ($-d_{31} \sim 69 \text{ pC/N}$) was obtained relative to those of {111}-oriented films ($-d_{31} \sim 35 \text{ pC/N}$) at a poling field of 85 kV/cm for 5 min. Since the typical d_{31} value of a 1 μm thick PZT (52/48) film was around -40 pC/N , even the lower PMN-PT is still comparable to that for sol-gel PZT films of the same thickness.¹⁵ This result also supports that the idea of crystallographic engineering is applicable to thin films as well as bulk crystals. That is, the differences in properties between {100} and {111} fiber textured samples suggest that the high piezoelectric coefficients reported here are not due simply to the lower T_{max} of PMN-PT relative to PZT.

The film thickness also affected the dielectric and piezoelectric properties of the PMN-PT films. Thicker layers had larger remanent polarizations and lower coercive fields. In addition, the piezoelectric coefficients of {100}-oriented film increased more rapidly with thickness compared to those of {111}-oriented films.

Figure 9 shows the different aging behavior of {100}- and {111}-oriented films. There were no significant discrepancies in aging rate between {100}- and {111}-oriented films. The aging rate of the {100}- and {111}-oriented films is about 4%–10% per decade. However, the aging rate is considerable when compared to the nearly 0% reported for epitaxial {100} PMN-PT films on LaAlO_3 which had strongly imprinted hysteresis loops. It is believed that the aging rates observed

here are due to progressive depoling of the films, as has previously been reported for PZT films.³⁴

CONCLUSIONS

The crystalline characteristics and dielectric properties of {100} fiber textured PMN-PT films grown on Pt (111)-coated substrates by sol-gel are described. It was shown that the introduction of a perovskite PT thin film as a buffer layer assists the nucleation of {111} textured PMN-PT films. The dielectric constant for {100}-oriented films is, in general, higher than those of {111}-oriented films. However, {100}-oriented films showed lower remanent polarizations in comparison with {111}-oriented films. Both of these observations are consistent with a substantial in-plane tensile stress in the ferroelectric films. The d_{31} coefficients of highly {100}-oriented PMN-PT films were found to range from -28 to -69 pC/N with increasing poling field and saturated at fields of 60–80 kV/cm. The {100}-oriented PMN-PT films showed larger piezoelectric coefficients than {111}-oriented films. The aging rate of piezoelectric coefficients $-d_{31}$ for the {100}- and {111}-oriented PMN-PT films were about 4%–10%/decade. Based on the results of d_{33} measurements of the PMN-PT films with different orientation, Young's moduli of 44–49 GPa may be used to estimate plausible d_{31} values of PMN-PT (70/30) films.

ACKNOWLEDGMENTS

The authors gratefully acknowledge support from the Office of Naval Research for this work. The authors would like to thank Dr. Seung-Eek Park for his helpful discussion on the anisotropic properties of single crystals.

- ¹J. F. Scott and C. A. Paz de Araujo, *Science* **246**, 1400 (1989).
- ²D. Dimos, S. J. Lockwood, and R. W. Schwartz, *IEEE Trans. Compon. Packag. Manuf. Technol.*, Part A **A18**, 174 (1995).
- ³H. D. Chen, K. R. Udayakumar, C. J. Gaskey, and L. E. Cross, *Appl. Phys. Lett.* **67**, 3411 (1995).
- ⁴S. Watanabe and T. Fujii, *Rev. Sci. Instrum.* **67**, 3898 (1996).
- ⁵C.-R. Cho, L.-F. Francis, and M. Jang, *Jpn. J. Appl. Phys.*, Part 2 **38**, L751 (1999).
- ⁶X.-H. Du, J. Zheng, U. Belegunda, and K. Uchino, *Appl. Phys. Lett.* **72**, 2421 (1998).
- ⁷K. Aoki, Y. Fukuda, K. Numata, and A. Nishimura, *Jpn. J. Appl. Phys.*, Part 1 **33**, 5155 (1994).
- ⁸J. H. Park, D. H. Kang, and K. H. Yoon, *J. Am. Ceram. Soc.* **82**, 2116 (1999).
- ⁹F. Xu, Ph.D. thesis, The Pennsylvania State University, 1999.
- ¹⁰S. E. Park and T. R. Shrout, *IEEE Trans. Ultrason. Ferroelectr. Freq. Control* **44**, 140 (1997).
- ¹¹S. E. Park and T. R. Shrout, *J. Appl. Phys.* **82**, 1804 (1997).
- ¹²S. Troler-McKinstry, J. F. Shepard, J. L. Lacey, T. Su, G. Zavala, and J. Fender, *Ferroelectrics* **206–7**, 381 (1998).
- ¹³J.-P. Maria, Ph.D. thesis, The Pennsylvania State University, 1998.
- ¹⁴K. D. Budd, S. K. Dey, and D. A. Payne, *Br. Ceram. Proc.* **36**, 107 (1985).
- ¹⁵J. F. Shepard, Jr., F. Xu, I. Kanno, and S. Troler-McKinstry, *J. Appl. Phys.* **85**, 6711 (1999).
- ¹⁶F. Xu, F. Chu, and S. Troler-McKinstry, *J. Appl. Phys.* **86**, 588 (1999).
- ¹⁷Z. Huang, Q. Zhang, and R. W. Whatmore, *J. Appl. Phys.* **85**, 7355 (1999).
- ¹⁸K. Ishikawa, K. Sakura, D. Fu, and S. Yamada, *Jpn. J. Appl. Phys.*, Part 1 **37**, 5128 (1998).
- ¹⁹E. Cattin, G. Velu, B. Jaber, D. Remiens, and B. Thierry, *Appl. Phys. Lett.* **70**, 1718 (1997).
- ²⁰K. H. Yoon, J. H. Shin, J. H. Park, and D. H. Kang, *J. Appl. Phys.* **83**, 3626 (1998).

- ²¹T. R. Shrout, Z. P. Chang, N. Kim, and S. Markgraf, *Ferroelectr. Lett. Sect.* **12**, 63 (1990).
- ²²J.-P. Maria, W. Hackenberger, and S. Trolrier-McKinstry, *J. Appl. Phys.* **84**, 5147 (1998).
- ²³T. Kumazawa, Y. Kumagai, H. Miura, and M. Kitano, *Appl. Phys. Lett.* **72**, 608 (1998).
- ²⁴J. F. Shepard, Jr., S. Trolrier-McKinstry, and M. A. Hendrickson, The 10th International Symposium on Applications of Ferroelectrics, New Brunswick, NJ, 1996, pp. 161–165.
- ²⁵Z. Kighelman, D. Damjanovic, A. Seifert, L. Sagalowicz, and N. Setter, *Appl. Phys. Lett.* **73**, 2281 (1999).
- ²⁶I. Kanno, S. Fujii, T. Kamada, and R. Takayama, *Appl. Phys. Lett.* **70**, 1378 (1997).
- ²⁷S. Timoshenko and S. Woinowsky-Krieger, *Theory of Plates and Shell* (McGraw-Hill, New York, 1959).
- ²⁸S. E. Park and T. R. Shrout, U.S. Navy Workshop on Acoustic Transduction Materials and Devices, University Park, PA, 13–15 April 1999.
- ²⁹Edo Electroceramics Piezoelectric Products catalog. Data for EC-98. <http://www.edoceramic.com>
- ³⁰S.-F. Liu, S.-E. Park, T. R. Shrout, and L. E. Cross, *J. Appl. Phys.* **85**, 2810 (1999).
- ³¹B. Jaffe, W. R. Cook, Jr., and H. Jaffe, *Piezoelectric Crystals* (Academic, New York, 1971).
- ³²Landolt-Bornstein III/18, *Elastic, Piezoelectric, and Related Constants of Crystals* (Springer, New York, 1984).
- ³³S.-F. Liu, S.-E. Park, T. R. Shrout, and L. E. Cross, *J. Appl. Phys.* **85**, 2810 (1999).
- ³⁴A. L. Kholkin, A. K. Tagantsev, E. L. Colla, D. V. Taylor, and N. Setter, *Integr. Ferroelectr.* **15**, 317 (1997).

APPENDIX 89

Dielectric and Piezoelectric Properties of PZT 52/48 Thick Films with (100) and Random Crystallographic Orientation

Q. F. Zhou, E. Hong, R. Wolf, and S. Trolier-McKinstry

Materials Research Laboratory, The Pennsylvania State University,
University Park, PA 16802

ABSTRACT

Ferroelectric $\text{Pb}(\text{Zr}_{1-x}\text{Ti}_x)\text{O}_3$ (PZT) films have been extensively studied for active components in microelectromechanical systems. The properties of PZT films depend on many parameters, including composition, orientation, film thickness and microstructure. In this study, the effects of crystallographic orientation on the dielectric and transverse piezoelectric properties of $\text{Pb}(\text{Zr}_{0.52}\text{Ti}_{0.48})\text{O}_3$ (PZT 52/48) films are reported. Crack free random and highly (100) oriented PZT(52/48) films up to $\sim 7 \mu\text{m}$ thick were deposited using a sol-gel process on Pt(111)/Ti/SiO₂/Si and Pt(100)/SiO₂/Si substrates, respectively. The dielectric permittivity (at 1kHz) for the (100) oriented films was 980-1000, and for the random films ~ 930 -950. In both cases, $\tan\delta$ was less than 0.03. The remanent polarization ($\sim 30 \mu\text{C}/\text{cm}^2$) of random PZT films was larger than that of (100) oriented PZT films. The transverse piezoelectric coefficient ($d_{31(\text{eff})}$) of PZT films was measured by the wafer flexure method. The $d_{31(\text{eff})}$ coefficient of random PZT thick films ($-80\text{pC}/\text{N}$) was larger than that of (100) oriented films ($-60\text{pC}/\text{N}$) when poled at 80 kV/cm for 15 min.

INTRODUCTION

Recently, there has been an increasing interest in ferroelectric lead zirconate titanate (PZT) films because of their wide range of applications in microelectronics, microelectromechanical systems (MEMS) and ultrasonic imaging. Potential applications include membrane sensors [1], micro-accelerometers [2] and micro-motors [3]. In general, these devices are based on films of thicknesses less than 1 μm . However, applications based on piezoelectric films are not limited to the realm of microdevices, and some potential applications require more thick films that have large piezoelectric coefficients and high energy densities. Therefore, PZT thick films are of interest.

There are a number of groups which have successfully fabricated PZT system thick films. Tsuzuki et al. [4] prepared PLZT thick films by multiple electrophoretic deposition and sintering processing. Sayer et al. [5] have reported the thick PZT ceramic coating using a sol-gel based ceramic-ceramic 0-3 composites. Cross et al. [6] prepared the PZT thick films by modified sol-gel process using acetic acid route. Milne et al. [7] also fabricated the PZT thick films using titanium diisopropoxide biacetylacetonate as raw materials. However, preparing thick uniform PZT films with large area by the sol-gel technique is still challenging due to cracking that results from large stresses between the substrate and film.

In this paper, crack-free sol-gel PZT thick films with the morphotropic phase boundary (MPB) composition of $\text{Pb}(\text{Zr}_{0.52}\text{Ti}_{0.48})\text{O}_3$ (PZT 52/48) were deposited on Pt(111)/Ti/SiO₂ and Pt(100)/SiO₂/Si substrates, respectively. The dielectric and piezoelectric properties of PZT films with different orientation were investigated.

EXPERIMENTAL PROCEDURES

The sol-gel PZT solutions were prepared using 2-methoxyethanol (2-MOE) as the solvent. Initially, lead acetate trihydrate was dissolved in 2-methoxyethanol at 80 °C, then refluxed at 115 °C for 1 hr under Ar. The water of hydration was distilled at 115 °C under vacuum (~130 mbar). Appropriate quantities of zirconium n-propoxide and titanium iso-propoxide were stirred in 2-MOE at 25°C. Upon completion of the dehydration step, the rotary flask containing the lead acetate complex was cooled well below 100°C and the zirconium and titanium precursors were added. This mixture was refluxed for 2 hr at 120°C. To compensate for lead volatilization during film heat treatments, 20mol% excess lead was added to the solutions.

Following the reflux step, the solution was distilled at 120°C again with the aid of vacuum. The mixture was allowed to cool to room temperature, and 22.5 vol% acetylacetonate (2,4 pentanedione) was introduced while stirring, which acted as a chelating agent to prevent solution hydrolysis in the presence of atmospheric moisture. 2-MOE was added to achieve a final solution with 0.75 molar concentration.

The solution was deposited onto platinized silicon substrates [Pt(111)/Ti/SiO₂/Si, Nova Electronics; Pt(100)/SiO₂/Si, Inostek Inc.] by spin-coating at 1500 rpm for 30 seconds on a photoresist spinner. After deposition, each layer was subjected to a two-stage pyrolysis sequence to drive out solvent and decompose organic compounds. A 1 minute heat treatment at 300°C was immediately followed by one at 450°C (1 minute). The amorphous layer was then crystallized to phase-pure perovskite at 700°C for 30 seconds using rapid thermal annealing (RTA). Every layer thickness is about 0.2 μm. Thicker PZT films were fabricated by repeating this procedure to achieve the desired film thickness [8]. Platinum top electrodes with diameters of 1.5 mm were sputter deposited and then annealed at 700°C for 20 seconds by RTA prior to electrical characterization.

The structure of the PZT films was examined using a Scintag x-ray diffractometer (XRD) with Ni filtered CuKα radiation. The x-ray diffraction (XRD) patterns were recorded at a rate of 1°/min in the 2θ range of 20°-60°. The thickness of the films was measured using a surface profiler (Tencor Instruments). The morphology of the films was observed using a scanning electron microscope (SEM; Hitachi, S-3500N) and atomic force microscope (AFM, Digital Instruments Nanoscope). The dielectric permittivity was measured using an impedance analyzer (HP4194A, Hewlett-Packard) with an oscillation amplitude of 30 mV. High field hysteresis properties were characterized using a RT66A (Radiant Technology, Albuquerque, NM) ferroelectric test system. The transverse piezoelectric (d_{31}) coefficients of the films were characterized using a modification of wafer flexure method described previously [9]. The aging rate of the d_{31} coefficients was measured after the poling field was removed.

RESULTS AND DISCUSSION

Figure 1 shows the XRD patterns of 0.45 μm to 7 μm PZT thick films deposited on (111)-Pt(120nm)/Ti(20nm)/Si(200nm)/ substrates heated at 700°C for 30 seconds. It can be seen that highly (111) preferred orientation occurs in PZT films with thicknesses less than 1.2 μm as shown in figure 1(a) and 1(b). At these thicknesses, orientation is strongly affected by the (111)

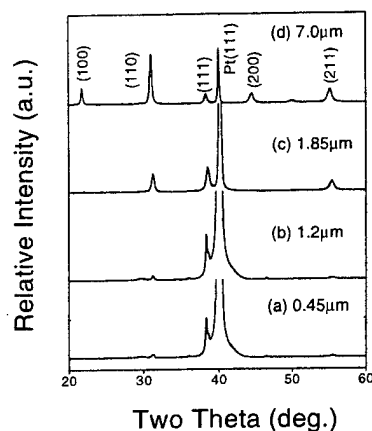


Figure 1. XRD patterns of the sol-gel derived PZT 52/48 films deposited on Pt(111)/Ti/SiO₂/Si substrates with different thickness (a) 0.45 μm , (b) 1.2 μm , (c) 1.85 μm and (d) 7.0 μm

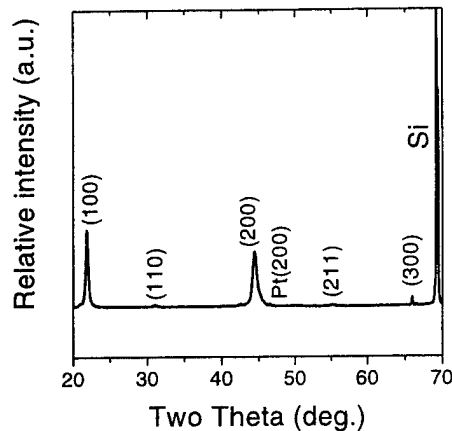
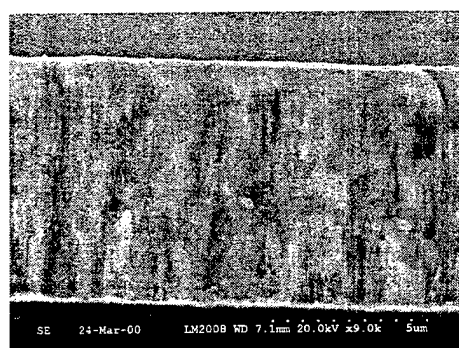


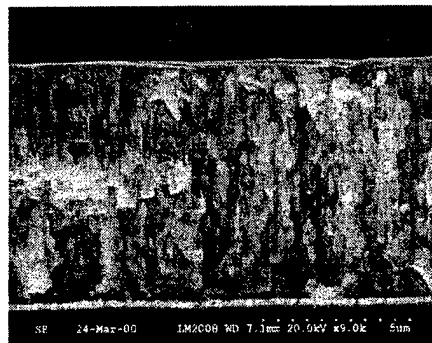
Figure 2. XRD patterns of sol-gel derived 7.3 μm PZT 52/48 film deposited on Pt(100)/SiO₂/Si substrates

Pt/Ti electrodes. However, the intensity of the (111) perovskite peak decreases with increasing thickness from 1.8 μm to 7.0 μm as shown in figure 1(c) and 1(d). That is, for this processing route, on (111)-oriented electrodes PZT films approach random orientation with increasing thickness. This may come from a mismatch between every layer during sol-gel deposition. Figure 2 shows the XRD patterns of 7.3 μm PZT thick films deposited on (100)-Pt(150nm)/SiO₂(300)nm/Si substrates. These films have highly (100) preferred orientation, suggesting nucleation dominated by the oriented Pt electrode. Only very small (110) and (211) peaks were observed in figure 2.

Figure 3 shows SEM pictures of random and (100) oriented PZT films. The cross sectional view of the films shows that the thickness was over 7 μm , every layer corresponds to one crystallization step, and grains are approximately equi-axed. Figure 4 shows AFM surface images of random and (100) oriented PZT films. From figure 4(a) it is seen that the (100)



(a)



(b)

Figure 3. SEM cross sectional views for sol-gel derived PZT films (a) (100) oriented film and (b) random film

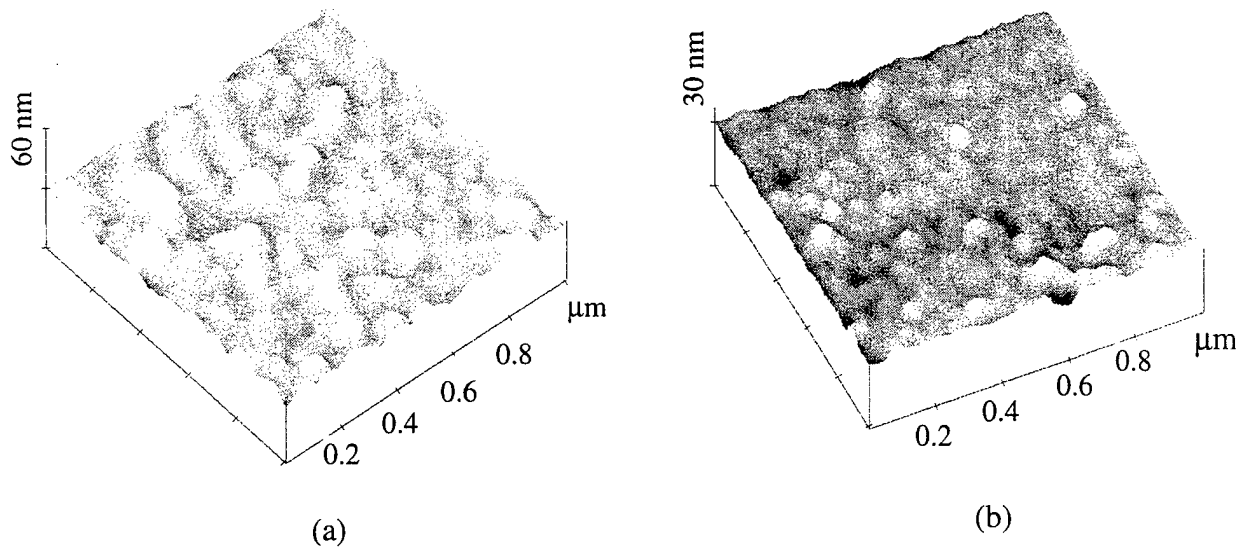


Figure 4. AFM images of surface sol-gel derived PZT (a) (100) oriented film and (b) random film

oriented film consisted of large grains with grain sizes ranging from 100 nm to 130 nm. Random PZT films consisted of uniform small grains as shown in figure 4(b), an average grain size of about 80 nm. The difference in grain size may stem either from the difference in the nucleation rate of films for the two different electrode orientations or from differences in the electrode grain sizes.

The frequency dependence of dielectric permittivity at room temperature for the random and (100)-oriented films is shown in figure 5(a) and (b). It can be seen that the dielectric constant (~ 985) of the (100) oriented film at 1 kHz was slightly higher than that (~ 950) of the random film. In both cases, the dielectric loss of the films was below 0.03 at 1 kHz (room temperature).

The ferroelectric hysteresis loops of random and (100) oriented PZT 52/48 thick films are

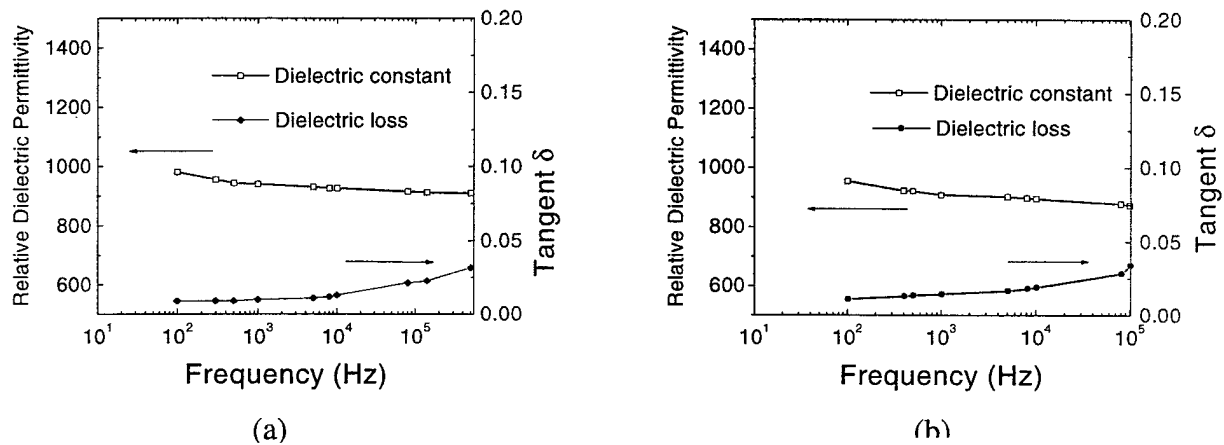


Figure 5. Frequency dependence of dielectric permittivity and loss at room temperature for PZT films (a)(100) oriented and (b) random films

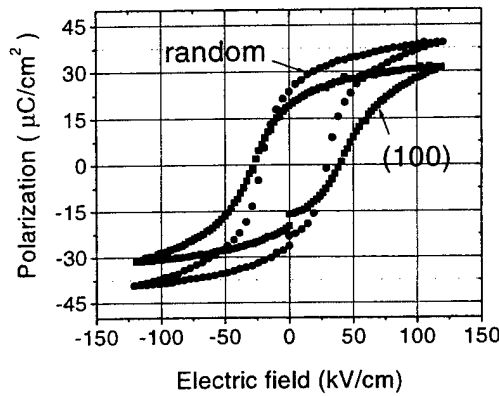


Figure 6. Polarization as a function of electric field for random and (100) oriented PZT 52/48 thick films

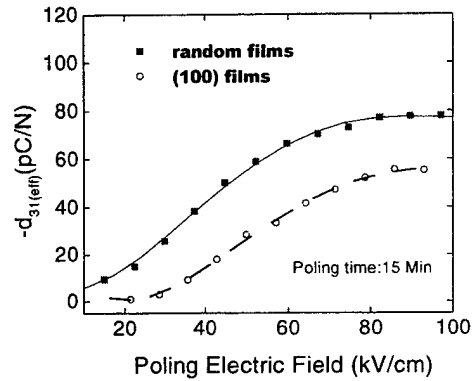


Figure 7. The d_{31} coefficient of random and (100) oriented PZT thick film with different poling electric field for 15 Min

shown in figure 6. The remanent polarization (P_r) in the random films is about $30 \mu\text{C}/\text{cm}^2$ for $E_{\text{max}} = 180 \text{ kV}/\text{cm}$, and the saturation polarization (P_s) is over $40 \mu\text{C}/\text{cm}^2$. When compared for the same field level the P_r and P_{max} of random PZT films are larger than those of (100) oriented PZT films shown in figure 6.

The d_{31} coefficients of the films were characterized using a modification of the wafer flexure technique [10]. The effective piezoelectric coefficient $d_{31(\text{eff})}$ of the films can be determined by the stress-strain relationship using plate theory [11]. The in-plane stress (σ_1) of the films generated by a pressure difference in the cavity is,

$$\sigma_1 = E \varepsilon / 1 - \nu, \quad (1)$$

where E is the Young's modulus of the film (Young's modulus of PZT films is 101 GPa), ν the Poisson's ratio of the sample ($\sim 1/3$), and ε the in-plane strain in the sample mounted on the stress rig measured with a strain gauge.

Supposing that the biaxial stress (σ_{tot}) is the same for the perpendicular direction on the sample surface,

$$\sigma = \sigma_1 + \sigma_2, \quad (2)$$

$d_{31(\text{eff})}$ can be obtained by

$$d_{31(\text{eff})} = Q / 2\sigma_1 A, \quad (3)$$

where Q is the charge, and A the area of top electrode. Figure 7 shows the $d_{31(\text{eff})}$ coefficient of random and (100) oriented PZT thick film with different poling electric fields (the poling time was 15 minutes). The $d_{31(\text{eff})}$ increased as the poling field approached the coercive field of the film, and then saturated at a poling field of about three times the coercive field. The random PZT films had a larger piezoelectric coefficient ($-80 \text{ pC}/\text{N}$) compared to the (100) oriented films ($-60 \text{ pC}/\text{N}$). It is suggested that this is due to the larger intrinsic contribution for piezoelectric properties in random PZT films which showed larger remanent polarizations than (100) oriented films (see figure 6).

The aging rates of the transverse piezoelectric coefficient for random and (100)- oriented PZT films were also measured using the wafer flexure technique. The $d_{31(\text{eff})}$ coefficients were monitored at regular intervals after poling at 80 kV/cm for 15 minutes, and normalized $d_{31(\text{eff})}$ were plotted versus the logarithm of time. The aging rates were then obtained from the slopes. The aging rate of the random PZT film was about 4.2% / decade, and (100) oriented films was about 9% / decade. In addition, it was found that the $d_{31(\text{eff})}$ coefficients is different when top electrode connect positive or negative during poling, detail results will be reported.

CONCLUSIONS

Random and (100) oriented PZT (52/48) films up to $\sim 7 \mu\text{m}$ thick were fabricated using a modified sol-gel process on Pt (111)/Ti/SiO₂/Si and Pt (100)/SiO₂/Si substrates, respectively. The dielectric permittivity (at 1kHz) of the (100)-oriented films was slightly higher than that of the random films. In both cases, the dielectric loss was less than 0.03. However, the remanent polarization of random PZT films was larger than that of (100) oriented PZT films. The transverse piezoelectric coefficient ($d_{31(\text{eff})}$) of random PZT thick films was also larger than that of (100)-oriented films when poled at 80 kV/cm for 15 min. The aging rates of PZT films was in the range of 4-9% per decade.

ACKNOWLEDGMENTS

Support from the office of Naval Research is gratefully acknowledged.

REFERENCES

1. D. L. Polla, SPIE, **24**, 3046(1997).
2. K. R. Udayakumayer, J. Chen, K. G. Brooks, L. E. Cross, A. M. Flynn, and D. J. Erlich, Mat. Res. Soc. Sym. Proc. **49**, 243(1991).
3. H. Van Lintel, F. Vander Pohl and S. Boustra, Sensors and Actuators A **153**, 15(1988).
4. S. Sugiyama, A. Takagi and K. Tsuzuki, Jap. J. Appl. Phys., **30**, 2170(1991).
5. D. A. Barrow, T. E. Petroff and M. Sayer, Surface and Coating Technology, **76**, 113(1995).
6. H. D. Chen, K. R. Udayakumar, C. J. Gaskey and L. E. Cross, J. Am. Ceram. Soc., **79**, 2189(1996).
7. R. Kurchania and S.J.Milne, J. Mater. Res., **14**, 1852(1999).
8. Q. F. Zhou, H. L. W. Chan and C. L. Choy, Thin Solid Films, **375**, 95(2000).
9. J. F. Shephard Jr., F. Xu, I. Kanno, and S. Trolier-McKinstry, J. Appl. Phys., **85**, 6711(1999).
10. J. F. Shepard, Jr., P. J. Moses, and S. S.Trolier-McKinstry, Sensors and Actuators A **71**, 133(1998).
11. S. Timoshenko and S. Woinowsky-Krieger, Theory of Plates and Shells (McGraw Hill Inc, New York 1959).

APPENDIX 90

Wet-etch Patterning of Lead Zirconate Titanate (PZT) Thick Films for Microelectromechanical Systems (MEMS) Applications

L.-P. Wang, R. Wolf, Q. Zhou, S. Trolrier-McKinstry, and R. J. Davis
The Penn State University, University Park, PA16802

ABSTRACT

Lead Zirconate Titanate (PZT) films are very attractive for Microelectro-mechanical-systems (MEMS) applications because of their high piezoelectric coefficients and good electromechanical coupling. In this work, wet-etch patterning of sol-gel lead zirconate titanate (PZT) films for MEMS applications, typically having films thicknesses ranging from 2 to 10 microns, was studied. A two-step wet-etch process was developed. In the first step, 10:1 buffered HF was used to remove the majority of the film at room temperature. Then a solution of $2\text{HCl}:\text{H}_2\text{O}$ at 45°C was used to remove residues from the first step. This enabled successful patterning of PZT films up to 8 microns thick. A high etch rate ($0.133\text{ }\mu\text{m}/\text{min}$), extremely high selectivity with respect to photoresist, and limited undercutting (2:1 lateral:thickness) were obtained. X-ray diffraction (XRD) and scanning electron microscopy (SEM) were used to analyze the residue produced in the first etching step and examine the etching profile, respectively. The residues are primarily metal fluorides. In addition, properties of etched films were examined by dielectric and polarization electric-field (PE) hysteresis measurements. The tested results show good properties of processed PZT films; relative permittivity is 1000, dielectric loss is 1.6%, remanent polarization (P_r) is $24\text{ }\mu\text{C}/\text{cm}^2$, and coercive field (E_c) is 42.1 kV/cm. They were the same as those of unpatterned films of the same thickness.

INTRODUCTION

Microelectromechanical systems (MEMS), a technology which permits the integration of micromachined mechanical structures with integrated circuits (IC), has been a growing area of research in the last two decades [1,2]. MEMS have a wide range of applications including automotive, industrial, biomedical, and information processing [3,4]. Ferroelectric lead zirconate titanate (PZT) films have been utilized for a variety of applications including microsensors, microactuators, and ferroelectric random access memory (FRAM) [5]. Their high piezoelectric coefficients ($d_{33} > 100\text{pC}/\text{N}$) and electromechanical coupling ($k^2 \sim 12\%$) are especially attractive for MEMS sensors and actuators [6]. For these applications, thicker PZT films are usually preferred since the piezoelectric response increases with increasing film thickness [7]. Therefore, patterning techniques for thick PZT films on the micron scale have to be developed.

Reactive ion etching (RIE) using capacitive [8], inductive [9], or electron cyclotron resonance (ECR) plasmas [10], has been utilized to pattern PZT films. These studies were driven primarily by ferroelectric random access memory (FRAM) applications where PZT films are used as capacitors. The film thickness used in these applications generally does not exceed 250nm. It has been reported that it is hard to form volatile species with etching gas at room temperature; hence, heating the substrate or increasing ion-bombardment energy is generally required for dry-etch patterning. As a result, the etch rate and selectivity with respect to photoresist developed in the above methods are not suitable to etch PZT films for MEMS

applications which require 2 to 10 μm thick PZT films. In this paper, a chemical route for patterning thick PZT films is described.

EXPERIMENTAL PROCEDURE

Starting with a 4-inch diameter n-type <100> silicon wafer, a $\text{Si}/\text{SiO}_2(800\text{nm})/\text{Ti}(20\text{nm})/\text{Pt}(150\text{nm})$ multilayer structure was used as the substrate to produce a high quality PZT film. SiO_2 was thermally grown and served as an electrical isolation layer. Ti and Pt were then sputtered deposited. Pt serves as the bottom electrode because of its low resistivity and good stability against oxidation and reaction with PZT during the subsequent high temperature processes [11]. However, its adhesion to SiO_2 is poor; therefore, a thin Ti layer was used as an adhesion layer. Thick PZT films were then deposited using a sol-gel method described elsewhere [12]. Cr and Au were deposited as the top electrode using electron-gun and thermal evaporation respectively. After film deposition, photolithography was employed to define etching patterns using Shipley 1813 photoresist. A Karl Suss MA6 contact aligner was used to provide UV radiation and alignment between photomask and wafer. After photolithography, samples were etched with different recipes.

RESULTS AND DISCUSSION

Etching of PZT Thick Films

Three wet etching recipes, 1) 0.34%HF:5%HCl:94.66% H_2O at room temperature; 2) HF at room temperature; and 3) HCl at 45°C, were first investigated to pattern the thick PZT films. However, there were some problems with each etchant. For the first recipe, residues on the etched area could not be removed even for a long etching time (30minutes); consequently, photoresist was delaminated from the PZT films after this long etching time. The whitish residues were clearly observed after drying the sample. SEM (see Figure 1) shows an example of residues on the etched area. Adjusting the ratio of HF and HCl, did not lead to markedly different results.

With the second recipe, residue formation was still a problem. Furthermore, the photoresist delaminated from the PZT films after just 10 minutes. For the third recipe, residue was not a problem. However, patterns with a feature size smaller than 50 μm could not be patterned, since HCl quickly etched the PZT films by dissolving material along the grains instead of etching them [13], which resulted in severe undercutting. This makes the etching process difficult to control. Table 1 summarizes the results of the above etching recipes.

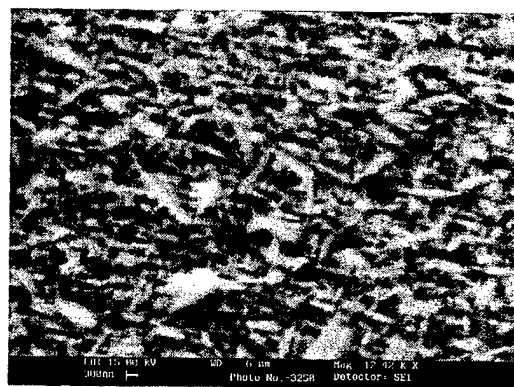


Figure 1. SEM micrograph shows residues on the etched area after a 4 μm PZT film was etched in 0.34%HF:5%HCl:94.66% H_2O for 40 minutes

Table 1. Comparison of different etching recipes for PZT thick films

Etching recipe	Etch Rate	Resist	Undercut (lateral to thickness)	Residue
0.34%HF 5%HCl 94.66%H ₂ O at 25°C	~0.2μm/min*	peeled after 30 minutes	3:1*	whitish residue
HF 25° C	~0.15μm/min*	peeled after 10 minutes	2:1*	whitish residue
HCl at 45° C	1 μm/min	does not provide good protection	10:1	clean surface
*Etch rate and undercutting are approximate since the end point of etching is difficult to define with the formation of residues				

Residue Analysis

From the above results, it is apparent that residue formation resulted from use of HF-based solutions. These residues were examined by X-ray diffraction (XRD). Results (see Figure 2) show that they primarily consist of the metal fluorides, $\text{Pb}_{0.85}\text{Zr}_{0.15}\text{F}_{2.3}$ and $\text{Pb}_5\text{ZrF}_{14}$, which have a very low solubility in the etching solution. It was found that these residues can be quickly removed by HCl in a short time (~30 seconds). Fig. 3 shows that after a brief HCl dip, only PZT peaks were detected (see Figure 3) in the XRD patterns, and no residue was observed.

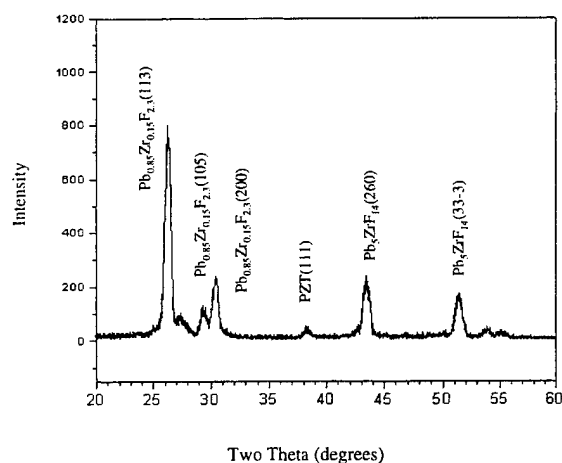


Figure 2. XRD shows residues primarily consist of metal fluorides; the sample were etched with HF-based solutions

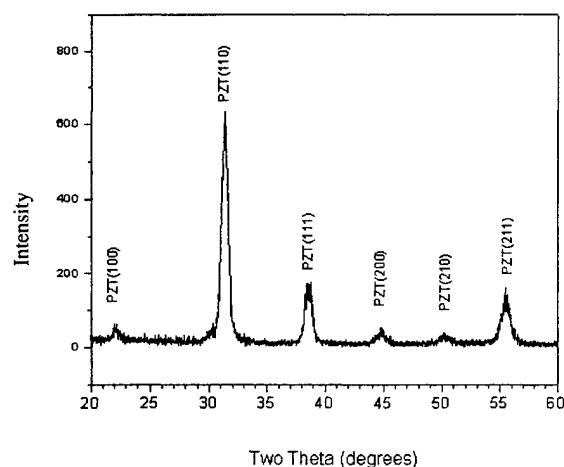


Figure 3. XRD pattern showing no residue on a sample which was incompletely etched in HF and then quickly dipped in HCl

Two-step Etching Process

From the above results, no single etching step was found that can provide a residue-free surface, good selectivity, and limited undercutting for thick film PZT patterning. Consequently, a two-step etching process was developed for this work. The procedures are summarized in Table 2. A 10:1 buffered oxide etch (BOE, which is $10\text{HN}_4\text{F}:1\text{HF}$) was used in the first etch step to remove most of the material. Here BOE is preferred rather than HF, because the photoresist delaminates from PZT films in straight HF after relatively longer etching times (~ 15 minutes for $2\mu\text{m}$ films). As stated earlier, after rinsing the sample with water and drying with a nitrogen gun, whitish residues on the etched area were observed. These residues resulted in a root mean square surface roughness of around $0.3\mu\text{m}$ (RMS). A second etch step was used to remove the residues in $2\text{HCl}:1\text{H}_2\text{O}$ solution for 30 seconds at an elevated temperature (45°C). The etching time needs to be kept short, since this can minimize any further undercutting. Using this two-step process, a cleaner etched surface and better pattern transfer were obtained, as shown in Figure 4. Figure 5 shows an etched profile. In addition, the etched surface was examined by XRD and no residue was found (see Figure 6). The etching was successfully stopped at the Pt bottom electrode.

Table 2. Two-step etching process for thick PZT film patterning

Step	Process	Remark
1	BOE (10:1) etching at room temperature	rate: $0.133(\mu\text{m}/\text{min})$
	DI water rinsing and nitrogen gun drying	whitish residues on the etched area
2	$2\text{HCl}:\text{H}_2\text{O}$ at 45°C	time: 30 second
	DI water rinsing and nitrogen gun drying	clean surface

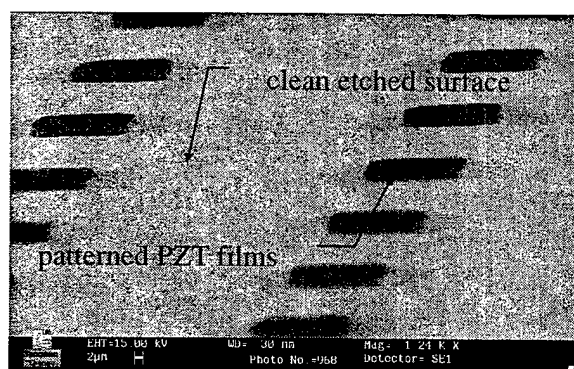


Figure 4. SEM micrograph shows well patterned PZT films and clean etched surface

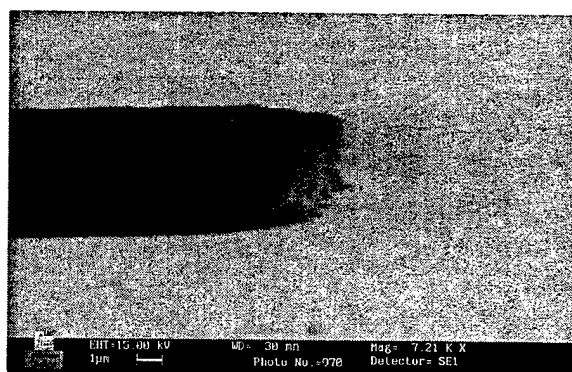


Figure 5. Etched profile of $2\mu\text{m}$ PZT films from lateral view

Since wet etching process is isotropic, lateral etching cannot be avoided. One way to describe the degree of undercutting is the ratio of lateral to thickness etching. To determine this, the size of an etched pattern after stripping the photoresist was measured by microscopy and compared to the original photomask size. A ratio of 2 to 1 lateral to thickness undercutting was measured. The second etch step contributed half of the overall undercutting even with a short etching time because HCl quickly attacked the PZT film from the sidewall. For most MEMS devices, 2:1 undercutting is acceptable since the feature size in MEMS is relatively larger than in microelectronics.

Characterization of Etched Films

Etched PZT films were characterized by dielectric and polarization electric-field (P-E) hysteresis loop measurements to examine any effect of the etching process. The thickness of the PZT films was first measured using a surface profilometer (Tencor Instrument Alpha step). The relative permittivity and dielectric loss of etched PZT films were measured using a Hewlett Packard 4274 multi-frequency LCR meter. The testing frequency was 1kHz and the electrical field was 0.5 kV/cm. Results show that the average relative permittivity is 1000 with a standard deviation of 50, and the average dielectric loss is 1.6% with a standard deviation of 0.15% across a 4" wafer (see Figure 7). The P-E hysteresis loop was measured by a Radiant Technologies RT66A ferroelectric tester. The measurement frequency was 30 Hz and the maximum electrical field was 500 kV/cm. With this measurement, remanent polarization (P_r) and coercive field (E_c) can be obtained. Figure 8 shows the average P-E hysteresis loop across a 4" wafer. The average P_r is $24 \mu\text{C}/\text{cm}^2$ with a standard deviation of $2.2 \mu\text{C}/\text{cm}^2$, and the average E_c is 42.1 kV/cm with a standard deviation of 3.7 kV/cm (see Figure 9). All tested results show good properties of etched PZT films. The observed properties were the same as those of unpatterned films of the same thickness.

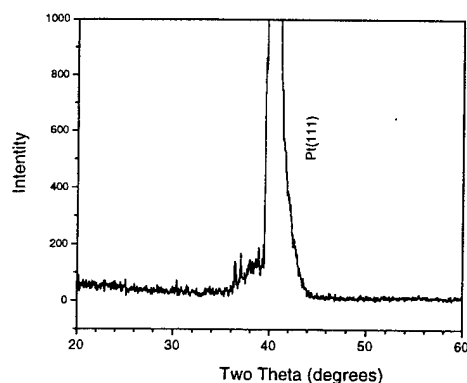


Figure 6. Etched surface was examined by XRD and no residue was found; Pt is the bottom electrode

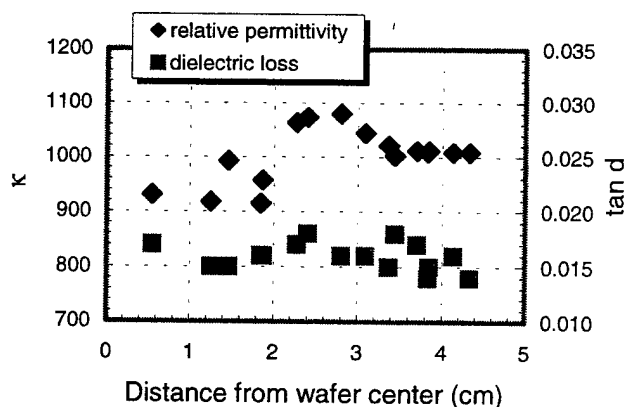


Figure 7. Permittivity and dielectric loss of etched $5.74 \mu\text{m}$ PZT films across a 4" wafer

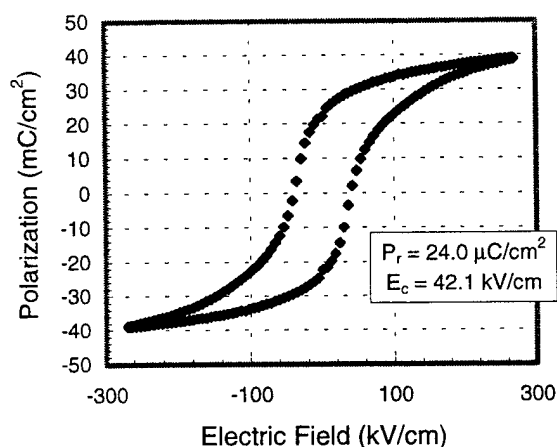


Figure 8. P-E hysteresis loop of etched 5.74 μm PZT films

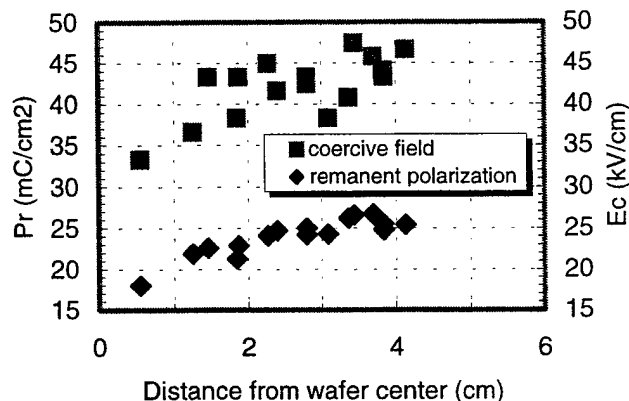


Figure 9. Coercive field and remanent polarization of etched 5.74 μm PZT films

CONCLUSIONS

A two-step etching process was demonstrated to pattern thick PZT films effectively. In the first step, 10:1 buffered HF was used to remove the majority of the film at room temperature. However, etching thick PZT films using HF-based solutions forms metal-fluoride residues, which have a low solubility. Therefore, a second etching step, 2HCl:H₂O at 45° C, was used to remove residues. A high etch rate (0.133 $\mu\text{m}/\text{min}$), extremely high selectivity with respect to photoresist, and limited undercutting (2:1 lateral to thickness) were obtained. Furthermore, no adverse effect on the properties of etched films were found in permittivity, dielectric loss, and P-E hysteresis loop measurements.

REFERENCES

1. K. Najafi, *VLSI Circuits, Digest of Technical Papers*, 6 (2000).
2. M. Pottenger, B. Eyre, E. Kruglick, and G. Lin, *Solid State Technology*, **40** (9), 89, (1997).
3. D. S. Eddy and D. R. Sparks, *Proceedings of The IEEE*, **86** (8), 9 (1998).
4. M. Mollendorf, *Proceedings of ASME Aerospace Division*, **52**, 761 (1996).
5. J. T. Evance and R. Wormack, *IEEE J. Solid-State Circuits*, **23**, 1171 (1988).
6. M. Hendrickson, T. Su, S. Trolrier-McKinstry, B. J. Rod, and R. J. Zeto, *10th IEEE International Symposium on Applications of Ferroelectrics, Part 2*, **2**, 683 (1996).
7. Q. M. Zhang, H. Wang, N. Kim, and L. E. Cross, *J. Applied Physics*, **75** (1), 454 (1994).
8. K. Saito, J. H. Choi, T. Fukuda, and M. Ohue, *Jpn. J. Applied Physics*, **31**, 1260 (1992).
9. C. J. Kim, J. K. Lee, C. W. Chung, I. Chung, *Integrated Ferroelectrics Proceedings of Technology*, **16** (1-4), 149 (1997).
10. S. Yokoyama, Y. Ito, K. Ishihara, K. Hamada, S. Ohnishi, J. Kudo, and K. Sakiyama, *Jpn. J. Applied Physics*, **34**, 767 (1995).
11. G. R. Fox, S. Trolrier-McKinstry, and S. B. Krupanidhi, *J. Mater. Res.*, **10** (6), 1508 (1995).
12. Q. F. Zhou, F. Hong, R. Wolf, and S. Trolrier-McKinstry, *Materials Research Society Symposium Proceedings*, 2000 Fall Meeting (in press).
13. S. E. Trolrier, *M.S. Thesis 1987i, The Pennsylvania University* (1987).

MODELING and CHARACTERIZATION

Domain Studies

APPENDIX 91

LETTER TO THE EDITOR

Domain geometry engineering and domain average engineering of ferroics**J Fousek^{1,2}, D B Litvin³ and L E Cross²**¹ Department of Physics and International Centre for Piezoelectric Research, Liberec University of Technology, Liberec, CZ 46117, Czech Republic² Materials Research Laboratory, The Pennsylvania State University, University Park, PA 16802, USA³ Department of Physics, The Pennsylvania State University, Berks Campus, Reading, PA 19610, USA

Received 5 October 2000

Abstract

Multidomain samples of ferroics (ferroelectrics, ferroelastics, and related materials) with *fixed* geometrical distribution of domains can offer new macroscopic properties required for particular applications. Two extreme cases of such applications are defined. In *domain-geometry-engineered* samples of ferroic crystals, the spatial distribution of domains and thus the spatial distribution of tensorial properties is tuned to correspond to the *k*-vectors of applied electric, optical or acoustic fields. For a given wavelength, the size, geometry, and distribution of domains give rise to a qualitatively new kind of response specified by the symmetry of the multidomain system. In *domain-average-engineered* samples of ferroic crystals, the specimen is subdivided into a very large number of domains, representing μ domain states where μ is smaller than the theoretically allowed maximum number, and forming a regular or irregular pattern. Its response to external fields is roughly described by tensorial properties averaged over all of the domain states involved. The effective symmetry of the domain-average-engineered system is given by a point group *H* and we show how it can be determined. As an example, all groups *H* are specified for domain-average-engineered samples which can arise in a material undergoing the phase transition with symmetry change from $m\bar{3}m$ to $3m$.

Ferroic materials (and here we concentrate on non-magnetic materials, i.e. on ferroelectrics, ferroelastics, and higher-order ferroics) play an essential role in a number of technical applications. In some of them, dynamic domain processes are essential (e.g. thin-film memories, electron emitters) while in others the static distribution domains in the sample play the crucial role. In this contribution we concentrate on the latter case and wish to specify a clear distinction between two kinds of such static multidomain system.

We have in mind materials undergoing a structural phase transition from the parent phase of point group *G* into the ferroic phase of symmetry $F \subset G$ (such a material is referred to

as belonging to the species $G - F$). This leads necessarily to the possibility of a coexistence of ν domain states [1]; $\nu = |G|/|F|$ where $|A|$ is the order of the group A . Assuming that domain walls are of negligible thickness compared with the size of the domains, there are two different ways of specifying—and utilizing—properties of a multidomain sample with a *fixed* distribution of domains; we propose to refer to them as *domain geometry engineering* and *domain average engineering*, respectively. It is the purpose of this contribution to give their definitions and in particular to specify symmetry properties of domain-average-engineered multidomain samples.

First, we consider *domain geometry engineering*. Consider a multidomain sample for which the geometry of the spatial distribution of domains and therefore that of the tensorial material coefficients is specified. Macroscopic responses of such samples to external fields (forces) of defined frequency are determined by this distribution. If the applied fields are static, the response of a multidomain sample is primarily determined by the spatial distribution of tensorial properties (domains) and of the applied field, and codetermined by the boundary conditions along domain walls. (Only in cases of the simplest geometry of domains, namely a single system of parallel domain walls in the case of ferroelastic species, can the latter be eliminated.) As an example, consider a multidomain piezoelectrically active sample. The spatial distribution of strain is

$$\varepsilon_{jk}(\mathbf{r}) = d_{ijk}(\mathbf{r}) E_i(\mathbf{r}) \quad (1a)$$

$$d_{ijk}(\mathbf{r}) = d_{ijk}^{(\alpha)} f^{(\alpha)}(\mathbf{r}) \quad (1b)$$

where d_{ijk} stands for the piezoelectric tensor, the factor $f^{(\alpha)}(\mathbf{r}) = 0$ or 1 , and α denotes the domain state: $\alpha = 1, 2, \dots, \mu$ with $\mu \leq \nu$. Domain geometry engineering related to *dynamic external fields* is of particular interest. The k -vector of the applied fields defines the wavelength whose magnitude is chosen to be appropriately related to the size of domains and whose direction is correlated with the domain geometry. For a given wavelength, the size, geometry, and distribution of domains give rise to a qualitatively new kind of response specified by the symmetry of the multidomain system. In the example specified above, we expect the presence of new piezoelectric resonance frequencies. It was this case which was suggested by Newnham *et al* [2], offering new resonance modes of a two-domain sample. Recently, more involved multidomain piezoelectric systems were suggested and realized [3] in crystals of LiNbO_3 and LiTaO_3 . Referred to as acoustic superlattices, they can be used to generate and detect ultrasonic waves with frequencies in the range up to several hundreds of MHz. Another example, which has received unusual attention, is quasi-phase-matched optical multipliers. When the conventional phase-matching condition ($n_{2\omega} = n_{\omega}$) cannot be realized in a particular material because of unsuitable dispersion of refractive indices, often a quasi-phase-matched system can be constructed which offers a high integrated non-linear optical response leading to frequency doubling [4]. This requires that a periodic domain pattern be fabricated with a period twice the coherence length l_c . Such domain-shape-engineered systems are now widely used. An even more intricate geometry-engineered domain pattern has been designed [5] in which two geometrically different building blocks A, B, each containing two domains with antiparallel spontaneous polarizations, are arranged to form a Fibonacci sequence. This leads to the possibility of second-harmonic light generation simultaneously for several optical frequencies.

While domain-geometry-engineered systems have been repeatedly realized and theoretically analysed, the alternative approach to studying and utilizing multidomain ferroic samples with static chaotic distribution of domains has only recently become extremely attractive. By the term *domain average engineering* we mean a situation in which the ferroic sample is subdivided into a very large number of domains, representing μ domain states where

$\mu < \nu$, and forming a regular or irregular pattern. Ideally, the domain size is expected to be much smaller than the wavelength of externally applied fields. Here, in contrast to the case for domain shape engineering, the spatial distribution of tensorial material coefficients is not defined or is irrelevant. The response of the sample can be to some approximation described by tensorial properties averaged over all domain states involved. Considering, as an example, again a sample consisting of piezoelectrically active domains, we expect for the multidomain sample

$$\bar{\epsilon}_{jk} = \bar{d}_{ijk} \bar{E}_i \quad (2a)$$

$$\bar{d}_{ijk} = \frac{1}{V} \sum_{\alpha=1}^{\mu} d_{ijk}^{(\alpha)} V^{(\alpha)} \quad \mu < \nu. \quad (2b)$$

Both equations (1), (2) can be easily generalized for tensors of higher order.

Recently, a case of this character was considered [6–8] to allow discussion of piezoelectric properties of PZN-PT single crystals poled along one of the {001} directions. Assuming that the material went through the phase transition from $G = m\bar{3}m$ to $F = 3m$, poling along [100] supports the coexistence of four domain states with spontaneous polarization along the directions $[111]$, $[\bar{1}\bar{1}1]$, $[11\bar{1}]$, and $[\bar{1}\bar{1}\bar{1}]$, with equal probability. In this statement, it is assumed that the domain wall orientation (i.e. mechanical compatibility) aspects can be neglected. In fact, in samples of ferroelastic crystals, strictly speaking, only one set of mechanically permissible parallel domain walls is allowed [9] while in real samples walls of various orientations coexist connected with additional elastic strains, paid for by increased elastic energy [10].

We now discuss the symmetry of *domain-average-engineered* samples in which the volumes of the domain states represented are identical, i.e. $V(\alpha) = V/\mu$. Such situations can be achieved by cooling samples through their phase transition temperatures under properly oriented stresses, electric fields or combinations of these. We introduce a classification of domain-average-engineered ferroic samples and determine their average point symmetries. This average symmetry is taken to be the symmetry of the subset of domain states contained in the multidomain ferroic sample.

Consider the phase transition from G to F . The symmetry analysis is based on the coset decomposition of the point group G with respect to its subgroup F , i.e.

$$G = F + g_2 F + g_3 F + \dots + g_\nu F$$

where the elements g_i are the coset representatives of the decomposition and $g_1 = 1$. We denote the ν domain states which may arise at the transition as S_1, S_2, \dots, S_ν . The symmetry groups F_i of the domain states and the relative orientations of the domain states and their polarizations P_i are all determined by the coset representatives, i.e. $F_1 = F$, $F_i = g_i F_1 g_i^{-1}$, $S_i = g_i S_1$, and $P_i = g_i P_1$, $i = 2, 3, \dots, \nu$. The closure of the group G under multiplication implies a permutation of the cosets of the coset decomposition and in turn a permutation of the domain states S_i under elements g of G . The action of an element g of G on S_i is defined as $gS_i = gg_i S_1 = g_j f S_1 = g_j S_1 = S_j$, where f is an element of F , and the domain state S_i is transformed by the element g into the domain state S_j . The action of an element g of G on a subset of domains is denoted by $g\{S_1, S_2, \dots, S_\mu\} = \{gS_1, gS_2, \dots, gS_\mu\}$.

Two subsets of domains $\{S_1, S_2, \dots, S_\mu\}$ and $\{S'_1, S'_2, \dots, S'_\mu\}$ are said to belong to the same class of subsets of domains if there exists an element g of G such that $g\{S_1, S_2, \dots, S_\mu\} = \{gS_1, gS_2, \dots, gS_\mu\} = \{S'_1, S'_2, \dots, S'_\mu\}$. The symmetry group H of a subset of domains $\{S_1, S_2, \dots, S_\mu\}$ is defined as the group of all elements g of G which leave the set invariant, i.e. $g\{S_1, S_2, \dots, S_\mu\} = \{S_1, S_2, \dots, S_\mu\}$. The group H represents the effective symmetry of the domain-average-engineered system consisting of the subset of domains $\{S_1, S_2, \dots, S_\mu\}$.

As an example, we consider the phase transition from $G = m\bar{3}m$ to $F = 3_{xy}m_{\bar{x}y}$. Here $\nu = 8$. The indexing of the domain states, the corresponding coset representatives of the coset decomposition of G with respect to F , the symmetry groups, and the corresponding polarizations in each domain state are given in table 1.

Table 1. Domain state index, coset representative, symmetry group, and polarization.

Index i	Coset representative g_i	$F_i = g_i F_1 g_i^{-1}$	$P_i = g_i P_1$
1	1	$3_{xyz}m_{\bar{x}y}$	(A, A, A)
2	2_x	$3_{\bar{x}yz}m_{\bar{y}z}$	(A, -A, -A)
3	2_z	$3_{xyz}m_{\bar{x}y}$	(-A, -A, A)
4	2_y	$3_{x\bar{y}z}m_{\bar{x}z}$	(-A, A, -A)
5	$\bar{1}$	$3_{xyz}m_{\bar{x}y}$	(-A, -A, -A)
6	m_x	$3_{\bar{x}yz}m_{\bar{y}z}$	(-A, A, A)
7	m_z	$3_{xyz}m_{\bar{x}y}$	(A, A, -A)
8	m_y	$3_{x\bar{y}z}m_{\bar{x}z}$	(A, -A, A)

All subsets of these domain states have been classified into classes as defined above. In table 2 we list one subset of domain states from each class. Each subset is denoted by listing, between square brackets, the indices of the domain states contained in that subset, the indices having been given in table 1, e.g. the subset $\{S_1, S_3, S_5\}$ is denoted by [135]. In the right-hand column is the subgroup H of elements of G which leave the corresponding subset invariant. This table, in fact, represents the list of domain-average-engineered systems which can arise in a material undergoing a phase transition from $m\bar{3}m$ to $3m$.

Table 2. Representative subsets of domain states for the species $m\bar{3}m - 3m$ and the subgroups of $m\bar{3}m$ which leave them invariant.

Representative subset	Symmetry H of the subset
[1] or [2345678]	$3_{xyz}m_{\bar{x}y}$
[13] or [245678]	$m_{xy}m_{\bar{x}y}2_z$
[15] or [234678]	$\bar{3}_{xyz}m_{\bar{x}y}$
[16] or [234578]	$m_xm_{\bar{y}z}2_{yz}$
[123] or [45678]	$3_{xyz}m_{\bar{x}z}$
[135] or [24678]	$m_{\bar{x}y}$
[136] or [24578]	m_{xy}
[1234]	$\bar{4}3m$
[1235]	$m_{\bar{x}z}$
[1238]	$3_{x\bar{y}z}m_{\bar{x}z}$
[1356]	$2_{\bar{x}z}$
[1357]	$m_{xy}m_{\bar{x}y}m_z$
[1368]	$4_zm_xm_{xy}$

In figure 1, for each subset listed in table 2, we schematically represent the array of domain states and their polarizations associated with the domain states of each subset. Each domain state is denoted by a heavy dot at a corner of the cube. This represents a polarization from the centre of the cube to that corner—that polarization given in table 1 associated with the corresponding domain state. Subfigure [1] denotes the single-domain state with polarization

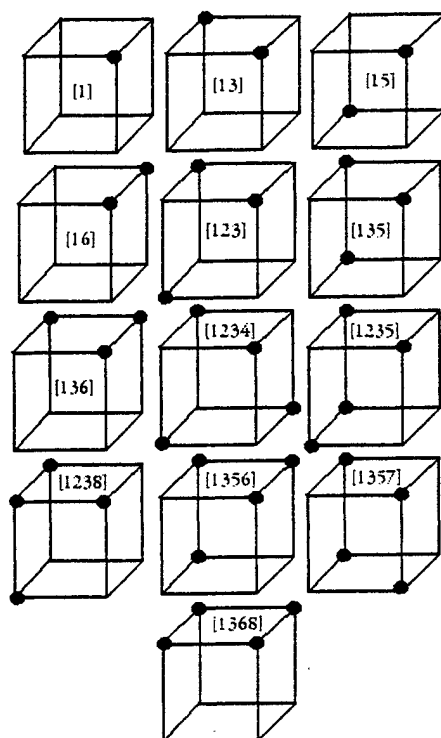


Figure 1. Graphical representation of the subsets of domain states whose symmetries are specified in table 1. Points at the cube vertices represent spontaneous polarization vectors: the origin is in the centre of the cube. The numbering is that of the indices of the domains and polarizations given in table 1.

in the $[111]$ direction. The figure denoted by $[1368]$, e.g., denotes a multidomain sample in which the following polarization vector directions are equally represented: $[111]$, $[\bar{1}\bar{1}1]$, $[1\bar{1}\bar{1}]$, and $[\bar{1}11]$. The corresponding symmetry groups of all these multidomain systems are listed, as already pointed out, in the right-hand-side column of table 2.

Taking into account the distribution of polarization vectors and corresponding strain tensors, one can determine which external forces should be applied in order to obtain any of the domain-average-engineered systems listed in table 1. The trivial example is the system $[1]$ produced by the electric field E along $[111]$. The system $[1368]$, discussed above (see references [6–8]) will be produced by the field along $[001]$ while the system $[16]$ requires the application of the field along $[011]$. The combination $[15]$ requires the application of a uniaxial stress along $[111]$ while the system $[13]$ calls for the application of both an electric field along $[001]$ and a uniaxial stress along $[\bar{1}10]$.

It is understood that in this symmetry approach we leave behind problems of coercive fields and stresses as well as, as already mentioned, problems of domain coexistence connected with their mechanical compatibility. It seems obvious that domain average engineering can successfully lead to the formation of crystalline systems with new desired properties, in particular in crystals where the domain size is small.

Each of the methods of domain engineering specified above can open a new vista of materials research possibilities in the area of ferroic materials and lead to multidomain assemblies with new desired properties.

JF appreciates the support of the Ministry of Education of the Czech Republic (Project No VS96006) and the assistance of the Materials Research Laboratory, The Pennsylvania State University; DBL acknowledges the hospitality of Dr V Kopsky and the Institute of Physics of the Czech Academy of Sciences, and the support of the Czech Ministry of Education under Grant ME336(1999) and of the National Science Foundation under Grants No DMR-9722799 and No DMR 0074550.

References

- [1] Aizu K 1970 *Phys. Rev. B* **2** 754–72
- [2] Newnham R E, Miller C S, Cross L E and Cline T W 1975 *Phys. Status Solidi a* **32** 69–78
- [3] Chen Y F, Zhu A N, Zhu Y Y, Ming N B, Jin B B and Wu R F 1997 *Appl. Phys. Lett.* **70** 592–4
- [4] Duan F, Ming N B, Hong J F, Yang Y S, Zhu J S, Yang Z and Wang Y N 1980 *Appl. Phys. Lett.* **37** 607–9
- [5] Zhu S N, Zhu Y Y, Qin Y Q, Wang H F, Ge C Z and Ming N B 1997 *Phys. Rev. Lett.* **78** 2752–5
- [6] Park S E and Shrout T R 1997 *J. Appl. Phys.* **82** 1804–11
- [7] Wada S, Park S E, Cross L E and Shrout T R 1999 *Ferroelectrics* **221** 147–55
- [8] Yin J and Cao W 2000 *J. Appl. Phys.* **87** 7438–41
- [9] Fousek J and Janovec V 1969 *J. Appl. Phys.* **40** 135–42
- [10] Salje E K H and Ishibashi Y 1996 *J. Phys.: Condens. Matter* **8** 8477–95

APPENDIX 92

Engineering Multidomain Ferroic Samples

J. FOUSEK^{ab} and L. E. CROSS^b

^a*Dept. of Physics and International Center for Piezoelectric Research,
University of Technology, Liberec, 46117 Czech Republic and* ^b*Materials
Research Laboratory, The Pennsylvania State University, University Park, PA
16802, U.S.A.*

(Received June 2, 2000)

The existence of domains is essential in many practical applications of ferroics. Here we discuss devices in which a *fixed* spatial distribution of domains plays the significant role. Depending on the prevailing attributes of multidomain single crystals, three different possibilities can be distinguished. In *domain-geometry-engineered* samples the spatial distribution of domains is tuned to correspond to the *k*-vectors of fields propagating through the material. In *domain-average-engineered* samples the crystal is subdivided into a very large number of domains, representing a *limited* number of domain states. In *domain-wall-engineered* samples the characteristics of static walls can play an essential role in the averaged macroscopic properties. Examples illustrating these approaches are given.

Keywords: domain engineering; domain-geometry engineering; domain-average-engineering; domain-wall-engineering; multidomain ferroics; static domain pattern

1. INTRODUCTION

Practical applications of ferroics (undergoing a phase transition from the point group G to F) are of two basically different characters: those which rely on properties of single domain samples and those in which the presence of domains is essential. The latter can be categorized into

devices based on dynamical domain processes or those in which a static distribution of domains plays a significant role. Here we discuss the last mentioned case: general characteristics of multidomain samples with fixed spatial distribution of domains.

Depending on the prevailing attributes of multidomain single crystal samples, several possibilities can be distinguished. Those discussed in the following sections 2 to 4 differ in general features of the geometry of domains and it is assumed that domain walls are of negligible thickness. In the last considered case, the thickness of domain walls is finite and specimens exhibit large wall density. Aspects of preparation and properties of such samples are discussed in the section 5.

2. DOMAIN-GEOMETRY-ENGINEERED FERROIC SAMPLES

As early as in 1964, Miller^[1] showed that a regular pattern consisting of 180° domains in BaTiO_3 with a period corresponding to the coherence length could substantially increase the effectiveness of optical second harmonic generation. The idea is based on two factors: a) domain states differ in the sign of nonlinear optical coefficient, b) the width of domains is tuned to the coherence length. It was Feng Duan et al.^[2] who succeeded in manufacturing a periodic domain pattern in LiNbO_3 and proved its efficiency in nonlinear optics. More recently, S. N. Zhu et al.^[3] initiated an essential progress in this field by producing a domain pattern whose geometry corresponds to a Fibonacci superlattice and which makes it possible to realize second harmonic generation for multiple wavelengths. But the significance of domain patterns with engineered geometry was proved also in acoustics. Meeks et al.^[4] produced tunable acoustic systems based on spatial modulation of elastic coefficients in a periodic domain pattern in $\text{NdP}_5\text{O}_{14}$ while Y. Y. Zhu et al.^[5] succeeded in producing transducers up to 800 MHz based on spatial modulation of piezoelectric coefficients in multidomain LiNbO_3 .

In all these applications the periodicity of domain patterns corresponds to k -vectors of propagating waves and the multidomain domain systems represent just two domain states. Up to now less than 10 ferroics have been utilized in this area, and in any of these materials the total number of domain states $\nu = |G| / |F| = 2$ (here $|G|$ and $|F|$ stand for the order of the parent and ferroic phase point groups, resp.). This is understandable since to produce a regular pattern in ferroics with $\nu > 2$ in which only two domain states are involved is not trivial.

To solve this task in particular cases experimentally is, however, possible. In fact the nature itself shows that patterns with a regular geometry of a limited number $\mu < \nu$ of domain states can be materialized. Several observations have been made of domain patterns with regular geometry, fulfilling this requirement. As an example, we refer to the Forsbergh's square-net pattern^[6] shown in Fig.1, which has been repeatedly observed in BaTiO_3 single crystals as well as ceramic grains. It might be inspiring to examine its macroscopic properties for external fields with both $k = 0$ and $k \neq 0$, based on its symmetry characteristics.

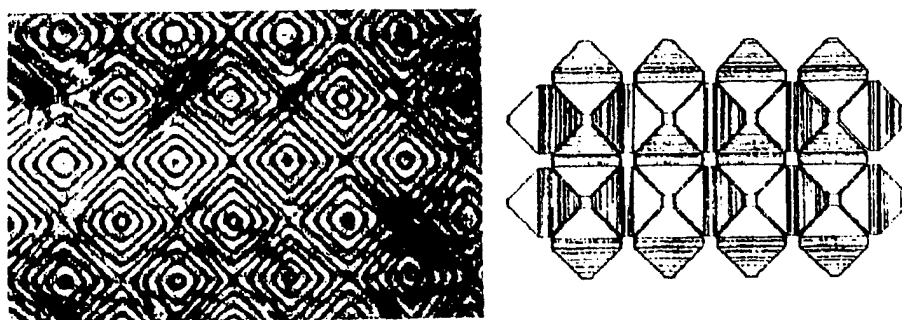


FIGURE 1 Example of a "natural" multi-axial domain-geometry engineered system: the Forsbergh's square-net pattern in tetragonal BaTiO_3 . Left: microscopic picture; right: arrangement of tetrahedral building blocks. From Ref. [6].

Several other multi-axial three-dimensional and reproducible patterns have been observed under natural conditions and there is little doubt that they could be produced artificially. To mention just one more example, we refer to the Arlt's^[7] patterns α and β ; till now they have been observed only in ceramic grains but very probably they could be created in crystals under properly designed external forces. Again, in order to deliberate about their properties, the symmetry analysis would be the first step to take.

Indeed, regular domain systems can offer unexpected symmetry properties. Thus, for instance, the well known Hallbach array of magnets with asymmetric distribution of magnetic field can have a simple analogy in thin ferroelectric plates containing a regular system of 90° domain pairs. While in the latter case, because of the existence of free charges, we do not expect pronounced external depolarizing field

effects, macroscopic properties of the array could offer new applicable aspects.

3. DOMAIN-AVERAGE-ENGINEERED FERROIC SAMPLES

In contrast to the previous cases, in *domain-average-engineered* samples of ferroic crystals the specimen is subdivided into a very large number of domains, representing just $\mu < \nu$ domain states. Such situations can be achieved by cooling samples through their phase transition temperatures under properly oriented stresses, electric fields or their combinations. The geometry of domains is irregular. The sample's response to external fields is roughly described by tensorial properties averaged over all involved domain states. Thus, e.g. for the piezoelectric response we can write in the zeroth approximation

$$\bar{\varepsilon}_{jk} = \bar{d}_{ijk} \bar{E}_i, \quad \bar{d}_{ijk} = \frac{1}{V} \sum_{\alpha=1}^{\mu} d_{ijk}^{(\alpha)} V^{(\alpha)}.$$

Here $V(\alpha)$ denotes the volume occupied by the domain state α .

In recent years, Park et al.^[8,9], Yin and Cao^[10] and other authors considered a case of this character to discuss piezoelectric properties of PZN-PT single crystals poled along one of the $\{001\}$ directions. Assuming that the material went through the phase transition from $G = m\bar{3}m$ to $F = 3m$, the poling along $[100]$ supports the coexistence of four domain states with spontaneous polarization along the directions $[111]$, $[1\bar{1}1]$, $[11\bar{1}]$ and $[1\bar{1}\bar{1}]$, with equal probability. In this statement, it is assumed that the domain wall orientation aspects (e.g. mechanical compatibility) can be neglected. In fact, in samples of ferroelastic crystals strictly speaking, only one set of mechanically permissible parallel domain walls is allowed^[11] while in real samples walls of various orientations coexist connected with additional elastic strains, paid by increased elastic energy.

The symmetry aspects of domain-average-engineered samples can be discussed in a general way. The task is to determine the average point symmetry H , i.e. the symmetry of the subset of domain states contained in the multidomain sample. This was addressed by Fousek et al.^[12] and the procedure can be facilitated by the use of the computer programme of Schlesmann and Litvin.^[13]

As an example, in Fig.2 we reproduce^[12] the average symmetry groups H of six selected subsets of domain states (out of 13 leading to

different symmetries F) which arise in the phase transition specified above (here $\mu = 8$). States are represented by self-explanatory numbers and dots indicating the directions of \mathbf{P}_S vectors.

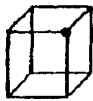
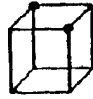
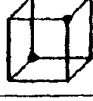



Representative subset	Subset symmetry H
[1] 	$3_{xyz} m_{\bar{x}y}$
[13] 	$m_{xy} m_{\bar{x}y} 2_z$
[15] 	$\bar{3}_{xyz} m_{\bar{x}y}$
[136] 	m_{xy}
[1356] 	$2_{\bar{x}z}$
[1368] 	$4_z m_x m_{xy}$

FIGURE 2 Examples of subsets of domain states corresponding to the transition $m\bar{3}m - 3m$ and their symmetries.

Taking into account the distribution of polar vectors and corresponding strain tensors, one can determine which external forces should be applied in order to obtain any of the domain-average-engineered systems. The trivial example is the subset [1] produced by the electric field \mathbf{E} along [111]. The subset [1368], discussed^[8-10] before, will be produced by the field along [001] while the combination [15] requires the application of a uniaxial stress along [111]. The subset [13] calls for the application of both electric field along [001] and uniaxial stress along $[\bar{1}10]$.

In addition to the applied fields, electrical or mechanical, there are other approaches which can eliminate particular domain states in a

given ferroic material. The stimulating example is based on chiral dopants. Keve et al.^[14] showed that doping TGS with *L*- α -alanine prefers just one of the two domain states with antiparallel P_s . Zikmund and Fousek^[15,16] generalized this approach and showed that chiral substituents can reduce the number of domain states by a factor of two in a number of ferroic species.

It is understood that in the mentioned approaches we leave behind the problems of domain coexistence connected with their mechanical compatibility. It seems obvious that domain average engineering can successfully lead to formation of crystalline systems with new desired properties in particular in crystals where the domain size is small. Crystalline systems exhibiting tweed microstructures similar to those observed in La-modified lead titanate^[17] or PLZT^[18] might serve as candidates for this approach.

4. PHASE- AND- DOMAIN-AVERAGE ENGINEERED FERROICS

The domain-average-engng concept can be generalized to systems in which the prescribed domain states represent two or more ferroic species. Such multiphase situations occur in PZT ceramics near the morphotropic boundary and originate^[19] in concentration gradients as well as in the independent nucleations of the ferroic phases since the transition is of the 1st order. It appears that PZN-PT single crystals with a pronounced piezoelectric response contain blocks of both tetragonal and rhombohedral symmetry^[20]. In the basic approximation, the piezoelectric coefficient of a properly poled sample is then described by

$$\bar{d}_{ijk} = \frac{1}{V_1} \left[\sum_{\alpha=1}^{\mu_1} d_{ijk}^{(\alpha)} V^{(\alpha)} \right] + \frac{1}{V_2} \left[\sum_{\beta=1}^{\mu_2} d_{ijk}^{(\beta)} V^{(\beta)} \right] + \\ + \Delta d_{ijk}(\text{walls}) + \Delta d_{ijk}(\text{phase bndrs})$$

where μ_1 and μ_2 are numbers of domain states represented in the phase 1 and 2, resp., after poling. The high piezoelectric response of PZN-PT single crystals originates in the combination of intrinsic coefficients $d_{ijk}^{(\alpha)}$, $d_{ijk}^{(\beta)}$ as well as in the extrinsic contributions due to the motion of domain walls and phase boundaries. The question what role is played by any of these contributions is still to be solved.

When addressing the problem of average symmetries of phase-and-domain-average-engineered samples one can follow^[21] a similar approach as mentioned above. Consider that two species coexist, namely $m\bar{3}m-3m$ and $m\bar{3}m-4mm$. It can be shown that when poling along principal directions, i.e. $E \parallel [001]$ or $E \parallel [011]$ or $E \parallel [111]$, regions of the two species differ in the systems of P_s vectors but are of the same averaged symmetries $4mm$, $mm2$ or $3m$, resp.

It has to be stressed that in both domain-average engineered and phase-and-domain-average engineered systems, electrical and mechanical compatibility conditions play, in the energy evaluations, a significant role. It is beyond the scope of this presentation to discuss these problems in detail and the subject will be addressed in another paper.

5. DOMAIN-WALL-ENGINEERING

In the last considered case, the thickness of domain walls is finite and the specimens exhibit large wall density. As before, the representation of specific walls can be influenced by external forces. In such *domain-wall-engineered* samples the characteristics of static walls can play an essential role in the averaged macroscopic properties.

It was predicted by Walker and Gooding^[22] that Dauphiné domain walls in nonpolar quartz can carry a dipole moment and this was later demonstrated experimentally by Snoeck et al.^[23], in the incommensurate phase of SiO_2 . In fact it is easy to demonstrate this possibility for ferroelastic walls. If in the free energy function the invariant $\mu_{ijkl}(\partial\epsilon_{ij}/\partial x_k)E_l$ is allowed by symmetry, a ferroelastic wall will carry polarization

$$P_l = \mu_{ijkl} \frac{\partial \epsilon_{ij}}{\partial x_k}.$$

Here the μ -tensor describes the flexoelectric effect. As an example, consider the species $m\bar{3}m-4/mmm$ represented by crystals of SrTiO_3 , or CsPbCl_3 and the species $m\bar{3}m-4mm$ describing the properties of BaTiO_3 . In both cases, ferroelastic walls (90° wall in the latter case) are, by symmetry, allowed to carry polarization

$$P_x = P_z = (\mu_{1111} - \mu_{3311}) \frac{\partial \epsilon_{xx}}{\partial x};$$

this is demonstrated in Fig. 3. Symmetries of nonferroelastic domain walls from which their possible macroscopic properties can be envisaged have been discussed by Pfiřvratřká and Janovec^[24].

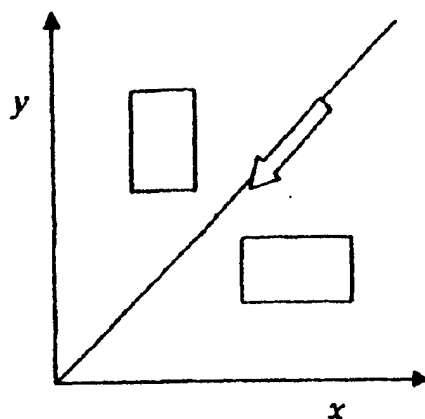


FIGURE 3 Due to flexoelectricity, domain wall separating two ferroelastic domains of species $m\bar{3}m - 4/mmm$ or $m\bar{3}m - 4mm$ can carry polarization represented by the arrow.

Should macroscopic properties of domain walls play a non-negligible role in the properties of a ferroic sample, they have to occupy a sizable volume. Realistic values of domain width and domain wall thickness are $d_{\text{domain}} = 1$ to $10 \mu\text{m}$ and $t_w = 3 \text{ nm}$, resp. Suppose that the required relative volume occupied by domain walls is 10% and that there is no way how to increase the wall thickness. Then we look for methods how to reduce the average domain width to about 30 nm, i.e. how to increase the wall density 30 times or more.

It appears that there is a significant number of experimental methods which could address this problem. Here we mention in passing only some of those which might be considered. The density of defect-induced order parameter gradients could be increased at crystal growth^[2]. The size of AFM-written domains^[25] could be further reduced, their density increased. Attempts to freeze-in high density tweed structures^[26] in some ferroelastics close above T_C or high density pattern of discommensurations in modulated phases close above the lock-in temperatures^[27] appear attractive. Fixing photorefractive gratings by domains^[28] in ferroelectrics with small P_s (small defect-

assisted nucleation energies to produce domains in real time) looks also promising.

6. CONCLUSIONS

Till now, the field of domain geometry engineering has been successfully developed and applied to ferroics representing five species of ferroelectrics and one species of ferroelastics, all with two domain states. Such specimens proved to be competitive in the field of nonlinear optics and promising in the field of ultrasonic generation and detection. But much more complex domain systems are obtainable and have not yet been considered and investigated.

Two new areas of research appear to be very promising. Domain- and phase-average engineered systems offer increased values of macroscopic properties, probably strengthened by domain wall and/or phase boundary induced motions. We still miss detailed data about the real structure of existing compounds like PZN-PT as well as theoretical analysis of multiple domain states compatibility, the more so for multiple phase systems. Domain-wall engineered samples with high density of walls also promise a new interesting research and application area. At present, particular systems useful in selected applications could be specified and methods to produce high density domain patterns investigated experimentally.

Acknowledgments

J.F. appreciates the support of the Ministry of Education of the Czech Republic (Project VS 96006) and the assistance of the Materials Research Laboratory, The Pennsylvania State University.

References

- [1] R. C. Miller, *Phys. Rev.* **134**, A1313 (1964).
- [2] D. Feng, N. B. Ming, J. F. Hong, Y. S. Yang, J. S. Zhu, Z. Yang and Y. N. Wang, *Appl. Phys. Lett.* **37**, 607 (1980).
- [3] S. N. Zhu, Y. Y. Zhu, Y. Q. Qin, H. F. Wang, C. Z. Ge and N. B. Ming, *Phys. Rev. Lett.* **78**, 2752 (1997).
- [4] S. W. Meeks, L. Clarke and B. A. Auld, IEEE Ultrasonics Symposium, San Francisco, CA (1985).
- [5] Y. Y. Zhu, N. B. Ming, W. H. Jiang and Y. A. Shui, *Appl. Phys. Lett.* **53**, 1381 (1988).
- [6] P. W. Forsberg, Jr., *Phys. Rev.* **76**, 1187 (1949).
- [7] G. Arlt and P. Sasko, *J. Appl. Phys.* **51**, 4956 (1980).
- [8] Seung-Eck Park and T. R. Shrout, *J. Appl. Phys.* **82**, 1804 (1997).
- [9] Seung-Eck Park, S. Wada, P. W. Rehrig, Shi-Fang Liu, L. E. Cross and T. R. Shrout, "Crystallographic Engineering in High-performance Piezoelectric Crystals." Paper presented at SPIE Smart Structures and Materials (New Port Beach, 1999).

- [10] Jianhua Yin and W. Cao, *J. Appl. Phys.* **87**, 7438 (2000).
- [11] J. Fousek and V. Janovec, *J. Appl. Phys.* **40**, 135 (1969).
- [12] J. Fousek, D. B. Litvin and L. E. Cross, submitted.
- [13] J. Schlessman and D. B. Litvin, *Acta Cryst.* **A51**, 947 (1995).
- [14] E. T. Keve, K. L. Bye, P. W. Whipps and A. D. Annis, *Ferroelectrics* **3**, 39 (1971).
- [15] Z. Zikmund and J. Fousek, *Ferroelectrics* **79**, 73 (1988).
- [16] Z. Zikmund and J. Fousek, *phys. stat. sol. (a)* **112**, 625 (1989) and **118**, 539 (1990).
- [17] G. A. Rossetti, Jr., W. Cao and C. A. Randall, *Ferroelectrics* **158**, 343 (1994).
- [18] C. A. Randall, G. A. Rossetti, Jr. and W. Cao, *Ferroelectrics* **150**, 163 (1993).
- [19] V. A. Isupov, *Ferroelectrics* **46**, 217 (1983).
- [20] K. Fujishiro, R. Vlokh, Y. Uesu, Y. Yamada, J.-M. Kiat, B. Dkhil and Y. Yamashita, *Jpn. J. Appl. Phys.* **37**, 5246 (1998).
- [21] J. Fousek, D. B. Litvin and L. E. Cross, to be published.
- [22] M. B. Walker and R. J. Gooding, *Phys. Rev. B* **32**, 7408 (1985).
- [23] E. Snoeck, P. Saint-Gregoire, V. Janovec and C. Roucau, *Ferroelectrics* **155**, 371 (1994).
- [24] J. Přívratská and V. Janovec, *Ferroelectrics* **191**, 17 (1997).
- [25] L. M. Eng, M. Bamberlin, Ch. Loppacher, M. Guggisberg, R. Bennewitz, R. Lüthi, E. Meyer, Th. Huser, H. Heinzelman and H.-J. Güntherodt, *Ferroelectrics* **222**, 153 (1998).
- [26] A. M. Bratkovsky, E. K. H. Salje and V. Heine, *Phase Transitions* **52**, 77 (1994).
- [27] V. Novotna, H. Kabelka, J. Fousek, M. Havrankova and H. Warhanek, *Phys. Rev. B* **47**, 11019 (1993).
- [28] J. Fousek, M. Marvan and R. S. Cudney, *Appl. Phys. Letters* **72**, 430 (1998).

APPENDIX 93

Domain configurations in domain engineered $0.955\text{Pb}(\text{Zn}_{1/3}\text{Nb}_{2/3})\text{O}_3-0.045\text{PbTiO}_3$ single crystals

Jianhua Yin and Wenwu Cao^{a)}

Materials Research Laboratory, The Pennsylvania State University, University Park, Pennsylvania 16802

(Received 21 September 1999; accepted for publication 3 February 2000)

We report an optical microscopy study on the domain structures of $0.955\text{Pb}(\text{Zn}_{1/3}\text{Nb}_{2/3})\text{O}_3-0.045\text{PbTiO}_3$ rhombohedral phase single crystals poled along [001] of the cubic coordinates. Both charged and uncharged domain walls are observed in domain engineered samples and they could join together to form "L" and "T" shaped domain walls, which are very unique. The observed domains are between 10 and 100 μm in size, which are much bigger than expected. Most of the samples have only two of the four possible degenerate domain states, making the macroscopic symmetry to be $mm2$ or lower rather than $4mm$ previously assumed. © 2000 American Institute of Physics. [S0021-8979(00)02710-9]

Single crystal $(1-x)\text{Pb}(\text{Zn}_{1/3}\text{Nb}_{2/3})\text{O}_3-x\text{PbTiO}_3$ (PZN-PT) system of the rhombohedral ferroelectric phase can have very high coupling constant and piezoelectric constant after being poled along [001].¹⁻³ It has triggered a new wave of material research recently to improve material properties using domain engineering, i.e., using a different poling scheme to manipulate domain structures. It also raised many interesting scientific questions, such as the origin of these superior properties and the role of domains in general. The very high electromechanical coupling coefficient ($k_{33} > 90\%$) and piezoelectric coefficient ($d_{33} > 2000 \text{ pC/N}$) produced by domain engineering method make the PZN-PT a much better candidate for transducer materials than the $\text{PbZrO}_3\text{-PbTiO}_3$ (PZT) solid solution system used for the past 40 years. The PZN-PT single crystal solid solution system has been made in the late 1960s⁴ and it was found that the electromechanical coupling coefficient k_{33} could be more than 90% in some samples.^{5,6} However, the composition studied was at the boundary composition of the tetragonal phase, therefore, properties were not as high and not as consistent. The newly established domain engineering method makes it possible to stabilize the polarization of the rhombohedral phase by poling the crystals in [001] rather than the polarization direction of [111].¹⁻³

Understanding the physical mechanism of this property enhancement is very important for extending this domain engineering idea to other materials. Naturally, the key issue is the domain structures since the off-polarization direction poling will create a multidomain single crystal system. This article reports an experimental study on the domain structures in a $0.955\text{Pb}(\text{Zn}_{1/3}\text{Nb}_{2/3})\text{O}_3-0.045\text{PbTiO}_3$ [PZN-4.5%PT] system, which has a microscopic symmetry of $3m$.

Because the dipoles of the PZN-4.5%PT form along the body diagonals of the parent cubic perovskite structure at the ferroelectric phase transition, the crystal has rhombohedral symmetry with the symmetry group $3m$ in the ferroelectric

state.^{4,5} Poling was done by applying an electric field along [001] of the cubic coordinates so that only four of the eight possible polarization orientations remain, i.e., $[111]$, $[\bar{1}\bar{1}\bar{1}]$, $[1\bar{1}\bar{1}]$, and $[\bar{1}11]$. Statistically, such a system would have a pseudomacroscopic tetragonal symmetry considering the degeneracy of these four domain states. All previous studies on this system were based on this $4mm$ symmetry assumption.^{1-3,7,8}

However, it was found experimentally that the material properties of the domain engineered PZN-4.5%PT could

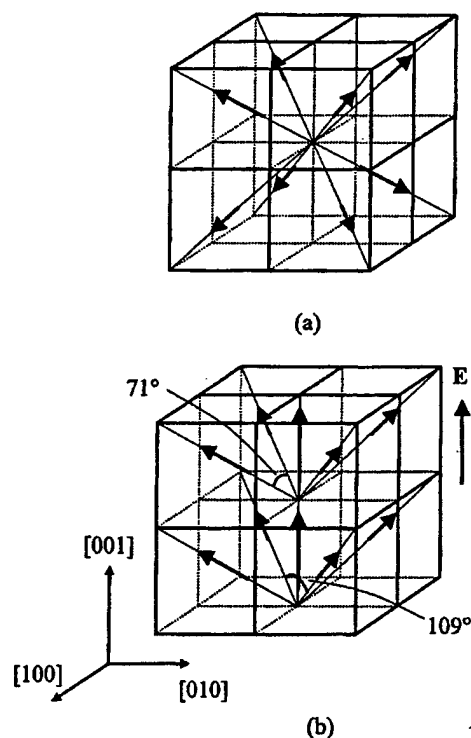


FIG. 1. Illustration of the assumed domain structure with cross intersecting charged domain walls for the PZN-4.5%PT. (a) There are eight possible orientations of dipoles before poling. (b) Four orientations remain after poling for the polarization. The structure is macroscopically tetragonal.

^{a)}Electronic mail: cao@math.psu.edu

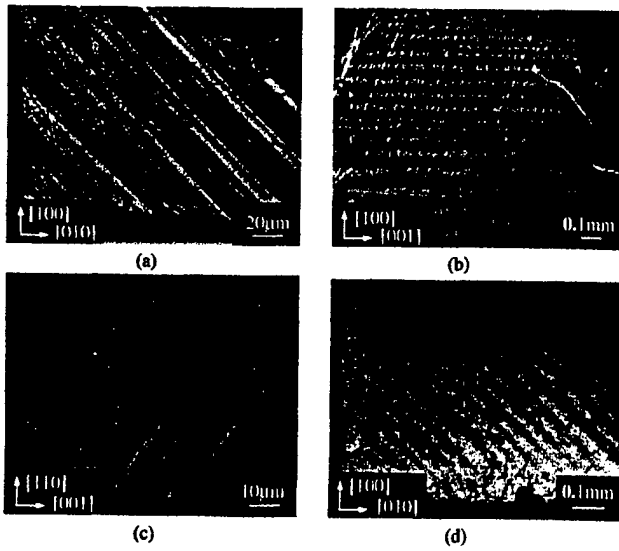


FIG. 2. Domain patterns observed on different sample surfaces. In each sample, there is only one set of twins with fairly large domain size. (a) On (001) surface; (b) on (010) surface; (c) on ($\bar{1}10$) surface; and (d) same as (a) but in different sample and different scale.

change substantially from sample to sample, particularly sensitive to the sample geometry.^{7,8} There are also indications from our ultrasonic measurements that the elastic properties deviate from the $4mm$ symmetry in many of the samples. In order to understand this issue, we used optical microscopy to exam the domain patterns in the $[001]$ poled PZN-4.5%PT multidomain single crystals and performed some simple analyses to interpret these observed domain structures. The most interesting phenomena observed was the coexistence of charged and uncharged domain walls, which has never been reported in the literature.

The macroscopic symmetry defined in this article is what reflected in the macroscopic material properties, which do not change with the overall shape of the sample but only with the domain configurations. The $4mm$ macroscopic tetragonal symmetry assumption implicitly assumed the following two conditions: (1) the domain size is very small compared to sample dimensions so that large amount of domains exist to allow the use of statistical principle; and (2) the domain walls are all charged and are parallel to the effective polarization direction (i.e., the wall normal is perpendicular to the applied poling field) as shown in Fig. 1.

For the domain observations, we prepared many samples with three pairs of mutually perpendicular surfaces. These samples have two types of orientations: $[001]/[010]/[100]$ and $[001]/[110]/[1\bar{1}0]$. The sample shapes are cubes, plates, or bars with the typical dimension of 1–5mm. Obser-

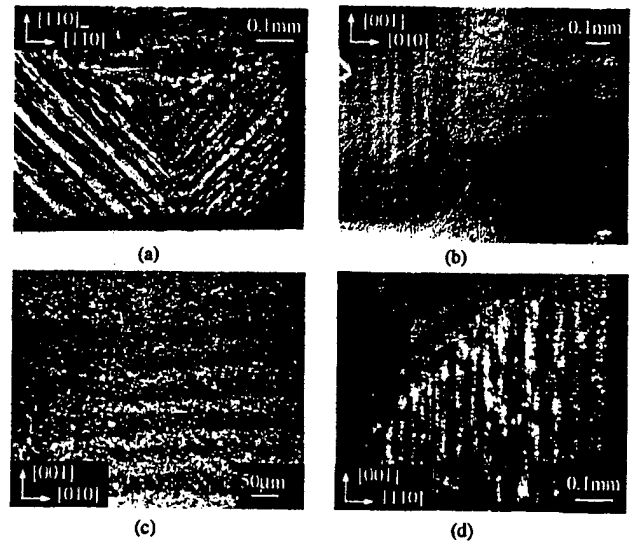


FIG. 3. A charged and an uncharged domain walls join together to form L or T shaped domain walls. (a) on (001) surface; (b) and (c) on (001) surface; and (d) on ($\bar{1}10$) surface.

vations were performed on the surfaces of the following three orientations: $[001]$, $[110]$, and $[100]$, with the samples being poled along $[001]$ in all cases. Because the crystal is translucent, domains could be observed by polarizing optical microscopy in either reflection mode or transmission mode.

Figures 2 and 3 show a few of the domain patterns obtained in the domain engineered PZN-4.5%PT system. One can see that the two implicit assumptions in treating the system to be macroscopic tetragonal are not satisfied. First of all, the domain size is fairly large compared to the sample size, ranging from 10 to 100 μm , so that there will be only 20–100 domains across the sample. Second, the domains are coupled strongly to each other in the form of elastic twins. These two facts invalidate the use of statistical description, which requires a large ensemble of independent elements. In fact, we found that only two of the four possible domains exist in most of the samples. This effectively reduced the macroscopic symmetry of this multidomain crystal from $4mm$ to $mm2$ or even lower. In addition, both charged and neutral domain walls are present in the system, while the $4mm$ macroscopic symmetry requires all the walls to be charged.

In a $m\bar{3}m \rightarrow 3m$ ferroelectric phase transition, such as occurred in the PZN-4.5%PT system, the permissible domain walls formed in the ferroelectric phase are orientated in $\langle 100 \rangle$ and $\langle 110 \rangle$ family. The angle between polarization vectors on the two sides of a domain wall can be either 109° or 71°. We listed in Table I, all the permissible domain walls

TABLE I. Permissible orientations of domain walls in $[001]$ poled PZN-4.5%PT crystals of rhombohedral phase. The polarization directions of P_s and P'_s in a twin structure are given in the first row.

P_s/P'_s	$[111]/[\bar{1}\bar{1}\bar{1}]$	$[111]/[1\bar{1}\bar{1}]$	$[111]/[\bar{1}\bar{1}1]$	$[\bar{1}\bar{1}1]/[1\bar{1}\bar{1}]$	$[\bar{1}\bar{1}1]/[\bar{1}\bar{1}1]$	$[1\bar{1}\bar{1}]/[\bar{1}\bar{1}\bar{1}]$
Charged	$[100]$	$[010]$	$[110]$	$[1\bar{1}0]$	$[010]$	$[100]$
Uncharged	$[011]$	$[101]$	$[001]$	$[001]$	$[\bar{1}01]$	$[0\bar{1}1]$

TABLE II. Illustration of possible twin patterns in $[001]/[010]/[100]$ and $[001]/[110]/[1\bar{1}0]$ oriented rhombohedral PZN-4.5%PT single crystals poled along $[001]$.

wall orientation	$[001]$	$[110]$	$[010]$	$[101]$
	(a)	(b)	(c)	(d)
	(e)	(f)	(g)	(h)

between different pairing schemes among the four remaining domains after poling. It can be shown that the intersection lines of the domain walls on the sample surface may form 0° , 45° , and 55° angles with respect to the edges of the samples as shown in Table II.

Figure 2 shows the domain patterns of types (b), (c), (f), and (g), respectively, listed in Table II. One can see that the intersection lines of domain walls with sample surfaces are either parallel or form a 45° angle with one of the edges of the sample. More importantly, contrary to the conventional reported ferroelectric twins of head to tail charge neutral configurations, the twin patterns type (b) and type (f) in Table II contain charged walls with the polarizations form either head to head or tail to tail configurations between the two domain states $P_s \parallel [111]$ and $P_s \parallel [\bar{1}\bar{1}\bar{1}]$. The polarization vectors of the two domains in the twins form a 109° angle in this case. Types (c) and (g) in Table II are the twin patterns between $P_s \parallel [111]$ and $P_s \parallel [1\bar{1}\bar{1}]$. The domain walls are also charged with the polarization vectors form a 71° angle. Uncharged walls, such as type (h) in Table II between $P_s \parallel [111]$ and $P_s \parallel [1\bar{1}\bar{1}]$, were also observed in some of the samples. The intersection lines between the charge neutral walls and the sample surfaces form either a 45° or 55° angle with respect to the sample edges as indicated in Table II.

Figure 3 shows several observed complex domain patterns. They are both charged and uncharged domain walls and it is very interesting to see that the charged and un-

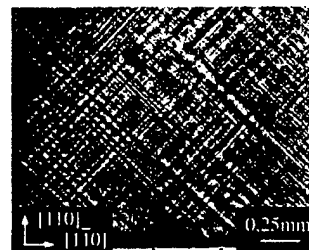


FIG. 4. Two sets of twins intersecting each other to form a network of four different domain states. This is the top view from $[001]$.

charged walls could join each other to form "L" and "T" shaped patterns. In part of one sample with the orientations of $[100]/[010]/[001]$ and the corresponding dimensions of $2.4\text{mm}/2.27\text{mm}/0.43\text{mm}$, respectively, all four possible domains were found to coexist after poling in $[001]$ as shown in Fig. 4.

In order to better understand these observed patterns, we have made simple analysis based on the crystal structure and illustrated in Fig. 5 some possible complex patterns made of two and four domain states. The observed patterns in Figs. 3 and 4 could be matched to those patterns of Fig. 5 as the following:

Fig. 3(a)→the top view of Fig. 5(e);

Fig. 3(b)→front view of the configuration Figs. 5(b) or 5(c);

Fig. 3(c)→front view of Fig. 5 (a);

Fig. 3(d)→front view of Fig. 5 (d) (upside down), and

Fig. 4→front view of Fig. 5(f).

Figure 4 is a pattern showing the coexistence of all four possible domains, $P_s \parallel [111]$, $P_s \parallel [1\bar{1}\bar{1}]$, $P_s \parallel [1\bar{1}1]$, and $P_s \parallel [\bar{1}\bar{1}\bar{1}]$. Statistically speaking, this configuration should be the most probable structure after poling in $[001]$, since the four ferroelectric variants are energetic degenerate. However, because the wall intersection causes energy, we only have seen such domain patterns in a small portion of one of the samples.

In summary, our optical microscopy studies showed that the domain patterns in the domain engineered PZN-4.5%PT single crystals are predominantly twins containing only two

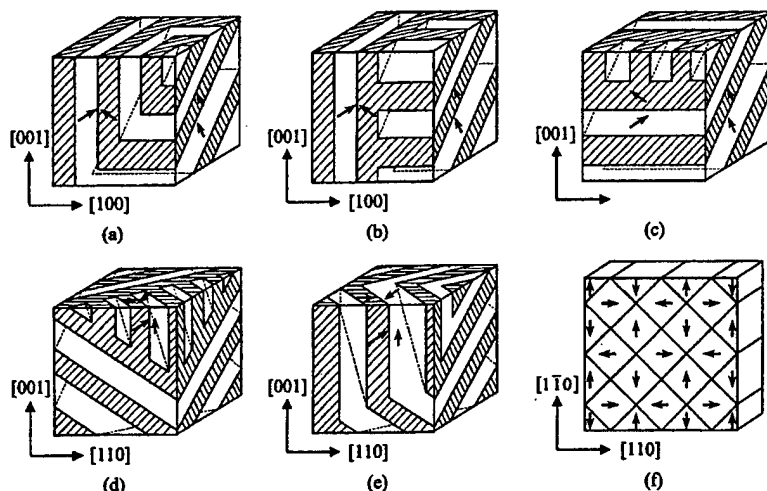


FIG. 5. Illustration of domain patterns that can be formed by the combination of charged and uncharged domain walls. (a)–(e) are patterns of twinning by two domains. One can see that L and T shaped domain walls are formed by joining a charged and an uncharged wall. (f) is the domain pattern for the coexistence of all four possible domains.

of the four possible domains after being poled in [001]. The size of the domains is relatively large, ranging from 10 to 100 μm , therefore, one may conclude that the previously assumed macroscopic $4mm$ symmetry for the [001] poled rhombohedral phase crystal might not be always appropriate. As theoretically predicted⁹ the highest macroscopic symmetry of a two-domain system is orthorhombic $mm2$. The symmetry could be even lower if the volume ratios of the two domains in the twin are different.¹⁰ The most intriguing phenomenon observed was the coexistence of charged and uncharged domain walls joining together in a poled PZN-4.5%PT system, and these joined walls could form either L or T shaped domain walls. Based on energy consideration, in order for the charged walls to exist, charged dopants or defects must be distributed near the wall region to reduce the electrostatic energy. On the other hand, the existence of these intersected domain walls could introduce high elastic strain energy, making the domain structures less stable, which could be one of the main reasons for the multidomain structure to be more responsive to external drive, producing high value of dielectric and piezoelectric coefficients.

This research was sponsored the Office of Naval Research under Grant No. N00014-98-1-0527 and the National Institute of Health under Grant No. P41 RR11795-01A 1. Crystals used for this study were provided by Dr. S. E. Park and Dr. T. R. Shrout and we are also indebted to the technical assistance of Bei Jiang in sample preparation.

¹S. E. Park and T. R. Shrout, IEEE Trans. Ultrason. Ferroelectr. Freq. Control **44**, 1140 (1997).

²S. E. Park and T. R. Shrout, J. Appl. Phys. **82**, 1804 (1997).

³S. F. Liu, S. E. Park, T. R. Shrout, and L. E. Cross, J. Appl. Phys. **85**, 2810 (1999).

⁴S. Nomura, T. Takahashi, and Y. Yokomizo, J. Phys. Soc. Jpn. **27**, 262 (1969).

⁵J. Kuwata, K. Uchino, and S. Noemura, Ferroelectrics **37**, 579 (1981).

⁶J. Kuwata, K. Uchino, and S. Noemura, Jpn. J. Appl. Phys., Part 1 **21**, 1298 (1982).

⁷J. Yin, B. Jiang, and W. Cao, Proc. SPIE, Medical Imaging, San Diego, CA (1999).

⁸J. Yin, B. Jiang and W. Cao, IEEE Trans. Ultrason. Ferroelectr. Freq. Control **43**, 285 (2000).

⁹J. Erhart and W. Cao, J. Appl. Phys. **86**, 1073 (1999).

¹⁰J. Erhart and W. Cao (unpublished).

APPENDIX 94

Computer Simulations of Domain Pattern Formation in Ferroelectrics

Rajeev Ahluwalia and Wenwu Cao

Materials Research Lab, The Pennsylvania State University, PA 16802, USA

Abstract. We study domain pattern formation in ferroelectrics based on a 2-D time-dependent Ginzburg Landau theory. The model includes electrostrictive and elastic effects in the form of a long-range interaction between the polarization fields that is obtained by eliminating the strain fields subject to the elastic compatibility constraint. We simulate a 2-D square to rectangle transition that has four equivalent polarization states in the ferroelectric phase. Starting from an unstable paraelectric state, we simulate the domain pattern evolution in the absence of external electric field. For the case without defects, the final pattern is a twinned state that has only head to tail (uncharged) domain walls. However, for the case with randomly distributed dipolar defects, head to head and tail to tail charged walls are observed. These results are in accordance with recent experiments where charged domain walls have been observed.

It is now well established that the ferroelectric transformation is accompanied by the formation of domains of the low temperature phase states. Ferroelectric materials that have only two polarization states usually form strain free 180° domains. However for multiple degenerate systems, such as BaTiO_3 and PZT, the electrostrictively generated strain is responsible for the creation of 90° domain walls. It is important to understand the mechanism of formation of these domain structures as physical properties like the dielectric constant and hysteresis are mainly governed by motion of the domain walls.

A useful technique to study the domain pattern formation in phase transitions is the time-dependent Ginzburg Landau (TDGL) theory. In the context of ferroelectric phase transitions, this approach has been successfully used to study the formation and growth of domains [1-4]. In this article, we use a TDGL model to study pattern formation in a model 2-D ferroelectric system that has four degenerate polarization states. We also include the electrostrictive coupling of polarization with the strain and the contributions due to randomly distributed dipolar defects.

The 3-D free-energy including strain and electrostrictive coupling has been given before [5]. For simplicity, we consider a 2-D square to rectangle ferroelectric transition in the absence of an external field with free-energy given as

$$F = \int d\vec{r} [f_l + f_g + f_{el} + f_{es} + f_d] \quad (1)$$

where f_l is a Landau free energy density given as

$$f_l = \frac{\alpha_1}{2} (P_x^2 + P_y^2) + \frac{\alpha_{11}}{4} (P_x^4 + P_y^4) + \frac{\alpha_{12}}{2} P_x^2 P_y^2 \quad (2)$$

Here, f_l is identical to the free energy density used in earlier works [4,5]. The gradient energy f_g is given as

$$f_g = \frac{g_1}{2} \left[\left(\frac{\partial P_x}{\partial x} \right)^2 + \left(\frac{\partial P_y}{\partial y} \right)^2 \right] + \frac{g_2}{2} \left[\left(\frac{\partial P_x}{\partial y} \right)^2 + \left(\frac{\partial P_y}{\partial x} \right)^2 \right] + g_3 \left(\frac{\partial P_x}{\partial x} \right) \left(\frac{\partial P_y}{\partial y} \right). \quad (3)$$

The free energy contribution due to randomly distributed dipolar defects is given as $f_d = -\vec{E}_d \cdot \vec{P}$, where $\vec{E}_d(\vec{r}) = -\vec{\nabla} V_d(\vec{r})$. The potential V_d represents a configuration of randomly placed defect dipoles given as

$$V_d(\vec{r}_i) = \sum_j^{n_d} \left[\frac{1}{|\vec{r}_i - (\vec{r}_j + \vec{\delta})|} - \frac{1}{|\vec{r}_i - (\vec{r}_j - \vec{\delta})|} \right] q_0(\vec{r}_j) \quad (4)$$

Here q_0 represents the coarse-grained charge and δ the displacement associated with the defect dipole centered at \vec{r}_j . The elastic energy of the system can be written in terms of the bulk strain $\phi_1 = (\eta_{xx} + \eta_{yy})/\sqrt{2}$, the deviatoric strain $\phi_2 = (\eta_{xx} - \eta_{yy})/\sqrt{2}$ and the shear strain $\phi_3 = \eta_{xy} = \eta_{yx}$. Here η_{ij} is the linear elastic strain tensor. The elastic free energy can then be written as

$$f_{el} = \frac{a_1}{2} \phi_1^2 + \frac{a_2}{2} \phi_2^2 + \frac{a_3}{2} \phi_3^2 \quad (5)$$

where a_1 , a_2 and a_3 are linear combinations of second order elastic constants. Similarly, the electrostrictive energy in terms of the electrostrictive constants q_1 , q_2 and q_3 is given as

$$f_{es} = -q_1 \phi_1 (P_x^2 + P_y^2) - q_2 \phi_2 (P_x^2 - P_y^2) - q_3 \phi_3 P_x P_y \quad (6)$$

Following the methodology used in earlier work [4], the elastic and electrostrictive contributions can be expressed as an effective long-range interaction between the polarization fields by eliminating the strain fields subject to the elastic compatibility conditions. The effective long-range interaction in fourier space is then given as

$$F_{eff} = \frac{q_2^2}{2a_2} \int d\vec{k} H(\vec{k}) |\Gamma_2(\vec{k})|^2 \quad (7)$$

$$H(\vec{k}) = h_1^2(\vec{k})/\alpha + h_2^2(\vec{k}) - 2h_2(\vec{k}) + h_3^2(\vec{k})/\beta \quad (8)$$

and $\Gamma_2(\vec{k})$ is the fourier transform of $P_x^2 - P_y^2$. The quantities h_1, h_2 and h_3 are given as $h_1(\vec{k}) = k^2 Q(\vec{k})$, $h_2(\vec{k}) = \{1 - (k_x^2 - k_y^2)Q(\vec{k})\}$ and $h_3(\vec{k}) = -\sqrt{8}k_x k_y Q(\vec{k})$, where

$$Q(\vec{k}) = \frac{(k_x^2 - k_y^2)}{(k^4/\alpha + (k_x^2 - k_y^2)^2 + 8k_x^2 k_y^2/\beta)} \quad (9)$$

where $\alpha = a_1/a_2$ and $\beta = a_3/a_2$. Here, we should remark that the above interaction has been obtained by assuming no coupling of the polarization with bulk and shear strains, i.e., $q_1 \rightarrow 0$ and $q_3 \rightarrow 0$. In order to catch the essential physics and reduce the computational difficulties, the coupling to bulk and shear strains are not included in this work. Based on experimental results, the bulk strain is small in most of the ferroelectric materials and the shear strain does not exist at all the single domain regions for the case under study. Thus we believe that this assumption will not introduce significant errors in the study of domain pattern formation.

In order to study the dynamics of domain pattern formation, we make use of the time-dependent Ginzburg-Landau equations (TDGL). We introduce rescaled variables as follows: $t = (t^*/|\alpha_1|L)$, where L is the kinetic coefficient, $\vec{r}^* = \vec{r}/\phi$ ($\phi = \sqrt{g_1/a|\alpha_1|}$), where a is a dimensionless constant. The polarization is transformed as $P_x = P_R u$ and $P_y = P_R v$, where $P_R = \sqrt{|\alpha_1|/|\alpha_{11}|}$ is the remnant polarization of the homogeneous state without elastic effects. With this set of rescaled parameters, the TDGL equations are given as

$$\begin{aligned} u_{,t} = & u - u^3 - duv^2 + au_{,x} \cdot x + bu_{,y} \cdot y + cv_{,x} \cdot y + \epsilon_x \\ & - \gamma u \int d\vec{k}^* H(\vec{k}^*) \Gamma(\vec{k}^*) \exp(-i\vec{k}^* \cdot \vec{r}^*) \\ v_{,t} = & v - v^3 - dvu^2 + av_{,x} \cdot x + bv_{,y} \cdot y + cu_{,x} \cdot y + \epsilon_y \\ & + \gamma v \int d\vec{k}^* H(\vec{k}^*) \Gamma(\vec{k}^*) \exp(-i\vec{k}^* \cdot \vec{r}^*) \end{aligned} \quad (10)$$

Here $\vec{\epsilon}$ is the rescaled electric field due to the randomly distributed defect dipoles, with $q_0^*(\vec{r}^*) = [q_0(\vec{r})/P_R \phi^2 |\alpha_1|]$. In the rescaled equations, the constant

$d = (\alpha_{12} / \alpha_{11})$, $\gamma = (q_2^2 / \alpha_{11} a_2)$, $b = (g_2 / |\alpha_1| \phi^2)$ and $c = (g_3 / |\alpha_1| \phi^2)$. $\Gamma(\vec{k}^*)$ is the fourier transform of $u^2 - v^2$.

To study the domain patterns, equation (10) is discretized using finite differences on a 128×128 grid with periodic boundary conditions. The space discretization step is set as $\Delta x^* = \Delta y^* = 1$ and the time interval $\Delta t^* = 0.02$. The parameters chosen for the simulation are $d=2$ and $\gamma=0.05$. The gradient coefficients are chosen as $a=b=c=10$ and the elastic parameters are $\alpha=\beta=1$. We first describe the simulation of domain pattern formation for the case without dipolar defects ($\epsilon_x = \epsilon_y = 0$), starting from small amplitude initial conditions corresponding to a paraelectric phase. Figure 1 displays the time evolution of domains for the defect free case. The direction of the arrows in figure 1 is the polarization direction and the magnitude is proportional to the length. In figure 1(a) ($t^* = 0.5$) we can clearly see the appearance of domains with non-zero polarization. However, these domains are still randomly oriented. In figure 1(b) ($t^* = 12.5$), four distinct kind of polarization domains corresponding to the minima of equation (2) can be observed. Note that at this stage both charged as well as uncharged domain walls are observed. We can also observe that the domain walls are beginning to get oriented along $[11]$ or $[1\bar{1}]$. This is due to the long-range anisotropic interaction which prefers alignment along the 45° directions. As we go further in time, the domain walls move in order to get rid of the head to head and tail to tail configurations. As we can observe in figure 1(c) ($t^* = 125$), head to tail domain walls aligned along $[11]$ or $[1\bar{1}]$ are dominant. Finally, in figure 1(d) ($t^* = 500$), we can see that we have a twinned pattern that has only head to tail uncharged domain walls.

Next, we describe our results for pattern evolution for the case with defects. For the defect field \vec{e} , we take q_0^* to be uniformly distributed in the interval $[0.01, 0.03]$. The charge separation $\vec{\delta}^*$ can take the value $(\pm c, 0)$ or $(0, \pm c)$, where c is a random number uniformly distributed in the interval $[0.08, 0.1]$. The defect field is initialized by selecting random points on the discrete grid. We choose the number of defects to $n_d = 327$ (2% of the total number of grid points). The initial conditions for the polarization fields are the same as in the defect free case. In figure 2(a) ($t^* = 0.5$), we can see the early time snapshot where most of the system is still paraelectric. It is clear that randomly distributed dipoles locally try to align the polarization. These defects strongly influence the dynamics and the eventual state. In figure 2(b) ($t^* = 25$), we can see domains of all four degenerate states coexisting. Interestingly, the number of charged and 180° walls for this case is much more compared to the defect free case at similar stages of the evolution. We believe that this is due to the dipolar defects which locally influence the domain pattern and lead to a pinning of the domains, which makes the domain dynamics slower. The system tries to get rid of charged walls, as can be seen by comparing figure 2(b) and figure 2(c) ($t^* = 250$). However, in this case the system gets arrested in a metastable state

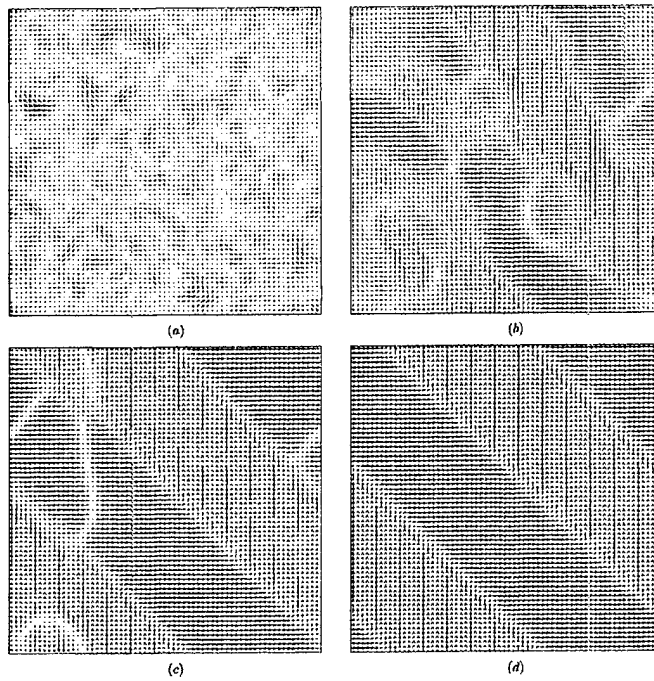


Figure 1. Domain evolution for defect free case

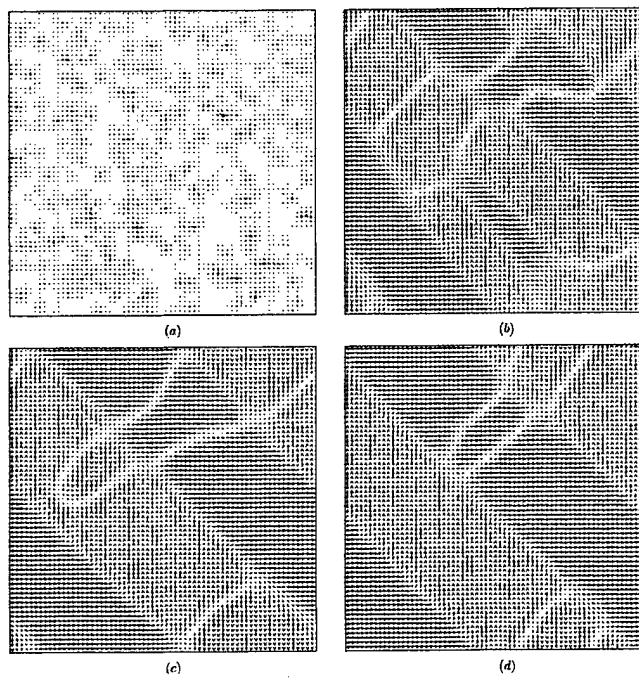


Figure 2. Domain evolution for case with defects

that has charged as well as uncharged walls. This is clear from figure 2(d)($t^* = 1000$), which is the final state as running the simulation longer does not change the domain pattern noticeably.

To conclude, we have made a study of domain pattern formation in ferroelectrics based on the TDGL approach and incorporating elastic coupling. Domain structures evolve with time with domain walls oriented along the $[11]$ or $[1\bar{1}]$ directions. This wall direction is preferred to ensure the strain compatibility at the interfaces. For the case with defects, we find that in addition to the uncharged 90° walls, charged walls and 180° walls are stabilized due to the dipolar defects. These results are in agreement with recent experiments on PZN-PT single crystals [6]. Although, our model is phenomenological, we have been able to simulate the ferroelectric microstructure qualitatively based on a coarse grained picture. Unfortunately, not all coefficients in the Landau theories are experimentally measured which makes it difficult to give more quantitative predictions. However, our results have demonstrated that the TDGL theory can be used to simulate domain related phenomena in ferroelectric systems if all parameters are measured experimentally.

ACKNOWLEDGEMENT

We acknowledge the support of Office of Naval Research.

REFERENCES

1. S. Nambu and D.A. Sagala, Phys. Rev. B 50, 5838(1994)
2. H.L Hu and L.Q. Chen, Materials. Science. Engineering A 238, 182(1997)
3. W. Cao, S. Tavener and S. Xie, J. Appl. Phys. 86, 5793(1999)
4. R. Ahluwalia and W. Cao, Phys. Rev. B 63, 012103(2001)
5. W. Cao and L. E. Cross, Phys. Rev. B 44, 5(1991)
6. J. Yin and W. Cao, J. Appl. Phys. 87, 133(2000)

APPENDIX 95

Influence of dipolar defects on switching behavior in ferroelectrics

Rajeev Ahluwalia and Wenwu Cao

Materials Research Laboratory, The Pennsylvania State University, University Park, Pennsylvania 16802

(Received 25 July 2000; published 11 December 2000)

By including the contributions of dipolar defects in the time-dependent Ginzburg-Landau theory, we have simulated the domain switching process in ferroelectrics. The model incorporates elastic effects in the form of an anisotropic long-range interaction that is obtained by integrating out the strain fields, subject to the elastic compatibility constraint. The defects are simulated by considering an inhomogeneous electric field due to randomly placed coarse-grained dipoles. It is shown that these defects act as nuclei for the formation of 90° twinned structures, resulting in a lower coercive field compared to the defect-free case. Due to these defects, the simulated polarization switching occurs by two successive 90° rotations, rather than a single 180° flipping as in the defect-free case.

DOI: 10.1103/PhysRevB.63.012103

PACS number(s): 77.80.Dj, 64.70.Kb, 77.80.Fm

The spontaneous polarization in ferroelectrics can be reversed when a strong electric field is applied opposite to the polarization direction. It is crucial to understand the details of this switching process in order to produce better materials for memory devices. It has been recognized that the switching process is influenced by the presence of defects which are present in the form of vacancies and dopants.¹ Due to the localized nucleation of domains of reversed polarization, the experimentally measured coercive field is usually smaller than the *intrinsic* value predicted by the simple one-dimensional (1D) Landau theory. A recent work indicated that the *intrinsic* coercive field can be realized in a Langmuir-Blodgett polymer film, which is thin enough to bypass localized nucleation.²

The exact mechanism of polarization switching is, however, still lacking at the moment. Although some interesting simulations on defect-free systems have been reported,³ a more realistic model is needed, which can take into account the defect nucleation and the motion of domain walls, as well as the influence of elastic strain.

Time-dependent Ginzburg-Landau (TDGL) equations have been used to study pattern formation in ferroelectrics.⁴⁻⁶ These works, however, have focused only on the domain pattern formation aspects and did not attempt to describe switching phenomena and the role played by defects. In this paper, we report a simulation study of polarization switching in ferroelectrics, based on the TDGL approach. Specifically, we will address the issue of nucleation from localized dipolar defects and the influence of elastic long-range interactions.

The 3D Ginzburg-Landau free energy for ferroelectric systems has been given before.⁷ In this work, we restrict ourselves to a 2D system undergoing a square to rectangle transition, which is analogous to the cubic to tetragonal phase transition in 3D. The total free energy is written as

$$F = \int d\vec{r} [f_l + f_g + f_{el} + f_{es} + f_{ext} + f_d], \quad (1)$$

where f_l is the local free-energy density given by

$$f_l = \frac{\alpha_1}{2} (P_x^2 + P_y^2) + \frac{\alpha_{11}}{4} (P_x^4 + P_y^4) + \frac{\alpha_{12}}{2} P_x^2 P_y^2, \quad (2)$$

and f_g is the gradient energy,

$$f_g = \frac{g_1}{2} \left[\left(\frac{\partial P_x}{\partial x} \right)^2 + \left(\frac{\partial P_y}{\partial y} \right)^2 \right] + \frac{g_2}{2} \left[\left(\frac{\partial P_x}{\partial y} \right)^2 + \left(\frac{\partial P_y}{\partial x} \right)^2 \right] + g_3 \left(\frac{\partial P_x}{\partial x} \right) \left(\frac{\partial P_y}{\partial y} \right). \quad (3)$$

It has been shown that the gradient energy may be obtained as a local approximation to the dipole-dipole interactions.¹ The term f_{el} represents the usual elastic energy of the square system. We consider the bulk strain $\phi_1 = (\eta_{xx} + \eta_{yy})/\sqrt{2}$, deviatoric strain $\phi_2 = (\eta_{xx} - \eta_{yy})/\sqrt{2}$, and shear strain $\phi_3 = \eta_{xy} = \eta_{yx}$. Here η_{ij} is the linear elastic strain tensor given as $\eta_{ij} = \frac{1}{2}(\partial u_i/\partial x_j + \partial u_j/\partial x_i)$. The elastic free energy can then be written as

$$f_{el} = \frac{a_1}{2} \phi_1^2 + \frac{a_2}{2} \phi_2^2 + \frac{a_3}{2} \phi_3^2, \quad (4)$$

where a_1 , a_2 , and a_3 are constants that can be expressed in terms of linear combinations of elastic constants of the system. The coupling energy f_{es} may be written as

$$f_{es} = -q_1 \phi_1 (P_x^2 + P_y^2) - q_2 \phi_2 (P_x^2 - P_y^2) - q_3 \phi_3 P_x P_y. \quad (5)$$

Here q_1 , q_2 , and q_3 are constants that are related to the electrostrictive constants of the system. The term f_{ext} is given by $f_{ext} = -\vec{E}_{ext} \cdot \vec{P}$. The amplitude of field \vec{E}_{ext} is a tunable parameter in our simulations for studying polarization switching. The term f_d represents the free-energy contribution due to randomly distributed coarse-grained dipolar defects given as $f_d = -\vec{E}_d \cdot \vec{P}$, where $\vec{E}_d = -\vec{\nabla} V_d$. The potential V_d represents a configuration of randomly placed dipoles given as

$$V_d(\vec{r}_i) = \sum_j \left[\frac{q_0(\vec{r}_j)}{|\vec{r}_i - (\vec{r}_j + \vec{\delta}_j)|} - \frac{q_0(\vec{r}_j)}{|\vec{r}_i - (\vec{r}_j - \vec{\delta}_j)|} \right]. \quad (6)$$

Here $q_0(\vec{r}_j)$ represents the coarse-grained charge and $\vec{\delta}(\vec{r}_j)$ the displacement associated with the defect dipole centered

at \vec{r}_i . We assume that the system reaches mechanical equilibrium very fast so that we may integrate out the elastic fields, subject to the elastic compatibility constraint.⁸ In terms of the strain components ϕ_1 , ϕ_2 , and ϕ_3 , the elastic compatibility relation is given as

$$\nabla^2 \phi_1 - \left(\frac{\partial^2}{\partial x^2} - \frac{\partial^2}{\partial y^2} \right) \phi_2 - \sqrt{8} \frac{\partial^2}{\partial x \partial y} \phi_3 = 0. \quad (7)$$

To incorporate the elastic compatibility constraint, we consider an effective elastic part of the free energy $F_{eff} = F_{el} + F_{es} + F_{cons}$, with Lagrangian multiplier λ , where

$$F_{el} = \int d\vec{k} \left[\frac{a_1}{2} |\phi_1(\vec{k})|^2 + \frac{a_2}{2} |\phi_2(\vec{k})|^2 + \frac{a_3}{2} |\phi_3(\vec{k})|^2 \right], \quad (8)$$

$$F_{es} = - \int d\vec{k} \{ q_1 \Gamma_1(\vec{k}) \phi_1(-\vec{k}) + q_2 \Gamma_2(\vec{k}) \phi_2(-\vec{k}) + q_3 \Gamma_3(\vec{k}) \phi_3(-\vec{k}) \} \quad (9)$$

$$F_{cons} = \int d\vec{k} \{ \lambda(\vec{k}) [-k^2 \phi_1(-\vec{k}) + (k_x^2 - k_y^2) \phi_2(-\vec{k}) + \sqrt{8} k_x k_y \phi_3(-\vec{k})] \}. \quad (10)$$

Here $k^2 = k_x^2 + k_y^2$ and $\Gamma_1(\vec{k})$, $\Gamma_2(\vec{k})$, and $\Gamma_3(\vec{k})$ are, respectively, the Fourier transforms of $P_x^2 + P_y^2$, $P_x^2 - P_y^2$, and $P_x P_y$. The condition of mechanical equilibrium and the compatibility relation demands $\delta F_{eff} / \delta \phi_i = 0$ ($i=1,2,3$) and $\delta F_{eff} / \delta \lambda = 0$. Since the square to rectangular transition does not involve shear strain and the bulk strain is isotropic, the first and third terms in Eq. (5) do not have much influence on the characteristics of the domain formation. For computational simplicity, we will consider only the deviatoric strain coupling, i.e., $q_1 \rightarrow 0$ and $q_3 \rightarrow 0$; using the equilibrium conditions, the free energy F_{eff} can be expressed in Fourier space as

$$F_{eff} = \frac{q_2^2}{2a_2} \int d\vec{k} H(\vec{k}) |\Gamma_2(\vec{k})|^2, \quad (11)$$

where $H(\vec{k}) = [h_1^2(\vec{k})/\alpha + h_2^2(\vec{k}) - 2h_2(\vec{k}) + h_3^2(\vec{k})/\beta]$. The quantities $h_1(\vec{k}) = k^2 Q(\vec{k})$, $h_2(\vec{k}) = \{1 - (k_x^2 - k_y^2) Q(\vec{k})\}$, and $h_3(\vec{k}) = -\sqrt{8} k_x k_y Q(\vec{k})$, with $Q(\vec{k})$ defined as

$$Q(\vec{k}) = \frac{(k_x^2 - k_y^2)}{[k^4/\alpha + (k_x^2 - k_y^2)^2 + 8k_x^2 k_y^2/\beta]}. \quad (12)$$

We have introduced the dimensionless constants $\alpha = a_1/a_2$ and $\beta = a_3/a_2$.

The effective interaction derived above is strongly direction dependent and is crucial to describe the domain wall orientations. Similar anisotropic interactions have been considered in context of martensitic transformations.^{9,10}

As we wish to study heterogeneous nucleation, a dynamical formalism is needed to describe the nonequilibrium effects associated with domain switching. Here the TDGL

model for the polarization fields is used. We introduce rescaled time variables $t^* = (t|\alpha_1|L)$ ($\alpha_1 < 0$) (L is the kinetic coefficient) and space variable $\vec{r}^* = \vec{r}/\phi$ ($\phi = \sqrt{g_1/a|\alpha_1|}$), where a is a dimensionless constant. The polarization field is transformed as $P_x = P_R u$ and $P_y = P_R v$, where $P_R = \sqrt{|\alpha_1|/\alpha_{11}}$ is the remnant polarization of the homogeneous state without elastic effects. With this set of normalized parameters, the dimensionless TDGL equations are given as

$$\begin{aligned} u_{,t^*} &= u - u^3 - duv^2 + au_{,x^*x^*} + bu_{,y^*y^*} + cu_{,x^*y^*} + \epsilon_x + e_x \\ &\quad - \gamma u \int d\vec{k}^* H(\vec{k}^*) \Gamma(\vec{k}^*) \exp(-i\vec{k}^* \cdot \vec{r}^*), \\ v_{,t^*} &= v - v^3 - dvu^2 + av_{,y^*y^*} + bv_{,x^*x^*} + cu_{,x^*y^*} + \epsilon_y + e_y \\ &\quad + \gamma v \int d\vec{k}^* H(\vec{k}^*) \Gamma(\vec{k}^*) \exp(-i\vec{k}^* \cdot \vec{r}^*). \end{aligned} \quad (13)$$

Here, $\vec{e} = \vec{E}_{ext}/(P_R|\alpha_1|)$ is the rescaled external electric field and $\vec{\epsilon}$ is the rescaled electric field due to the dipoles, with $q^*_0(\vec{r}^*) = [q_0(\vec{r})/P_R\phi^2|\alpha_1|]$. The constants defined are $b = (g_2/|\alpha_1|\phi^2)$, $c = (g_3/|\alpha_1|\phi^2)$, $d = (\alpha_{12}/\alpha_{11})$, and $\gamma = (q_2^2/\alpha_{11}\phi^2 a_2)$. The quantity $\Gamma(\vec{k}^*)$ is the Fourier transform of $(u^2 - v^2)$.

We now describe the details of our simulations on the switching behavior. Equation (13) is discretized using the Euler scheme on a 128×128 grid. Periodic boundary conditions are applied in both x^* and y^* directions, corresponding to a clamped infinite system. The space discretization step $\Delta x^* = \Delta y^* = 1$ and the time interval $\Delta t^* = 0.02$. The parameter values chosen for the simulation are $d = 0.5$ and $\gamma = 0.05$. The gradient coefficients are chosen as $a = b = c = 2$. Similarly, we choose the elastic parameters as $\alpha = \beta = 1$. For the defect field $\vec{\epsilon}$, we take q^*_0 to be uniformly distributed in the interval $[0.01, 0.03]$. The charge separation $\vec{\delta}^*$ can take the value $(\pm c, 0)$ or $(0, \pm c)$, where c is a random number uniformly distributed in the interval $[0.08, 0.1]$. The defect field is initialized by selecting random points on the discrete grid. We choose the number of defects to be $n_d = 81$ ($\sim 0.5\%$ of the total points on the discrete grid). Then, the electric field due to these defects is calculated at each grid point. We start the simulations by taking a trial single-domain configuration $u(\vec{r}^*, t^* = 0) = 4$, $v(\vec{r}^*, t^* = 0) = 0$, and $e_x(t = 0) = 25$. Under the external electric field, the trial configuration rapidly evolves into a single-domain state with the polarization in the positive x^* direction (except in the vicinity of the defects, where the polarization field is distorted, according to the defect field). After every interval of $t_w^* = 50$ (2500 iterations), the electric field is changed with time as $e_x(t^*) = 25 - 50(t^*/t_{max}^*)$, where $t_{max}^* = 10\,000$ is the total number of time steps. Figure 1 displays sequence of domain snapshots for different values of t^* and e_x . The direction of the arrow shows the local polarization direction and the length of the arrows is proportional to the magnitude of \vec{P} . In Fig. 1(a), we can see a single domain poled along the $+x^*$ direction, corresponding to $t^* = 4499$ and e_x

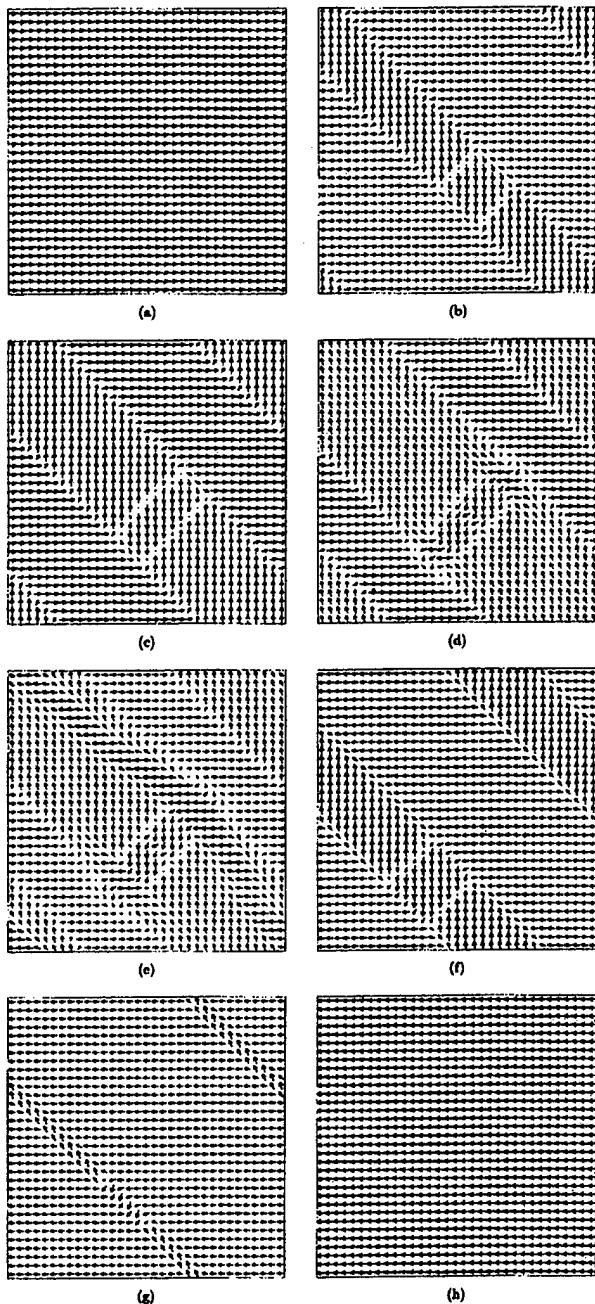


FIG. 1. Pattern evolution for the simulated quasistatic switching. The snapshots correspond to (a) $t^*=4499$, $e_x=2.75$; (b) $t^*=4749$, $e_x=1.5$; (c) $t^*=5049$, $e_x=0$; (d) $t^*=5110$, $e_x=-0.5$; (e) $t^*=5115$, $e_x=-0.5$; (f) $t^*=5249$, $e_x=-1$; (g) $t^*=8499$, $e_x=-17.25$; (h) $t^*=9249$, $e_x=-21$.

$=2.75$. However, at defect sites, polarization inhomogeneities are observed. As we quasistatically decrease the field further, we find that the polarization decreases almost instantaneously in response to change in e_x . However, as the field value reaches $e_x=2$, some of the polarization inhomogeneities nucleate orthogonally polarized domains. In Fig. 1(b) ($t^*=4749$, $e_x=1.5$), we can see a well-developed domain pattern with 90° as well as 180° twin boundaries. Notice that

there are head to head as well as head to tail configurations. This is in agreement with recent experiments where charged domain walls have been observed in bulk multidomain single crystals.¹¹ It is believed that charged domain walls may be stabilized due to charged defects. On decreasing the field further, the orthogonally polarized domains grow by sideways motion. The 180° domain walls also move in order to get rid of head-head and tail-tail domain walls. This growth can be clearly seen by comparing Fig. 1(b) with Fig. 1(c) (corresponding to $t^*=5049$ and $e_x=0$). Figures 1(d) ($t^*=5110$) and 1(e) ($t^*=5115$) show the nucleation and growth of domains with reversed polarization when the field value becomes $e_x=-0.5$. It is clear that these domains nucleate at the 90° twin boundaries. The nucleation of reverse polarization domains from 90° twin boundaries has indeed been observed in recent experiments on lead zirconate titanate thin films.¹² The nucleated reverse domains grow anisotropically along the twin boundary, as reported in the experiments of Ganpule *et al.*¹² As we can see, contrary to the classical picture of 180° polarization flipping, the growth of reversed domains occurs by 90° reorientations in our simulations. Figure 1(f) shows the domain pattern at $t^*=5249$ and $e_x=-1$. Thus, even beyond the coercive field ($e_c \sim -0.5$), complete reversal is not achieved as the defects tend to pin the domain pattern. In Fig. 1(g) we can see that at $t^*=8499$ and $e_x=-17.25$. The reversed polarization domains grow sideways at the expense of orthogonally polarized domains. Finally, when the external field is high enough, we get a single-domain state of the reversed phase as shown in Fig. 1(h) ($t^*=9249$, $e_x=-21$). We continue decreasing the field until $t^*=t^*_{max}$ and $e_x=-25$. The reverse cycle is studied by increasing the field in the same way until $e_x=25$, starting from the final single-domain configuration at $e_x=-25$.

The hysteresis loop, obtained by computing the average x^* component of the rescaled polarization $\langle u \rangle$, is plotted in Fig. 2(a). Also plotted in Fig. 2(a) is the hysteresis loop corresponding to the case without defects. We observe that due to the nucleation of 90° domains, the coercive field for the loop with defects is less than half of the coercive field for the defect-free case. It is also interesting to note that within the range shown in Fig. 2(a), the curves for the defect-free case and the case with defects do not coincide. We have to go to much higher field values for the two curves to match. This is due to the fact that defects pin the domain walls. Another interesting consequence of the dipolar defects is the dependence of the hysteresis loop on the waiting time t_w^* . In Fig. 2(b), we plot the hysteresis loops obtained from identical simulations but with different values of waiting times. We can see that the coercive field seems to increase as the waiting time is decreased. This behavior has also been observed in experiments on ceramics and single crystals.^{13,14} The waiting time dependence can be understood on the basis of the defect nucleation mechanism. If the waiting times are short, the nucleated domains have no time to grow, thereby delaying the switching process.

To summarize, we have studied the influence of dipolar

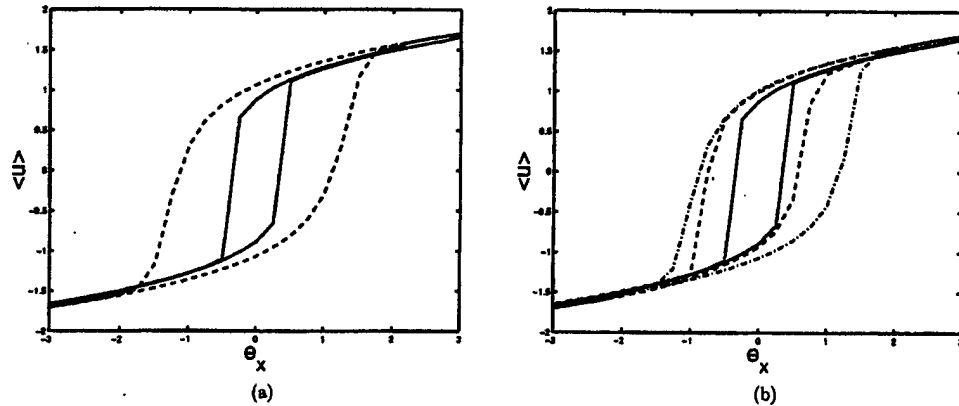


FIG. 2. Plots of $\langle u \rangle$ vs e_x showing the hysteresis loops: (a) the simulated loops for the case with defects (solid line) and the defect-free case (dashed line); (b) the waiting time dependence of the loops for the case with defects for $t_w^* = 50$ (solid line), $t_w^* = 5$ (dashed line), and $t_w^* = 1$ (dot-dashed line).

defects on switching in ferroelectrics, based on the TDGL approach. We find that defects have a remarkable effect on the hysteresis; in particular, the coercive field is reduced due to nucleation events which assist the polarization reversal. We also find that switching occurs by successive 90° rotations for a clamped system. Recent ultrasonic measurements¹⁵ on PZN-PT single crystals have demon-

strated that such a mechanism may indeed be occurring in some ferroelectrics. We also observe the dependence of the coercive field on waiting time, in accordance with several reported experiments.

This research was supported by the Office of Naval Research.

¹M. E. Lines and A. M. Glass, *Principles and Applications of Ferroelectrics and Related Materials* (Clarendon, Oxford, 1979).

²Stephen Ducharme, V. M. Fridkin, A. V. Bune, S. P. Palto, L. M. Blinov, N. N. Petukhova, and S. G. Yudin, *Phys. Rev. Lett.* **84**, 175 (2000).

³S. C. Hwang and G. Arit, *J. Appl. Phys.* **87**, 869 (2000).

⁴S. Nambu and D. A. Sagala, *Phys. Rev. B* **50**, 5838 (1994).

⁵Hong-Liang Hu and Long-Qing Chen, *Mater. Sci. Eng., A* **238**, 182 (1997).

⁶Wenwu Cao, S. Tavener, and S. Xie, *J. Appl. Phys.* **86**, 5739 (1999).

⁷Wenwu Cao and L. E. Cross, *Phys. Rev. B* **44**, 5 (1991).

⁸E. A. H. Love, *A Treatise on the Mathematical Theory of Elas-*

ticity (Dover, New York, 1944), p. 49.

⁹S. Kartha, J. A. Krumhansl, J. P. Sethna, and L.K. Wickham, *Phys. Rev. B* **52**, 803 (1995).

¹⁰S. R. Shenoy, T. Lookman, A. Saxena, and A. R. Bishop, *Phys. Rev. B* **60**, R12 537 (1999).

¹¹Jianhua Yin and Wenwu Cao, *J. Appl. Phys.* **87**, 7438 (2000).

¹²C. S. Ganpule, V. Nagarajan, H. Li, A. S. Ogale, D. E. Steinhauer, S. Aggarwal, E. Williams, R. Ramesh, and P. De Wolf, *Appl. Phys. Lett.* **77**, 292 (2000).

¹³Yun-Han Chen and Dwight Viehland, *Appl. Phys. Lett.* **77**, 133 (2000).

¹⁴Jianhua Yin and Wenwu Cao (unpublished).

¹⁵Wenwu Cao and Jianhua Yin (unpublished).

APPENDIX 96

Field Induced Acoustic Emission (AE) in Ferroelectric Ceramics

Kenji Uchino and Hideaki Aburatani

International Center for Actuators and Transducers (ICAT),
Intercollege Materials Research Laboratory, The Pennsylvania State University,
University Park, PA 16802, USA

Abstract — Electric field induced acoustic emission (AE) in ferroelectric PZT ceramics has been studied. It was shown that the field induced AE originated from where the displacement was induced and ended when the applied field was being reduced during poling. A larger electric field than the previously applied maximum field was required for new AE generation (Kaiser effect). From the AE event rate and the AE signal amplitude distribution, it was assumed that there were two origins of the bipolar field induced AE in the ferroelectric ceramics: deformation related to domain reorientation and piezoelectric deformation without domain reorientation.

§1. Introduction

In ferroelectric materials, the AE method has been used to determine phase change,¹⁻³⁾ to detect domain reorientation⁴⁻⁶⁾ and to monitor crack propagation.⁷⁻⁹⁾ It has been believed that ferroelectric domain motion is a dominant AE source in the ferroelectrics. However, our recent research has shown a significant measurement problem in the most of previous field induced AE studies.¹⁰⁾ A mechanical vibration of sample is easily excited by an electrical coupling between the power supply feedback and the piezoelectricity of sample, resulting in a vibro-acoustic emission. The vibro-acoustic emission could vary with electric field, and was similar to the reported field induced AE results. The sample vibration could be eliminated by increasing the time constant τ of the voltage (field) application system. It was shown that this modified voltage (field) application method makes the field induced AE measurements at high sensitivities possible without vibro-acoustic emissions. Considerably different AE results from the reported field induced AE were obtained using the modified method. The AE appeared to be

observed from where the displacement was induced during poling. New AE will not be generated after sufficient poling.

This paper deals with the electric field induced AE generations in a ferroelectric lead zirconate titanate $\text{Pb}(\text{Zr}_x\text{Ti}_{1-x})\text{O}_3$ (PZT) ceramics. The field induced AE activities were analyzed by comparing them with obtained induced displacement. A fractal dimension analysis of the AE signal amplitude distribution was also applied.

§2. Experimental Setup

Figure 1 shows the field induced AE and displacement measurement system. The sample was placed on the AE sensor (NF Corporation, AE-904E) with its resonant frequency of 450 kHz. The induced displacement was also observed using a L.V.D.T (Millitoron, Nr. 1301). The AE signal was amplified by 40 dB through a low noise pre-amplifier (NF Corporation, AE-9913) and again up to 60 dB with a main amplifier (NF Corporation, AE-922). The amplified AE signals were counted after passing through a high-pass filter ($f > 100$ kHz) and a discriminator.

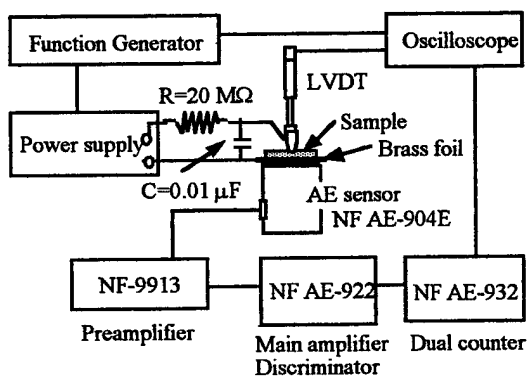


Figure 1 Field induced AE and displacement measurement system.

Disc specimens of commercialized ferroelectric lead zirconate titanate PZT ceramic (Morgan Matroc, PZT-5A) with 12.7 mm in diameter and 0.4 mm in thickness were employed for this study. Gold electrodes were formed on both surfaces by sputtering. The AE sensor was attached to the sample through brass-foil with 0.025 mm in thickness. A silicone grease was used as a couplant to make a better acoustical contact. An external resistor R ($R = 20 \text{ M}\Omega$) and a capacitor C ($C = 0.01 \text{ }\mu\text{F}$) were installed to the power supply in order to eliminate the vibro-acoustic emission.

§3. Results and Discussions

3.1 The Kaiser Effect in Field Induced AE

Figure 2 shows the AE event, induced displacement and applied electric field as a function of time for a cyclic application of various electric fields. The threshold level of the AE signal were set to be 400 mV at 100 dB. An unpoled sample was employed for this measurement. At the first cycle (poling), an electric field of 20 kV/cm was applied to the sample. The amplitude of the field was increased to be 25 kV/cm at the second cycle, and again up to 30 kV/cm at the third cycle.

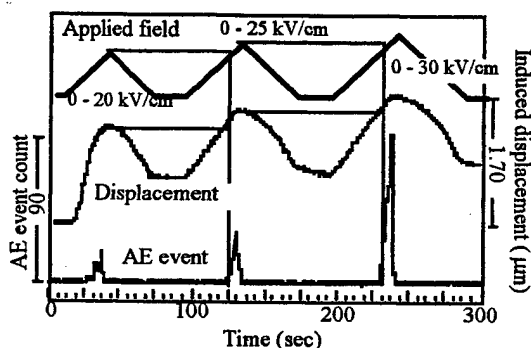


Figure 2 The AE event, induced displacement and applied electric field as a function of time for a cyclic application of various electric fields.

The sample was poled at the first cycle. The induced displacement and total residual displacement observed as a zero point shift

increased with amplitude of applied field, because the higher degree of poling is achieved by the applications of the larger electric fields. At first cycle, the AE event occurred from where the displacement was induced and increased with field. The AE was not generated during the field was being reduced. In the second cycle, no AE events were observed until the electric field reached $E = 20 \text{ kV/cm}$. New AE generation was observed above $E = 20 \text{ kV/cm}$, and increased with the electric field. In the third cycle, this AE onset field again shifted to be $E = 25 \text{ kV/cm}$. The AE was generated only when the applied field exceeded the previous maximum value. This pre-applied electric field (induced displacement) dependence of the AE generation implies a Kaiser effect in the electric field induced deformation of the PZT ceramics.

The domain motion has been believed to be origin of the field induced AE. However, it is shown that all domain motions can not be the origin of the field induced AE, because the field induced AE depends on the pre-applied electric field (Kaiser effect). Therefore, particular domain reorientation processes rather than domain motion should be considered to be the origins of the AE. Another possible AE source is a mechanical stress, since the mechanical stress is supposed to be induced in the sample at high strain (electric field) state.

3.2 The Electric Field Induced AE

Figure 3 shows the AE event count rate and the induced displacement as a function of applied field at 0.0015 Hz with field of $E = \pm 35 \text{ kV/cm}$. The AE measurement conditions were set to be at 100 dB with a threshold level of 400 mV. A butterfly shape induced displacement due to the domain reorientation was obtained. The critical electric field, where the AE started to be generated, corresponded to the point of inflection of the displacement with respect to the field. (In Fig 3, $d(\text{displacement})/dE$ is shown for the point of inflection.)

The maximum of AE event count rate was not observed at the maximum applied field. The maximum AE event rate was found to be around $E = 27 \text{ kV/cm}$. Considering that internal stress increases with the applied field in the ferroelectrics, this decrease in the AE event rate might imply that the internal stress could be the origin of the AE, but not only one source. The induced displacement in the ferroelectric

ceramics consists of the deformation related to domain reorientation and piezoelectric deformation without the domain reorientation. Therefore, it was supposed that the field induced AE under bipolar electric fields in the PZT ceramics was generated first through deformation related to domain reorientation. After the domain reorientation was completed, the piezoelectric deformation unrelated to domain reorientation, which accompanied with the induced internal stress, was expected to be the origin of the AE. The decrease in the AE event rate might indicate the completion of the domain reorientation related deformation.

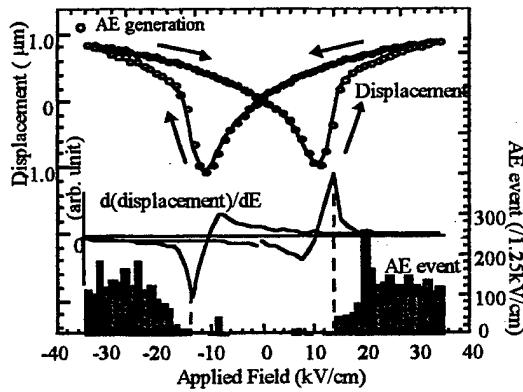


Figure 3 AE event count and the induced displacement as a function of applied field.

3.3 The Fractal Dimension of the Electric Field Induced AE

When the AE event rate $f(x)$ is the minus m -th power of x , where x is the AE signal amplitude,

$$f(x) = cx^{-m} \quad (c: \text{constant}). \quad (1)$$

The number of m is defined as a fractal dimension.¹¹⁾ The fractal dimension m is used to estimate the damage in the materials.

The integrated AE event $F(x)$,

$$F(x) = \int_x^\infty f(x) \cdot dx = \frac{1}{m-1} cx^{-m+1} \quad (m > 1) \quad (2)$$

was observed through changing the AE signal threshold level in the measurements.

Figure 4 shows the AE event count per cycle as a function of the AE signal threshold level.

The observed AE event count logarithmically decreased with the AE signal threshold level when a field of $E = \pm 25$ kV/cm was applied. Thus, a fractal dimension of $m=1$ ($\frac{d}{dx}[c \log x + A] = cx^{-1}$) was obtained for the logarithmic decrease. In general, the fractal dimension is found to be more than 2 for the AE generated from the plastic deformation. The fractal dimension of $m = 2$ is a critical number to evaluate the condition of materials. If there is a damage (i.e., crack) in the material, the fractal dimension becomes lower than 2. From this concept of the fractal dimension, the obtained dimension indicated that the sample had been damaged. However, it is supposed that the lowered fractal dimension was due to the existence of ferroelectric domain and the effect of the deformation related to domain reorientation, instead of the crack in the material, since repeatable and stable field induced AE events were observed.¹²⁾

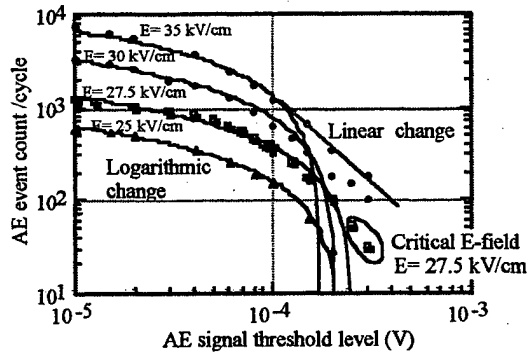


Figure 4 AE event count per cycle as a function of the AE signal threshold level for various bipolar electric field amplitudes.

When the amplitude of electric field was increased, the higher AE signal threshold level parts did not follow to the logarithmic change. A critical amplitude of the electric field, above which non-logarithmic AE distributions were observed, was found to be around $E = 27$ kV/cm. The lower signal threshold level region still could be fitted to a logarithmic curve and the extended line also ended around the AE signal threshold level obtained for ± 25 kV/cm. The higher AE signal threshold level parts ($>10^{-4}$ mV) showed a linear decrease with the threshold level. When an electric field of $E = \pm 35$ kV/cm

was applied, a fractal dimension of $m = 2.8$ was obtained. Figure 5 shows the induced displacement under unipolar and bipolar fields. Although the butterfly shape induced displacement for the bipolar field is due to the domain reorientation, the bipolar field induced displacement coincided with the unipolar field induced displacement above the electric field $E = 27$ kV/cm. Thus, it is assumed that the domain reorientation was completed at higher electric fields than the critical electric field $E = 27$ kV/cm. The origin of the AE with the fractal dimension of 2.8 was assumed not to be the deformation related to domain reorientation, but the piezoelectric deformation without domain reorientation.

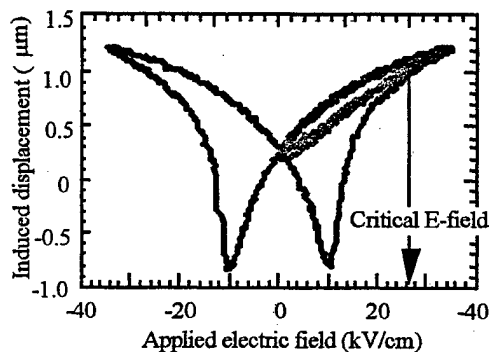


Figure 5 Field induced displacement under unipolar and bipolar fields.

It was shown that the fractal dimension of the field induced AE for the deformation related to domain reorientation ($m = 1$) was lower than that for the piezoelectric deformation without domain reorientation ($m = 2.8$). The fractal dimension greater than two corresponded to the plastic deformation. However, it was difficult to categorize the electrically induced deformation of ferroelectric ceramics as the plastic deformation, because the induced displacement recovers to the initial state after removing the field. Hence, it should be noted that the AE generation process in the ferroelectric ceramics could be different from that of reported AE in the materials such as metals and structural ceramics.

§4. Conclusion

The electric field induced acoustic emissions (AE) in the ferroelectric PZT ceramics were

studied. It is shown that the Kaiser effect in terms of applied electric field (displacement) took place in the electric field induced deformation of ferroelectric PZT ceramics. The AE event rate as a function of applied field and AE signal threshold level distribution were employed to identify the origin of field induced AE. The AE event rate in ferroelectric PZT showed two origins: deformation related to domain reorientation and piezoelectric deformation without domain reorientation. It is assumed that the fractal dimension of the ferroelectric PZT ceramics consisted of the domain reorientation related $m = 1$ and the domain reorientation unrelated $m = 2.8$. A critical bipolar electric field for the domain reorientation unrelated AE generation was found to be $E = 37$ kV/cm.

Acknowledgment

This work was partially supported by the Office of Naval Research through Contract No. N00014-92-J-1510

Reference

- 1) P. Buchman: Solid State Electronics. 15 (1972) 142.
- 2) I. J. Mohamad, E. F. Lambson, A. J. Miller and G. A. Saunders: Phys. Lett. A71 (1979) 115.
- 3) V.A. Kalitenko, V. M. Perga and I. N. Salivonov: Sov. Phys. Solid State 22 (1980) 1067.
- 4) H. Iwasaki and M. Izumi: Ferroelectrics 37 (1981) 563.
- 5) Y. Saito and S. Hori: Jpn. J. Appl. Phys 33 (1994) 5555.
- 6) W. Pan, H. Cao: Ferroelectrics, 129 (1992) 119.
- 7) D.G. Choi and S.K. Choi: J. Mat. Sci., 32 (1997) 421.
- 8) E.C. Subbarao, V. Srikanth, W. Cao, L.E. Cross: Ferroelectrics 145 (1993) 271.
- 9) H. Aburatani, S. Harada, K. Uchino, A. Furuta and Y. Fuda: Jpn. J. Appl. Phys. 33 (1994) 3091.
- 10) H. Aburatani and K. Uchino, Jpn. J. Appl. Phys. 35(1996) L516.
- 11) H. Nakasa: Theoretical Bases and Applications of Acoustic Emission, (Chijin Shokan Co. Ltd., Tokyo, 1994) 1st ed. (in Japanese).
- 12) H. Aburatani, J. P. Witham and K. Uchino, Jpn. J. Appl. Phys. 37(1998) 602.